The Henryk Niewodniczański
INSTITUTE OF NUCLEAR PHYSICS
Polish Academy of Sciences
ul. Radzikowskiego 152, 31-342, Kraków, Poland

www.ifj.edu.pl/publ/reports/2026
Kraków, January 2026

Studies of forward–backward multiplicity correlations with the observable Σ at LHC energies: from experimental data to superposition formalisms

Iwona Sputowska

Habilitation Thesis

This work was supported by the Polish National Science Centre (NCN), grant no. 2021/43/D/ST2/02195.

Wydano nakładem Instytutu Fizyki Jądrowej im. Henryka Niewodniczańskiego
Polskiej Akademii Nauk
Kraków: 2026

ISBN: 978-83-63542-47-4 (print)
ISBN: 978-83-63542-49-8 (pdf)
DOI: https://doi.org/10.48733/978-83-63542-49-8

Abstract

This thesis investigates forward-backward multiplicity correlations in high-energy nucleus-nucleus collisions using the observable Σ, introduced to heavy-ion physics as a strongly intensive quantity. The aim is to determine what physical information is carried by Σ, how it is connected to other correlation and fluctuation observables, and whether it reflects the genuine dynamics of the collision.

The first experimental study of Σ at LHC energies is presented. It is based on ALICE Xe–Xe collisions at $\sqrt{s_{NN}} = 5.44$ TeV and Pb–Pb collisions at $\sqrt{s_{NN}} = 2.76$ and 5.02 TeV, with comparison to pp collisions in the energy range $\sqrt{s} = 0.9 - 13$ TeV. In heavy-ion collisions, Σ appears independent of the centrality estimator and volume fluctuations, but shows a pronounced centrality and system-size dependence. None of the commonly used phenomenological models (HIJING, AMPT, EPOS-LHC) reproduce this behaviour. Proton-proton results, which are quite well described by string-based models, show an opposite trend with multiplicity class, suggesting different mechanisms in small and large systems.

To interpret these findings, Σ is studied within the Wounded Nucleon Model and the Wounded Quark Model. The superposition formalism is then extended to a generalised multi-source framework. This approach allows for separating contributions from source number, type, and emission properties. A new method for reconstructing the wounded constituent fragmentation function is proposed. Finally, a connection is established between the observable Σ and the Chebyshev polynomial expansion used to describe longitudinal fireball fluctuations. Together, these results demonstrate that Σ serves as a robust measure for studies of multiparticle production.

Dla Mojej Rodzinki

Contents

Chapter 1

Introduction

1.1 Scientific context: Why study fluctuations and correlations?

The field of heavy-ion collisions is one of the most challenging areas of modern high-energy physics. Its main goal is to understand how strongly interacting matter behaves under extreme temperatures and densities — and, in particular, whether a new state of matter, **the quark–gluon plasma**, can form.

In relativistic nucleus-nucleus collisions, most of the produced particles come from processes with low four-momentum transfer. These belong to the so-called soft sector, where standard **perturbative QCD** (Quantum Chromodynamics) methods are no longer applicable. In this **non-perturbative** regime, exact calculations from first principles are not possible, so most studies rely on **phenomenological models** or, in some cases, on lattice QCD calculations.

A key challenge in this field is that much of the interesting physics, including signals of a new phase of matter, originates in the *early stage* of the collision, but what we measure in experiments are only the final-state particles. This creates a need for observables that are sensitive to the early stages of the reaction, despite being constructed from final-state particles.

In this context, **event-by-event fluctuation and correlation observables** have gained a lot of attention. In particular, higher-order cumulants of net-particle numbers can be directly compared to lattice QCD predictions near the (pseudo)critical point. At the same time, observables based on forward-backward multiplicity correlations offer complementary information: they reflect the spatial structure and the number of particle-emitting sources in the soft, non-perturbative particle production regime. As this work will also demonstrate, the analysis of longitudinal correlations is an excellent tool for validating the phenomenological models of particle production.

Although such observables are expected to be sensitive to the early stage of the collision, a key open question remains: *to what extent are the results affected by spurious effects originating from final-state interactions (e.g. hadronic re-scattering, resonance decays), global conservation laws, or fluctuations in the system volume due to variations in the initial geometry?* One of the main themes of this work is to help find answers to some aspects of this broad question.

1.2 Phenomenological and experimental limitations: What makes correlations and fluctuations observables difficult to interpret?

Many fluctuation and correlation observables are constructed and interpreted within specific theoretical frameworks, which may deviate from actual experimental conditions and independently limit the interpretability of the observables themselves. Their sensitivity to experimental effects, such as detector acceptance, centrality estimator choice, or event-by-event geometry fluctuations, can obscure the underlying physics and introduce biases that are not always well controlled. An observable may show apparent trends that reflect detector configuration or event selection rather than genuine dynamical effects.

Two examples help to illustrate this general issue. One comes from comparisons between lattice QCD and experimental data; the other relates to the effect of geometric fluctuations on forward-backward correlations.

(1) Among the wide range of proposed observables, only a few — such as the cumulants of conserved charges — can be directly compared with ab initio results from lattice QCD. However, even in these cases, the comparison is far from straightforward. As pointed out in Ref. [1], heavy-ion collisions produce systems that are dynamical, finite in size, highly fluctuating, and only partially observed within a limited detector acceptance. In contrast, lattice QCD calculations are performed in equilibrium, in the thermodynamic limit, and are limited by the sign problem.

(2) For a long time, forward-backward multiplicity correlations were studied using the Pearson correlation coefficient. While this approach worked well in proton-proton collisions, its application to heavy-ion data led to signals initially interpreted as signs of new physics [2]. It was later shown that these results were largely driven by geometry (volume) fluctuations from event to event,

which strongly affect the observable but are not related to the underlying collision dynamics.

Therefore, any observable used for physics interpretation must be carefully validated, both in terms of statistical properties and response to trivial effects. Forward-backward multiplicity correlations, which are the main subject of this thesis, are especially sensitive to volume fluctuation biases, motivating the need for robust, model-independent tools to describe them.

1.3 The observable Σ: promise and open questions

The observable Σ was originally introduced in heavy-ion physics as a strongly intensive quantity within the Independent Source Model (ISM) [3], which is a simple superposition framework where each source emits particles independently. In this framework, Σ is constructed to be free from the effect of the system size and its fluctuations. This makes it an attractive candidate for analyses in which volume effects can bias the interpretation of correlation or fluctuation observables, such as forward-backward multiplicity correlation studies.

This work presents an overview of the first-ever application of Σ as an alternative measure of forward-backward multiplicity correlations. Early results on the longitudinal fluctuations obtained with this quantity, presented in this thesis, are encouraging: Σ appears stable with respect to volume fluctuations and independent of the choice of centrality selection method in the experiment, while revealing nontrivial and potentially meaningful dependencies on the system size and collision energy.

Despite its promising features and growing attention among the physics community, the properties of Σ and the information it provides still *seem not fully understood*. The nature of a strongly intensive quantity follows from the assumptions of a specific model, and it is an open question whether the interesting experimental features of Σ reflect this construction or result from a combination of statistical effects or other system-specific factors. As highlighted in Ref. [1]:

> *"While the strongly intensive quantities have been or are being measured by several experimental collaborations, the question of how to relate them to lattice QCD and other theoretical predictions remains open."*

The intention of the author is to provide at least partial clarification of how the Σ quantity, particularly studied in the context of forward-backward multiplicity correlations, relates to other correlation and fluctuation measures, how it behaves

within a broader range of theoretical frameworks, what kind of information it provides in these models, and to explore its potential as a meaningful observable in the study of nucleus-nucleus collisions.

1.4 Motivation for this study

This work addresses the above issues by undertaking a systematic investigation of forward-backward correlations with Σ, both experimentally and within phenomenological models. The motivation stems from the need to better understand what physical information this observable carries in the context of longitudinal fluctuation analysis, how it can be interpreted in terms of particle-emitting source dynamics, and under what conditions it fulfils its intended properties.

The study presented in this thesis develops along two complementary lines:

(1) a detailed experimental study of forward-backward multiplicity correlations with Σ in heavy-ion and proton-proton collisions, carried out under varying experimental conditions, providing new and interesting information about particle production mechanisms and, at the same time, constraints on models; and

(2) a theoretical and phenomenological investigation of Σ, including placing it in the broader context of other fluctuation and correlation measures, and the development of a more general interpretative framework suited to multi-source systems.

Together, these two components form a unified approach: experimental data challenge the models of particle production, while models provide the tools to interpret the measurements.

The experimental analysis includes Pb–Pb collisions at centre-of-mass energies per nucleon pair, $\sqrt{s_{NN}} = 2.76$ and 5.02 TeV, and Xe–Xe collisions at $\sqrt{s_{NN}} = 5.44$ TeV, as well as pp collisions at $\sqrt{s} = 0.7$–13 TeV. The data were collected by the ALICE experiment at the Large Hadron Collider (LHC).

This work focuses on a detailed analysis of the observable Σ and its application to the study of forward-backward correlations in nuclear collisions. Although Σ was defined in the context of the Independent Source Model, the analysis does not assume that the model itself provides a complete or accurate description of reality. Instead, the aim is to investigate how Σ behaves in experimental data and within different theoretical approaches, and what kind of physical information — particularly

regarding fluctuations, correlations, and particle emission — can be extracted from it.

Special attention is given to how Σ relates to other correlation- and fluctuation-sensitive observables, and whether or under which conditions it reveals features of the system that other variables remain insensitive to. This study aims to show that Σ, even if it does not fulfil all the theoretical assumptions of ISM, can still serve as a highly sensitive and valuable diagnostic tool, especially for exploring source structure and spatial asymmetries in the particle-emission process.

Ultimately, the aim is not only to test how Σ performs, but to understand what it actually *means*—and what it can tell us about the structure of particle production in the experimental reality of high-energy heavy-ion collisions.

1.5 Author's Contribution

The results presented in this habilitation thesis are based on experimental data from the ALICE experiment at the CERN Large Hadron Collider. ALICE is a large scientific collaboration, currently comprising around 1,900 members from 38 countries and 166 institutes [4]. As is standard in modern high-energy nuclear physics, data taking, detector operation, calibration, and the preparation of analysis-level data are part of a collective effort within this international team. It therefore seems appropriate to specify the role of the author in the process of obtaining the results presented in this thesis. This includes participation in data taking, contributions to the Collaboration's physics and coordination activities, and execution of the experimental analysis and its phenomenological interpretation.

This role can be quantified as follows:

- I have been a member of the ALICE Collaboration since 2011, and I have actively participated in data-taking shifts since then as a TPC and DCS (Detector Control System) and QC (Quality Control) shifter. I became a QC Expert shifter in 2023.

- I have been a member of the ALICE Conference Committee since December 2022, contributing to the coordination of conference presentations and speaker selections. As part of this role, I ensure that all presentations and posters comply with the ALICE policy guidelines for data presentation and public communication. I actively participate in the review process, helping to shape how ALICE results are communicated to the broader community and ensuring they reflect the high standards of the Collaboration.

– Since June 2025, I have served as the Coordinator of the Physics Analysis Group "Event-by-Event Correlations and Fluctuations" (PWG-CF-PAG-EbyE), overseeing physics analyses in this domain and ensuring they meet the high-quality standards expected within the ALICE Collaboration.

– I have been actively involved in the experimental analysis workflow through participation in several Analysis Review Committees (ARCs) and Internal Review Committees (IRCs) as well as an Internal Referee, contributing to the validation of ALICE analyses and publications.

– I am the author and initiator of the forward-backward correlations analysis using the Σ quantity in heavy-ion collisions at the LHC, presented in this habilitation thesis. The results of this analysis are described in Chapter 5. I performed the full experimental analysis, including the extraction of the Σ observable from ALICE data, application of corrections, and systematic uncertainty studies.

– I developed the theoretical framework and phenomenological interpretation of the Σ observable within this thesis. This includes its formulation in a two-component wounded constituent model and its extension to a multi-source scenario. Within this model, I propose a new method for extracting the fragmentation function of wounded constituents, applicable for the first time to symmetric collisions. I established a connection between the Σ observable and the decomposition of the two-particle correlation function into Chebyshev polynomials (Chebyshev expansion), linking Σ to specific harmonic components of the longitudinal structure of the system. I also demonstrated how Σ in the wounded constituent model relates to the partial covariance technique.

The experimental results presented in this thesis already have the ALICE preliminary status. A full journal publication is in preparation. The results have been shown at multiple international conferences and are included in several peer-reviewed conference proceedings. The results of a phenomenological study of Σ in the two-component wounded constituent model have already been published in *Physical Review C* [5]. It should be noted that the present paper also presents new phenomenological calculations that have not been published hitherto.

1.6 Outline of the paper

The structure of this thesis is as follows. Chapter 2 introduces the basic terminology and observables used in fluctuation and correlation analyses. Chapter 3 discusses the general formalism of event-by-event fluctuations, with a focus on strongly intensive quantities Σ and Δ. The main aim of Chapters 2 and 3 is to guide the reader through a wide range of existing approaches to measuring correlations and fluctuations, to reveal the conceptual links between them, and to embed quantities Σ and Δ in this broader context. This theoretical foundation provides the necessary basis for the experimental and phenomenological studies presented in the following chapters.

Chapters 4 and 5 are dedicated to the experimental studies of Σ carried out by the author within ALICE at the LHC. Chapter 4 describes the experimental analysis, including the ALICE detector setup, event and track selection, and applied corrections. In Chapter 5, results on forward-backward correlations with Σ are presented for Pb–Pb, Xe–Xe, and pp collisions.

Chapters 6 and 7 build upon the experimental results by examining how the observable Σ can be understood in the context of phenomenological models. Chapter 6 provides a model-based interpretation of Σ using wounded-nucleon and wounded-quark frameworks. The multi-source approach and decomposition of Σ into distinct fluctuation components are developed in Chapter 7. Finally, Chapter 8 summarises the key conclusions and outlines directions for future work. Supplementary derivations, extended formulas, and additional material are collected in Appendices A–E.

Chapter 2

Defining basic terms in heavy-ion correlations and fluctuations

This chapter introduces the fundamental terms and concepts in heavy-ion collisions, essential for understanding the multiplicity correlations and fluctuations of produced charged particles, which are the central topics of the study presented in this work.

The discussion begins with a brief overview of the kinematic variables crucial for categorising events in heavy-ion collisions. Then, the geometry of collisions and its impact on particle distributions will be addressed. Finally, concepts such as multiplicity distributions and multiparticle density functions will be introduced.

2.1 Kinematic variables

Momentum components and kinematic angles

In general, particles produced in high-energy collisions are identified by their momenta, denoted as $\vec{p} = (p_x, p_y, p_z)$, and their energies, E, measured in a detector.

In heavy-ion collisions, it is customary to decompose the particle momentum $\vec{p}$ into components relative to the beam direction (z-axis), such as:

- **longitudinal momentum**, a component parallel to the beam axis, $p_{\mathrm{L}} = p_z$.
- **transverse momentum**, a component perpendicular to the beam axis, $p_{\mathrm{T}} = \sqrt{p_x^2 + p_y^2}$.

The orientation of the particle's transverse momentum in the plane perpendicular to the beam direction, called transverse plane (x–y plane), can be determined by providing information about its **azimuthal angle** φ, defined as $\varphi = \tan^{-1}\left(\frac{p_{\mathrm{y}}}{p_{\mathrm{x}}}\right)$.

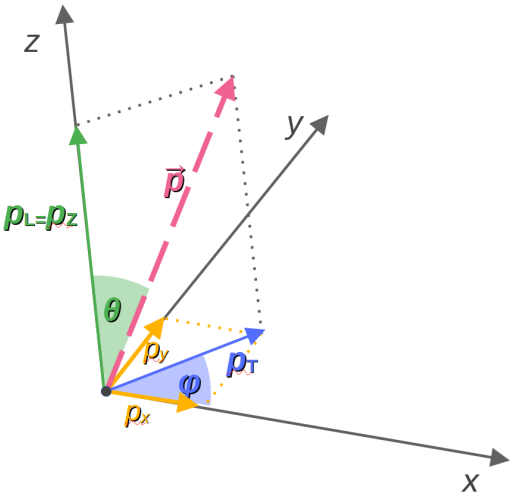

Figure 2.1: Decomposition of a particle's total momentum $\vec{p}$ into longitudinal momentum (p_{L}) along the beam axis (z-axis) and transverse momentum (p_{T}) in the x–y plane (transverse plane). The polar angle θ and azimuthal angle φ describe the particle's emission direction.

In addition to the transverse momentum, the related *transverse energy* ($E_{\mathrm{T}} = E\sin\theta$) is often introduced to describe the energy deposited in the transverse plane, especially in calorimetric measurements and global event observables.

Rapidity and pseudorapidity

Rapidity (y) and **pseudorapidity** (η) are fundamental kinematic variables used to describe the angular/spatial distribution of particles produced in high-energy collisions.

The rapidity of a particle with longitudinal momentum p_z (the component of momentum along the beam axis) and energy E is defined as:

$$y = \frac{1}{2}\ln\left(\frac{E+p_z}{E-p_z}\right) \tag{2.1}$$

Rapidity, y, is a convenient dimensionless measure for relativistic velocity since it transforms additively under the Lorentz boost along the z-axis.

Pseudorapidity, η, is a variable related conceptually to rapidity, which is easier to determine experimentally as it does not require identifying the particle's mass. The η variable depends only on the angle of the particle θ with respect to the direction of the beam. It is particularly useful when the momentum or energy of the particle is unknown or difficult to measure in the experiment. The following expression defines pseudorapidity in two equivalent ways. In the first one, η is expressed as a function of particle emission angle θ in relation to the axis of the beam:

$$\eta = -\ln\left[\tan\left(\frac{\theta}{2}\right)\right] \tag{2.2}$$

Alternatively, it can also be represented through a function that is dependent on the momentum of the particle:

$$\eta = \frac{1}{2} \ln \left(\frac{|\vec{p}| + p_z}{|\vec{p}| - p_z} \right) \tag{2.3}$$

It is immediately apparent from the comparison of expressions Eq. 2.1 and Eq. 2.3 that for highly relativistic particles ($E \approx |\vec{p}|$) the difference between pseudorapidity and rapidity becomes negligible, namely $\eta \approx y$.

2.2 Key concepts used to define heavy-ion collision geometry

Atomic nuclei vary in size, with diameters typically ranging from about 2–4 femtometers (fm) for light nuclei to approximately 15 fm for heavy nuclei such as lead (Pb). During collisions between atomic nuclei, the degree of overlap can vary significantly, from head-on collisions, referred to as central collisions, to those where the nuclei barely touch, known as peripheral collisions[1].

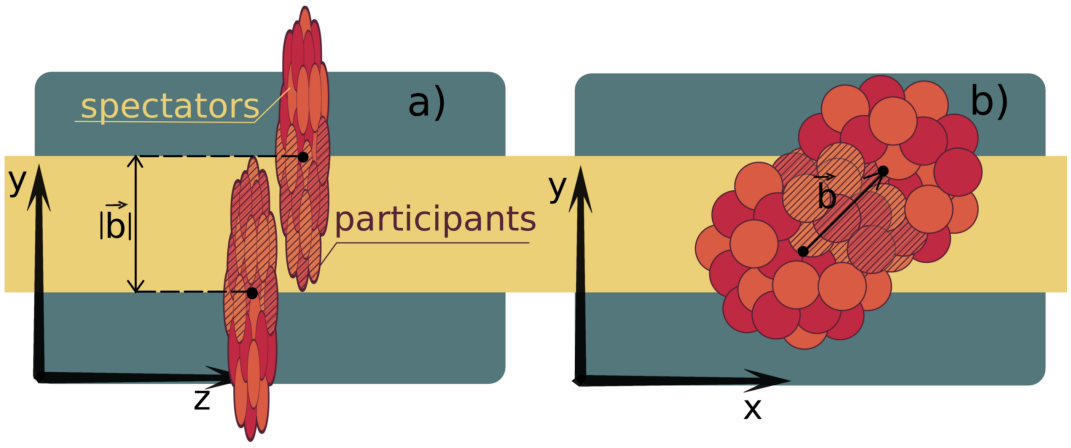

Figure 2.2: Schematic representation of a non-central heavy-ion collision at impact parameter $\vec{b}$. Panel (a) shows the projection in the y–z plane, highlighting the spatial separation between the two colliding nuclei defined by the impact parameter vector $\vec{b}$, as well as nucleons classified as **participants** and **spectators**. Panel (b) presents a transverse view (x–y plane) of the colliding nuclei, where the overlapping region corresponds to participants and the vector $\vec{b}$ connects the centres of the nuclei.

[1]One can also distinguish so-called ultraperipheral collisions (UPC) as interactions where the nuclei have no direct contact via strong interactions, often leading to photon-mediated processes. These are not the subject of this work.

Participants, spectators and impact parameter

The total volume of the interacting region during a nucleus-nucleus collision can be classified with the absolute value of the **impact parameter** ($\vec{b}$). The impact parameter is defined as the vector between the centres of the colliding nuclei in a plane perpendicular to the beam direction, as illustrated in Fig. 2.2.

Another way to categorise the event's geometry is based on the semi-classical geometrical picture of a nuclear collision, known as the **Glauber framework** [6]. This framework views a nuclear collision as a series of individual nucleon interactions, with each nucleon travelling on a straight-line trajectory. Within this approach, collision geometry can be defined using concepts such as **the number of participants** (N_{part}), which refers to the nucleons that undergo at least one inelastic collision. Nucleons not involved in any collisions are termed **spectator nucleons** (N_{spec}).

Centrality

In experimental physics, the geometry of the collisions is usually quantified using the concept of **centrality**. The centrality of a nucleus-nucleus collision with an impact parameter b is defined as a percentile of the total nuclear interaction cross section (σ_{AA}) as follows:

$$\mathrm{c}(b) = \frac{\int_0^b \frac{d\sigma}{db'} db'}{\int_0^\infty \frac{d\sigma}{db'} db'} = \frac{1}{\sigma_{\mathrm{AA}}} \int_0^b \frac{d\sigma}{db'} db'. \tag{2.4}$$

In the above formula, $\frac{d\sigma}{db'}$ is the differential cross-section with respect to the impact parameter b'.

Quantities, such as the impact parameter or the number of participants, widely used in theoretical literature to describe the geometry of heavy-ion collisions, *are not directly measurable*. As a result, experimentally, centrality is inferred from observables that scale monotonically with these quantities, such as particle multiplicity, transverse energy or the energy of non-interacting spectators measured by zero-degree calorimeters. In that context, centrality is often redefined as, e.g. the percentile of events with the largest number of produced particles (as registered in detectors), largest E_{T}, or the lowest energy of spectator (as determined from zero-degree calorimeters).

2.3 Basic observables in particle production

2.3.1 Charged-particle multiplicity and its distribution

Information about the number of charged particles (**charged-particle multiplicity**), n_{ch}, emitted in collisions is one of the fundamental observables in high-energy physics. Most of our knowledge about particle production in high-energy nuclear collisions comes precisely from measurements of charged particles. On the one hand, this is due to their abundance, since charged particles constitute about two-thirds of all produced particles, and on the other, to the fact that charged particles are much easier to detect than neutral ones [7].

The charged-particle multiplicity distribution

The charged-particle multiplicity distribution $P(n_{ch})$ is defined experimentally, in terms of the frequency probability based on a large set of collision events N_{ev}, as the probability of observing n_{ch} charged particles in an event. This definition is expressed mathematically as follows:

$$P(n_{ch}) = \frac{N_{\mathrm{ev}}(n_{ch})}{N_{\mathrm{ev}}^{tot}}, \tag{2.5}$$

where $N_{\mathrm{ev}}(n_{ch})$ represents the number of events with n_{ch} charged particles, and N_{ev}^{tot} is the total number of events analysed.

A wide range of studies over the years have examined the meaning and implications of multiplicity distributions in high-energy collisions, offering valuable insights into the mechanisms of particle production Refs. [1, 8, 9, 10, 11]. A particularly comprehensive summary of these developments is presented in Ref. [8], which also serves as a basis for the discussion presented below.

The multiplicity distribution can be studied over the entire phase space or in its selected sub-regions. Analysing the multiplicity distribution over the whole phase space provides comprehensive information about all sub-processes contributing to particle production, which are subject to the constraints of conservation laws, such as energy, momentum, charge, and baryon number conservation. The study in a limited region of the phase space, such as in chosen ranges of η or p_T, allows for the selection of mechanisms contributing to particle production, as different sub-processes may dominate in different phase space regions.

Shape of multiplicity distribution

During heavy-ion collisions, multiple processes originating from distinct particle production sources might influence the shape of the multiplicity distribution. Analysis of the distribution's shape and its variations gives us a chance to gain insights into the mechanisms underlying particle production. For instance, independent particle emission, characterised by the absence of correlations between the emission of individual particles, results in a Poisson multiplicity distribution. A particular focus on the shape of the multiplicity distribution, especially its deviation from a Poisson distribution, might reveal the degree of correlation among final-state particles [8].

Two main strategies for analysing the shape of the multiplicity distribution can be distinguished: fitting analytical formulas to the measured distribution or determining its statistical moments, including first-, second-, and higher-order moments.

When it comes to the first method, over the years, researchers have used various models to describe how particle multiplicity behaves in collision experiments, especially as the collision energy increases. One of the early ideas, known as the Koba-Nielsen-Olesen (KNO) scaling [12], suggested that when the number of charged particles is scaled by its average, the resulting distribution should look the same regardless of collision energy. This seemed to work well at lower $\sqrt{s}$, and remained approximately valid up to the highest energies at the Intersecting Storage Rings (ISR) [13]. Although small deviations, particularly in the high-multiplicity region, were already visible. On the other hand, the Negative Binomial Distribution (NBD) matched the experimental data quite well up to about $\sqrt{s}$=540 GeV in full phase space; nevertheless, small discrepancies appeared in the tails. However, the model often needs to be adjusted at even higher energies (starting around $\sqrt{s}$= 900 GeV), usually by combining two NBD components to account for both soft and semi-hard particle production processes [11, 14].

Moments of multiplicity distribution

The second approach is more general and does not require assuming any specific distribution shape. In general, **the k-th order moment of multiplicity distribution** is defined as:

$$\langle n_{\alpha_i}^k \rangle = \sum_{n_{\alpha_i}=0}^{\infty} n_{\alpha_i}^k \, P_{\alpha_i}(n_{\alpha_i}), \tag{2.6}$$

where $P_{\alpha_i}(n_{\alpha_i})$ is the probability of observing n_{α_i} particles in the region α_i. In this context, α_i may represent a pseudorapidity interval of width $\delta\eta = [\eta_1, \eta_2]$, as

illustrated in Fig. 2.3.

The **mixed moment of orders k and l of the multiplicity distribution**, characterizing the joint distribution of particle counts in regions α_1 and α_2, is given by:

$$\langle n_{\alpha_1}^k n_{\alpha_2}^l \rangle = \sum_{n_{\alpha_1}=0}^{\infty} \sum_{n_{\alpha_2}=0}^{\infty} n_{\alpha_1}^k n_{\alpha_2}^l \, P(n_{\alpha_1}, n_{\alpha_2}), \tag{2.7}$$

where $P(n_{\alpha_1}, n_{\alpha_2})$ denotes the joint probability of finding n_{α_1} particles in α_1 and n_{α_2} particles in α_2 within the same event.

While the first moment of multiplicity distribution ($k = 1$), $\langle n_{\alpha_i} \rangle$, characterises the global properties of final-state hadrons and their evolution with energy and system size, it does not provide any information on the shape of the distribution or the event-by-event fluctuations in particle production. To access this information, one must consider higher-order ($k \geq 2$) and mixed moments, and their combinations.

The moments of the multiplicity distribution provide integrated information about particle production over phase space and lack sensitivity to the spatial and momentum structure of the final state. Capturing the spatial structure of particle production requires a differential approach, which is provided by the framework of multi-particle density functions.

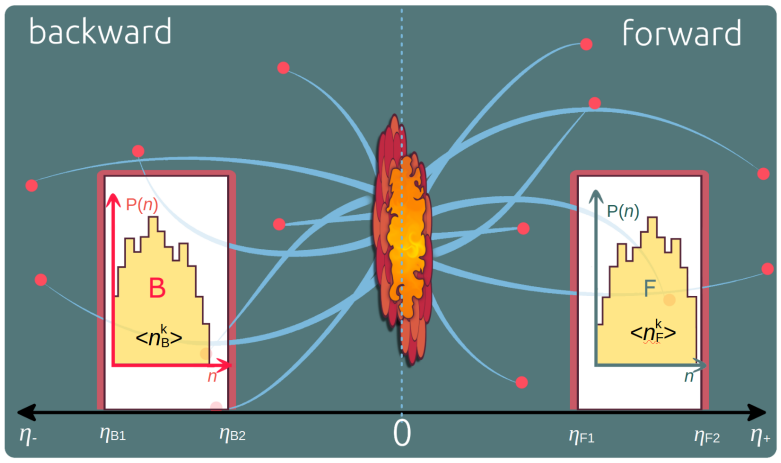

Figure 2.3: Schematic illustration of the multiplicity distributions $P(n)$ measured in two separated pseudorapidity intervals: backward (B) and forward (F), defined by the regions $\eta \in [\eta_{B1}, \eta_{B2}]$ and $\eta \in [\eta_{F1}, \eta_{F2}]$, respectively. The k-th order moments $\langle n_B^k \rangle$ and $\langle n_F^k \rangle$ characterise the shape and fluctuations of the multiplicity distributions in each region.

2.3.2 Multi-particle density functions and factorial moments

Multi-particle density functions encode information about particle production in phase space. The general form of an N-particle density function is given by:

$$\rho_n^{\alpha_1,\alpha_2...,\alpha_n}(y_1, y_2, ..., y_n), \tag{2.8}$$

where the indices α_i denote either the particle species (e.g., π^+, K^-, p) or a selection based on kinematic properties (e.g., particles in a forward-rapidity range), and y_i represents phase-space coordinates such as rapidity (y) or transverse momentum (p_T). Specific cases include:

- **Single-particle density (N=1):** $\rho_1^{\alpha_1}(y)$, and describes the probability density of finding a particle of type α_1 at position y.
- **Two-particle density (N=2):** $\rho_2^{\alpha_1\alpha_2}(y_1, y_2)$ the joint probability density of simultaneously finding one particle of type α_1 at position y_1 and another of type α_2 at position y_2.

The single- and two-particle densities can be expressed by inclusive differential cross sections σ^{α_m} for particles of type α_m via:

$$\rho_1^{\alpha_1}(y) = \frac{1}{\sigma_{\text{inel}}}\frac{d\sigma^{\alpha_1}}{dy}, \tag{2.9}$$

$$\rho_2^{\alpha_1\alpha_2}(y_1, y_2) = \frac{1}{\sigma_{\text{inel}}}\frac{d^2\sigma^{\alpha_1\alpha_2}}{dy_1 dy_2}, \tag{2.10}$$

where σ^{inel} is the total inelastic cross section.

Factorial moments as integrated multiparticle densities

By integrating particle densities over a phase space element Ω, we obtain what is known as the **factorial moments** of the number of particles. These moments provide information on the average over the event ensemble number of n-tuples of particles emitted within the specified volume regions.

The first and second factorial moments are given by:

$$\int_\Omega \rho_1(y)\, dy = \langle n \rangle \tag{2.11}$$

$$\int_{\Omega_1}\int_{\Omega_2} \rho_2^{\alpha_1\alpha_2}(y_1, y_2)\, dy_1\, dy_2 = \langle n_{\alpha_1}(n_{\alpha_2} - \delta^{\alpha_1\alpha_2})\rangle \tag{2.12}$$

In higher-order analysis, the general factorial moment takes the form:

$$\int_{\Omega_1}\int_{\Omega_2}\cdots\int_{\Omega_N}\rho_N(y_1,y_2,\ldots,y_N)\,dy_1\,dy_2,\ldots,\,dy_N = \tag{2.13}$$

$$\langle n_{\alpha_1}\left[n_{\alpha_2}-\delta^{\alpha_1,\alpha_2}\right]\cdots\left[n^{\alpha_N}-\delta^{\alpha_1,\alpha_N}-\cdots-\delta^{\alpha_{N-1},\alpha_N}\right]\rangle \tag{2.14}$$

Here, the Kronecker delta $\delta^{\alpha_i,\alpha_j}$ ensures that contributions from indistinguishable particles are properly accounted for.

The factorial moments introduced above can be expressed in terms of raw moments of multiplicity distribution defined in Eq. 2.6 and Eq. 2.7. This equivalence highlights the complementarity between the event-based, discrete multiplicity framework and the continuous formalism based on multi-particle density functions.

Chapter 3

Correlations and fluctuations

This chapter introduces the formal framework necessary for conducting event-by-event analyses of forward-backward multiplicity correlations in heavy-ion collisions. It focuses on the use of strongly intensive quantities Σ and Δ. These quantities are placed within the broader context of correlation and fluctuation observables, including cumulants, two-particle correlation functions, and their normalised forms. The aim is to highlight the distinct insights and methodological advantages offered by Σ and Δ, as well as their connection to other analytical approaches.

3.1 Covariance and correlation: fundamental concepts

A wide range of techniques is employed in heavy-ion physics to study correlations and fluctuations, as illustrated in Fig. 3.1. These methods differ in their sensitivity to specific phenomena and their adaptability to experimental conditions. Despite these differences, they share fundamental properties and rely on the core concept of the correlation function [15].

This section summarises the **basic statistical concepts** central to correlation and fluctuation analyses. The starting point is the definitions of **covariance** and **correlation**, which are essential for introducing more advanced observables, particularly strongly intensive quantities that are central to the analyses in this thesis. The discussion closely follows Refs. [8, 15], which provide detailed derivations.

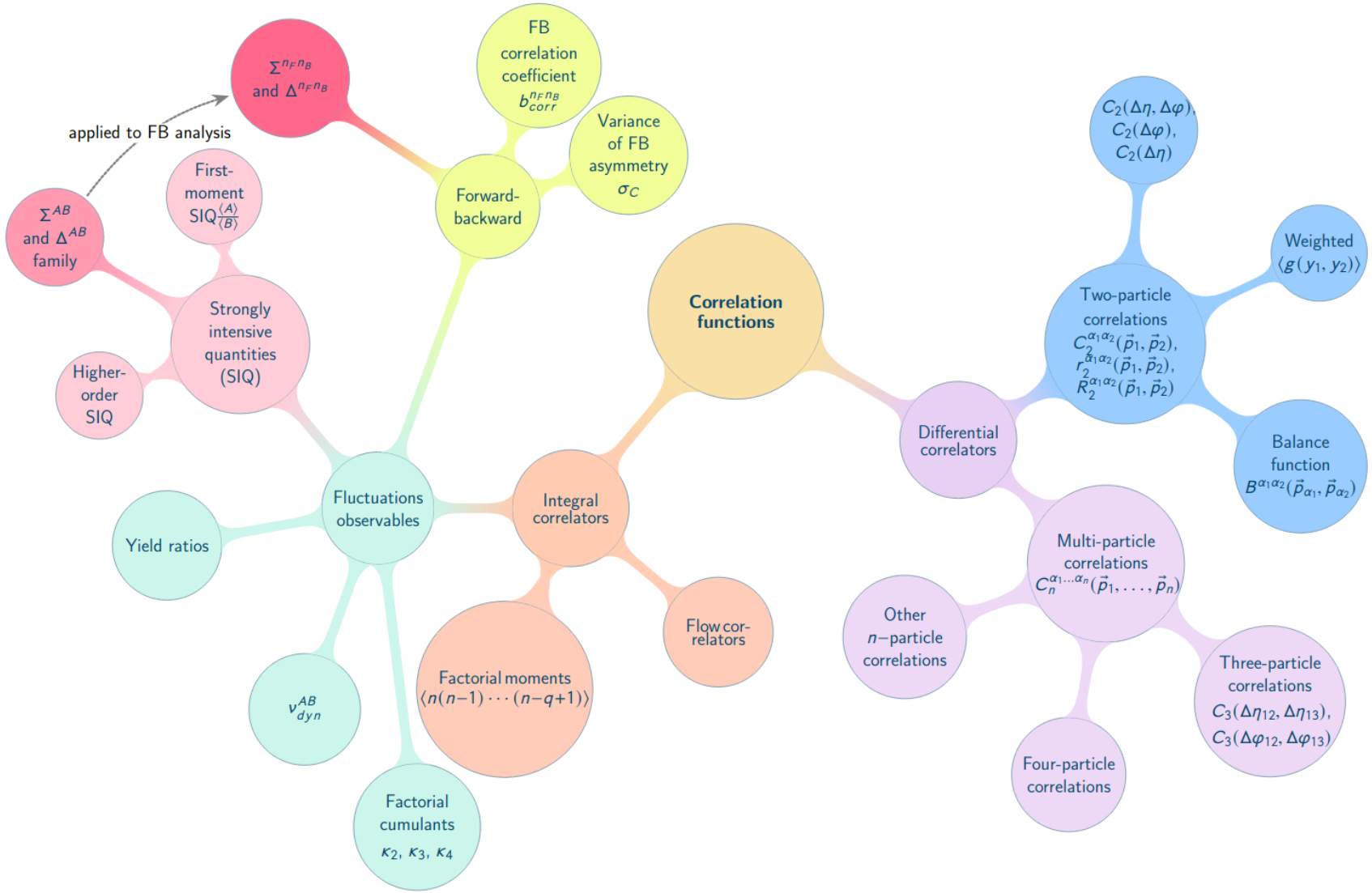

Figure 3.1: The diagram presents the analysis techniques discussed in this work, together with the relations between them, used in the study of correlations and fluctuations in high-energy collisions. The figure is inspired by a diagram in Ref. [15].

3.1.1 Covariance: a measure of joint variability

The covariance is a quantitative measure of the joint variability between two random variables, X and Y, defined by the equation:

$$\mathrm{Cov}(X,Y) = \mathbb{E}[(X - \mathbb{E}[X])(Y - \mathbb{E}[Y])] = \mathbb{E}[XY] - \mathbb{E}[X]\mathbb{E}[Y], \tag{3.1}$$

The special case where $X{=}Y$ corresponds to the covariance of a random variable with itself, which is known as **the variance**:

$$\mathrm{Var}(X) = \mathrm{Cov}(X,X) = \mathbb{E}[X^2] - \mathbb{E}[X]^2. \tag{3.2}$$

In these formulas, $\mathbb{E}[X]$ represents the expectation value of the random variable X. In the remainder of this work, we denote averages by angle brackets, $\langle\cdot\rangle$, so that the covariance can be equivalently written as

$$\mathrm{Cov}(X,Y) = \langle XY\rangle - \langle X\rangle\langle Y\rangle. \tag{3.3}$$

3.1.2 Correlation functions

In heavy-ion collisions, the concept of covariance between particle densities is the foundation of the notion of the **correlation function**. The formalism of the correlation function and its application to nuclear collision studies have already been extensively described in the literature. This section briefly summarises the main concepts, drawing primarily from Refs. [8, 16], to provide the necessary theoretical background for the later discussion of forward-backward multiplicity correlations with strongly intensive quantities.

3.1.2.1 Differential correlators

Two-particle correlation function

The two-particle correlation function is formally defined as

$$C_2^{\alpha_1\alpha_2}(\vec{p}_1,\vec{p}_2) = \rho_2^{\alpha_1\alpha_2}(\vec{p}_1,\vec{p}_2) - \rho_1^{\alpha_1}(\vec{p}_1)\,\rho_1^{\alpha_2}(\vec{p}_2), \tag{3.4}$$

where $\vec{p}_1$ and $\vec{p}_2$ are the momentum vectors of the two particles. The indices α_1 and α_2 may denote either different particle species or, more generally, particles selected from distinct kinematic regions. Here, $\rho_1^{\alpha}(\vec{p})$ represents the single-particle

density distribution, while $\rho_2^{\alpha_1\alpha_2}(\vec{p}_1, \vec{p}_2)$ denotes the corresponding two-particle density distribution.

There are alternative ways to define the correlation function. Normalising this quantity by dividing it by the product of the single-particle densities is sometimes convenient. This makes the resulting function dimensionless and easier to interpret, especially when comparing results across different collision systems or event centralities. Normalised definitions of the correlation function usually take one of two forms:

$$r_2^{\alpha_1\alpha_2}(\vec{p}_1, \vec{p}_2) = \frac{\rho_2^{\alpha_1\alpha_2}(\vec{p}_1, \vec{p}_2)}{\rho_1^{\alpha_1}(\vec{p}_1)\,\rho_1^{\alpha_2}(\vec{p}_2)} \tag{3.5}$$

$$R_2^{\alpha_1\alpha_2}(\vec{p}_1, \vec{p}_2) = \frac{C_2^{\alpha_1\alpha_2}(\vec{p}_1, \vec{p}_2)}{\rho_1^{\alpha_1}(\vec{p}_1)\,\rho_1^{\alpha_2}(\vec{p}_2)} = r_2^{\alpha_1\alpha_2}(\vec{p}_1, \vec{p}_2) - 1. \tag{3.6}$$

The quantities defined by expressions (3.5) and (3.6) are also called *normalised inclusive density* and *normalised cumulant*, respectively.

The general form of the two-particle correlation function, defined in the domain of particle momenta $\vec{p}_1$ and $\vec{p}_2$, depends on six variables (three momentum components per particle), and offers a complete description in momentum space. Such a general definition is not always necessary nor practical. Often, some of these degrees of freedom can be integrated[1]. The resulting correlation functions are then expressed in terms of more experimentally relevant variables, such as transverse momentum (p_T), rapidity (y) or pseudorapidity (η), and azimuthal angle (φ).

Below, we discuss several common differential correlation functions used in heavy-ion collision studies:

- The two-particle azimuthal correlation function $C_2(\varphi_1, \varphi_2)$ describes the angular relationship between particle pairs at azimuthal angles φ_1 and φ_2 in the transverse plane. In case of azimuthal symmetry, it is usually expressed as a function of the relative angle $\Delta\varphi = \varphi_1 - \varphi_2$:

$$C_2(\Delta\varphi) = \frac{dN_{\text{pair}}}{d\Delta\varphi}. \tag{3.8}$$

[1]This procedure corresponds to the marginalisation in the statistical sense:

$$C_2^{\alpha_1\alpha_2}(\eta_1, \eta_2) = \int \mathrm{d}p_{T1}\, p_{T1} \int \mathrm{d}\phi_1 \int \mathrm{d}p_{T2}\, p_{T2} \int \mathrm{d}\phi_2\, C_2^{\alpha_1\alpha_2}(\vec{p}_1, \vec{p}_2), \tag{3.7}$$

The azimuthal correlations can be decomposed into a Fourier series,

$$C_2(\Delta\varphi) \propto 1 + \sum_{n=1}^{\infty} 2\,\Delta V_n \cos(n\Delta\varphi), \tag{3.9}$$

where the coefficients ΔV_n quantify the harmonic modulation of particle pairs [15, 17]. In the literature, different notations are in use: experimental works often denote these coefficients as ΔV_n or $V_{n\Delta}$, while the single-particle flow harmonics are written as v_n. If the observed correlations arise only from collective hydrodynamic anisotropy, the extracted ΔV_n coefficients reflect the underlying flow harmonics, namely the relation $\Delta V_n \approx v_n^2$ holds [15, 17].

- Two-particle pseudorapidity correlation functions $C_2(\eta_1, \eta_2)$ characterise the longitudinal structure of particle production, by providing information on how pairs of particles are distributed as a function of their pseudorapidities η_1 and η_2. Similar to azimuthal correlations, in collider experiments with symmetric rapidity coverage near mid-rapidity, they can be parametrised in terms of the relative pseudorapidity $\Delta\eta = \eta_1 - \eta_2$, namely $C_2(\Delta\eta)$.

  Theoretical studies suggest that long-range correlations in rapidity may arise from fluctuations in the rapidity density of the produced fireball[2]. Bzdak and Teaney proposed in Ref. [18] a new approach to studying the longitudinal shape of the fireball based on the orthogonal polynomial decomposition of the two-particle correlation functions, employing, for instance, Chebyshev polynomials. This approach is summarised in Appendix A and is analogous to the decomposition of azimuthal correlations into a Fourier series.

  According to Ref. [18], the two-particle correlation function $C(\eta_1, \eta_2)$ for particles with (pseudo)rapidities η_1 and η_2 can be expanded in terms of Chebyshev polynomials in the form:

$$C_2(\eta_1, \eta_2) = \rho(\eta_1)\rho(\eta_2) \sum_{i,k=0}^{\infty} \langle a_i a_k \rangle T_i\left(\frac{\eta_1}{Y}\right) T_k\left(\frac{\eta_2}{Y}\right), \tag{3.10}$$

  where Y is the half-width of the pseudorapidity acceptance. The choice of orthogonal polynomials, in this case Chebyshev polynomials, ensures that each term in the expansion represents an independent fluctuation mode. The coefficients a_i determine the contribution of each mode. The formal definition

[2]The term "fireball" refers to the hot and dense medium of strongly interacting matter, created shortly after the collision, which subsequently expands and cools.

and properties of Chebyshev polynomials are provided in Appendix A.

Later in this chapter, we will discuss the existence of a direct relationship between the forward-backward strongly intensive quantity Σ and the asymmetric Chebyshev coefficients $\langle a_{2n+1}a_{2m+1}\rangle$ obtained from the decomposition of the two-particle correlation function. The formal derivation of this result is presented in Appendix A. This connection provides a novel interpretation of forward-backward fluctuations in terms of the asymmetry in the longitudinal structure of particle production. Experimentally, two-particle longitudinal correlations have been extensively studied in heavy-ion collisions, for example by the ATLAS Collaboration [19, 20].

- Two-particle correlations are also studied as joint distributions in both relative pseudorapidity and azimuthal angle, expressed as $C(\Delta\eta, \Delta\varphi)$ [21, 22]. By projecting $C_2(\Delta\eta, \Delta\varphi)$ onto the $\Delta\varphi$ axis, one obtains the azimuthal correlation function $C_2(\Delta\varphi)$. Similarly, projection onto the $\Delta\eta$ axis yields the longitudinal correlation function $C(\Delta\eta)$.

- A specific type of two-particle correlation that provides information on how a conserved quantity, such as the electric charge, is locally balanced in the process of particle production, is referred to as the **balance function** [16, 23, 24, 25, 26, 27]. In the notation introduced above, it is defined as [26]:

$$B^{\alpha_1\alpha_2}(\vec{p}_{\alpha_1}, \vec{p}_{\alpha_2}) = \frac{1}{2}\Bigg\{ \frac{1}{\rho_1^{\alpha_2^-}(\vec{p}_{\alpha_2^-})}\Big[R_2^{\alpha_1^+\alpha_2^-}(\vec{p}_{\alpha_1^+}, \vec{p}_{\alpha_2^-}) - R_2^{\alpha_1^-\alpha_2^-}(\vec{p}_{\alpha_1^-}, \vec{p}_{\alpha_2^-})\Big] + \frac{1}{\rho_1^{\alpha_2^+}(\vec{p}_{\alpha_2^+})}\Big[R_2^{\alpha_1^-\alpha_2^+}(\vec{p}_{\alpha_1^-}, \vec{p}_{\alpha_2^+}) - R_2^{\alpha_1^+\alpha_2^+}(\vec{p}_{\alpha_1^+}, \vec{p}_{\alpha_2^+})\Big]\Bigg\}, \tag{3.11}$$

where α_1 and α_2 denote arbitrary particle species carrying a conserved quantum number (e.g., electric charge or baryon number) and labels + and − stand for positive and negative charges.

The multi-particle correlation function

Similar to the two-particle correlation function $C_2^{\alpha_1\alpha_2}(\vec{p_1}, \vec{p_2})$, one can define a multi-particle correlation function $C_N^{\alpha_1\ldots\alpha_N}(\vec{p}_1, \ldots, \vec{p}_N)$, where N denotes the number of particles considered in the correlation function. In general, $C_N^{\alpha_1\ldots\alpha_N}(\vec{p}_1, \ldots, \vec{p}_N)$ is the

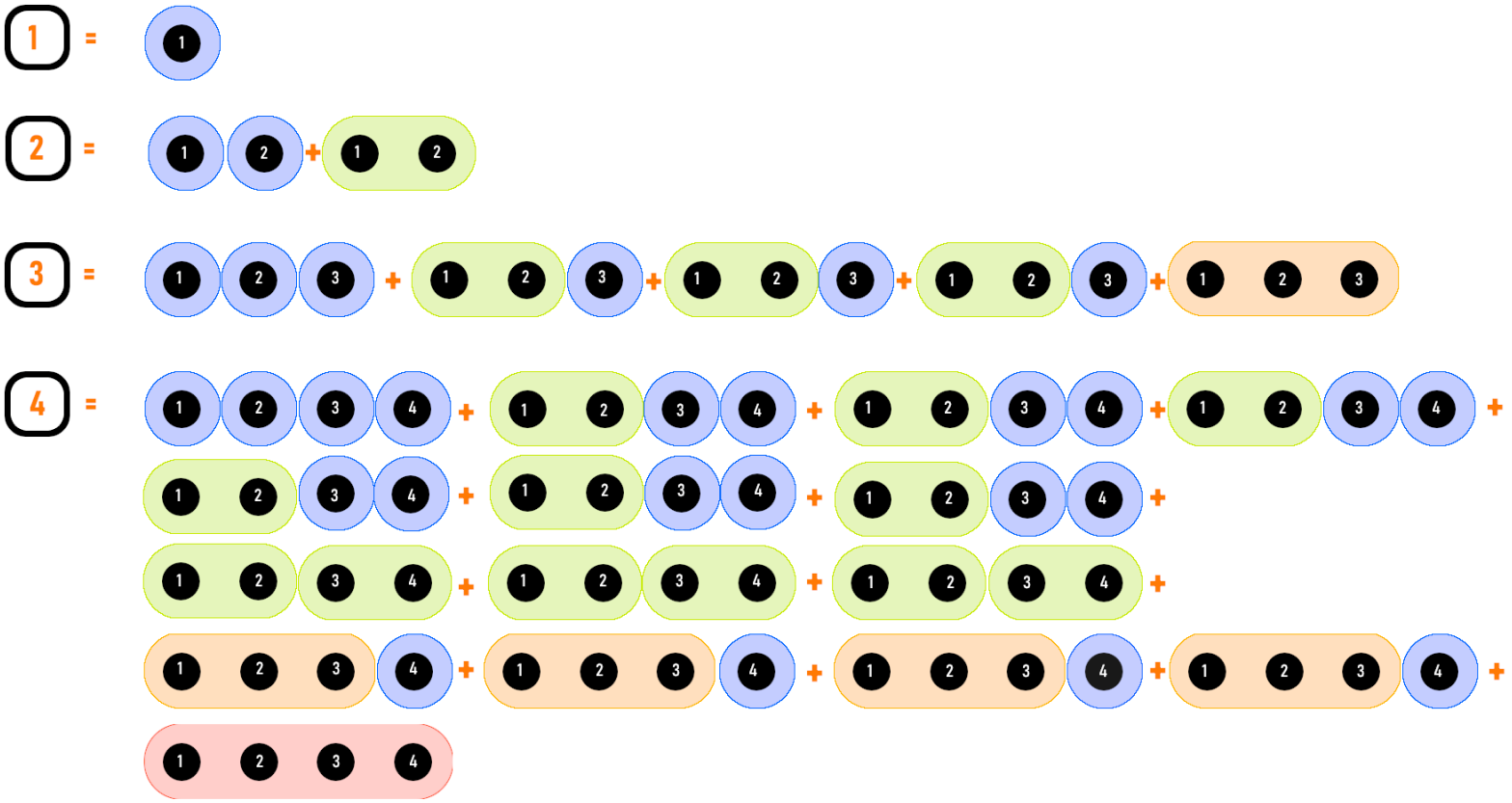

Figure 3.2: Diagram illustrating N-particle densities expressed in terms of factorial cumulant correlation functions. Squares represent multi-particle densities, while circles and ovals denote cumulants. The diagram focuses on the cases $N = 1$ to $N = 4$. Inspired by the original figure in Ref. [16].

N-th order *factorial cumulant*. It vanishes whenever any subset of its arguments is statistically independent of the others and therefore captures the *genuine* N-particle correlations, produced in the same physical process, that cannot be factorised into lower-order correlations [15]. A general derivation for multi-particle correlation functions can be found in Ref. [8, 15] and the references therein. Figure 3.2 shows how N-particle densities can be decomposed, using the cluster expansion, into contributions from factorial cumulant correlation functions of different orders.

3.1.2.2 Integral correlators

Similar to the differential correlation functions, one can define **integral correlation functions**. Just as differential correlation functions describe correlations and fluctuations as functions of momentum or other kinematic variables, integral correlation functions capture the average level of correlation between observables over specified phase-space intervals.

Factorial cumulants as integrated correlation functions

The integrated two-particle correlation function, $C_2^{\alpha_1\alpha_2}$ is obtained by integrating $C_2^{\alpha_1\alpha_2}(\vec{p_1}, \vec{p_2})$, over the selected phase-space regions $d\Omega_{\alpha_1}$ and $d\Omega_{\alpha_2}$. In the following, the particle momentum $\vec{p}$ is expressed in terms of the commonly used kinematic variables $(y, \varphi, p_{\mathrm{T}})$. Accordingly, the differential two-particle correlation function can be written as $C_2^{\alpha_1\alpha_2}(y_1, \varphi_1, p_{\mathrm{T}1};\, y_2, \varphi_2, p_{\mathrm{T}2})$. Its integrated counterpart then reads:

$$\begin{aligned} C_2^{\alpha_1\alpha_2} &= \int_{\Omega_{\alpha_1}} \overbrace{dy_1\, d\varphi_1\, dp_{\mathrm{T}1}}^{d\Omega_{\alpha_1}} \int_{\Omega_{\alpha_2}} \overbrace{dy_2\, d\varphi_2\, dp_{\mathrm{T}2}}^{d\Omega_{\alpha_2}} C_2^{\alpha_1\alpha_2}(y_1, \varphi_1, p_{\mathrm{T}1};\, y_2, \varphi_2, p_{\mathrm{T}2}) \\ &= \int_{\Omega_{\alpha_1}} d\Omega_1 \int_{\Omega_{\alpha_2}} d\Omega_2 \left[\rho_2^{\alpha_1\alpha_2}(y_1, \varphi_1, p_{\mathrm{T}1};\, y_2, \varphi_2, p_{\mathrm{T}2}) - \rho_1^{\alpha_1}(y_1, \varphi_1, p_{\mathrm{T}1})\, \rho_1^{\alpha_2}(y_2, \varphi_2, p_{\mathrm{T}2})\right]. \end{aligned} \tag{3.12}$$

Taking into account Eqs. (2.12), the above expression takes form:

$$\begin{aligned} C_2^{\alpha_1\alpha_2} &= \int_{\Omega_1} d\Omega_1 \int_{\Omega_2} d\Omega_2\, C_2^{\alpha_1\alpha_2}(y_1, \varphi_1, p_{T1};\, y_2, \varphi_2, p_{T2}) \\ &= \langle n_{\alpha_1}(n_{\alpha_2} - \delta^{\alpha_1\alpha_2})\rangle - \langle n_{\alpha_1}\rangle\langle n_{\alpha_2}\rangle. \end{aligned} \tag{3.13}$$

In the general notation, the superscript α_i is used to distinguish either particle species or, equivalently, particles counted in distinct phase-space regions. Here, the Kronecker delta $\delta^{\alpha_1\alpha_2}$ ensures that self-pair subtraction only occurs when both the

particle species are identical or the phase-space regions are the same (i.e., when a single particle might otherwise be double-counted).

Higher-order integrated correlation functions can be obtained from **factorial cumulant generating function**:

$$\ln G(z) = \ln \left(\sum_{n=0}^{\infty} P(n) z^n \right), \tag{3.14}$$

where $P(n)$ is the multiplicity distribution. The N-th factorial cumulant is:

$$C_N = \frac{d^N}{dz^N} \ln G(z) \bigg|_{z=1}. \tag{3.15}$$

The first few factorial cumulants are:

$$C_1 = \langle n \rangle, \tag{3.16}$$

$$C_2 = \langle n(n-1) \rangle - \langle n \rangle^2, \tag{3.17}$$

$$C_3 = \langle n(n-1)(n-2) \rangle - 3\langle n(n-1) \rangle \langle n \rangle + 2\langle n \rangle^3. \tag{3.18}$$

In this formulation, the index α_i is dropped because the analysis is limited to one type of particle, understood as either a single species or those selected within the same phase-space region. For a broader discussion of factorial cumulants, including also the derivation of mixed factorial cumulants, see Refs. [8, 15, 28, 29, 30, 31] and references therein.

Recently, factorial cumulants have been measured by the STAR Collaboration in heavy-ion collisions [32], and by NA61/SHINE in proton–proton collisions at SPS energies [33]. Despite their direct connection to genuine correlation functions, factorial cumulants seem less commonly used in experimental analyses compared to "ordinary" cumulants.

Cumulants and ratio of net-charge cumulants

Cumulants characterise the overall shape of event-by-event distributions and are widely used in fluctuation analyses. They are directly related to thermodynamic susceptibilities via derivatives of the grand potential, allowing for direct comparison with theory (e.g., lattice QCD) [29, 30, 34, 35]. However, unlike factorial cumulants, ordinary cumulants mix contributions from integrated correlation functions of different orders, so the microscopic interpretation of higher orders is less transparent. By contrast, factorial cumulants map one-to-one onto genuine multi-particle correla-

tions (after removing self-correlations), but they generally lack a direct connection to the partition function and are therefore less straightforward to connect with thermodynamic calculations.

Cumulants[3] κ_N are the alternative measures to traditional moments of the distribution. The N-th **cumulant** κ_N can be determined by the Nth derivative of the **cumulant generating function** $K(t)$ evaluated at $t = 0$:

$$\kappa_N = \left. \frac{d^N K(t)}{dt^N} \right|_{t=0} \tag{3.19}$$

where the $K(t)$ of a random variable n is defined as:

$$K(t) = \ln \left(\sum_{n=0}^{\infty} P(n) e^{tn} \right). \tag{3.20}$$

The first four ordinary cumulants κ_N describe progressively higher-order features related to a multiplicity distribution and can be expressed in terms of statistical moments or, in terms of **factorial cumulants** C_N, as follows:

$$\begin{aligned}
\kappa_1 &= \langle n \rangle & &= C_1 \\
\kappa_2 &= \langle n^2 \rangle - \langle n \rangle^2 & &= C_1 + C_2 \\
\kappa_3 &= \langle (n - \langle n \rangle)^3 \rangle & &= C_1 + 3C_2 + C_3 \\
\kappa_4 &= \langle (n - \langle n \rangle)^4 \rangle - 3\langle (n - \langle n \rangle)^2 \rangle^2 & &= C_1 + 7C_2 + 6C_3 + C_4
\end{aligned} \tag{3.21}$$

Cumulants expressed by moments — Cumulants expressed by factorial cumulants

In addition to single-variable cumulants, one can also define *mixed cumulants* involving multiple observables, such as multiplicities of different particle species or in different kinematic intervals [8, 15, 30]. For example, the second-order mixed cumulant between two multiplicity observables n_A and n_B is equivalent to their covariance:

$$\kappa_{1,1}(n_A, n_B) = \langle n_A n_B \rangle - \langle n_A \rangle \langle n_B \rangle = \mathrm{Cov}(n_A, n_B). \tag{3.22}$$

In lattice QCD, the cumulants κ_N^{net} of conserved net-charge distributions, such as net-electric charge, net-baryon number, and net-strangeness, are directly related to generalised quark-number susceptibilities, see Refs. [29, 30, 34, 35, 36]. Here, *net*

[3]Note that different experiments adopt different notational conventions: ALICE uses κ_N, while STAR refers to the same quantities as C_N, which may lead to confusion in cross-comparisons.

cumulants refer to cumulants of the event-by-event distributions of net conserved charges, e.g.

$$n_B^{\text{net}} = n_B - n_{\bar{B}},$$

where n_B and $n_{\bar{B}}$ denote the baryon and anti-baryon multiplicities. The exact relationship is given by:

$$\kappa_N^{\text{net}} = VT^3\chi_N = VT^3\frac{\partial^N(P/T^4)}{\partial(\mu/T)^N}, \tag{3.23}$$

where χ_N is the N-th order quark number susceptibility, V is the system volume, T is the temperature, and μ is the chemical potential associated with the conserved charge.

As Eq. (3.23) shows, these net cumulants depend on both the volume and the thermodynamic susceptibilities of the system. Since the system volume varies from event to event in heavy-ion collisions, to eliminate volume dependence and obtain observables that can be directly compared to lattice QCD calculations, experimental analyses often focus on *ratios of cumulants*, such as κ_2/κ_1, κ_3/κ_2, or κ_4/κ_2, which correspond to *ratios of susceptibilities* χ_2/χ_1, χ_3/χ_2, etc.

3.1.2.3 Event-by-event correlations and fluctuations

Observables such as cumulants, variances, and covariances are evaluated over an ensemble of collision events. They are therefore referred to as *event-by-event fluctuation observables*, since they quantify how much a given measure varies from one event to another.

Using moments, cumulants, or their factorial counterparts, one can construct a variety of derived observables, some of which have been widely used in experimental studies and provide complementary insight into the dynamics of particle production. Importantly, the formalism of moments and cumulants is not limited to particle multiplicity: it can be naturally extended to other extensive event quantities, such as the total transverse momentum or the total energy of the system. Their statistical moments can be analysed within the same framework as multiplicity cumulants and integrated correlation functions. This extension beyond multiplicity has been discussed in the literature [15, 37].

The next sections will focus on event-by-event correlation and fluctuation observables particularly suited for the study of forward–backward correlations, with special attention to the class of **strongly intensive quantities**.

3.2 Forward-backward multiplicity correlations

In heavy-ion physics, the term **forward-backward correlations** refers to the dependence between the numbers of particles produced in pseudorapidity η or rapidity y intervals located in the forward (F) and backward (B) hemispheres of the collision. The rapidity intervals can be positioned either symmetrically or asymmetrically around mid-rapidity ($\eta = 0$), as shown in Fig. 3.3.

Forward-backward multiplicity correlations

Event-by-event forward-backward multiplicity correlations can be expressed as integrals of the two-particle correlation function $C_2(\eta_1, \eta_2)$ over the forward and backward regions. The function $C_2(\eta_1, \eta_2)$ is integrated over transverse momentum and azimuthal angle within the specified kinematic acceptance, $p_T \in [p_{T1}, p_{T2}]$ and $\varphi \in [\varphi_1, \varphi_2]$.

FB covariance of particle multiplicity:

$$\mathrm{Cov}(n_F, n_B) = \int_{\eta_{F1}}^{\eta_{F2}} d\eta_1 \int_{\eta_{B1}}^{\eta_{B2}} d\eta_2 \, C_2(\eta_1, \eta_2) = \\ = \langle n_F n_B \rangle - \langle n_F \rangle \langle n_B \rangle. \tag{3.24}$$

Variance of particle multiplicity in a single interval (forward or backward):

$$\mathrm{Var}(n_{F(B)}) = \int_{\eta_{F(B)1}}^{\eta_{F(B)2}} d\eta_1 \int_{\eta_{F(B)1}}^{\eta_{F(B)2}} d\eta_2 \, C_2(\eta_1, \eta_2) \\ + \int_{\eta_{F(B)1}}^{\eta_{F(B)2}} d\eta \, C_1(\eta) = \\ = \langle n_{F(B)}^2 \rangle - \langle n_{F(B)} \rangle^2. \tag{3.25}$$

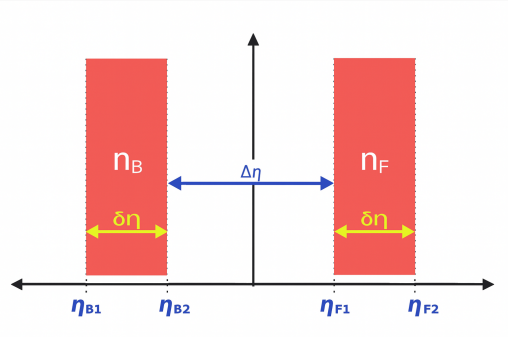

Figure 3.3: Schematic representation of forward (F) and backward (B) pseudorapidity intervals used in FB studies.

Symbols n_F and n_B denote the total number of particles in the forward interval $\eta \in [\eta_{F1}, \eta_{F2}]$ and backward interval $\eta \in [\eta_{B1}, \eta_{B2}]$, respectively, where $\eta_{F2} = \eta_{F1} + \delta\eta$ and $\eta_{B2} = \eta_{B1} + \delta\eta$.

3.2.1 The forward-backward correlation strength

To quantify **the strength of forward-backward correlations**, researchers employ several methodologies. Among these, two techniques have been the most prevalent: (a) the FB slope parameter method and (b) Pearson's correlation coefficient measurement.

Forward-backward correlations with the slope parameter

One of the first methods implemented to study forward-backward correlations was the determination of the slope parameter relating the average number of particles produced in the forward (or backward) hemisphere to the number of particles in the corresponding opposite region. It is defined through the linear relationship between forward and backward multiplicities:

$$\langle n_{F(B)} \rangle = a + b_{corr}^{\langle n_{F(B)} \rangle} \cdot n_{B(F)}, \tag{3.26}$$

where $\langle n_{F(B)} \rangle$ corresponds to the average number of particles observed in the forward (backward) pseudorapidity region for events with a given number of particles $n_{B(F)}$ measured in the backward (forward) region. The slope parameter $b_{corr}^{\langle n_{F(B)} \rangle}$ quantifies the correlation strength, with larger values indicating a stronger dependence between particle production in the two regions.

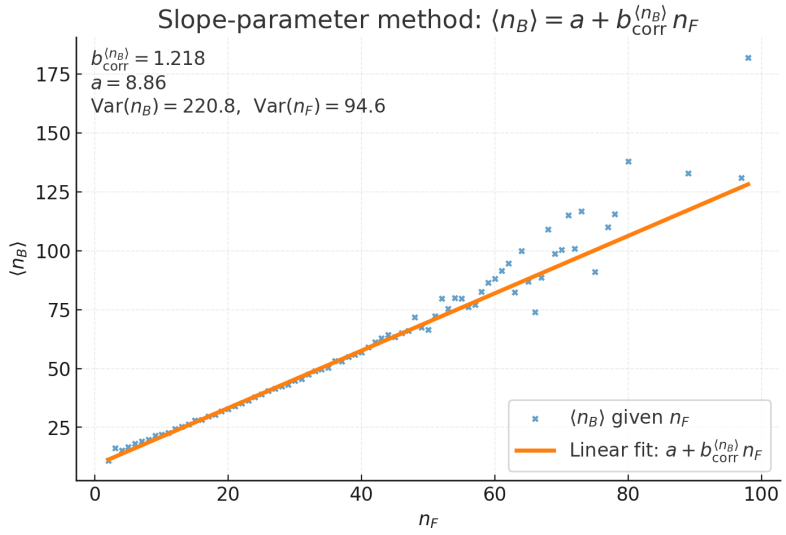

Figure 3.4: Forward-backward slope parameter illustration: $\langle n_B \rangle = a + b_{\mathrm{corr}}^{\langle n_B \rangle} n_F$. Note that in general $b_{\mathrm{corr}}^{\langle n_F \rangle} \neq b_{\mathrm{corr}}^{\langle n_B \rangle}$.

Although both equations describe the same underlying correlation, the slope parameters are generally not equal, $b_{corr}^{\langle n_F(n_B) \rangle} \neq b_{corr}^{\langle n_B(n_F) \rangle}$. However, they are related by the expression:

$$b_{corr}^{\langle n_F \rangle} = b_{corr}^{\langle n_B \rangle} \cdot \frac{\mathrm{Var}(n_B)}{\mathrm{Var}(n_F)}. \tag{3.27}$$

From this, it is evident that if the variances of forward and backward multiplicities are different ($\mathrm{Var}(n_B) \neq \mathrm{Var}(n_F)$), the two slope parameters also differ.

The slope parameter method, popular in early forward-backward correlation studies, has largely been replaced by Pearson's correlation coefficient measurement.

Pearson's correlation coefficient as standardised covariance

The integrated correlation function, as defined by Eq. (3.24), quantifies the covariance of the multiplicity distributions between the forward and backward pseudorapidity intervals. Since this covariance is not normalised, its absolute magnitude alone does not allow for a straightforward interpretation of the correlation strength between the two variables.

To allow for a more meaningful comparison, a standardised version of the covariance, known as the Pearson correlation coefficient, is commonly used. This quantity is defined as:

$$b_{\text{corr}}^{n_F n_B} = \frac{\text{Cov}(n_F, n_B)}{\sqrt{\text{Var}(n_F)\text{Var}(n_B)}}. \tag{3.28}$$

In the expression Eq. (3.28), the covariance is scaled by the square root of the product of the forward and backward variances, giving a dimensionless measure with values between -1 and 1.

It can be shown that all of the discussed FB correlation strength measures, such as the slope parameter $b_{corr}^{\langle n_{F(B)} \rangle}$ and correlation coefficient $b_{corr}^{n_F n_B}$, are related as follows:

$$b_{corr}^{\langle n_B \rangle} \cdot b_{corr}^{\langle n_F \rangle} = (b_{corr}^{n_F n_B})^2. \tag{3.29}$$

For symmetric collisions, where $\langle n_F \rangle = \langle n_B \rangle$ and $\text{Var}(n_F) = \text{Var}(n_B)$, all of these measures are equivalent.

Pearson's correlation coefficient provides *a more robust, direct, and straightforward measure of correlation strength* than the slope parameter approach. Consequently, it has become more popular. However, this observable has its limitations, particularly when external factors influence the relationship between the variables of interest. In such cases, as will be discussed later in this manuscript, the Pearson correlation coefficient can give misleading or false indications of correlation.

3.2.2 Methodology of forward-backward correlation analysis

Over the years, various experimental and phenomenological analysis strategies have been employed to study forward-backward multiplicity correlations, depending on the specific physics phenomena under investigation. These approaches include studying the FB correlation coefficient as a function of:

– pseudorapidity gap ($\Delta\eta$);

– pseudorapidity window width ($\delta\eta$);

– collision energy and centrality;

– separation in azimuthal angle ($\Delta\varphi$);

– charge combinations (all, like-sign, and unlike-sign).

Dependence on pseudorapidity gap $\Delta\eta$

The analysis of forward-backward correlations as a function of varying pseudorapidity **separation gap** $\Delta\eta$ between the forward and backward intervals, as illustrated on the right, helps to distinguish between contributions coming from **short-range correlations (SRC)** and **long-range correlations (LRC)**.

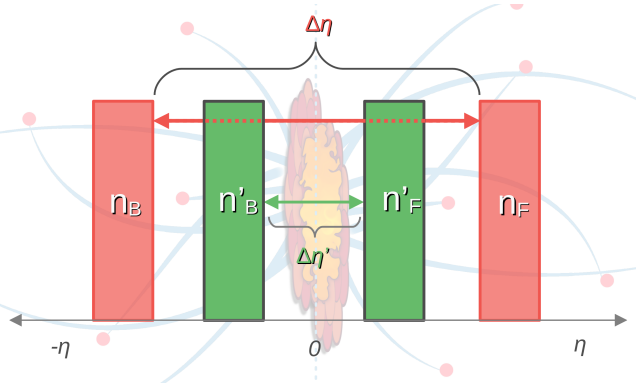

Short-range correlations

Short-range correlations refer to particle pairs that are close in longitudinal phase space, typically $|\Delta y| < 1$ *or* $|\Delta\eta| < 1$, depending on whether rapidity y or pseudorapidity η is used. These correlations arise from processes such as hadronic resonance decays, particle clustering, jet fragmentation, and final-state interactions. Such mechanisms predominantly produce particles close in (pseudo)rapidity, thereby contributing to the observed SRC.

Long-range correlations

Long-range correlations refer to correlations that extend over large distances in pseudorapidity, with $|\Delta\eta| \geq 1 - 2$ (or equivalently, large $|\Delta y|$). LRCs are expected to arise at the early stages of collision before the longitudinal expansion of the system created during the collision separates particles over large distances [37]. Thus, their analysis provides a means to probe the initial stages of heavy-ion collisions before hadronisation. Long-range rapidity correlations can arise via different mechanisms. In the Dual Parton Model, they are generated by event-by-event fluctuations in the number of cut Pomerons (colour strings) produced by multiple

inelastic scatterings [38]. In the Colour Glass Condensate (CGC/glasma) framework, LRC are initial-state correlations linked to nearly boost-invariant longitudinal colour fields ("flux tubes") present immediately after the collision [2]. In colour-string percolation, LRC arise from fluctuations in the number and overlap (clustering) of colour-string sources as the string density increases [39]. In the wounded-nucleon model, they result from fluctuations in the number of wounded nucleons within a centrality class, which correlate forward and backward multiplicities [40]. The latter will be discussed in great detail in Chapter 6

Dependence on pseudorapidity window width $\delta\eta$

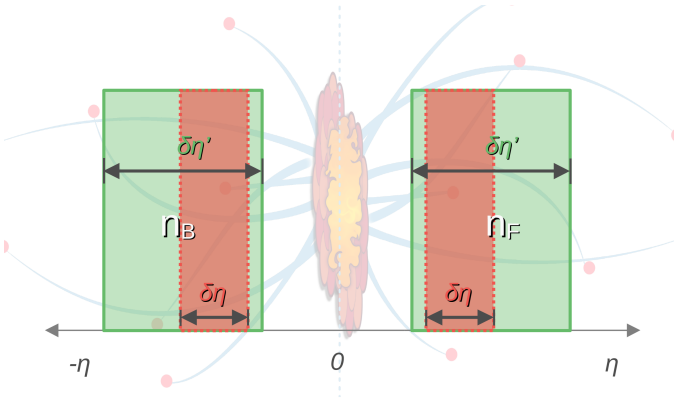

By varying the pseudorapidity interval width ($\delta\eta$), one can probe how the strength of forward-backward correlations depends on the size of the pseudorapidity acceptance. Larger $\delta\eta$ windows improve the statistical precision and make measurements more sensitive to global event features, whereas smaller $\delta\eta$ windows are better suited to probe local fluctuations.

Dependence on azimuthal separation $\Delta\varphi$

Forward-backward correlations can also be studied by introducing a separation gap in the azimuthal angle ($\Delta\varphi$), in addition to the separation gap between FB pseudorapidity windows. It was suggested in Ref. [41] that varying $\Delta\varphi$ at fixed $\Delta\eta$ may be particularly informative, as it provides sensitivity to different correlation components. Consequently, the $\Delta\varphi$ dependence can enhance sensitivity to short-range effects and may enable a cleaner separation of SRC and LRC contributions, see Refs. [41, 42].

Dependence on collision energy and centrality

Finally, studying FB correlations as a function of centrality (or multiplicity class) and $\sqrt{s_{NN}}$ helps to determine how correlation strength varies with system size and collision energy.

3.2.2.1 History of forward-backward correlation studies: A brief overview

Studies of forward-backward multiplicity correlations have a rich history in particle physics. Over the years, this research has spanned a broad range of energies and collision types, including electron-positron, lepton-proton, hadron-hadron, and nucleus-nucleus interactions. A brief overview of some of the most important of those studies, categorised by collision type, is outlined below.

In the literature, the forward-backward correlation coefficient has appeared under different notations, most commonly b, b_{corr}, or b_{corr}^{n-n}. In the present work, for the sake of consistency, we adopt the notation $b_{\mathrm{corr}}^{n_F n_B}$. When discussing historical results, the original notation is retained only where it is essential to remain faithful to the cited references.

Electron-positron (e^+e^-) and lepton-proton (l^+p) collisions:

Studies of e^+e^- over a wide energy range" (TASSO at PETRA [43], $\sqrt{s} = 14$–46.8 GeV; HRS at SLAC [44], $\sqrt{s} = 29$ GeV; DELPHI/OPAL at LEP [45], $\sqrt{s} \approx 91$ GeV) reported that forward-backward multiplicity correlations are weak and show little energy dependence. Unlike-sign particle pairs dominated the observed signal. Similarly, studies of lepton–proton reactions (μp, νp, $\bar{\nu} p$) at CERN [46, 47] found weak or negligible FB correlations. Together, these observations support independent single-string fragmentation of the primary system, $q\bar{q}$ in e^+e^- and quark-diquark in ℓp.

Acronyms: TASSO – Two Arm Spectrometer Solenoid; DELPHI – Detector with Lepton, Photon and Hadron Identification; OPAL – Omni Purpose Apparatus at LEP; HRS – High Resolution Spectrometer.

Hadron-hadron (hh) collisions:

In contrast to lepton-lepton and lepton-proton collisions, **stronger positive forward-backward correlations** were measured in hadron-hadron interactions such as pp, p$\bar{\mathrm{p}}$, $\pi^+ p$ and $K^+ p$.

Results from the CERN ISR ($\sqrt{s} = 23.6$–62.8 GeV) [49] and from the UA5 experiment at the SPS ($\sqrt{s} = 200$–900 GeV) [50] showed that the FB correlation strength grows logarithmically with energy and depends on the size and position of the pseudorapidity gap $\Delta\eta$. The separation between short-range and long-range correlations becomes evident and recognised.

Analysis carried out by NA22 Collaboration at CERN SPS for $\pi^+ p$, $K^+ p$, and

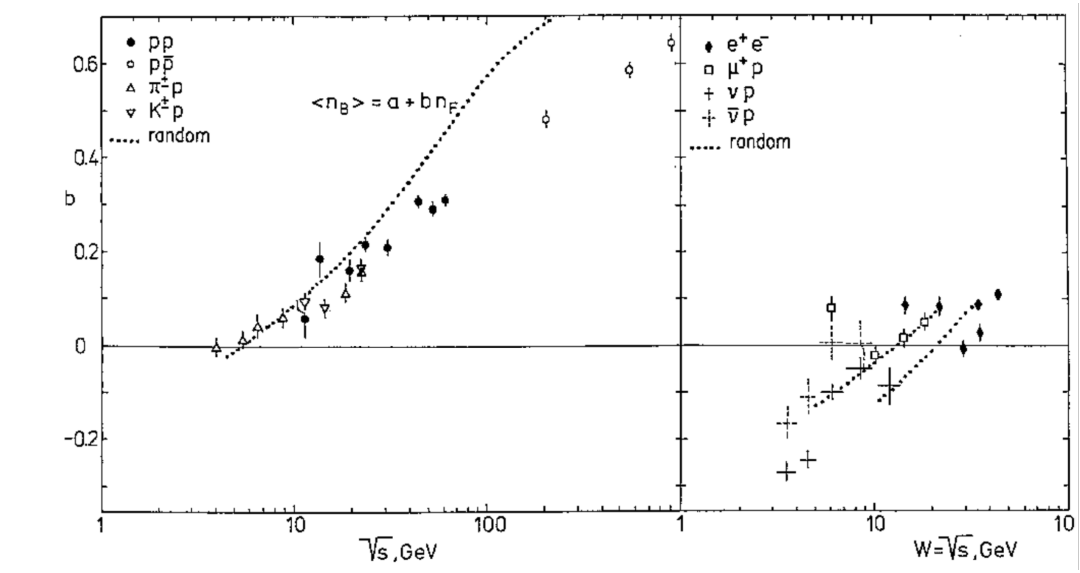

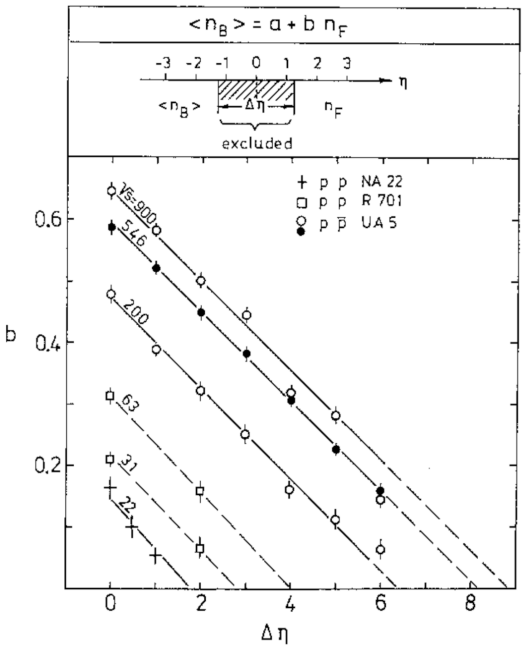

Figure: 3.5: The top panels show the correlation strength b as a function of the c.m.s. energy for hadron–hadron (hh), e^+e^-, and lepton–nucleon collisions. The dotted lines show the expectation for random particle partitioning based on the negative binomial distribution. The bottom panel shows the correlation strength b as a function of an excluded central pseudorapidity gap $\Delta\eta$, for several collision energies. Figure adapted from Figs. 3 and 13 of Ref. [48].

pp collisions at $\sqrt{s}$ =22 GeV [48] showed results that are in agreement with the findings obtained for p(p̄p) at the ISR and SPS colliders. It is found that unlike-sign pairs dominate FB correlations; results are consistent with TASSO's findings in e^+e^- collisions [43]. NA22 reported **no significant correlations** for same-charge pairs.

Figure 3.5, adapted from Ref. [48], presents a compilation of the values of correlation coefficient b obtained from hadron-hadron interactions alongside results from lepton-nucleon (l^+p) collisions and electron-positron (e^+e^-) annihilation. The

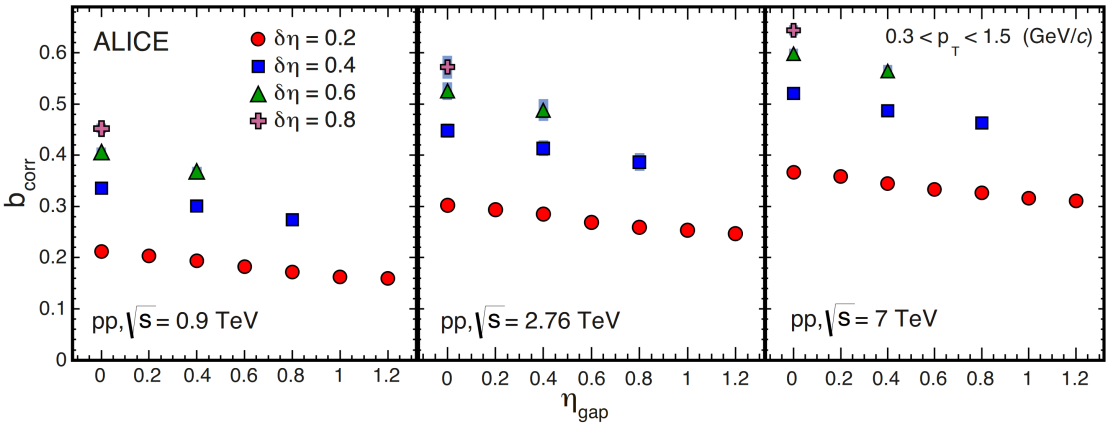

Figure 3.6: Forward-backward correlation strength b_{corr} as a function of η_{gap} and for different window widths $\delta\eta = 0.2, 0.4, 0.6$ and 0.8 in pp collisions at $\sqrt{s} = 0.9, 2.76$ and 7 TeV. In that publication, η_{gap} is defined as the distance in pseudorapidity between the centres of the forward and backward η windows. Figure taken from [42].

explanation of observed large FB correlations in hadronic collisions compared to e^+e^- was proposed in terms of a simple **geometrical model** according to which they arise from an incoherent event-by-event superposition of interactions with varying impact parameters. This interpretation was explicitly discussed and tested in the NA22 analysis [48].

Studies by the E735 experiment at the Tevatron at Fermilab at an energy range $\sqrt{s} = 0.3$–1.8 TeV [51] confirmed findings at ISR and SPS, showing a linear relationship in FB correlations that persisted over large pseudorapidity gaps between forward and backward intervals, up to five units in pseudorapidity.

Most recent FB multiplicity correlation studies in pp collisions were conducted by STAR (RHIC, $\sqrt{s} = 200$ GeV) [52], ATLAS [20] and ALICE [42] (LHC, $\sqrt{s} = 0.9$, 2.76, and 7 TeV). Experiments at RHIC and LHC focused on measuring forward-backward correlations with narrower windows ($\delta\eta = 0.2$–0.5). This approach contrasts with older experiments, making direct comparisons more challenging. A closer examination of these measurements highlights the following key trends:

- **Significant positive FB correlations** in pp collisions.
- Correlation strength **increases** with energy and window width ($\delta\eta$) but **decreases** with pseudorapidity gap ($\Delta\eta$), see Fig. 3.6.
- ALICE confirms the presence of **short- and long-range correlations**.

Acronyms: ISR – Intersecting Storage Rings (CERN); UA5 – Underground Area 5 (CERN SPS); NA22 – North Area Experiment 22 (CERN SPS); E735 – Experiment 735 (Tevatron); STAR – Solenoidal Tracker at RHIC; ATLAS – A Toroidal LHC Apparatus; ALICE – A Large Ion Collider Experiment SPS – Super Proton Synchrotron.

Nucleus-nucleus (AA) and hadron-nucleus (hA) collisions:

Early studies at Fermilab investigated proton-nucleus and pion-nucleus collisions at 200–400 GeV with nuclear emulsion [53]. The results revealed the asymmetry in FB correlation coefficients, extracted as slope parameters. These are stronger in the backward (target) than forward (projectile) hemisphere ($b^{\langle n_B \rangle} > b^{\langle n_F \rangle}$). This asymmetry is **most pronounced in the fragmentation region**. The correlation strength depends on energy and the mass of the projectile.

Nuclear emulsion experiments (EMU01, EMU08) at the CERN SPS studied asymmetric collisions of ^{16}O and ^{32}S projectiles with nuclear emulsion (AgBr) at 60 and 200 GeV/nucleon [54, 55, 56]. Findings indicated **stronger FB correlations in nucleus-nucleus** than in pp and pA collisions, with the correlation strength **increasing with energy**. The analysis also showed that the slope parameter varies with projectile energy and collision type. Similar to results from hadron-nucleus reactions, an asymmetry in FB correlations was reported, due to a higher number of participating nucleons in the target fragmentation region, leading to $b^{\langle n_B \rangle} > b^{\langle n_F \rangle}$.

Analyses as a function of the pseudorapidity separation gap showed that correlations were predominantly short-range, consistent with cluster decays, with no statistically significant long-range component.

The STAR experiment at RHIC studied FB correlations in Au–Au collisions at $\sqrt{s} = 200$ GeV in wide (10% width) centrality classes [52]. These studies revealed that:

- FB correlations were significantly stronger in central Au–Au collisions than in pp (Fig. 3.7, panels (a) and (b) vs. (c)). Values of the correlation coefficient decrease with centrality of the collision, and for more peripheral Au–Au events, the correlation strength is comparable with the values measured in pp.
- Both SRC and LRC **increased with centrality**; in the most central events (0–10%), correlations remained strong even at large pseudorapidity gaps, $\Delta\eta \sim 2$.
- In STAR, a comparison between centrality classes defined via the TPC multiplicity and those based on the Zero Degree Calorimeters was carried out only for the most central Au–Au collisions. The ZDC estimator yielded slightly

smaller absolute values of the correlation strength, but the overall dependence on $\Delta\eta$ remained unchanged. Consequently, the STAR study was not sensitive enough to reveal a significant dependence on the choice of centrality estimator. ALICE later performed a more systematic investigation of this effect, as will be discussed below.

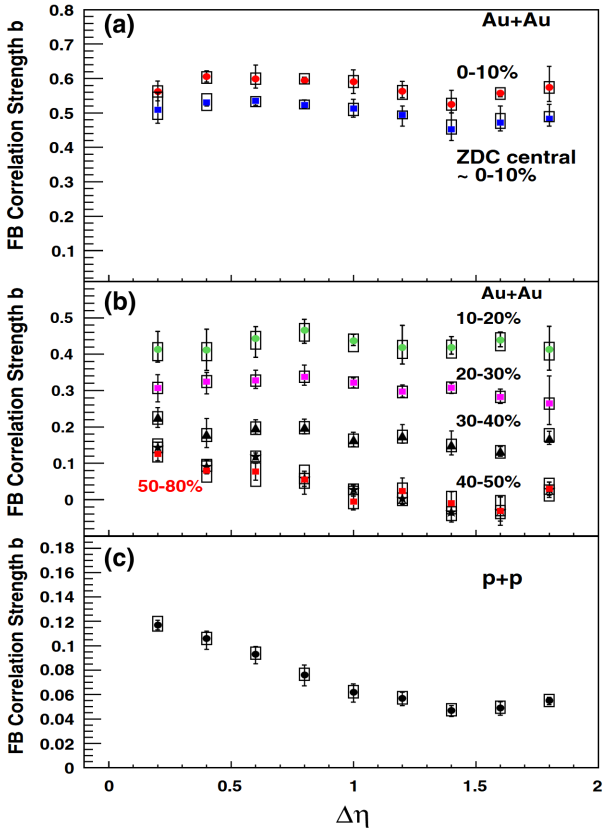

Figure 3.7: Forward–backward correlation strength b as a function of the pseudorapidity gap $\Delta\eta$ at $\sqrt{s_{\mathrm{NN}}} = 200$ GeV measured by STAR. Panels (a) and (b) show results for Au–Au collisions in different centrality classes, while panel (c) shows pp collisions. Error bars represent statistical uncertainties; boxes indicate correlated systematic uncertainties. Figure reproduced from Ref. [52].

These results drew theoretical interest, see Ref. [2], suggesting new physical effects as the origin of the high correlation values. However, further theoretical studies, such as Refs. [57, 40] linked the high forward-backward correlations observed in nucleus-nucleus collisions to significant contributions from **volume fluctuations**. This demonstrates the necessity of a careful interpretation of the correlation coefficient in order to distinguish genuine dynamical effects from trivial fluctuations of the number of participating nucleons, particularly in analyses involving wide centrality intervals.

The ALICE experiment at the LHC has extended the study of FB correlations to even higher energies in heavy-ion collisions. The results obtained by the author in Pb–Pb collisions at $\sqrt{s_{\mathrm{NN}}} = 2.76$ TeV provide, for the first time, an in-depth experimental analysis of the behaviour of the forward-backward correlation coefficient in heavy-ion collisions not only as a function of collision centrality but also of its

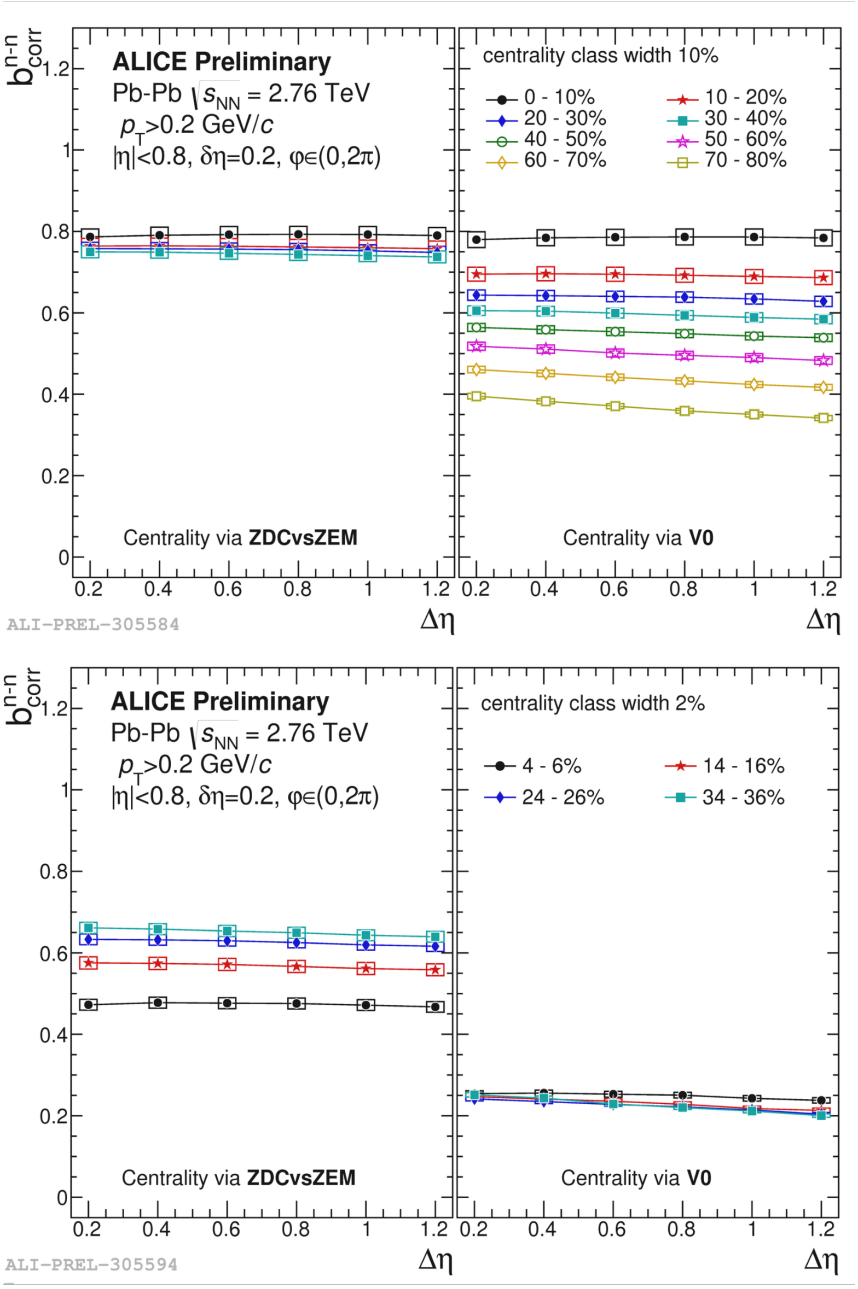

Figure 3.8: Forward–backward correlation coefficient b_{corr}^{n-n} as a function of the separation gap between forward and backward pseudorapidity intervals, $\Delta\eta$, in Pb–Pb collisions at $\sqrt{s_{\mathrm{NN}}} = 2.76$ TeV. The left figure presents results for centrality classes of width 10%, while the right figure corresponds to classes of width 2%. In each figure, the two panels display results obtained with different centrality estimators: ZDCvsZEM (left panel) and V0 (right panel). Statistical uncertainties are smaller than the marker size; rectangles indicate systematic uncertainties. The figure is taken from Ref. [58].

evolution in the function of the width of the centrality interval. Moreover, results were studied for two different centrality selection methods.

As first reported by the author in [58], the following conclusions can be drawn from the experimental Pb–Pb data regarding the behaviour of the forward-backward correlation coefficient as a function of the centrality class, its width and the applied centrality selection method:

- For wide (10%) centrality bins, the largest values of the correlation coefficient are observed in the most central collisions, and they decrease towards peripheral collisions, similar to the findings reported by the STAR Collaboration.
- **The correlation strength weakens as the width of the centrality class decreases** (from 10% to 1%), regardless of the chosen centrality selection method, see Fig. 3.8. This behaviour can be related to the reduction of contribution coming from **the volume fluctuations** when narrowing centrality class intervals.
- **A clear dependence of the correlation coefficient on the centrality selection methods** is visible for all investigated centrality classes. It becomes most evident for narrow centrality classes, as shown in the two right panels of Fig. 3.8.

Key takeaways:

- FB correlations are **weak in e^+e^- and lepton-proton collisions**, significantly smaller than in hadron-hadron and nucleus-nucleus interactions.
- In hadron-hadron and nucleus-nucleus collisions, the correlation strength **increases with energy** and **decreases with increasing pseudorapidity gap $\Delta\eta$**. The latter behaviour is related to the **reduction of the short-range correlation contribution** as the separation between forward and backward intervals increases.
- ALICE results have shown that the measured correlation strength **strongly depends on the method of centrality selection**.
- Nucleus-nucleus collisions show the strongest FB correlations, but these are **likely dominated by volume fluctuations rather than purely dynamical effects**.

3.2.3 Spurious effect of volume fluctuations

Limitations of correlation coefficient observable

A major limitation of the correlation coefficient between two random variables X and Y, defined in Eq. (3.28), is its sensitivity to confounding variables Z. These are external factors that may generate spurious correlations by simultaneously affecting both X and Y. As a result, an apparent correlation between X and Y may in fact arise from their common dependence on Z, rather than from a direct relationship between them.

This issue is particularly relevant in forward-backward multiplicity correlation studies in nucleus-nucleus collisions, where the relationship between two groups of particles produced in forward (n_F) and backward (n_B) pseudorapidity intervals is measured.

Role of collision geometry as a confounding factor

The collision geometry, defined by the degree of nuclear overlap during the interaction, acts as a confounding factor. The larger the overlap region between the colliding nuclei, corresponding to a greater number of participating nucleons N_{part} and lower impact parameter values, the higher the average values of n_F and n_B will be. As a result, the fact that both forward and backward multiplicities, n_F and n_B, depend on the number of participating nucleons N_{part} or on the impact parameter on average introduces an additional correlation between them, which does not originate from intrinsic dynamical effects. Instead, these spurious correlations arise directly from event-by-event fluctuations of the collision geometry, often referred to as "volume fluctuations", associated with fluctuations of N_{part} or the impact parameter.

The effect of event-by-event fluctuations of the initial geometry on measured values of $b_{corr}^{n_F n_B}$ was recognised early on in correlation studies. In Ref. [48], it was hypothesised that the high correlation coefficient values observed in hadron-hadron interactions, compared to electron-positron interactions, might result from the superposition of collisions with varying impact parameters. However, in one of the first interpretations of the high correlation coefficient values in Au–Au collisions reported by the STAR experiment [2], the emphasis was placed on novel dynamical mechanisms, without explicitly addressing the possible role of geometry (volume) fluctuations. Only later, in the Refs. [40, 57], it was pointed out that correlation coefficient results in nucleus-nucleus collisions should be interpreted with greater caution, considering the significant influence of external factors, particularly collision

geometry and its event-by-event fluctuations. For heavy-ion collisions at the LHC, this fact was confirmed for the first time by the author of this work, as shown in Fig. 3.9 and discussed below.

Understanding the impact of volume fluctuations on forward-backward correlation measurements

- **Dependence on centrality bin width:** Figure 3.9 illustrates the impact of volume fluctuations, reflected by centrality fluctuations in a given centrality class sample, on the measured strength of forward-backward correlations. The correlation coefficient is shown as a function of centrality bin width for different centrality classes, using two centrality selection methods employed by the ALICE experiment. The figure clearly demonstrates that the highest correlation coefficient values are observed for the widest centrality bin widths (Δ centrality = 10%), where the largest contribution from volume fluctuations is expected. Wide centrality bins include a broader range of events with varying geometry (different N_{part} or impact parameters), which boosts the effect of these fluctuations. Narrowing the centrality bins reduces the contribution of volume fluctuations, and the values of the correlation coefficient drop, regardless of the chosen centrality estimation method.

  The trends observed in Fig. 3.9 are in qualitative agreement with theoretical predictions from the Wounded Nucleon Model (WNM)[4], as expressed by the formula derived in Ref. [40]. In the midrapidity region, this formula for the correlation coefficient takes a particularly simple form:

$$b^{n_F n_B}_{corr(WNM)} = 1 - \left[1 + \frac{\overline{n}}{4} \left(\frac{2}{k} + \underbrace{\frac{\langle w^2 \rangle - \langle w \rangle^2}{\langle w \rangle}}_{\text{“volume fluctuations”}} \right) \right]^{-1}, \tag{3.30}$$

  where w is the number of wounded nucleons in both colliding nuclei, $\langle \dots \rangle$ denotes an event-by-event average over the distribution of wounded nucleons within a given centrality class, and $\overline{n}$ and k are the parameters of the negative binomial distribution that governs particle production from a single wounded

[4]The Wounded Nucleon Model is a simple superposition model. In this framework, the correlation coefficient is derived under the assumption that each wounded nucleon emits particles according to a negative binomial distribution characterised by two parameters: $\overline{n}$, the average multiplicity, and k, which controls the shape of the distribution. A detailed discussion of the model will be given in Chapter 6.

nucleon.

A clear implication of Eq. (3.30) is that narrowing the centrality bin width from 10% to 1%, which reduces wounded nucleon fluctuations $\frac{\langle w^2\rangle - \langle w\rangle^2}{\langle w\rangle}$, leads to a smaller forward-backward correlation coefficient.

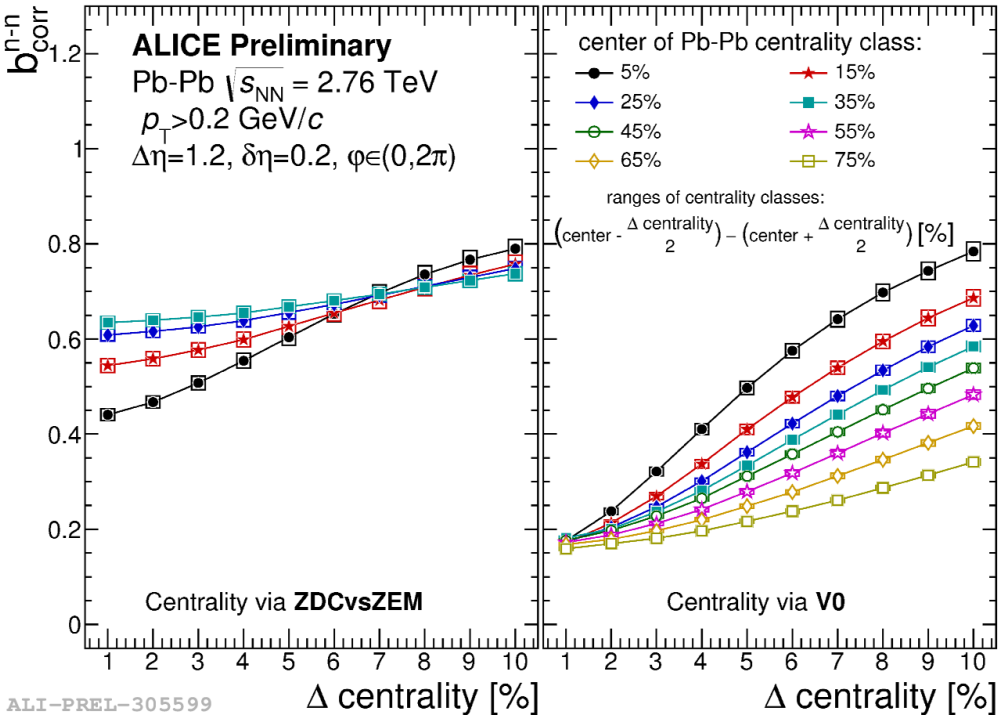

Figure 3.9: The forward-backward correlation coefficient b^{n-n}_{corr} obtained for all charged particles in experimental Pb–Pb collision data at $\sqrt{s_{\rm NN}}$ = 2.76 TeV, shown as a function of the centrality class width (Δcentrality) for a fixed pseudorapidity gap of $\Delta\eta = 1.2$. Results are presented for different centrality selection methods: ZDCvsZEM and V0. The centrality class width varies from 1% to 10%. Different colours correspond to the central values of the centrality classes. Rectangles indicate systematic uncertainties; statistical uncertainties are smaller than the marker size. Figure taken from Ref. [58].

- **Dependence on centrality selection method:** Comparison between the behaviour of data points in the left and right panels of Figure 3.9 shows that the correlation coefficient values depend on the centrality estimator selection. This observation aligns with the conclusions presented in Ref. [57], where it was shown that although different estimators may yield the same average number of participants $\langle N_{\rm part}\rangle$ or average impact parameter, they still can differ in their event-by-event fluctuations, leading to discrepancies in the measured values. Narrowing the centrality bins reduces these fluctuations, but also increases the sensitivity of $b^{n_F n_B}_{\rm corr}$ to the definition of centrality, since

the same nominal bin (e.g. cuts on N_{part} versus cuts on impact parameter) may contain different sets of events and thus produce significantly different correlation values. This behaviour is also consistent with Eq. (3.30), since different centrality selections may lead to samples with different distributions of wounded nucleons, and provides a natural interpretation of the differences observed in Fig. 3.9. The broader implications of centrality selection within the wounded nucleon framework will be addressed in Chapter 6.

3.2.4 Reducing the impact of confounding variables

To mitigate the spurious effects of volume fluctuations on FB multiplicity correlations, several methods can be used, including:

- **Conditional correlation:** In general, this method quantifies the correlation between X and Y while holding a confounding variable Z fixed. In the context of FB multiplicity studies, this corresponds to determining the FB correlation at approximately fixed event geometry. One of the implementations of this idea is the *profile method* of Ref. [59], which conditions measured characteristics of forward and backward multiplicity distributions explicitly on the reference multiplicity and thereby removes the bias from centrality fluctuations. In experimental analyses, the same concept can also be approximated by using very narrow centrality classes (e.g. 1%), where fluctuations of N_{part} and the impact parameter are strongly reduced but not entirely eliminated. Such an approach has been adopted in heavy-ion measurements by ALICE (e.g. Ref. [58]).

- **Partial correlation:** this technique aims to isolate the direct relationship between X and Y, independent of the effects of external random variable(s) Z. The formula for the partial correlation coefficient with control random variable Z, is expressed as:

$$b_{\mathrm{corr}}^{XY\cdot Z} = \frac{b_{\mathrm{corr}}^{XY} - b_{\mathrm{corr}}^{XZ} b_{\mathrm{corr}}^{YZ}}{\sqrt{(1-(b_{\mathrm{corr}}^{XZ})^2)(1-(b_{\mathrm{corr}}^{YZ})^2)}} \tag{3.31}$$

  Here, b_{corr}^{XY},b_{corr}^{XZ}, and b_{corr}^{YZ} are the pairwise correlation coefficients between the variables X, Y, and Z, respectively. Partial correlation has been employed in heavy-ion analyses as a tool to suppress the effects of centrality fluctuations in the study of forward–backward multiplicity correlations in Refs. [60, 61]. In

the latter, the relation between partial and conditional correlations is discussed in detail.

An exploratory experimental analysis of this method, carried out by the author (see Ref. [62]), shows that while the partial correlation approach effectively suppresses volume fluctuations, it remains sensitive to the choice of centrality estimator. In this study, the control variable Z was defined as the centrality measured with a given estimator. Different estimators (e.g. V0, ZDCvsZEM, or their combination) might select slightly different sets of events even within the same nominal centrality class. As a result, the partial correlations obtained with different Z differ and show a clear dependence on the centrality selection method.

- **Strongly intensive quantities (SIQ):** This class of observables was introduced to heavy-ion physics in Ref. [3]. By construction, they are designed to eliminate the influence of event-by-event volume fluctuations, providing a robust framework for analysing correlations and fluctuations in multiparticle production. Strongly intensive quantities are a major focus of this thesis and will be discussed in greater detail in the following section.

3.3 Forward-backward multiplicity correlations and fluctuations with strongly intensive quantities

In the previous sections, we showed that the standard forward-backward multiplicity correlation measures, such as Pearson's correlation coefficient, are strongly affected by event-by-event system volume fluctuations. To reduce these spurious effects and to extract more genuine information about correlations and fluctuations, we now introduce a class of observables known as **strongly intensive quantities**, which are specifically designed to be volume fluctuation-free measures. In particular, we focus on two families of SIQ, namely $\Sigma^{n_F n_B}$ and $\Delta^{n_F n_B}$, which provide a direct framework for analysing forward-backward multiplicity correlations and fluctuations. To motivate their definition and embed them in the bigger context of correlation and fluctuation studies, we first discuss the general construction of strongly intensive quantities for arbitrary extensive observables A and B and then specialise to the case of forward (n_F) and backward (n_B) particle numbers.

3.3.1 Introduction to strongly intensive quantities

In statistical physics, system properties can be classified as either **extensive** or **intensive** [63]:

- **Extensive quantities** depend on system size (e.g., total particle number, energy, entropy).
- **Intensive quantities** remain independent of system size but are still influenced by its fluctuations.

This classification can also be applied to the domain of heavy-ion physics. However, to account for event-by-event system volume fluctuations, Gaździcki and Gorenstein introduced the concept of **strongly intensive quantities** in Ref. [3]. These observables are specifically designed to remain unaffected by both system volume and its fluctuations, which helps eliminate spurious contributions in correlation and fluctuation analyses.

The explicit formalism of strongly intensive observables is constructed as a specific combination of extensive quantities under the assumption of the **Independent Source Model (ISM)**.

3.3.1.1 Independent Source Model

The **independent source model** describes a class of superposition frameworks where particles are produced from statistically identical, independent sources [3].

In the ISM framework, the extensive quantities A and B are proportional to the number of sources N_s, which fluctuates from event to event. The event-averaged values of extensive quantities A and B are given by:

$$\langle A \rangle = \langle \mu_a \rangle \langle N_s \rangle, \tag{3.32}$$

$$\langle A^2 \rangle = \langle \mu_a^2 \rangle \langle N_s \rangle + \langle \mu_a \rangle^2 \left(\langle N_s^2 \rangle - \langle N_s \rangle \right), \tag{3.33}$$

$$\langle B \rangle = \langle \mu_b \rangle \langle N_s \rangle, \tag{3.34}$$

$$\langle B^2 \rangle = \langle \mu_b^2 \rangle \langle N_s \rangle + \langle \mu_b \rangle^2 \left(\langle N_s^2 \rangle - \langle N_s \rangle \right), \tag{3.35}$$

$$\langle AB \rangle = \langle \mu_a \mu_b \rangle \langle N_s \rangle + \langle \mu_a \rangle \langle \mu_b \rangle \left(\langle N_s^2 \rangle - \langle N_s \rangle \right). \tag{3.36}$$

The terms $\langle \mu_a \rangle$, $\langle \mu_b \rangle$, $\langle \mu_a^2 \rangle$, $\langle \mu_b^2 \rangle$, and $\langle \mu_a \mu_b \rangle$ represent the first and second moments of the single-source distribution, $P(\mu_a, \mu_b)$.

Using these fundamental relations, it is easy to construct more complex observables, such as variances and covariances, which provide deeper insight into

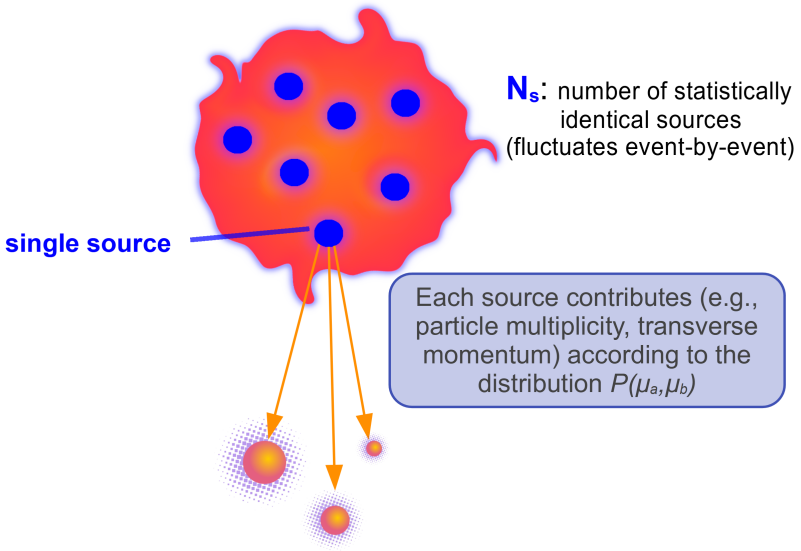

Figure 3.10: Schematic illustration of the independent source model. Each event consists of N_s statistically identical sources, which emit particles independently. The contribution of a single source to the extensive observables A and B is described by a single-source emission probability distribution $P(\mu_a, \mu_b)$. Here μ_a and μ_b denote the single–source values of the observables A and B, respectively. Fluctuations in measured observables arise from both fluctuations of N_s and from intrinsic fluctuations within each source.

fluctuations in the system. One such important observable is the scaled variance:

$$\omega = \frac{\mathrm{Var}(A)}{\langle A \rangle}, \tag{3.37}$$

which in the framework of the ISM emerges as an intensive quantity independent of the number of sources (N_s) but still sensitive to their fluctuations. Using the relations Eqs. (3.32) and (3.33), the scaled variance of the extensive quantity A in the framework of the independent source model can be expressed as:

$$\omega_A = \frac{\mathrm{Var}(A)}{\langle A \rangle} = \underbrace{\frac{\mathrm{Var}(\mu_a)}{\langle \mu_a \rangle}}_{\omega_{\mu_a}} + \underbrace{\frac{\mathrm{Var}(N_s)}{\langle N_s \rangle}}_{\omega_{N_s}} \cdot \langle \mu_a \rangle, \tag{3.38}$$

where ω_{μ_a} represents the contribution from single-source scaled variance, ω_{N_s} captures the fluctuations in the number of sources.

3.3.1.2 Classification of strongly intensive quantities

Strongly intensive quantities can be classified according to the order of moments of the distributions of extensive observables, such as A and B.

1. **First-moment strongly intensive quantities**
   The simplest class of strongly intensive quantities is based on **the first moments** of extensive observables. Within the framework of the independent source model, it becomes evident that the ratio of the first moments of two extensive quantities, A and B, given by:

   $$\frac{\langle A \rangle}{\langle B \rangle} = \frac{\langle \mu_a \rangle}{\langle \mu_b \rangle} \tag{3.39}$$

   is a strongly intensive quantity. Here, terms involving the average number of sources, $\langle N_s \rangle$, cancel, making the ratio dependent only on intrinsic single-source properties.

   Particle yield ratios, such as those between different hadron species, are widely employed to study chemical properties in the system created during high-energy collisions [64, 65, 66].

2. **Second-moment strongly intensive quantities**
   The construction of strongly intensive quantities involving **second moments** is more involved than that of first-moment ratios, as these observables are

sensitive to event-by-event fluctuations and correlations. For two extensive quantities, A and B, there are exactly two linearly independent combinations of the second moments, namely variances and covariances, for which all terms proportional to $\langle N_s \rangle$ and $\langle N_s^2 \rangle$ cancel out within the independent source model. These combinations define two families of strongly intensive quantities, denoted as Σ^{AB} and Δ^{AB}, whose explicit forms are:

$$\Sigma^{AB} = \frac{1}{C_\Sigma} \left(\langle B \rangle \cdot \omega_A + \langle A \rangle \cdot \omega_B - 2 \cdot \mathrm{Cov}(A, B) \right), \tag{3.40}$$

$$\Delta^{AB} = \frac{1}{C_\Delta} \left(\langle B \rangle \cdot \omega_A - \langle A \rangle \cdot \omega_B \right), \tag{3.41}$$

where ω_A and ω_B are the scaled variances of A and B, respectively. The terms C_Σ and C_Δ are normalisation factors proportional to the first moments of the extensive quantities — either $\langle A \rangle$, $\langle B \rangle$, or a combination thereof.

Normalisation of Σ^{AB} and Δ^{AB} quantities

The normalisation factors C_Σ and C_Δ for the strongly intensive quantities Σ^{AB} and Δ^{AB} must be proportional to the extensive observables in order to properly cancel out the term related to the average number of sources $\langle N_s \rangle$. This proportionality ensures that the observables remain invariant under changes in system size, within the framework of the independent source model.
Unless specified otherwise, in this work, the following normalisation factors are adopted for Σ and Δ quantities:

$$C_\Sigma = \langle A \rangle + \langle B \rangle, \tag{3.42}$$

$$C_\Delta = \langle A \rangle - \langle B \rangle, \tag{3.43}$$

which are well-suited to the study of multiplicity fluctuations.
This choice ensures that:

- The strongly intensive quantities Σ^{AB} and Δ^{AB} are **dimensionless and independent of system size** (normalisation),
- The observables are **standardised** to the values $\Sigma^{AB} = \Delta^{AB} = 1$ under independent particle production, and $\Sigma^{AB} = \Delta^{AB} = 0$ in the absence of fluctuations.

General forms of normalisation factors applicable to a broader class of extensive observables can be found in Refs. [3, 67].
Since multiplicities are by definition non-negative, in most practical cases (with standard kinematic cuts, reasonable acceptances), $\langle A \rangle$ and $\langle B \rangle$ are positive, and so $C_\Sigma > 0$.
In contrast, scenarios where $C_\Delta = 0$ make the normalisation of the Δ quantity infeasible. This situation occurs, for example, in forward-backward multiplicity correlation studies, when the average multiplicities in forward and backward rapidity intervals are equal ($\langle n_F \rangle = \langle n_B \rangle$).

By substituting the expressions for the moments (Eqs. (3.32)–(3.36)) into the definitions of Σ^{AB} and Δ^{AB} (Eqs. (3.40), (3.41)), one finds that, under the assumptions of the independent source model, both strongly intensive quantities depend exclusively on the characteristics of the single-source distributions:

$$\Sigma^{AB} = \Sigma^{\mu_a \mu_b}, \tag{3.44}$$

$$\Delta^{AB} = \Delta^{\mu_a \mu_b}. \tag{3.45}$$

This confirms that Σ^{AB} and Δ^{AB} are insensitive to event-by-event fluctuations in the number of sources, and instead reflect only the intrinsic fluctuations and correlations associated with particles emitted from a single source.

3. **Higher-order strongly intensive quantities**

We can also define strongly intensive quantities associated with **higher moments** of extensive observables distributions. A technique to determine higher-order strongly intensive quantities corresponding directly to higher-order cumulants, such as third, fourth, and higher moments, was proposed in the paper Ref. [68]. Since cumulants are typically extensive quantities, constructing their strongly intensive equivalent eliminates volume dependence, highlights intrinsic fluctuation properties, and improves their reliability in the study of critical phenomena. See also Ref. [31] for a related discussion of higher-order strongly intensive measures and their construction.

3.3.1.3 Relation of strongly intensive quantities Σ^{AB} and Δ^{AB} to other fluctuation observables

Although Ref. [3] formally introduced the concept of strongly intensive quantities, similar observables had been studied much earlier in high-energy nucleus-nucleus collisions. A list of observable measures related to Σ^{AB} and Δ^{AB} include:

1. **The fluctuation measure Φ_x:** The earliest example of the observable belonging to the Σ family is the well-known fluctuation measure Φ_x, introduced in Ref. [69] for analysing transverse momentum fluctuations. A comprehensive discussion of this observable, including its properties and generalisations, can be found in Refs. [70, 71].

   The fluctuation measure Φ_x describes the correlations (fluctuations) of a single-particle quantity x, which can represent a kinematic variable (e.g. transverse momentum p_T) or particle type. To define Φ_x, the single-particle variable is introduced $z \stackrel{def}{=} x - \overline{x}$, where $\bar{x}$ represents the average value of x across all particles. At the event level, one can define $Z \stackrel{def}{=} \sum_{i=1}^{N}(x_i - \overline{x})$ variable that sums single-particle deviation across all particles N in the event. The fluctuation measure Φ_x is then expressed as:

$$\Phi_x = \sqrt{\frac{\langle Z^2 \rangle}{\langle N \rangle}} - \sqrt{\overline{z^2}}, \tag{3.46}$$

   where $\overline{z^2}$ represents the variance of x in the inclusive single-particle distribution, and $\langle \dots \rangle$ denotes averaging over all events.

   A particular case of this construction is when the single-particle variable x takes indicator values for two particle types A and B (e.g. $x_i = 1$ for a particle of type A, $x_i = 0$ otherwise), which leads to the definition of the measure Φ^{AB}. As discussed in Ref. [3], in this case one then finds $\bar{x} = \overline{x^2} = \langle A \rangle / [\langle A \rangle + \langle B \rangle]$ and thus $\overline{x^2} - \bar{x}^2 = \langle A \rangle \langle B \rangle / [\langle A \rangle + \langle B \rangle]^2$ with A and B denoting particle numbers. Taking into account these relations, and using $X = A$ and $N = A + B$ in Eq. (3.46), the expression for the Φ^{AB} reads

$$\Phi^{AB} = \frac{\sqrt{\langle A \rangle \langle B \rangle}}{\langle A + B \rangle} \left(\sqrt{\Sigma^{AB}} - 1 \right), \tag{3.47}$$

   where Σ^{AB} is given by Eq. (3.40) with $C_\Sigma = \langle A + B \rangle$.

2. **Fluctuation measure $\nu_{\mathbf{dyn}}^{AB}$:** Another commonly used variable for analysing correlations and fluctuations is the dynamic fluctuation measure $\nu_{\rm dyn}$, introduced in work Ref [16] to study net-charge fluctuations. It is defined in a flowing way:

$$\nu_{\rm dyn} = \frac{\langle A(A-1)\rangle}{\langle A\rangle^2} + \frac{\langle B(B-1)\rangle}{\langle B\rangle^2} - 2\frac{\langle AB\rangle}{\langle A\rangle\langle B\rangle}. \tag{3.48}$$

From the above expression, a direct relationship can be easily determined between the strongly intensive observable Σ^{AB} and the dynamic measure $\nu_{\rm dyn}^{AB}$:

$$\nu_{\rm dyn}^{AB} = \frac{\langle A+B\rangle}{\langle A\rangle\langle B\rangle}\left(\Sigma^{AB}-1\right). \tag{3.49}$$

From the formula Eq. (3.49), it is evident that the observable $\nu_{\rm dyn}^{AB}$ provides information similar to Σ^{AB}, and it is also independent of volume fluctuations. However, due to the scaling factor $\frac{\langle A+B\rangle}{\langle A\rangle\langle B\rangle}$, it is clear that $\nu_{\rm dyn}^{AB}$ depends directly on the system size. Thus, it is not a strongly intensive quantity within ISM. To minimise the impact of system size on the measured value of $\nu_{\rm dyn}^{AB}$, this quantity is often scaled by a factor proportional to $\propto \langle A\rangle, \langle B\rangle$ or $\langle A+B\rangle$.

3. **Ratio of cumulants of net-particle distributions $\frac{\kappa_2(A-B)}{\kappa_1(A+B)}$:** A particularly relevant Σ^{AB}-related observable in high-energy nuclear physics is the ratio of the second cumulant of the net-particle distribution, $\kappa_2(A-B)$, to the first cumulant of the distribution of their sum, $\kappa_1(A+B)$.

The second-to-first cumulant ratio for net particles is defined as

$$\frac{\kappa_2(A-B)}{\kappa_1(A+B)} = \frac{\mathrm{Var}(A-B)}{\langle A+B\rangle} = \frac{\mathrm{Var}(A)+\mathrm{Var}(B)-2\mathrm{Cov}(A,B)}{\langle A+B\rangle} \tag{3.50}$$

The comparison of formula above to Σ^{AB} quantity shows that the two expressions are equivalent when $\langle A\rangle = \langle B\rangle$, namely:

$$\Sigma^{AB} = \frac{\kappa_2(A-B)}{\kappa_1(A+B)}. \tag{3.51}$$

This situation might occur, for example, in **symmetric collisions**.

The study of cumulant ratios is gaining significant interest in the heavy-ion physics community, as they can provide insights into the QCD phase structure.

This work studies the Σ^{AB} quantity, exploring and analysing its characteristics across different phenomenological models. Given the link between cumulant ratios and strongly intensive observables, the study of Σ^{AB} provides a complementary perspective on fluctuation phenomena across different dynamical scenarios to the cumulant ratio discussed here.

3.3.2 Forward-backward correlations and fluctuations with $\Sigma^{n_F n_B}$ and $\Delta^{n_F n_B}$

Having established the general properties and advantages of strongly intensive quantities Σ^{AB} and Δ^{AB}, this section focuses on their **specific application in forward-backward multiplicity correlation and fluctuation analysis**.

Definition of $\Sigma^{n_F n_B}$ and $\Delta^{n_F n_B}$

In terms of forward-backward multiplicity correlation analysis, the fluctuating extensive quantities A and B correspond to the number of particles in the forward n_F and backward n_B (pseudo)rapidity regions, respectively. Using this framework, the expressions for $\Sigma^{AB} = \Sigma^{n_F n_B}$ and $\Delta^{AB} = \Delta^{n_F n_B}$ take the following form:

Definitions of $\Sigma^{n_F n_B}$ and $\Delta^{n_F n_B}$ quantities

$$\Sigma^{n_F n_B} = \frac{\langle n_B \rangle \cdot \omega_F + \langle n_F \rangle \cdot \omega_B - 2 \cdot \mathrm{Cov}(n_B, n_F)}{\langle n_F \rangle + \langle n_B \rangle}, \tag{3.52}$$

$$\Delta^{n_F n_B} = \frac{\langle n_B \rangle \cdot \omega_F - \langle n_F \rangle \cdot \omega_B}{\langle n_B \rangle - \langle n_F \rangle}. \tag{3.53}$$

3.3.2.1 Properties of $\Sigma^{n_F n_B}$ and $\Delta^{n_F n_B}$

This section presents a systematic overview of the key properties of $\Sigma^{n_F n_B}$ and $\Delta^{n_F n_B}$, highlighting both the general features arising from (1) the independent source model and (2) the specific aspects related to their statistical definition. Special attention is given to their behaviour in symmetric collision systems, their relation to the standard forward-backward correlation coefficient, and their connection to the underlying longitudinal structure of the fireball formed in heavy-ion collisions.

1. **Properties arising from ISM assumptions**

   - **Volume-independence:** Both $\Sigma^{n_F n_B}$ and $\Delta^{n_F n_B}$ are strictly independent of the system size (the number of sources N_s) and its fluctuations. This

is ensured by their specific construction within the ISM framework.

- **Sensitivity to single-source properties:** A fundamental property of the strongly intensive quantities $\Sigma^{n_F n_B}$ and $\Delta^{n_F n_B}$, as already discussed in Section 3.3.1.2 point 2, is their exclusive dependence on the intrinsic characteristics of the single-source distributions within the independent source model. This means that the observables are determined only by the average emissions μ_F and μ_B into the forward and backward rapidity intervals, respectively, and not by the total number of sources or their event–by–event fluctuations, namely:

$$\Sigma^{n_F n_B} = \Sigma^{\mu_F \mu_B}$$

and

$$\Delta^{n_F n_B} = \Delta^{\mu_F \mu_B}.$$

Consequently, within the ISM, $\Sigma^{n_F n_B}$ and $\Delta^{n_F n_B}$ provide clean, volume-independent measures of the genuine forward-backward event-by-event fluctuations and correlations originating from a single source.

- **Poissonian baseline for $\Sigma^{n_F n_B}$ and $\Delta^{n_F n_B}$:** In the case where each source emits particles according to a Poisson distribution, the mean $\langle \mu_{F(B)} \rangle$ equals the variance $\mathrm{Var}(\mu_{F(B)})$, resulting in $\omega_{\mu_{F(B)}} = 1$, and $\mathrm{Cov}(\mu_F, \mu_B) = 0$. Under these conditions, and with the normalisation factors defined in Eqs. (3.52) and (3.53), the strongly intensive quantities take the standardised values:

$$\Sigma^{n_F n_B} = 1, \quad \text{and if } \langle \mu_F \rangle \neq \langle \mu_B \rangle, \quad \Delta^{n_F n_B} = 1.$$

2. **Properties emerging from the statistical structure**

- **Symmetry under forward-backward exchange:** With the normalisation adopted in this work (see frame in point 2 of Sec. 3.3.1.2), namely $C_\Sigma = \langle n_F \rangle + \langle n_B \rangle$ and $C_\Delta = \langle n_B \rangle - \langle n_F \rangle$, both strongly intensive quantities $\Sigma^{n_F n_B}$ and $\Delta^{n_F n_B}$ are symmetric under the exchange $n_F \leftrightarrow n_B$:

$$\Sigma^{n_F n_B} = \Sigma^{n_B n_F}, \quad \text{and} \quad \Delta^{n_F n_B} = \Delta^{n_B n_F}.$$

- $\Sigma^{n_F n_B}$ **as the variance of the difference:** By transforming Eq. (3.52), the quantity $\Sigma^{n_F n_B}$ can be expressed as the variance of the difference

between scaled multiplicities n_F and n_B:

$$\Sigma^{n_F n_B} = \frac{\lambda \operatorname{Var}(n_F) + \frac{1}{\lambda} \operatorname{Var}(n_B) - 2 \cdot \operatorname{Cov}(n_F, n_B)}{\langle n_F + n_B \rangle} = \frac{\operatorname{Var}\left(\sqrt{\lambda}\, n_F - \frac{1}{\sqrt{\lambda}}\, n_B\right)}{\langle n_F + n_B \rangle}. \tag{3.54}$$

Here, $\lambda = \frac{\langle n_B \rangle}{\langle n_F \rangle}$ is a scaling factor. This expression, Eq. (3.54), simplifies for collisions, where $\langle n_F \rangle = \langle n_B \rangle \implies \lambda = 1$, to the form:

$$\Sigma^{n_F n_B} = \frac{\operatorname{Var}(n_F - n_B)}{2\langle n_F \rangle}. \tag{3.55}$$

- $\Delta^{n_F n_B}$ **as the difference of variances:** The expression for $\Delta^{n_F n_B}$, Eq. (3.53), can be reformulated as the difference of weighted variances between n_F and n_B:

$$\Delta^{n_F n_B} = \frac{\lambda \operatorname{Var}(n_F) - \frac{1}{\lambda} \operatorname{Var}(n_B)}{\langle n_B - n_F \rangle}. \tag{3.56}$$

  The parameter λ is defined as introduced previously.

- **Relation to the Pearson correlation coefficient:** The strongly intensive observable $\Sigma^{n_F n_B}$ can be expressed analytically in terms of the Pearson correlation coefficient $b_{\text{corr}}^{n_F n_B}$, scaled variances ω_F, ω_B, and mean multiplicities in the forward and backward pseudorapidity intervals. The general expression takes the form:

$$\Sigma^{n_F n_B} = \frac{\omega_F \cdot \langle n_B \rangle + \omega_B \cdot \langle n_F \rangle - 2 b_{\text{corr}}^{n_F n_B} \cdot \sqrt{\omega_F \omega_B \langle n_F \rangle \langle n_B \rangle}}{\langle n_F \rangle + \langle n_B \rangle}. \tag{3.57}$$

  Formula above simplifies significantly for the symmetric case when $\langle n_F \rangle = \langle n_B \rangle$ and $\omega_F = \omega_B \equiv \omega$ to the following expression:

$$\Sigma^{n_F n_B} = \omega \cdot (1 - b_{\text{corr}}^{n_F n_B}). \tag{3.58}$$

  This relation demonstrates that $\Sigma^{n_F n_B}$ encapsulates both the magnitude of fluctuations (via the scaled variance ω) and the strength of forward-backward correlations (via $b_{\text{corr}}^{n_F n_B}$). It thus provides a direct link between the concept of strongly intensive quantities and the standard measure of forward-backward correlations used in experimental analyses. Specifically,

$\Sigma^{n_F n_B} = \omega$ if there is no correlation present ($b_{\mathrm{corr}}^{n_F n_B} = 0$), and $\Sigma^{n_F n_B} = 0$ if there is a perfect correlation ($b_{\mathrm{corr}}^{n_F n_B} = 1$) between particles produced into forward and backward pseudorapidity intervals.

- **Relation to longitudinal asymmetry coefficients in the Chebyshev decomposition:** In their paper, Bzdak and Teaney [18] proposed to analyse longitudinal fluctuations in the shape of the fireball via an expansion of the two-particle correlation function in Chebyshev polynomials.

  In Appendix A we derive a new relation showing that, in symmetric collisions at midrapidity, where $\langle n_F \rangle = \langle n_B \rangle$ and $\mathrm{Var}(n_F) = \mathrm{Var}(n_B)$ holds, the observable $\Sigma^{n_F n_B}$ is particularly sensitive to longitudinal shape fluctuations of the fireball since it can be expressed analytically through odd Chebyshev polynomial coefficients $\langle a_{2n+1} a_{2m+1} \rangle$ obtained from the expansion of the two-particle correlation function.

  For two pseudorapidity intervals of width $\delta\eta$, symmetrically located around $\eta = 0$, namely the forward interval $[\eta_1, \eta_1 + \delta\eta]$ and the backward interval $[-\eta_1 - \delta\eta, -\eta_1]$, the observable $\Sigma^{n_F n_B}$ can be expressed as:

$$\Sigma^{n_F n_B} = 1 + \frac{2\rho_0}{\delta\eta} \sum_{n,m \geq 0} \langle a_{2n+1} a_{2m+1} \rangle \, J_n \, J_m, \tag{3.59}$$

  with

$$J_0 = \frac{Y}{2} \left[\sin^2 \theta_1 - \sin^2 \theta_2 \right],$$

$$J_n = \frac{Y}{2} \left[\frac{\cos(2n\theta_1) - \cos(2n\theta_2)}{2n} - \frac{\cos((2n+2)\theta_1) - \cos((2n+2)\theta_2)}{2n+2} \right], \quad n \geq 1,$$

  where $\theta_1 = \arccos(\eta_1 / Y)$ and $\theta_2 = \arccos((\eta_1 + \delta\eta)/Y)$ correspond to the lower and upper edges of the forward interval, respectively. Here, Y denotes the maximal pseudorapidity used to rescale the variable η to the domain $[-1, 1]$, which is the natural domain of the Chebyshev polynomials.

  In a special case, for forward and backward pseudorapidity intervals of width $\delta\eta = Y$, symmetrically placed about midrapidity, so that $\eta_1 = 0$ and $\theta_1 = \frac{\pi}{2}$, $\theta_2 = 0$, one gets:

$$J_0 = \frac{Y}{2}, \quad J_n = Y \, \frac{(2n+1)(-1)^n - 1}{4n(n+1)}, \quad n \geq 1.$$

Finally:

$$\boxed{\Sigma^{n_F n_B} = 1 + \frac{2\rho_0}{Y} \sum_{n,m\geq 0} \langle a_{2n+1} a_{2m+1} \rangle \, J_n \, J_m}. \tag{3.60}$$

This shows that $\Sigma^{n_F n_B}$ is sensitive only to *odd-order* Chebyshev modes. This selectivity arises from the symmetry of the integrated correlation function: when the forward and backward pseudorapidity intervals are placed symmetrically around midrapidity, contributions from even-order modes cancel due to the Chebyshev polynomials' parity properties under reflection. As a result, only odd-order components of the longitudinal fluctuations contribute. Moreover, the contribution of each mode to $\Sigma^{n_F n_B}$ is weighted inversely with its order, leading to a diminishing influence of high-index coefficients.

This conclusion remains also valid for expansions in Legendre polynomials, $P_n(\eta/Y)$, which form another standard orthogonal basis on $[-1, 1]$. The parity property of Legendre polynomials is the same as for Chebyshev polynomials:

$$P_n(-x) = (-1)^n P_n(x).$$

Thus, when forward and backward pseudorapidity intervals are chosen symmetrically about midrapidity, even-order contributions cancel identically, and $\Sigma^{n_F n_B}$ depends only on *odd-order Legendre coefficients* $\langle a_n a_m \rangle$ with $n, m = 2k + 1$.

Although the numerical values of the coefficients $\langle a_n a_m \rangle$ differ between Chebyshev and Legendre decompositions, the set of contributing modes is the same. Thus, the physical sensitivity of $\Sigma^{n_F n_B}$ to longitudinal asymmetry is independent of whether the expansion is performed in Chebyshev or Legendre polynomials.

The forward–backward correlation analysis using a Legendre polynomial decomposition was studied by ATLAS [19] and ALICE [72].

- **Relation to the PHOBOS forward-backward σ_C^2 observable:** The PHOBOS Collaboration [73] introduced the forward-backward asymmetry variable $C = \frac{n_F - n_B}{\sqrt{n_F + n_B}}$, with variance

$$\sigma_C^2 = \left\langle \frac{(n_F - n_B)^2}{n_F + n_B} \right\rangle, \tag{3.61}$$

used to study longitudinal correlations in heavy-ion collisions.

It has been shown through an analytical expansion (see Appendix of Ref. [74]) that in the limit of small multiplicity fluctuations,

$$n_B = \langle n_B \rangle (1 + \varepsilon_B), \quad n_F = \langle n_F \rangle (1 + \varepsilon_F), \quad \text{where } |\varepsilon_{F(B)}| \ll 1, \quad (3.62)$$

σ_C^2 can be approximated by the expression:

$$\sigma_C^2 \approx 1 + \frac{\langle n_B(n_B - 1) \rangle - \langle n_B n_F \rangle}{\langle n_B \rangle}. \quad (3.63)$$

For collisions for which $\langle n_F \rangle = \langle n_B \rangle$ and $\mathrm{Var}(n_F) = \mathrm{Var}(n_B)$, the following approximate relation holds:

$$\sigma_C^2 \approx 1 + \frac{\langle n_B(n_B - 1) \rangle - \langle n_B n_F \rangle}{\langle n_B \rangle} = \frac{\mathrm{Var}(n_B) - \mathrm{Cov}(n_B, n_F)}{\langle n_B \rangle} = \Sigma^{n_B n_F}. \quad (3.64)$$

As stressed above, this approximation is valid for symmetric collisions and pseudorapidity bins and when forward-backward multiplicity fluctuations are small. It suggests that although σ_C^2 is not strictly strongly intensive, it behaves approximately as such under controlled conditions.

In the remainder of this thesis, as we focus mostly on forward–backward multiplicity fluctuations and correlations, the superscript in $\Sigma^{n_F n_B}$ will be omitted. We shall therefore simply denote it by Σ, which by default refers to forward–backward correlations, unless specified otherwise.

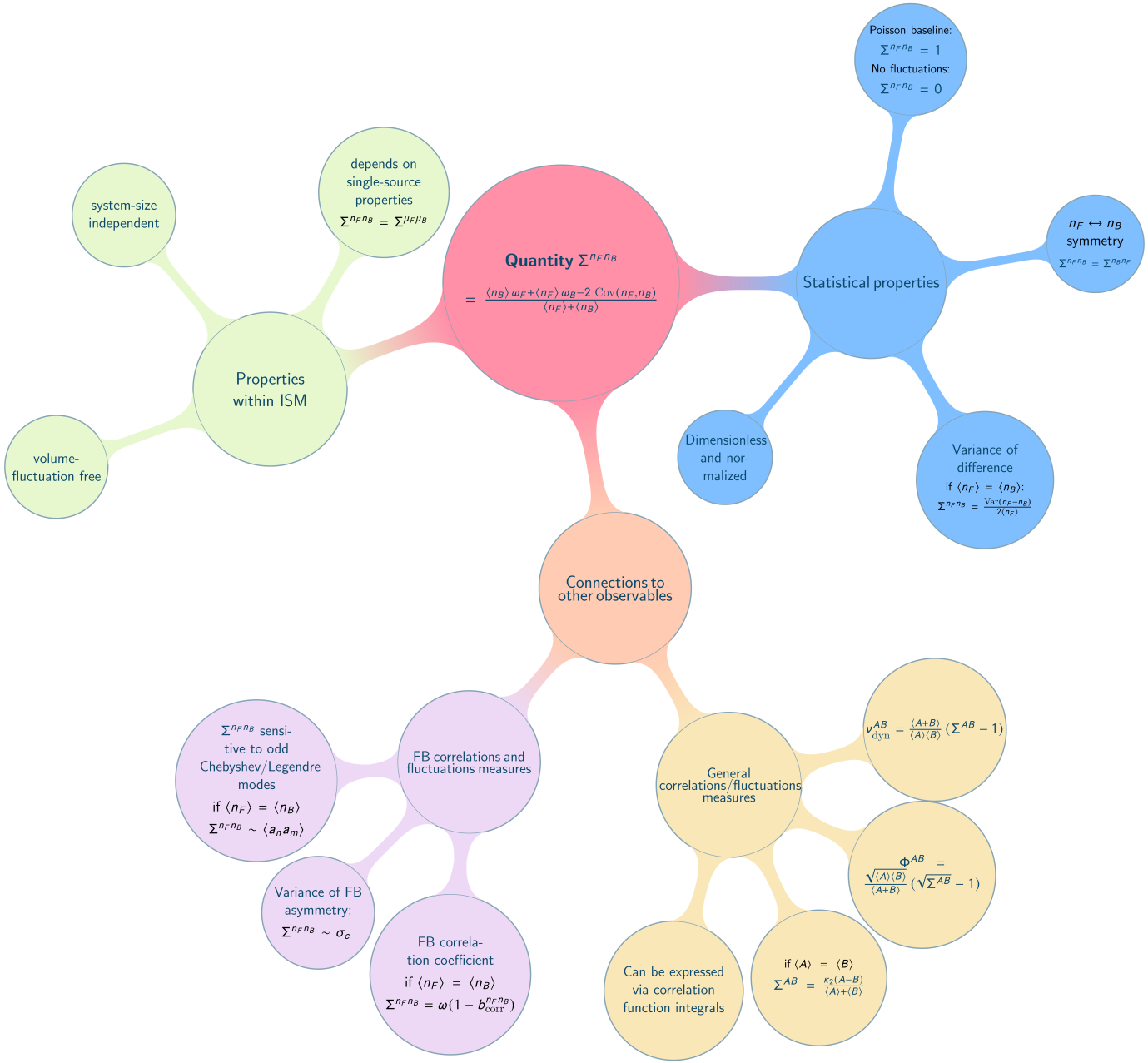

Figure 3.11: Schematic overview of the properties and relations of the strongly intensive quantity $\Sigma^{n_F n_B}$.

Chapter 4

Data analysis of Pb–Pb and Xe–Xe collisions

This chapter presents the ALICE detector, detailing the experimental setup, relevant subsystems configuration, and the operational conditions important to the measurements. Particular emphasis is placed on a description of the methodology used to extract the forward-backward correlation with Σ, as well as the analysis procedure, including the estimation of both statistical and systematic uncertainties associated with the measurements.

4.1 The ALICE Detector

Data for the forward–backward correlation analysis with Σ were collected with the ALICE (A Large Ion Collider Experiment) detector, one of the four major experiments operating at the LHC at CERN [75]. ALICE is dedicated to studying strongly interacting matter under extreme conditions created in ultra-relativistic heavy-ion collisions such as lead–lead (Pb–Pb) interactions.

Although ALICE is primarily dedicated to investigating heavy-ion collisions, it also measures smaller collision systems, such as p–Pb and pp collisions. The study of these systems serves as a reference for nucleus-nucleus interactions and provides an important benchmark for comparison with other experiments. In addition, they offer the possibility to study fundamental QCD processes and to explore the mechanisms underlying the emergence of collective-like effects even in the smallest systems [76, 77].

The layout of the ALICE detector, as used during the Run 2 data-taking period, is shown in Fig. 4.1. In this context, a "Run" refers to a specific data-taking period at the LHC, during which collisions are recorded under defined experimental conditions. At the end of 2021, ALICE completed a major upgrade in preparation for Run 3. However, since the studies presented in this thesis are based solely on data collected during Run 1 (2010–2013) and Run 2 (2015–2018), the focus of this chapter remains

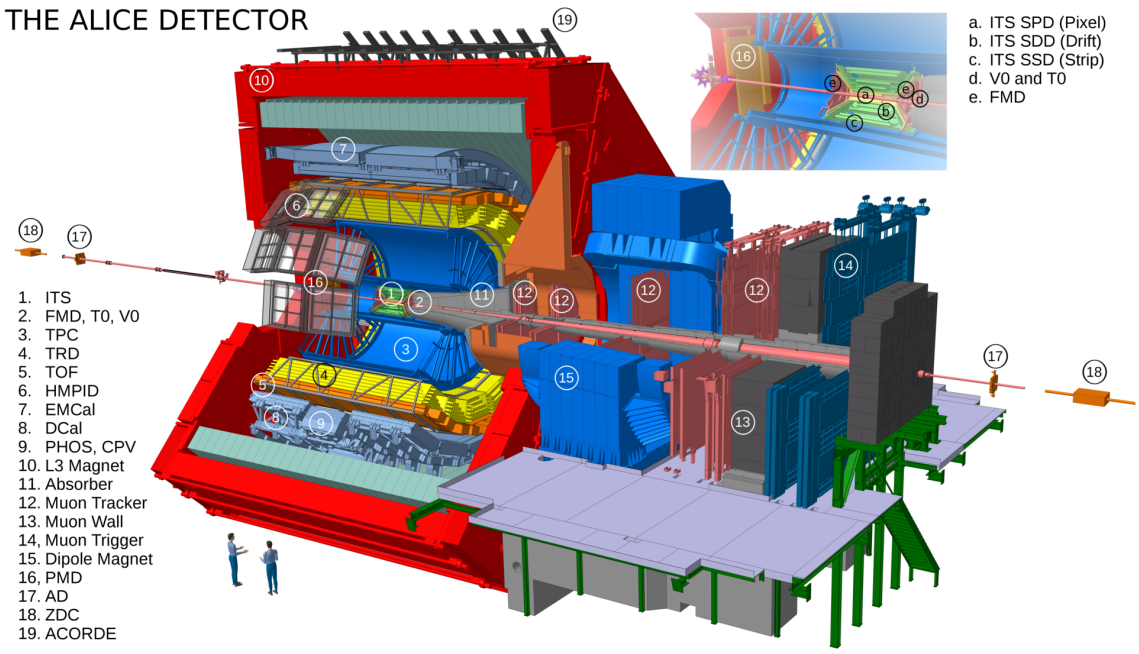

Figure 4.1: ALICE Run 2 detector systems. Details of the relevant subsystems are described in the text. Figure from Ref. [80].

on the detector configuration and performance during those periods. A comprehensive overview of the physics results obtained by ALICE during Run 1 and Run 2 can be found in Ref. [78].

4.1.1 Summary of the ALICE detector architecture

The ALICE detector has been described in detail in numerous technical publications and performance reports. Here, only a brief overview of its subsystems relevant to the present analysis is provided. This summary is largely based on the official performance report of the experiment [79] and the recent overview publication [78]. For more detailed and technical discussions, the reader is referred directly to those publications.

ALICE is a 10,000-tonne detector experiment specifically designed to operate under extreme conditions of high temperature and particle density, as produced in heavy-ion collisions. It consists of three main regions listed below.

Central barrel. It is a main part of the ALICE detector system. It surrounds the interaction point and is located inside the L3 solenoid magnet, which provides a magnetic field of 0.5 T. Its primary tasks include charged-particle tracking, reconstruction of primary and secondary vertices, momentum and energy measurement, time-of-flight determination, and particle identification for hadrons, electrons, and

photons. To fulfil these tasks, the central barrel consists of several dedicated detectors, which are described in the following.

- **ITS (Inner Tracking System)** – the innermost detector in ALICE, consisting of six tracking layers listed in Ref. [81]. It is dedicated to precise vertexing, low-momentum tracking, and enhancing the momentum and angular resolution of measured particles [81].

- **TPC (Time Projection Chamber)** – the main central barrel detector, designed for tracking of charged particles and particle identification with a method based on specific energy loss (dE/dx) in a gas volume [82].

- **TRD (Transition Radiation Detector)** – a detector specialised in electron identification and electron/pion separation at higher transverse momentum (p_{T}) [83].

- **TOF (Time of Flight)** – it is a device that provides electron and charged particle identification at intermediate momenta based on time-of-flight measurement [84].

- **PHOS (Photon Spectrometer)** – it is a high-resolution calorimeter dedicated to photon and neutral meson detection, based on the scintillation process in $PbWO_4$ crystals [85].

- **EMCal (Electromagnetic Calorimeter)** – it is an electromagnetic calorimeter system used for jet reconstruction and measurement of electromagnetic energy [86].

- **HMPID** – is a Ring imaging Cherenkov detector providing particle identification at intermediate-p_{T} [87].

The first four detectors (ITS, TPC, TRD and TOF) provide full azimuthal coverage within the pseudorapidity range $|\eta| < 0.9$. The remaining central barrel detectors, EMCal, PHOS and HMPID, cover only limited regions in azimuth within their corresponding pseudorapidity ranges.

From the perspective of the analysis presented in this work, the most important detectors for extracting the charged-particle multiplicity in a given pseudorapidity interval are the ITS and TPC, which together provide high tracking efficiency and precise vertex and momentum reconstruction in the central region of the ALICE detector.

Forward region. The forward detectors in ALICE are located at small angles relative to the beam axis, covering regions in pseudorapidity beyond the acceptance of the central barrel. Their role is triggering, centrality determination, background rejection, and event characterisation. For the analysis presented in this work, the most relevant forward detectors are:

- **V0 detector** – composed of two scintillator arrays, V0A and V0C, placed on either side of the interaction point, covering the pseudorapidity ranges approximately $2.8 < \eta < 5.1$ (V0A) and $-3.7 < \eta < -1.7$ (V0C). It provides fast triggering, background rejection, and is used in centrality and event plane determination [88].

- **ZDC (Zero Degree Calorimeters)** – hadronic calorimeters located at ± 116 m on both sides of the interaction point, designed to detect spectator neutrons and protons emitted at very small angles, close to the beam axis. The ZDC system is used for centrality estimation, triggering on ultraperipheral collisions, and pileup suppression.

Other forward detectors, such as the T0, PMD, FMD and AD, are also installed in ALICE, but they are not used directly in the analysis discussed in this work. Their main features can be briefly summarised as follows: **T0 detector** – it is a fast-timing Cherenkov detector providing precise measurements of the collision time (t_0) [89]; **PMD (Photon Multiplicity Detector)** – it is located on the one side of ALICE setup (A-side) and dedicated to measures the multiplicity and spatial distribution of photons in the pseudorapidity range $2.3 < \eta < 3.5$, this detector was decommissioned and removed during Run 2. **FMD (Forward Multiplicity Detector)** – it is another forward detector based on silicon strip sensor technology, designed to measure the multiplicity and distribution of charged particles in the forward pseudorapidity region [89]. **AD (ALICE Diffractive Detector)** – it is a forward scintillator array system installed during Run 2, designed to enhance the detection of diffractive and ultraperipheral events [90].

Muon spectrometer. Although the muon spectrometer is technically located in the forward region, it is often classified separately due to its distinctive design, as shown in Fig. 4.1 extending outward from the main body of the ALICE detector. The location of the muon spectrometer determines the so-called *C-side* of the ALICE detector. It is a forward detector, specifically designed for muon reconstruction in the pseudorapidity range $-4.0 < \eta < -2.5$ [91].

4.2 Off-line Data Analysis

4.2.1 Data Samples and Event Selection

The analysis presented in this thesis is based on data recorded by the ALICE experiment at the CERN Large Hadron Collider. Two distinct types of collision systems are considered:

- *heavy-ion collisions* (Pb–Pb and Xe–Xe), which constitute the core dataset analysed in this work. The Pb–Pb samples were collected at centre-of-mass energies per nucleon pair of $\sqrt{s_{\mathrm{NN}}} = 2.76$ TeV (Run 1) and 5.02 TeV (Run 2), while the Xe–Xe sample corresponds to $\sqrt{s_{\mathrm{NN}}} = 5.44$ TeV (Run 2).
- *proton–proton* (pp) collisions, which are used as a reference sample and provide important comparative insight into the system-size dependence of the studied observable. The pp data were taken at $\sqrt{s} = 0.9$, 2.76, and 7 TeV (Run 1), and at $\sqrt{s} = 5.02$ and 13 TeV (Run 2).

Event selection:

Trigger: Due to the large read-out time of the ALICE detector and data storage limitations, it is unable to record every event. Thus, data acquisition begins only if some non-negligible signal is registered in the selected ALICE detectors. For the minimum-bias trigger, a coincidence of signals on the two V0 detectors (V0A and V0C) was used in Pb–Pb and Xe–Xe, based on the requirement to capture the full spectrum of *inelastic* nucleus-nucleus interactions.

In the case of proton–proton collisions, the trigger configuration varied depending on the data-taking period. In the early runs (2010–2011), minimum-bias events were selected using a general minimum-bias condition (a trigger requiring activity in at least one of the V0A, V0C, or SPD detectors) together with the requirement of simultaneous signals in both V0A and V0C. From 2012 onwards, minimum-bias events were simply defined by a coincidence between V0A and V0C.

In all cases, the analyses presented in this work are based on the appropriate minimum-bias trigger for the considered system and period, with further technical details available in Ref. [92], the ALICE Data Preparation Group (DPG) presentation.

Primary Z-vertex: The primary vertex is the reconstructed spatial point of the collision. Only events containing a reconstructed primary vertex are included in the analysis. The vertex is obtained from the standard ALICE reconstruction

using combined ITS and TPC tracking information. To ensure uniform detector acceptance to the analysis, enter only those events for which the position of the primary vertex component along the beam axis (z direction) is no further than 7 cm from the interaction point.

For pp collisions, a looser cut of $\pm$10cm on the z-vertex position is commonly used and found to be sufficient.

Pileup rejection: Pileup refers to the occurrence of multiple collisions within the same or neighbouring bunch crossings, leading to overlapping interactions being reconstructed as a single event. Due to the high luminosity in Run 2, pileup became a significant issue. A dedicated rejection procedure was therefore implemented for Pb–Pb data at $\sqrt{s_{\mathrm{NN}}} = 5.02$ TeV. For the 2018 Pb–Pb run, pileup suppression relied on the correlation between the number of TPC clusters and the sum of SDD and SSD clusters. For the pp data samples, pileup rejection was performed by removing events with multiple reconstructed vertices in the SPD.

Centrality and multiplicity class selection

The classification of heavy-ion collisions according to their collision geometry was based on two distinct centrality selection methods provided by ALICE. The first method relies on the measurement of energy deposited by spectator nucleons in the Zero Degree Calorimeters (ZNA and ZNC), located on both sides of the interaction point. Since the formation of nuclear fragments in spectator remnants breaks the monotonic relation between the energy measured in the ZDC and the collision geometry, the ZDC signal is correlated with the energy measured in the ZEM calorimeters ($4.8 < \eta < 5.7$) to restore monotonic scaling with the collision geometry, and hence with the average number of participants. Thus, this centrality selection method is called the ZDCvsZEM estimator. This centrality estimator allows for centrality determination in ranges $0 - 40\%$ of the total hadronic cross section.

The second method is based on the sum of amplitudes of charged particles measured in the V0A and V0C segments of the V0 detector, covering the pseudorapidity ranges $2.8 < \eta < 5.1$ (V0A, on the A-side) and $-3.7 < \eta < -1.7$ (V0C, on the C-side), respectively. This method is widely used for centrality determination due to its excellent resolution and efficiency across a broad range of impact parameters. This centrality estimator, often referred to as V0 or V0M, allows for centrality selection in ranges of $0 - 80\%$ of the total hadronic cross section.

In Run 2 Pb–Pb and Xe–Xe collisions, centrality was determined using V0 multiplicity alone, and the use of the ZDC for centrality estimation was discontinued.

More information about the procedure used for centrality determination in the ALICE experiment can be found in Refs. [93, 94].

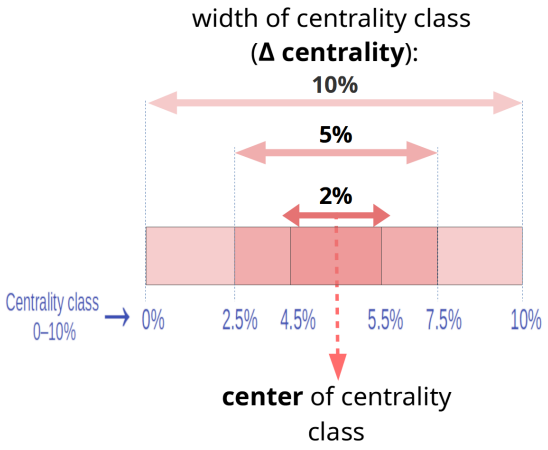

Figure 4.2: Illustrative representation of the selection of different widths of centrality class intervals.

In this analysis, events for Pb–Pb and Xe–Xe were divided into 10% centrality classes (e.g., 0–10%, 10–20%, etc.). To study the effect of the centrality class bin width, each interval corresponding to 10% was symmetrically narrowed around the class centre to widths as small as 2%, see Fig. 4.2.

The pp collisions were studied in the minimum bias sample. In addition, the pp data sample at $\sqrt{s} = 13$ TeV was divided into multiplicity classes based on the V0 estimator, using percentile intervals such as 0–1%, 1–5%, up to 70–100%

4.2.2 Track selection

The forward-backward correlations were measured for charged-particle tracks. Only those charged particles whose tracks fulfilled specific selection criteria were studied. In the case of Pb–Pb and Xe–Xe collisions, the analysis was performed using charged particle tracks selected within the transverse momentum range $0.2 < p_{\mathrm{T}} < 5$ GeV/c, the pseudorapidity interval $|\eta| < 0.8$, and covering the full azimuthal angle range $\varphi \in [0, 2\pi]$.

In the case of pp collisions, a significantly more restrictive transverse momentum selection was applied, namely $0.2 < p_{\mathrm{T}} < 2$ GeV/c.

4.3 Evaluation of forward-backward correlations with Σ

Pseudorapidity binning and interval definitions:

The pseudorapidity region is divided into smaller intervals of width $\delta\eta = 0.2$, symmetrically placed around midrapidity ($\eta = 0$). Intervals located at positive η values are referred to as forward bins, while those at negative η are referred to as backward bins. The separation gap between the forward and backward intervals is labelled as $\Delta\eta$, defined as the distance between the upper edge of the forward interval and the lower edge of the backward interval (see Fig. 3.3). For pp, this distance is denoted as η_{gap} and is defined as the distance between the centres of the forward and backward η intervals. The relation between these two definitions of the separation gap is: $\eta_{gap} = \Delta\eta + 0.2$.

Procedure for Σ evaluation:

To quantify forward–backward multiplicity correlations, the charged-particle multiplicity was evaluated event-by-event in each defined forward and backward pseudorapidity interval. For each interval, the first and second statistical moments, namely, the mean and the variance, were determined. In addition, for each symmetric pair of forward and backward intervals, separated by a fixed pseudorapidity gap $\Delta\eta$, the covariance between the multiplicities in the forward and backward regions was calculated. Based on the measured moments, more complex statistical observables were constructed, including:

- the correlation coefficient $b_{corr}^{n_F n_B}$,
- the scaled variance ω, and
- Σ,

as defined by formulas Eqs. (3.28), (3.37), and (3.52), respectively.

The analysis was performed across different centrality classes and with varying centrality bin widths. The pseudorapidity separation $\Delta\eta$ between the forward and backward intervals was systematically changed in the range from 0.2 to 1.2. Where applicable, the study was repeated using different centrality selection methods (e.g., V0, ZDCvsZEM) in order to evaluate possible estimator dependencies.

Data correction

Two detector effects are significant and can contribute to uncontrolled systematic uncertainties in charged-particle multiplicity measurements within the ALICE experiment. These are: *the presence of secondary particles* and *the limited acceptance and efficiency losses* of the ALICE detector. Both of these factors directly distort the final particle yield measured in nuclear collisions.

Secondary particles are not produced directly at the collision point. They come from weak decays of light-flavour hadrons (e.g., $\Lambda \to p\pi^-$) or from interactions with detector material (e.g., $\gamma \to e^+e^-$), see Ref. [95]. The presence of such particles affects the measured charged-particle multiplicity distributions and can distort the calculation of their statistical moments, thereby introducing biases into key observables such as Σ.

To suppress non-primary contributions, reconstructed tracks were selected based on stringent quality cuts, including constraints on the distance of closest approach to the primary vertex. Additionally, Monte Carlo simulations, incorporating realistic detector geometry and response, were utilised to estimate the fraction of secondary particles contributing to each measured moment of the multiplicity distribution and to apply a statistical correction factor accordingly.

Detector acceptance refers to the geometric and kinematic coverage of the detector. Acceptance losses occur when a particle is produced outside the sensitive region or within inactive (dead) zones of the detector and thus cannot be registered. In this analysis, acceptance losses are considered small. Most of the measured particles originate from the central barrel region, the majority of which is covered by the TPC. This part of the ALICE detector provides full azimuthal coverage. The only acceptance-related losses arise from small inactive areas between the TPC's readout chambers.

Detector efficiency refers to the probability that a charged particle produced in the collision is detected and reconstructed by the ALICE tracking system. Not all particles are registered, and such losses affect the particle multiplicity and distort its statistical properties, such as the mean, variance, and consequently Σ.

The detection efficiency is commonly modelled as a binomial process, in which each particle is reconstructed independently with a given probability [96]. In the present analysis, this probability was assumed to be constant across the considered phase space, while in Ref. [96] a more general, phase-space-dependent efficiency is discussed. In practice, efficiency corrections applied in ALICE include both the geometrical acceptance and the intrinsic detection probability of the tracking system.

To estimate these effects and correct the measured observables, dedicated Monte Carlo simulations were employed. The efficiency correction was applied only to primary particles, after suppressing the contribution of secondaries through track-quality cuts and a dedicated correction procedure for secondary particles described above.

The detector efficiency estimated based on MC HIJING simulation for Pb–Pb collisions at 5.02 TeV is reported in Fig. 4.3.

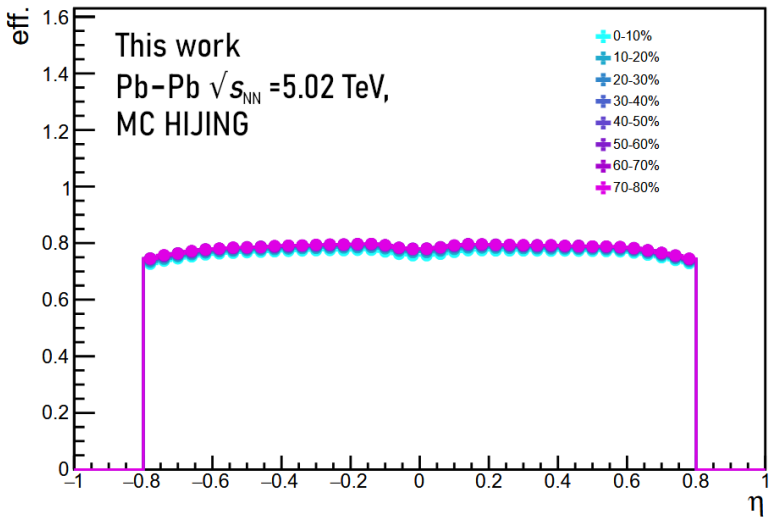

Figure 4.3: Detection efficiency as a function of pseudorapidity for different centrality classes in Pb–Pb collisions at $\sqrt{s_{\mathrm{NN}}} = 5.02$ TeV, obtained from HIJING Monte Carlo simulations.

The effect of the full correction procedure, including secondary particle removal and efficiency correction, for Pb–Pb collisions at $\sqrt{s_{NN}} = 5.02$ TeV is shown in Fig. 4.4. For all studied systems, the total correction effect did not exceed 2.5%.

4.4 Statistical and systematic uncertainties

This section summarises the main sources of uncertainty considered in the analysis.

4.4.1 Statistical uncertainties

Statistical uncertainties arise from the finite size of the event sample analysed to determine the values of Σ. In Pb–Pb and Xe–Xe collisions, they were evaluated analytically using the *delta method* [97], which applies a linear approximation to estimate the variance of non-linear functions such as Σ. As a cross-check, a bootstrap

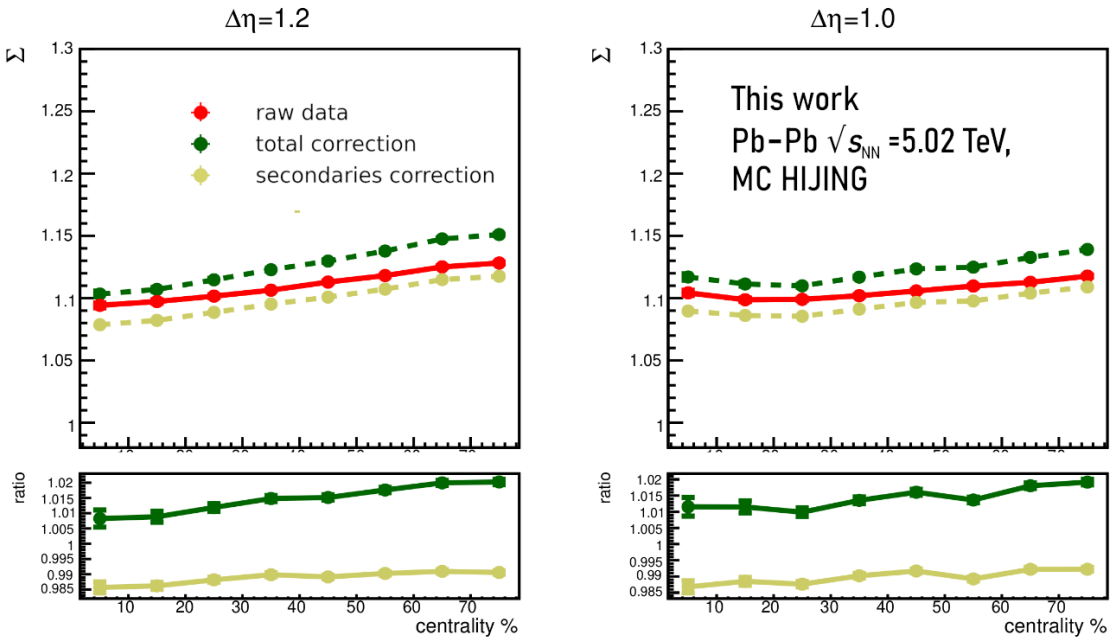

Figure 4.4: Effect of efficiency and secondary-particle corrections on the measured values of Σ in Pb–Pb collisions at $\sqrt{s_{\mathrm{NN}}} = 5.02$ TeV (MC HIJING). Results are shown for two pseudorapidity intervals, $\Delta\eta = 1.2$ (left) and $\Delta\eta = 1.0$ (right). The top panels compare raw data with results after secondary-particle corrections and after the full correction procedure (including secondary-particle and detector-efficiency corrections). The bottom panels show the ratios of corrected to raw data, illustrating the relative impact of the applied corrections.

approach [98] was also employed. Statistical uncertainties were estimated using both techniques, and their values were found to be in good agreement.

4.4.2 Systematic uncertainties

Several sources of systematic uncertainty were investigated by repeating the analysis under modified conditions. Each test probed the sensitivity of the measured Σ observable to specific analysis choices and assumptions.

Only variations that produced statistically significant deviations, quantified according to the Barlow criterion [99], were included in the final estimate of systematic uncertainties. This criterion compares the difference between the nominal and varied results to the combined statistical uncertainty of both. If the difference exceeds twice the combined standard deviation ($\geq 2\sigma$), the effect is classified as systematic rather than statistical. This procedure prevents statistical fluctuations from being misidentified as systematic effects.

Table 4.1 summarises the sources of systematic uncertainty that did not pass the Barlow criterion, together with their maximum observed impact on the Σ observable. Systematic uncertainties were evaluated separately for each pseudorapidity separation $\Delta\eta$, each centrality class, and each data sample. Since the listed maximum deviations originate from independent variations under different conditions, they do not occur simultaneously. Consequently, the total systematic uncertainty, obtained by adding contributions in quadrature, is smaller than the direct sum of the individual maxima.

4.5 Monte Carlo simulations

As mentioned earlier, detector efficiency corrections were based on Monte Carlo simulations using the HIJING event generator. HIJING (Heavy Ion Jet INteraction Generator) is a perturbative QCD-inspired model that incorporates multiple minijet production, nuclear shadowing, and soft interactions. For more details on HIJING, see Ref. [100]. For this analysis, simulations were produced as part of the ALICE data-anchored MC production, ensuring consistency with the experimental conditions.

To evaluate the robustness of the correction procedure, the particle composition in HIJING was varied. The effect on correction factors was found to be negligible.

In addition to HIJING, other models were used to compare theoretical predictions to the measured observables. These include:

- **EPOS-LHC**, which features a core-corona approach with collective hydrodynamic expansion of the dense core and hadronisation of the dilute corona [101].

Source	Description / Variation	Max. effect [%]
Magnetic field orientation	Comparison between opposite field polarities	0.6
z-vertex cut	Variation of primary vertex z-position range	0.5
DCA_z cut	Changed longitudinal DCA cut to check secondary suppression	0.5
TPC cluster requirement	Varied minimum number of TPC clusters per track	0.35
Pile-up rejection	Tightened/loosened pile-up rejection selection	0.2
MC closure test	Effectiveness of the total correction procedure tested on MC data	2.2
Multiplicity outliers	Tested tails of the multiplicity distribution	0.6
Total	**Sum in quadrate**	**2.2**

Table 4.1: Summary of systematic uncertainty sources with their maximum observed effect on Σ, and whether they were included in the final uncertainty budget (according to the Barlow criterion).

- **AMPT** (A Multi-Phase Transport model), which includes partonic scatterings, string melting, and hadronic rescattering. Results were obtained both with and without the string melting mechanism [102].

These models provide complementary physics scenarios for describing final-state interactions and are used for direct comparison with experimental data. The focus of this chapter is on the experimental setup, data selection, analysis procedure, and the evaluation of statistical and systematic uncertainties. A comparison of the measured results with theoretical model predictions, including AMPT, EPOS-LHC, and HIJING, is presented and discussed in the following chapter.

Chapter 5

Event-by-event forward-backward correlations and fluctuations with Σ at the LHC energies

This chapter presents new experimental results and phenomenological insights into forward-backward correlations, studied through the strongly intensive quantity Σ at LHC energies. The discussion is largely based on works [58, 103, 104], and partially summarises their content, but its aim is to offer a more comprehensive and integrated picture than what was formulated in the references cited. The results discussed in this chapter represent the author's original contributions, building upon the existing framework to refine and extend the understanding of forward-backward correlations in particle production.

5.1 Centrality bin width and centrality estimator dependence of Σ

The Σ observable is constructed to be a strongly intensive quantity and, as such, should be independent of the system volume and its fluctuations. The first step of this analysis is to verify to what extent this independence is maintained across varying centrality interval widths, which serve as a proxy for fluctuations of the system size.

Figure 5.1 (a) shows the experimental results on the Σ observable as a function of centrality bin width (Δ centrality) for Pb–Pb collisions at $\sqrt{s_{\mathrm{NN}}} = 2.76$ TeV. Data points are presented for different centrality classes selected with two different centrality selection methods provided by ALICE. They are based on the calorimetric centrality estimator (ZDCvsZEM) and the V0 detector (see Sec. 4.2.1). Experimental findings are compared to corresponding Monte Carlo HIJING simulations. Results for HIJING were also obtained using two different centrality selection methods: one

based on the determination of the impact parameter and the other on multiplicity measurements in the acceptance of the V0 detector. The latter directly corresponds to the centrality estimator used in the experimental data.

From the figure, it emerges that Σ exhibits the following characteristics:

- Σ values exceed unity ($\Sigma > 1$) across all studied centrality classes, independent of the centrality selection method used for both experimental data and HIJING. Thus, $\Sigma > 1$ reflects multiplicity fluctuations exceeding the Poisson baseline.

- For each chosen centrality class, Σ values do not change when varying the width of centrality class interval from wide Δ centrality =10% (where the largest contribution for volume fluctuations is present), down to narrow Δ centrality= 1% (where a significant reduction of system size fluctuations is expected). This behaviour, the independence Σ of volume fluctuations within a given centrality class, is in alignment with one of the properties of a strongly intensive quantity.

- The values of Σ are consistent across different centrality estimators, such as V0 and ZEMvsZDC. This result suggests that the Σ observable is insensitive to varying methods of centrality selection in the experiment. This is an experimentally non-trivial finding, as many observables, such as b_{corr}^{n-n}, the partial correlation coefficient, and ω, exhibit a strong sensitivity to the chosen method for determining collision centrality, see Sec. 3.2.3. Unlike many standard correlation and fluctuation measures, Σ retains its independence, demonstrating its potential as an overall robust measure in heavy-ion collision studies.

- From the comparison of experimental data to MC HIJING prediction, Fig. 5.1 (b), it is evident that the model reproduces basic features of the data, namely reports insensitivity to the volume fluctuations and independence from centrality selection method.

- A final yet intriguing observation is the clear ordering of the Σ values with centrality observed in both the experimental results and the HIJING simulations. The experimental data show an evident *increase* in Σ from central to peripheral collisions. In contrast, the HIJING results display the opposite trend, with the Σ values *decreasing* as the collisions become more peripheral.

While independence from centrality bin width is a property of a strongly intensive quantity, the independence from the centrality estimator is an unexpected outcome. In the original introductions of strongly intensive measures (Ref. [3]), the authors did not

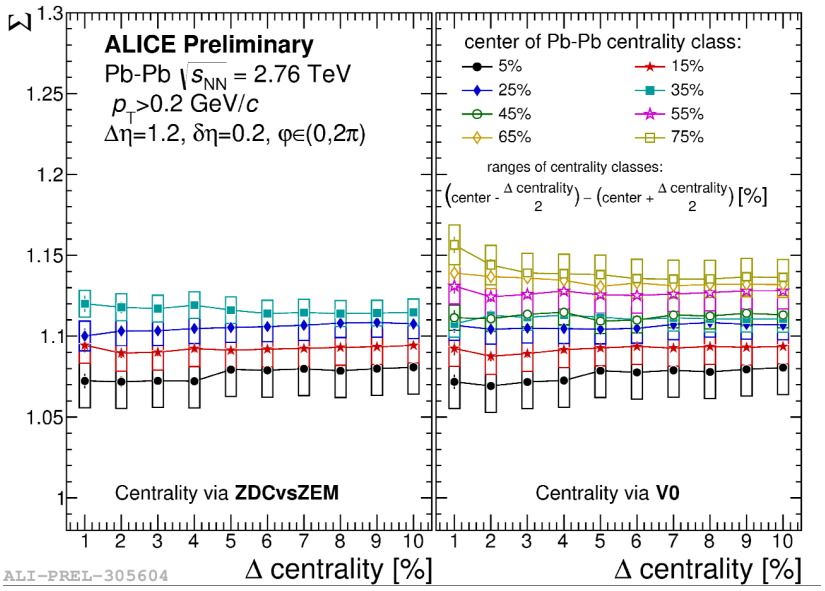

(a)

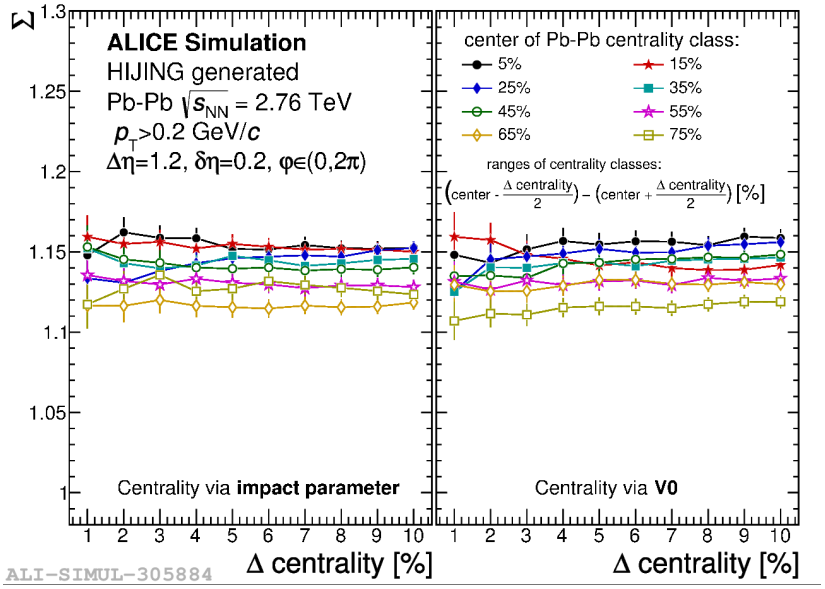

(b)

Figure 5.1: Dependence of the Σ observable on the centrality bin width in Pb–Pb collisions at $\sqrt{s_{\mathrm{NN}}}$ = 2.76 TeV, for a fixed separation gap between forward and backward pseudorapidity intervals of $\Delta\eta = 1.2$. The results are presented for (a) experimental data and (b) HIJING-generated Pb–Pb collisions. The results are presented for different centrality selection methods: ZDCvsZEM, V0, and impact parameter selection. The centrality bin width ranges from 1% to 10%. Different colours of the data points correspond to different centralities in Pb–Pb collisions. Rectangles represent systematic uncertainties, while vertical lines indicate statistical uncertainties. Figure taken from Ref. [58].

focus on a possible dependence on the centrality estimator. Still, under independent source model assumptions, this property arises directly from the construction of Σ. This quantity within ISM depends only on single-source production characteristics, and these single-source properties do not change with the choice of the centrality estimator.

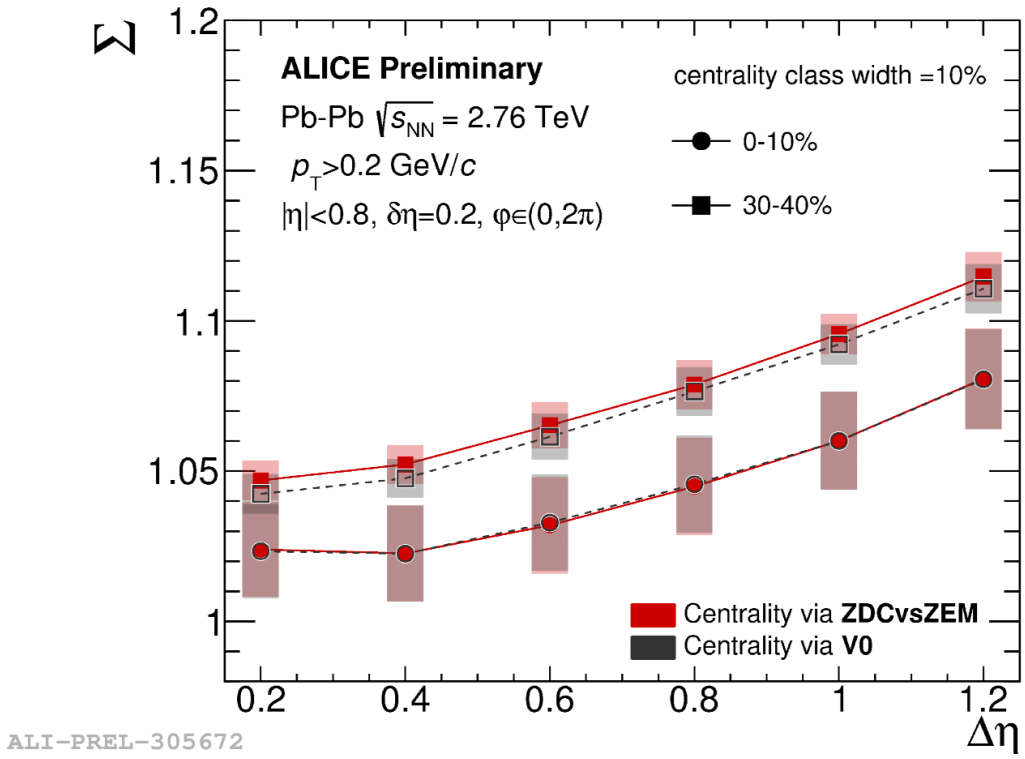

Figure 5.2: Dependence of the Σ observable on the pseudorapidity gap $\Delta\eta$ in Pb–Pb collisions at $\sqrt{s_{\mathrm{NN}}} = 2.76$ TeV for two centrality classes (0–10% and 30–40%). Results are shown for two centrality selection methods via ZDCvsZEM (red) and V0 (black). The width of the centrality class is fixed to 10%. Vertical lines indicate statistical uncertainties, while shaded boxes represent systematic uncertainties. ALICE preliminary result (ALI-PREL-305672).

Figure 5.1 focuses on Σ results for a specific value of $\Delta\eta$, whereas Figure 5.2 provides a more comprehensive view across the pseudorapidity range $|\eta| < 0.8$. This figure confirms that Σ's independence from the centrality estimator is maintained across different pseudorapidity intervals.

Figures 5.1 and 5.2 provide two independent checks of the robustness of Σ. The first tests its stability against the centrality bin width, i.e. residual volume fluctuations, while the second examines its dependence on the choice of centrality estimator. This is the first systematic verification of these properties, made possible by the availability of two independent centrality estimators in ALICE, as described

in Chapter 4.

It is important to note that for all the results presented in subsequent sections, particularly for Xe–Xe at $\sqrt{s_{\rm NN}}$ = 5.44 TeV and Pb–Pb at $\sqrt{s_{\rm NN}}$ = 5.02 TeV, a cross-check was always systematically performed to ensure that the Σ values are independent of volume fluctuations and centrality estimators, both for the experimental data and Monte Carlo models. This verification has become a standard procedure in the analyses performed by the author. Given that Σ consistently exhibits this independence, the results shown in the rest of this chapter are mostly presented for a wide centrality bin width of 10% and only one type of centrality estimator, V0.

5.2 Σ as a function of forward-backward separation gap $\Delta\eta$

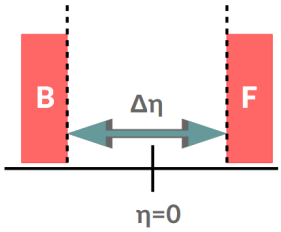

FB separation gap $\Delta\eta$

Having established the independence of the Σ from volume fluctuations (centrality bin width) and confirmed its robust behaviour across two different centrality estimators, this section shifts focus to another key aspect of forward-backward correlations: their dependence on separation gap $\Delta\eta$ between the forward and backward intervals. In general, the dependence on the separation gap $\Delta\eta$ provides sensitivity to the relative contributions of short–range and long–range correlations (see Sec. 3.2.2).

Figures 5.3– 5.5 present the overview of the behaviour of Σ as a function of $\Delta\eta$ for different colliding systems, Pb–Pb at $\sqrt{s_{\rm NN}}$ = 2.76 and 5.02 TeV and Xe–Xe at $\sqrt{s_{\rm NN}}$ = 5.44 TeV. Experimental results presented on panels (a) are compared to the selected MC predictions, such as MC HIJING with and without resonances[1], and EPOS-LHC.

[1]In this work, the term *MC without resonances* refers to Monte Carlo HIJING events in which particles originating from hadronic resonance decays have been removed from the analysis. Technically, this was achieved by excluding both strong and weak resonances, in particular: neutral and charged kaons (K^0, $\bar{K}^0$, K_S, K_L, K^* and $\bar{K}^*$), the ϕ meson, Λ and $\bar{\Lambda}$ hyperons, Σ hyperons and anti-hyperons (Σ^0, $\bar{\Sigma}^0$, $\Sigma^{\pm}$, $\bar{\Sigma}^{\mp}$), Δ baryons and their antiparticles, as well as $\rho^{+,0,-}$ mesons. In addition, neutral pions (π^0) and photons, which are immediate products of such resonance decays, were also excluded.

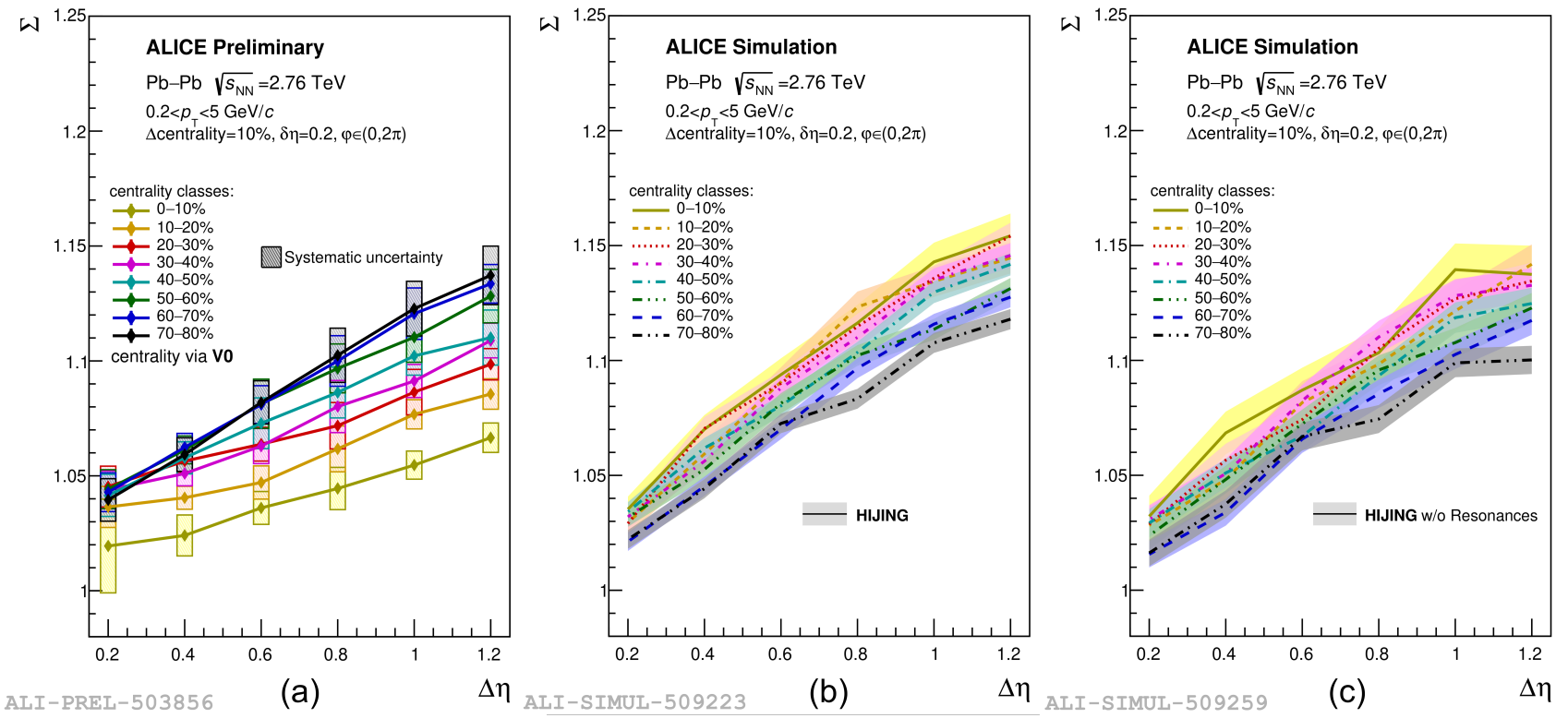

Figure 5.3: Σ obtained from Pb–Pb collisions at $\sqrt{s_{NN}} = 2.76$ TeV is presented as a function of $\Delta\eta$ for different centrality classes of width 10%. All results are shown for centrality determined with the V0 estimator. Results are shown in three panels: (a) experimental data, (b) HIJING model, (c) HIJING without resonance decays. ALICE preliminary results (ALI-PREL-503856, ALI-SIMUL-509223, ALI-SIMUL-509259), see ALICE Figure Repository [105].

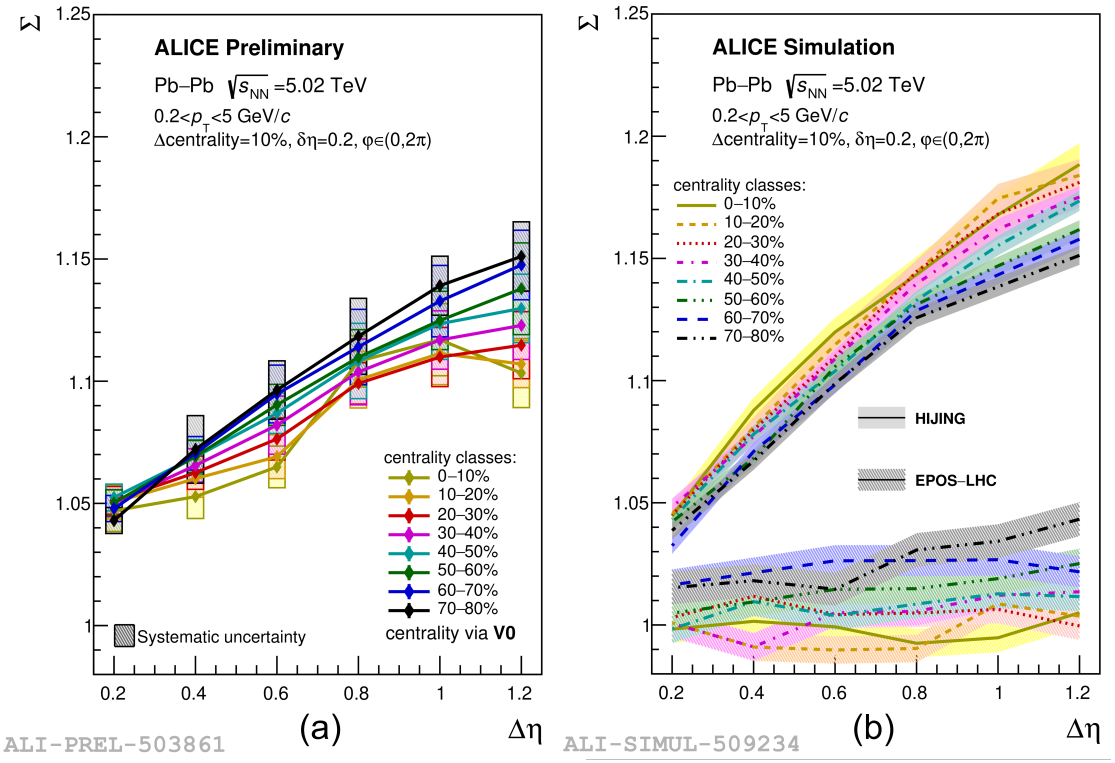

Figure 5.4: Σ as a function of $\Delta\eta$ in Pb–Pb collisions at $\sqrt{s_{NN}} = 5.02$ TeV. Centrality classes of width 10% are defined using the V0 estimator. Panel (a) shows the experimental results. Panel (b) presents the corresponding Monte Carlo simulations (HIJING and EPOS-LHC). ALICE preliminary results (ALI-PREL-503861, ALI-SIMUL-509234), see ALICE Figure Repository [105].

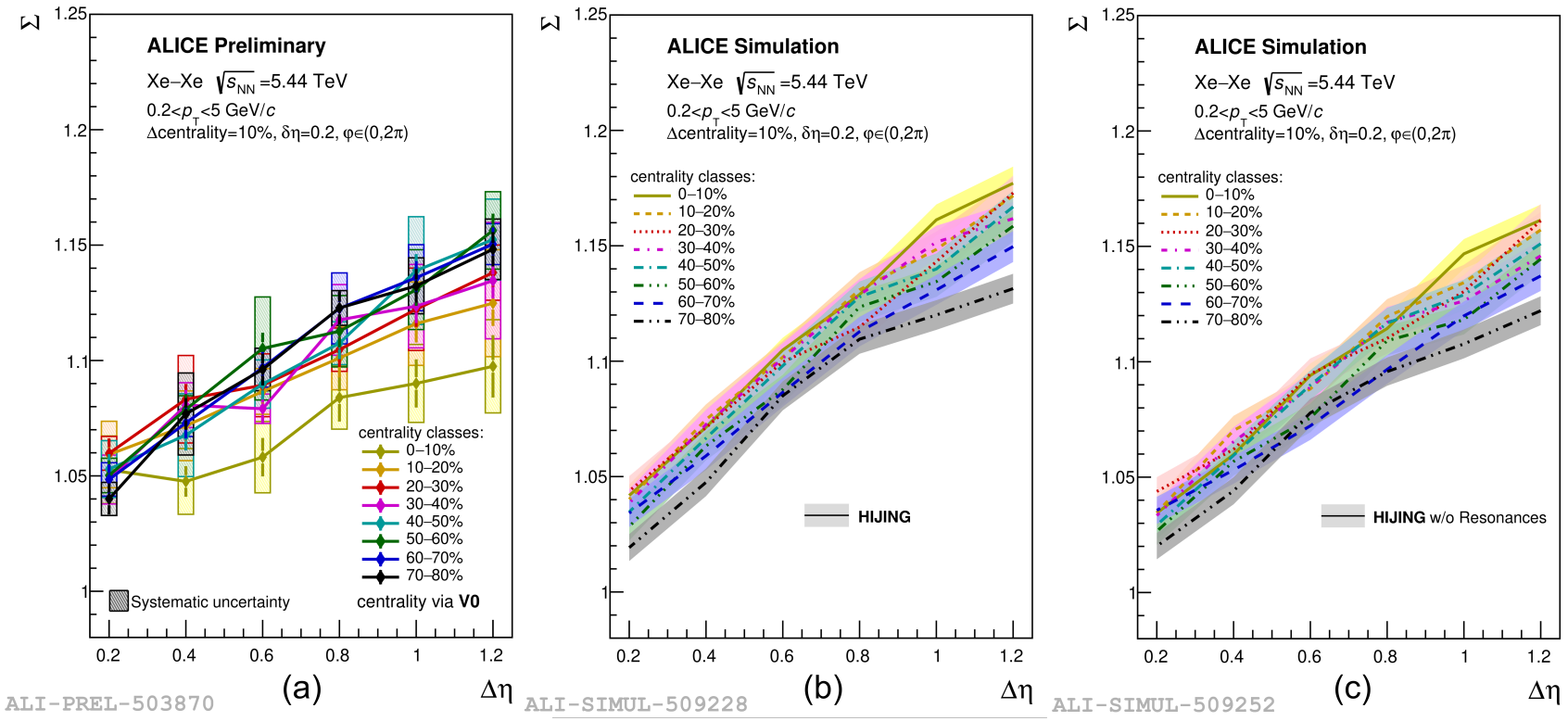

Figure 5.5: Σ obtained from Xe–Xe collisions at $\sqrt{s_{NN}} = 5.44$ TeV is presented as a function of $\Delta\eta$ for different centrality classes of width 10%. All results are shown for centrality determined with the V0 estimator. Results are shown in three panels: (a) experimental data, (b) HIJING model, (c) HIJING without resonance decays. ALICE preliminary results (ALI-PREL-503870, ALI-SIMUL-509228, ALI-SIMUL-509252), see ALICE Figure Repository [105].

Based on the results of this analysis, one can make the following observations:

- The values of Σ remain above unity ($\Sigma > 1$) for all $\Delta\eta$ intervals and for all collision systems studied.
- A growth of Σ with increasing separation window between forward and backward interval $\Delta\eta$ is observed for all the colliding systems and is mirrored by all MC model predictions. This increase likely results from a reduced contribution of short-range correlations as the distance between the forward and backward pseudorapidity intervals grows. This behaviour directly follows from relation Eq. (3.58).
- From Fig. 5.4 it is apparent that while the HIJING model shows an overall agreement with experimental data, capturing the magnitude of measured values, the MC EPOS-LHC exhibits more than 10% quantitative discrepancy across all studied ranges of $\Delta\eta$.
- As already mentioned in the previous section, an *ordering* of Σ values with centrality can be observed. This pattern is evident in the experimental data for all collision systems studied, as well as in the model predictions selected for analysis (HIJING and EPOS-LHC). One interesting finding from the presented results is that, although the EPOS-LHC doesn't match the magnitude of the experimental data, it does qualitatively exhibit the same centrality-based ordering. In contrast, for MC HIJING, the ordering of Σ with centrality is *opposite* to what is observed in the experimental data and MC EPOS-LHC. The values decrease as collisions become more peripheral in MC HIJING, while they increase in the actual data.
- The comparison between the data points in panels (b) and (c) in Figures 5.3 and 5.5 shows that removing the influence of hadronic resonances in HIJING only somewhat reduces the strength of Σ while still maintaining its trend with centrality.

The observed inconsistency in the ordering of Σ between the experimental data and the theoretical models prompted a comprehensive analysis of Σ as a function of centrality, which will be discussed in the next section.

5.3 Centrality dependence of Σ

The results for Σ measured in Pb–Pb and Xe–Xe collisions at $\sqrt{s_{\rm NN}}$ = 2.76, 5.02, and 5.44 TeV, as a function of centrality, are presented in Figure 5.6. While the findings from higher-energy Pb–Pb and Xe–Xe collisions are presented using the V0 centrality estimator, the results from lower-energy Pb–Pb collisions have also been reported for the calorimetric centrality estimator. Experimental results presented on the left panel of the figure are compared to the outcome of some of the most commonly used MC models in heavy-ion physics, such as HIJING, AMPT and EPOS-LHC, presented in the right panel of the figure.

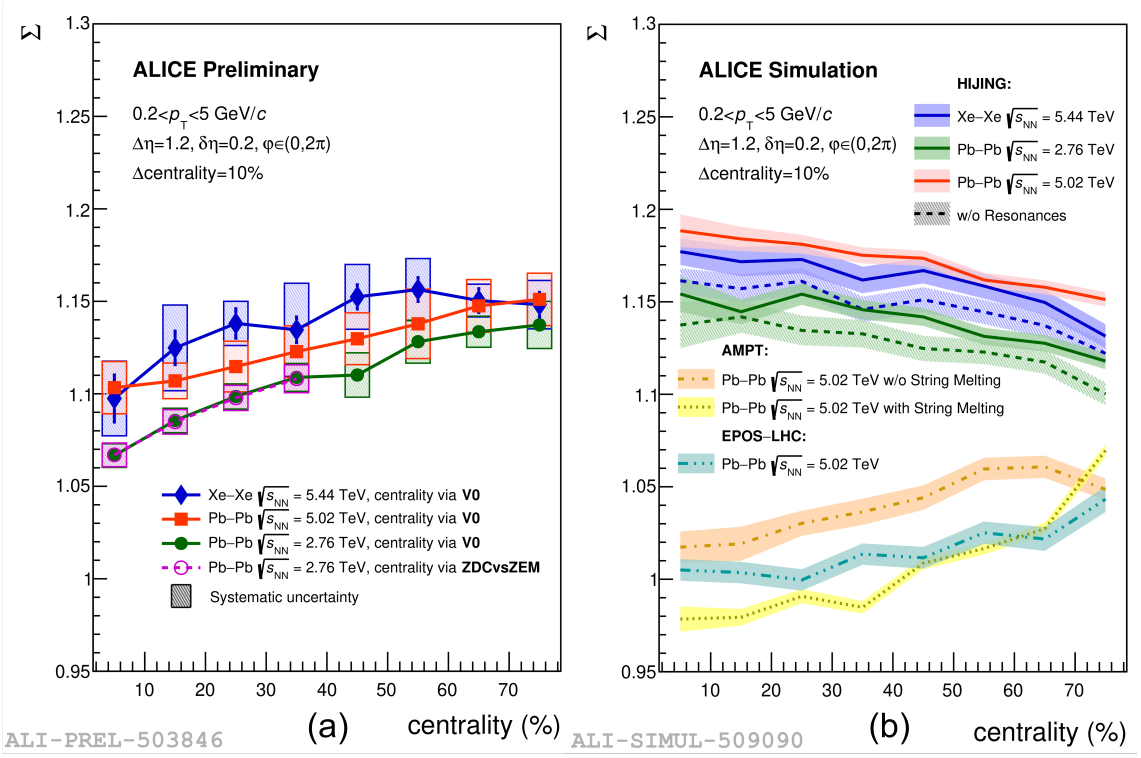

Figure 5.6: Centrality dependence of Σ obtained for Pb–Pb collisions at $\sqrt{s_{\rm NN}}$ = 2.76 and 5.02 TeV and Xe–Xe collisions at $\sqrt{s_{\rm NN}}$ = 5.44 TeV. Results are presented for a fixed value of the pseudorapidity separation gap between forward and backward intervals, $\Delta\eta = 1.2$. The experimental data presented in the left panel are compared with the results from HIJING, EPOS-LHC, and AMPT simulations, as shown in the right panel. Figure taken from Ref. [104].

Figure 5.6, reveals four key characteristics of the Σ in nucleus-nucleus collisions as a function of system size:

- A comparison of results for two centrality estimators, V0 and ZDCvsZEM, in Pb–Pb collisions at $\sqrt{s_{\rm NN}}$ =2.76 TeV supports the findings reported in Fig. 5.1,

that Σ values are unaffected by the choice of centrality estimator.

- From the figure, it is also evident that values of the Σ increase with the increasing energy of the collision, regardless of the colliding system size, with the highest values observed in Xe–Xe collisions at $\sqrt{s_{\rm NN}}$ =5.44 TeV.

- In Fig. 5.6 (a), a distinct trend can be observed in the evolution of Σ values with centrality; Σ values increase from central to peripheral collisions for all studied collision systems.

- A key result of this study is related to a direct comparison between experimental data and model predictions. All selected MC models, namely HIJING, AMPT, and EPOS-LHC, fail to accurately represent the experimental data, either qualitatively or quantitatively.

The most perplexing observation highlighted above is the evident mismatch between the theoretical model predictions and the experimental results. A detailed analysis of the HIJING simulation reveals that while the model overall reproduces the experimental values for Pb–Pb and Xe–Xe collisions in terms of quantitative magnitude, it fails to capture two important qualitative aspects. Firstly, the HIJING model does not reproduce the observed *energy dependence* in the experimental data. Second, it fails to replicate the expected *trend* in Σ values as a function of centrality; rather than the anticipated pattern, the model predicts a decrease in Σ values as collisions become more peripheral. The reduction of contribution coming from resonances only decreases the magnitude of Σ values predicted by HIJING, but does not change their ordering with centrality.

Regarding the predictions of AMPT and EPOS-LHC, while the models seem to reproduce the qualitative behaviour of Σ with centrality, they completely fail to match the quantitative values of experimental data. The discrepancies are substantial, exceeding 10%.

Additionally, the predictions obtained from the two versions of the AMPT model show somewhat different patterns in the behaviour of the data points. The default AMPT scenario (labelled as AMPT w/o String Melting in Fig. 5.6) assumes the Lund string fragmentation mechanism to hadronise excited strings. The string melting variant converts all excited strings into partons based on their quark flavour and spin, followed by hadronisation through quark coalescence. From the results of MC AMPT, it is clear that the Σ is sensitive to the assumed mechanism of particle production in the model.

As shown in Ref. [106], the dipole-string Monte Carlo with string fusion seems to reproduce both the magnitude of the strongly intensive measure Σ and its centrality trend for Pb–Pb at $\sqrt{s_{\rm NN}} = 2.76$ TeV. However, the agreement is only apparent since the model was evaluated in a different acceptance, using wide pseudorapidity windows of $\delta\eta = 0.8$, i.e. four times the experimental width. A fair comparison requires matching the experimental acceptance. For $\delta\eta$ =0.2, which corresponds to experimental conditions, the values of Σ are expected to decrease sharply, falling below the experimental data points.

5.4 Comparison between nucleus-nucleus and proton-proton collisions

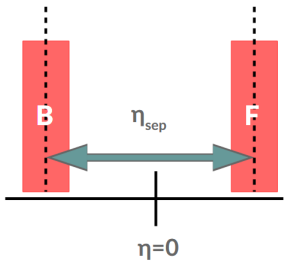

FB separation gap η_{sep} in pp analysis
$\Delta\eta = \eta_{sep} - 0.2$

The author's first-ever results of the Σ observable in nucleus-nucleus collisions at the LHC energies have motivated the ALICE Collaboration to conduct similar analyses in proton-proton collisions Ref. [107]. This section will compare the initial findings of Σ in Pb–Pb and Xe–Xe collisions with the subsequent outcomes in small collision systems of pp interactions.
Figures 5.7 and 5.8 report the results of the forward-backward correlations with Σ observable across varying energies ranging from $\sqrt{s} = 900$ GeV to 13 TeV in pp collisions, plotted as a function of the separation gap η_{sep}.

This gap is defined as the distance between the centres of forward and backward η intervals, and it is related to $\Delta\eta$ as follows: $\Delta\eta = \eta_{sep} - 0.2$. The results obtained for $0.2 < p_{\rm T} < 2$ GeV/c reflect a slightly softer $p_{\rm T}$ regime, as compared to those obtained for $0.2 < p_{\rm T} < 5$ GeV/c in heavy-ion collisions. In Figure 5.7, values of Σ were presented for selected multiplicity classes in pp collisions at $\sqrt{s} = 13$ TeV. The classifications of events by multiplicity were based on measurements from the V0 detector.

Figure 5.8 provides a comprehensive energy scan of Σ (in analogy to nucleus-nucleus collisions, Fig. 5.6), showing its evolution across the selected energy ranges. The experimental results presented in the figure were compared to PYTHIA model predictions with and without the Colour Reconnection (CR) mechanism (Ref. [108,

109]), as well as the phenomenological string model described in Ref. [41, 110].

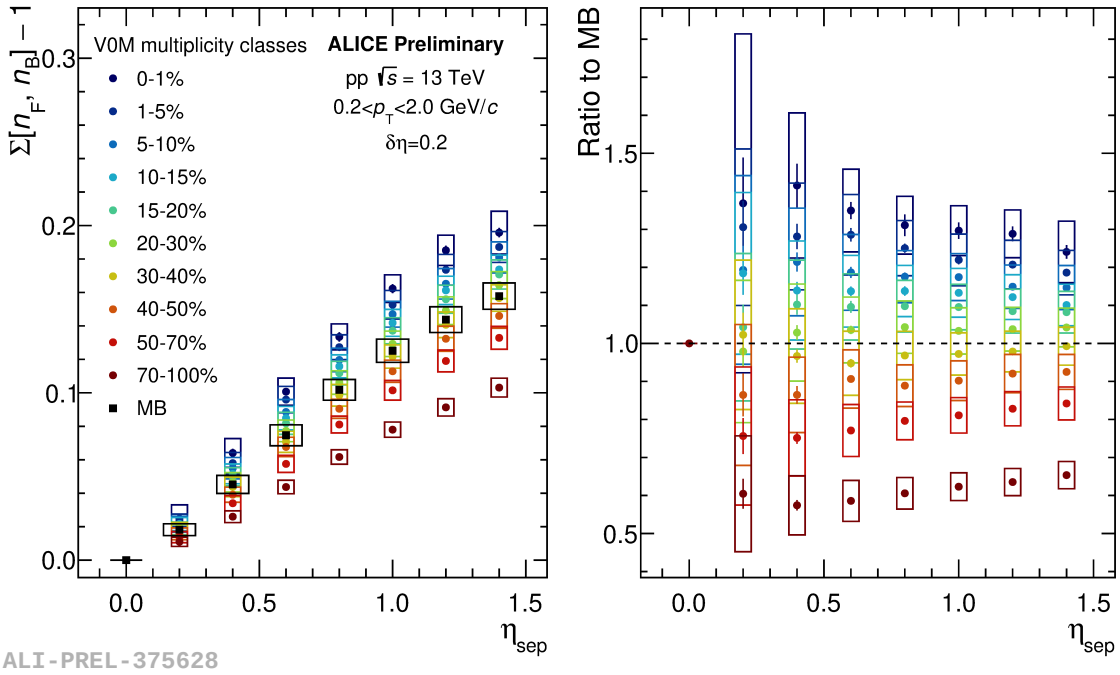

Figure 5.7: (Left) Results $\Sigma[n_F, n_B]-1$ as a function of $\eta_{\rm sep} = \Delta\eta+0.2$ in pp collisions at $\sqrt{s} = 13$ TeV. Results are presented for different V0 multiplicity classes, as well as minimum bias (MB) pp collisions. (Right) Ratio of $\Sigma[n_F, n_B] - 1$ results obtained for different multiplicity classes to the minimum-bias. Statistical uncertainties are shown as error bars, and boxes represent systematic uncertainties. *Notation:* in the text the observable is denoted by Σ, while in the figures it appears as $\Sigma[n_F, n_B]$. Both notations refer to the same quantity. Figure taken from Ref. [107].

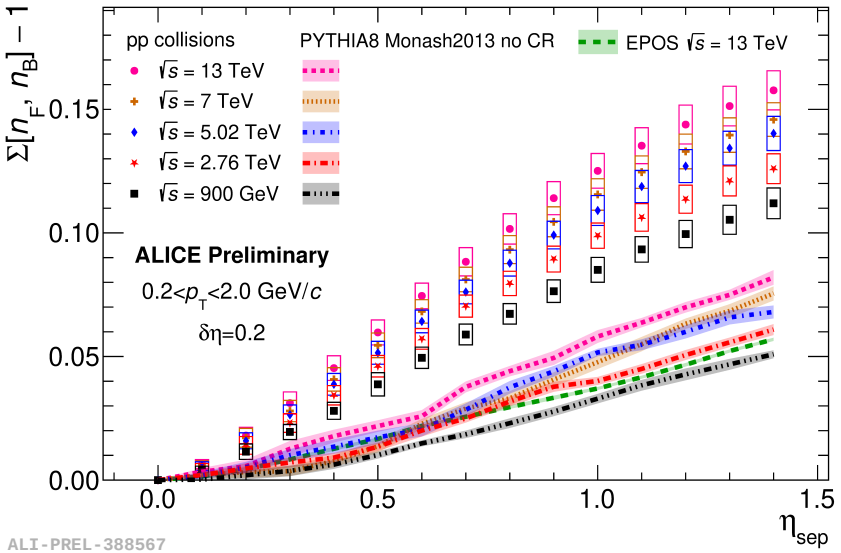

(a)

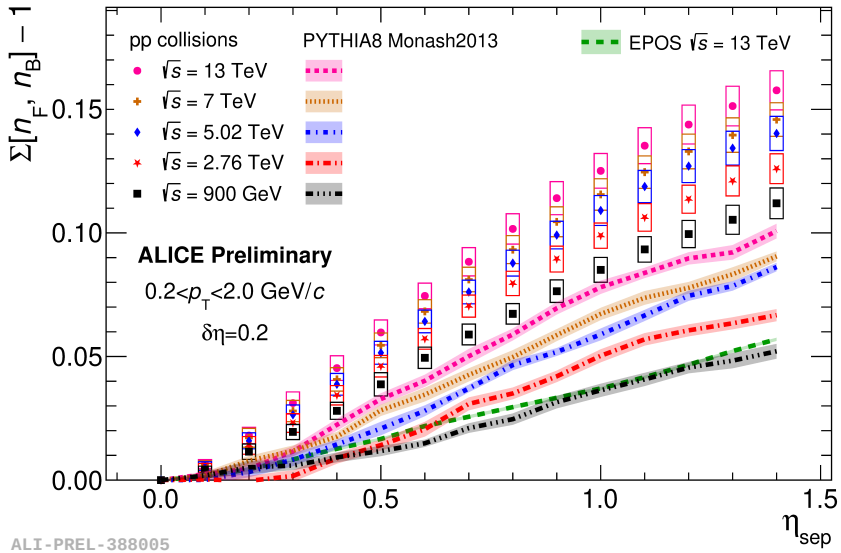

(b)

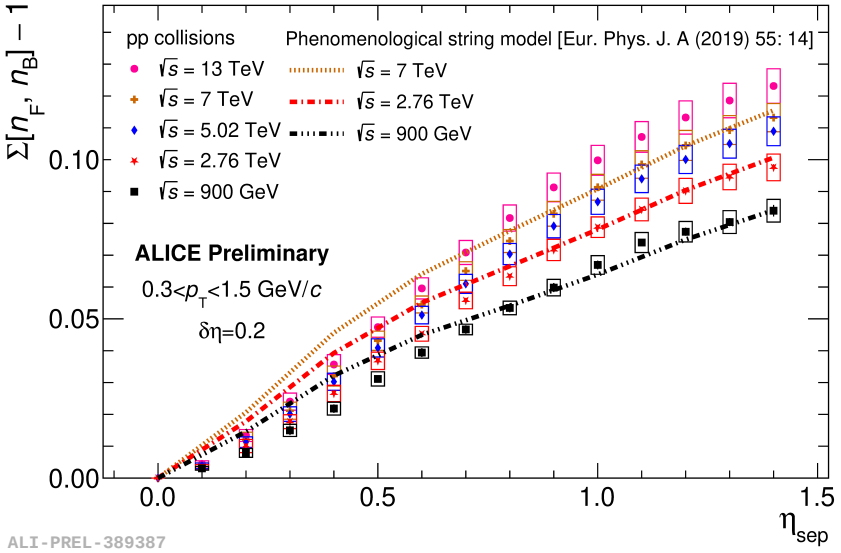

(c)

Figure 5.8: $\Sigma[n_F, n_B] - 1$ as a function of $\eta_{\text{sep}} = \Delta\eta + 0.2$ in pp collisions at $\sqrt{s} = 0.9$, 2.76, 5.02, 7, and 13 TeV. ALICE preliminary results are compared to various Monte Carlo models. Panel (a) shows a comparison to PYTHIA8 Monash2013 without color reconnection and EPOS-LHC at $\sqrt{s} = 13$ TeV. Panel (b) presents the same comparison including PYTHIA8 Monash2013 with color reconnection. Panel (c) compares the data to a phenomenological string model Ref. [110]. Statistical uncertainties are shown as error bars, and boxes represent systematic uncertainties. *Notation:* in the text the observable is denoted by Σ, while in the figures it appears as $\Sigma[n_F, n_B]$. Both notations refer to the same quantity. Figure taken from Ref. [107].

The comparative analysis below highlights the key similarities and differences observed in forward-backward correlations using Σ between pp and nucleus-nucleus collisions and the model's predictions:

- From the figures, it is evident that the Σ values in pp collisions increase with increasing separation gap, a trend similar to that reported in Xe–Xe and Pb–Pb collisions. This behaviour is also consistent with theoretical predictions used for comparison in pp analysis, specifically the PYTHIA model predictions (with and without Colour Reconnection) and the phenomenological string model. These findings suggest a reduction of the influence of short-range correlations as the window between forward and backward intervals increases.

- The analysis of the energy dependence of the Σ observable in pp collisions, as shown in Fig. 5.8, reveals a visible increase in its values with collision energy. This trend is qualitatively consistent with the observations in nucleus-nucleus collisions depicted in Fig. 5.6. Moreover, predictions from PYTHIA (with and without Colour Reconnection) and of the phenomenological string model, Ref. [41, 110], accurately capture the increase in Σ as collision energy rises.

- The comparison of the two predictions of the PYTHIA model reveals the sensitivity of the Σ observable, and thus forward-backward longitudinal fluctuations, to the scenarios with and without Colour Reconnection. The results obtained with the Colour Reconnection feature for the PYTHIA model approach closer to the experimental values. It is not surprising since the CR mechanism was implemented to provide a more realistic description of particle multiplicity distributions in the soft QCD region. The Colour Reconnection procedure allows colour strings from different partons to be "reconnected" or rearranged before the final hadronisation. This scenario favours shorter, more compact string formation, which leads to a lower multiplicity of hadrons and, in consequence, a reduction of FB correlation strength and enhancement of the values of Σ (see Eq. (3.58)).

- Even though PYTHIA8 and EPOS capture the qualitative behaviour of the data points, as presented in panels (a) and (b) in Fig. 5.8, models struggle to match the experimental results quantitatively. Among the different models' predictions, it appears that the phenomenological string model [41, 110] offers the closest agreement, especially in the region of larger η_{sep}.

- The most striking finding of this analysis comes from the study of the ordering of the Σ with multiplicity classes in pp collisions, shown in Fig. 5.7. The data points indicate a consistent increase in Σ values with increasing forward event multiplicity of pp collisions. This behaviour aligns with the phenomenological string model predictions suggested in Ref. [110]. Remarkably, the *ordering* in pp collisions is reversed compared to the one observed in Pb–Pb and Xe–Xe collisions (see Fig. 5.6). Interestingly, the qualitative trend of Σ with multiplicity in pp collisions coincides with the classification of Σ values with centrality predicted by the HIJING model for heavy-ion collisions.

5.5 Discussion

In this chapter, a detailed experimental study of forward-backward correlations with the strongly intensive quantity Σ in high-energy nucleus-nucleus and proton-proton collisions at the LHC is presented. The measurements were performed using the definition given in Eq. (3.52), which, within the framework of the independent source model, ensures that Σ remains insensitive to both the number of particle-emitting sources and their fluctuations. Instead, it provides direct information about the intrinsic statistical characteristics of a source.

It should be emphasised that the Σ observable had never been used to study forward-backward correlations before. The results obtained at LHC energies are the first application of this observable in this context. The findings offer valuable insights into the characteristics and behaviour of Σ regarding FB multiplicity correlation analysis, providing a deeper understanding of this observable.

A central question of this study is the validity of the strongly intensive properties of Σ at LHC energies. At first glance, the results indicate that Σ exhibits a notable degree of robustness in high-energy nucleus-nucleus collisions. It is insensitive to volume fluctuations, which aligns with general expectations for an SIQ. However, the observed independence of Σ on the choice of centrality estimator is a significant and non-trivial empirical finding.

One of the key issues addressed in this study is the mechanism responsible for the behaviour of Σ, in particular its robustness. Two possibilities need to be considered. One scenario is that particle production at LHC energies can still be adequately described by the independent source model despite its simplifying assumptions. On the other hand, the apparent agreement may be coincidental, and the observed stability of Σ may result from more complex mechanisms that need to

be understood. Distinguishing between these scenarios requires further theoretical insight and complementary measurements. The following discussion focuses on the key experimental results and their implications for forward-backward multiplicity correlations in **symmetric collision systems.**

Robustness of Σ observable

The insensitivity of Σ to volume fluctuations and to the choice of centrality estimator confirms that it is an effective observable for probing intrinsic fluctuations and correlations in heavy-ion collisions.

From these properties, several **practical advantages** emerge. One is that Σ can be determined across wide centrality classes without concerns about being influenced by volume fluctuations. So far, this has been verified only for 10% centrality bins. Another key benefit is its insensitivity to the choice of centrality estimator. While analysing data over broad centrality ranges helps reduce the impact of statistical fluctuations, the independence of the centrality selection method enables comparisons of results across different experiments. Both of these features are highly beneficial for experimental measurements and for comparisons with theoretical predictions. These characteristics fit well within the independent source model and present **a clear advantage over other commonly used measures**, such as the forward-backward correlation coefficient or the scaled variance, which tend to depend strongly on these factors.

Interestingly, when strongly intensive quantities, such as Σ, were first introduced, Ref [3], their independence from the choice of centrality estimator was not explicitly emphasised. In fact, recent studies on heavy-ion collisions (Figs. 5.1 and 5.2) have demonstrated that Σ remains independent of the centrality selection method. By construction, strongly intensive variables remove sensitivity to the system volume and its fluctuations; hence, under standard assumptions of ISM, Σ is expected to be independent of the choice of centrality estimator, even though it is not explicitly stated in Ref. [3].

The recognition that Σ does not depend on system size (volume) fluctuations alone does not automatically prove that it is a strongly intensive quantity. To meet this classification, it must also be independent of system size. While Σ shows no dependence on volume fluctuations, it is evidently sensitive to system size, as indicated by its ordering with centrality class, Fig. 5.6.

Dependence on system size and centrality

The observed **centrality dependence of** Σ is the finding that stands out most clearly from the results reported earlier, and it is interesting to examine it in more detail. This result is intriguing for several reasons.

- First, as was emphasised before, the observed trend with the centrality of the values of Σ **implies system size dependence**. This challenges the independent source model, indicating that the per-source particle production depends on the number of sources. Consequently, the factorisation presented in Sec. 3.3.1.1 (i.e. $\langle A \rangle \neq \langle \mu_a \rangle \cdot \langle N_\mathrm{s} \rangle$) no longer holds.

- Second, some theoretical models predict that **the properties of the matter** created in the early stages of the collision **can lead to a characteristic centrality dependence** of specific correlation measures [2].

- Third, **the trend of** Σ **with centrality observed in heavy-ion collisions is reversed** compared to the ordering of Σ with multiplicity class reported for pp collisions.

- Fourth, while the string models, such as PYTHIA or the string framework proposed in Ref. [110], seem to qualitatively and quantitatively explain the trend with multiplicity class observed in pp collisions, the situation is more complex for heavy-ion collisions. **Most commonly used models fail to describe the dependence of** Σ **on centrality** in Pb–Pb and Xe–Xe collisions.

The fact that Σ exhibits a clear centrality ordering directly contradicts the assumptions of the independent source model. This contradiction makes it necessary to consider alternative production scenarios that involve different types of sources, their emission properties, and possible correlations among different source types, to which Σ might be particularly sensitive.

For all the theoretical models considered in this chapter, in both nucleus-nucleus and proton-proton collisions, the centrality dependence of Σ is found to be highly sensitive to the specific model assumptions. In particular, the two AMPT configurations, with and without string melting, both predict an increase of Σ towards peripheral collisions, but with different magnitudes and shapes. The fact that the two settings lead to visibly different behaviours provides clear evidence that Σ responds to the modelling details of the production mechanism.

Dependence on FB separation window and energy:

Energy dependence. The reported growth of Σ with collision energy is observed in both proton-proton and heavy-ion collisions, independent of the colliding system. This trend is likely related to the increase in the average number of particles produced by a single source as $\sqrt{s_{NN}}$ increases. Such an interpretation is consistent with the expectations of both the string model proposed in Refs. [41, 110][2] and the wounded constituent model, which will be discussed later in this work.

Dependence on pseudorapidity gap. The increase of Σ with the separation gap $\Delta\eta$ between the forward and backward pseudorapidity intervals is also a robust feature of the data, seen in both pp and nucleus–nucleus collisions. Given the complementary relationship between Σ and b_{corr} in symmetric collisions, the observed rise of Σ with $\Delta\eta$ is consistent with the expected decrease of b_{corr}. This behaviour is most likely related to the diminishing contribution of short-range correlations as the distance between the forward and backward intervals increases, as already discussed in an earlier work by the author [103, 104].

Understanding the contribution from resonances

As mentioned in Section 3.2.2, short-range correlations are expected to arise from several key mechanisms, such as jet fragmentation, clustering, and resonance decay. Results for MC HIJING predictions in Pb–Pb and Xe–Xe collisions obtained for all-charged particles and a simulation sample with resonance sources removed, show a decrease in Σ values when resonance sources are excluded. Since resonance sources contribute significantly to short-range correlations, the reduction in Σ values with their removal might seem contradictory to the observed increase in Σ with increasing $\Delta\eta$, driven by a decrease in short-range correlation contributions as the separation gap widens. However, these two effects arise from different mechanisms.

With increasing $\Delta\eta$, short-range correlations between F and B pseudorapidity intervals diminish as short-range correlation sources (e.g., resonances) are less likely to populate both intervals. This effect leads to an increase in Σ values with $\Delta\eta$.

In contrast, removing resonance sources lowers Σ by eliminating one of the primary sources of particle correlations altogether.

[2] In the string model, the rise of Σ with $\sqrt{s_{NN}}$ is further supported by the shortening of the correlation length between particles produced during string fragmentation as the collision energy grows.

Further studies

In nucleus-nucleus collisions, Σ exhibits a clear dependence on centrality, while remaining independent of both the choice of centrality estimator and event-by-event system volume fluctuations. This combination of properties goes beyond the assumptions of ISM and therefore calls for interpretation within a more general theoretical framework. In the next chapters, this subject is addressed first within the wounded constituent model and then in the broader multi-source superposition approach. In the latter, not only the number of sources, but also their type composition and emission properties are allowed to fluctuate.

Additionally, to complete the picture of the evolution of Σ with system size, it is crucial to study the trend of Σ with centrality (or multiplicity) class in p–Pb and lower-energy pp collisions. Moreover, ALICE Collaboration has recently collected data from OO and Ne–Ne collisions at $\sqrt{s_{\mathrm{NN}}} = 5.36$ TeV, opening new opportunities to test the observable Σ in smaller nucleus-nucleus systems. These systems bridge the gap between pp, p–Pb and Pb–Pb collisions, allowing us to assess whether the robustness of Σ against volume fluctuations and centrality estimator is universal. At the same time, they may reveal distinct mechanisms of forward-backward correlations characteristic of smaller systems. Such an analysis remains a task for future studies, which could provide an essential extension of the results presented in this work.

Chapter 6

Forward-backward correlations and fluctuations in the wounded-constituent framework

This chapter presents a phenomenological analysis of Σ within the wounded constituent model. It highlights the role of this observable in characterising forward-backward correlations in heavy-ion collisions at LHC energies. The main results presented in this chapter originate from the author's work published in Ref. [5]. The majority of the material presented here is based on, and further elaborates, the concepts and results introduced in that publication.

The motivation for using the wounded nucleon and wounded quark models stems from the limitations of commonly used heavy-ion Monte Carlo models. Models such as HIJING, AMPT, and EPOS fail to accurately reproduce experimental data on Pb–Pb and Xe–Xe collisions at LHC energies, as discussed in the previous chapter.

As shown in this chapter, a wounded constituent framework offers an alternative approach that better captures the observed phenomena in forward-backward correlations with Σ in heavy-ion collisions, outperforming traditional models.

6.1 Wounded Nucleon and Wounded Quark Models

The wounded constituent framework is a **superposition model** based on the assumption that the total particle production in nucleus-nucleus collisions results from the incoherent sum of contributions from individual wounded constituents.

In this framework, a **wounded constituent** (also called wounded source) emits particles **independently of the number of collisions** it has undergone. The predictions of this model depend on the nature of these sources, which are typically classified into three categories: wounded nucleons, wounded quarks, and wounded diquarks.

The first iteration of this model, known as **the Wounded Nucleon Model**

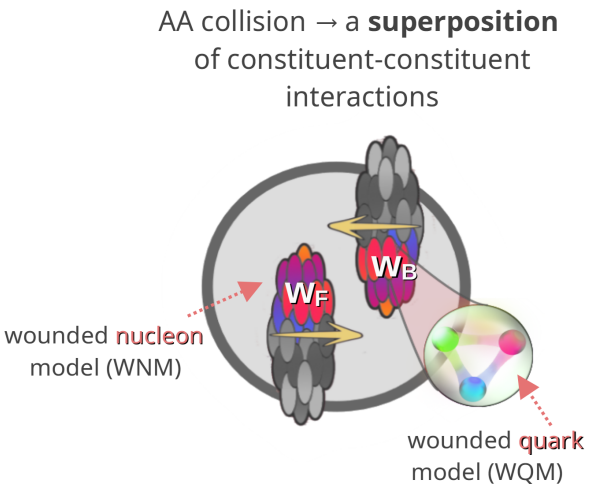

Figure 6.1: Conceptual illustration of the wounded nucleon model and its extension to the wounded quark model. A zoom-in on a single nucleon reveals its three valence quarks, illustrating the transition from wounded nucleons to wounded quarks as particle-producing sources.

(WNM), treated nucleons as the primary constituents [9]. The WNM has successfully described various phenomena observed in heavy-ion collisions, including particle multiplicities, rapidity distributions, and the forward-backward correlation coefficient (see Refs. [18, 40, 74, 111, 112]).

The WNM provided a strong foundation for further refinement. To extend the WNM framework, researchers introduced the **Wounded Quark Model (WQM)** [113, 114], and **the Wounded Quark-Diquark Model (WQDM)** [115, 116], where quarks or quark-diquark pairs replace nucleons as the fundamental particle-producing constituents.

The WNM has been known for many decades and is extensively documented in the literature. Only its main assumptions will be summarised below:

1. A **wounded nucleon** is a nucleon that has undergone **at least one inelastic collision**. Each wounded nucleon contributes equally to particle production and emits particles according to the same particle distribution, independently of the number of collisions it went through inside the nucleus.

2. The model assumes **two distinct types of sources** that contribute to particle production: **forward-moving nucleons**, originating from the forward-moving nuclei w_F, and **backward-moving nucleons**, coming from the backward-going

nuclei w_B, see Fig. 6.1.

3. The particle production for each wounded nucleon can be described by a universal **fragmentation function** $F(\eta)$, representing the pseudorapidity distribution of particles emitted by a single wounded nucleon. The fragmentation function $F(\eta)$ is not restricted to the hemisphere of the wounded nucleon, and each wounded source can emit particles into both forward and backward pseudorapidity regions.

4. In a nuclear collision, the single-particle density $N(\eta) \equiv \frac{dN(\eta)}{d\eta}$ can be described using a combination of the mean number of forward-moving, $\langle w_F \rangle$, and backward-moving, $\langle w_B \rangle$, wounded nucleons, as referenced in Ref. [111, 112]. This relationship is expressed as:

$$N(\eta) = \langle w_F \rangle F(\eta) + \langle w_B \rangle F(-\eta). \tag{6.1}$$

5. The particle production from a wounded nucleon is treated statistically and, in this work, is characterised by the negative binomial distribution (NBD):

$$P(n, \bar{n}, k) = \frac{\Gamma(n+k)}{\Gamma(n+1)\Gamma(k)} \left(\frac{\bar{n}}{k}\right)^n \left(1 + \frac{\bar{n}}{k}\right)^{-(n+k)}, \tag{6.2}$$

where $\bar{n}$ denotes the average multiplicity and $1/k$ controls the deviation from the Poisson distribution. The parameters $\bar{n}$ and k are obtained from pp collisions, where the negative binomial distribution is often used to parametrise particle multiplicity distributions. Since a pp collision involves two wounded nucleons, the distribution for a single wounded nucleon is represented by rescaled parameters $\bar{n} \to \bar{n}/2$ and $k \to k/2$, consistently with the wounded nucleon model. This rescaling is already incorporated in the formulas used throughout this work.

Particle redistribution into F and B pseudorapidity intervals

In addition to the fundamental assumptions of WNM, to study forward-backward correlations requires specifying how particles are distributed between the forward and backward η intervals. We assume that each wounded nucleon, whether moving forward or backward, emits particles according to the NBD, Eq. (6.2), into the combined F+B pseudorapidity interval.

Particles produced in the F+B interval are then randomly assigned to the F or B pseudorapidity region. The assignment probability is determined by the spatial position and the width of the respective intervals, as shown in Fig. 6.2.

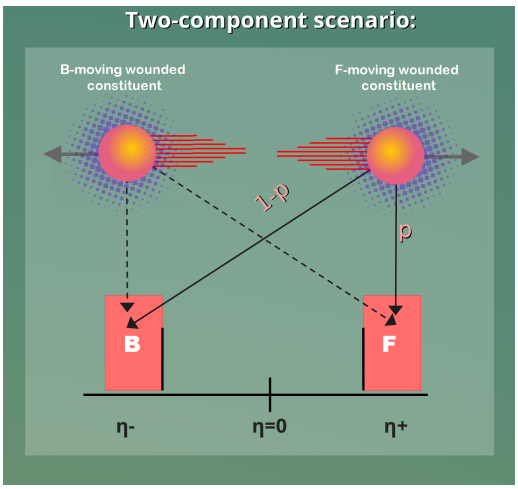

Figure 6.2: Particle redistribution into F and B pseudorapidity intervals from forward and backward-moving wounded constituents.

The probability, denoted as p, that a particle originating from a wounded nucleon in a forward-moving nucleus is assigned to the forward η bin can be calculated using the following relationship:

$$p = \frac{\int_F F(\eta)\, d\eta}{\int_B F(\eta)\, d\eta + \int_F F(\eta)\, d\eta} \tag{6.3}$$

The probability that a particle from the same wounded nucleon ends up in the backward interval is $1 - p$. This study considered the symmetric placement of the forward and backward bins around midrapidity ($\eta = 0$). Under this symmetry, a backward-moving wounded nucleon has a probability p of emitting into the backward bin, and a probability $1 - p$ of emitting into the forward bin.

Although the above assumptions were originally formulated within the wounded nucleon model, they remain fully applicable when extending the framework to the wounded quark model. In this case, the sources, w_F and w_B, are wounded quarks, and the fragmentation function $F(\eta)$ is reinterpreted accordingly as the emission profile of a single wounded quark. **The analytical formulas introduced in the next section will therefore apply to both wounded nucleons and wounded quarks; how-**

ever, for the sake of notational consistency, the term "wounded nucleon" will be used throughout the derivation.

6.1.1 Analytical calculations and toy model simulations

Analytical formula

We will begin our discussion of Σ in the wounded nucleon model by examining the analytical formula that defines this observable within the framework. The complete derivation of the analytical formulas for Σ is based on the methodology proposed in Refs. [40, 74, 116]. These formulas have been comprehensively detailed in Ref. [5]. Therefore, we will not repeat that derivation here.

Equation (6.4) presents the final expression for the Σ quantity in the wounded nucleon model:

Σ in the wounded constituent model (WNM/WQM):

$$\Sigma = 1 + \frac{\overline{n}}{2} \cdot C^2 \cdot \left[\left(\frac{4\langle w_B \rangle \langle w_F \rangle}{\left(\langle w_F \rangle + \langle w_B \rangle\right)^2 - C^2 \left(\langle w_B \rangle - \langle w_F \rangle\right)^2} \right) \left(\frac{\langle (\sqrt{\lambda_w} w_F - \sqrt{\frac{1}{\lambda_w}} w_B)^2 \rangle}{\langle w_F \rangle + \langle w_B \rangle} + \frac{2}{k} \right) \right]. \tag{6.4}$$

In this expression:

- $\lambda_w = \frac{\langle w_B \rangle}{\langle w_F \rangle}$ is the ratio of average backward to forward wounded sources.
- C is a parameter encoding the asymmetry of particle emission into forward and backward pseudorapidity intervals and is related to the probability p by $C = 2 \cdot p - 1$.

From Equation (6.4), the following conclusions regarding **the properties of** Σ can be drawn:

1. **Dependence of Σ on the number of wounded nucleons:**

   The variable Σ, as determined within the WNM model, exhibits an explicit *intrinsic dependence* on the number of wounded nucleons w_F and w_B and therefore the centrality of the collision. This direct dependence on the number

of wounded nucleons implies that Σ is **not a strongly intensive quantity**. This dependence arises because, within the WNM, the forward and backward sources are not identical; this violates the assumptions of the Independent Source Model under which Σ is constructed to be a strongly intensive quantity.

2. **Dependence of Σ on the probability p:**

The observable Σ exhibits *sensitivity to the probability* p, which plays the role of a parameter in the model. The dependence of Σ on p is governed by the term $C^2 = (2p-1)^2$, meaning it is symmetric around $p = 0.5$ and depends only on how much p deviates from the centre. As p approaches 0.5, the contribution from fluctuations of forward- and backward-moving sources (w_F and w_B) is suppressed by the multiplicative factor $(2p-1)^2$, while deviations from 0.5 enhance their impact on Σ.

This dependence becomes clearer when analysing the following scenarios:

(i) **Case:** $\mathrm{p} = 0.5 \rightarrow \Sigma = 1$

When $p = 0.5$, particles produced by a wounded source (regardless of whether moving forward or backward) are emitted equally into the forward and backward pseudorapidity intervals. In this case, the term $C = 2p - 1$ vanishes, and all p–dependent contributions to Σ drop out. As a result, Σ **reduces to unity**, and the observable becomes insensitive to forward-backward fluctuations in the number of wounded sources.

The probability $p = 0.5$ corresponds to a situation where forward- and backward-moving sources are *statistically indistinguishable*. In this regime, the wounded nucleon model reduces to a special case of the Independent Source Model. Under these conditions, Σ satisfies the assumptions proposed by Gaździcki and Gorenstein for a strongly intensive quantity [3]. It becomes insensitive to fluctuations in the number of sources and reflects only the intrinsic fluctuations of particle production. Thus, for $p = 0.5$, Σ **recovers its status as a strongly intensive quantity.**

(ii) **Case:** $p \neq 0.5 \rightarrow \Sigma > 1$

When the probability p deviates from 0.5, the term related to wounded nucleon fluctuations contributes to the values of Σ. This contribution grows stronger as p departs from 0.5, leading to a corresponding increase in the value of Σ. In this regime, the assumptions of the ISM are no longer

satisfied, as the model now includes two statistically distinct classes of sources, forward- and backward-moving, which differ in their contribution to particle production.

(iii) **Case:** $p = 1$ or $p = 0 \rightarrow \Sigma^{n_F n_B} = 1 + \frac{\overline{n}}{2}\left[\frac{\langle(\sqrt{\lambda_w}w_F - \sqrt{\frac{1}{\lambda_w}}w_B)^2\rangle}{\langle w_F\rangle + \langle w_B\rangle} + \frac{2}{k}\right]$

This is a specific realisation of Case 2 (ii). At $p = 0$ or $p = 1$, each wounded constituent emits all particles into either the forward or backward pseudorapidity interval. There is no overlap between the emission regions of forward- and backward-moving sources.

In this limit, the parameter $C^2 = (2p-1)^2$ reaches its maximum, namely 1, and the Σ likewise saturates at its highest possible value. It no longer depends on probability p, but solely on the fluctuations in the number of wounded sources (w_F and w_B) that contribute to its value.

Taking all the cases above into account, we conclude that the emission probability p acts as a parameter controlling the symmetry between forward- and backward-moving wounded sources. When $p = 0.5$, the two types of sources are statistically identical, and Σ behaves like a strongly intensive quantity. When $p \neq 0.5$, this symmetry is broken, and differences between the source types lead to increased forward-backward fluctuations in the observable.

3. **Symmetric collisions**

For symmetric collisions, such as Pb–Pb and Xe–Xe systems, where $\langle w_F\rangle = \langle w_B\rangle = \frac{\langle w\rangle}{2}$, the formula for the Σ quantity simplifies to the following form:

Σ in the wounded constituent model (WNM/WQM) for symmetric collisions:

$$\Sigma = 1 + \frac{\overline{n}}{2}(2p-1)^2\left[\frac{\langle(w_B - w_F)^2\rangle}{2\langle w_F\rangle} + \frac{2}{k}\right]. \tag{6.5}$$

4. **Sensitivity to longitudinal fluctuations of the fireball**

In Chapter 3, it was shown that the observable Σ in symmetric collisions is directly sensitive to odd-order terms in the Chebyshev polynomial decomposition of single-particle density fluctuations, specifically $\Sigma \propto \langle a_{2m+1}a_{2n+1}\rangle$. According to Ref. [18], these coefficients can be interpreted as measures of longitudinal fireball asymmetry fluctuations. In this paragraph, we demonstrate that

the correspondence between Σ and odd-order Chebyshev coefficients becomes particularly transparent within the wounded nucleon model.

In Ref. [18], the authors show that in the framework of the wounded nucleon model, the longitudinal asymmetry of the fireball arises from event-by-event fluctuations in the number of forward- and backward-going wounded nucleons.[1] Specifically, they obtain $a_1 \propto w_F - w_B$, where a_1 is the leading odd Chebyshev coefficient. This leads to the relation:

$$\langle a_1^2 \rangle \propto \langle (w_F - w_B)^2 \rangle \tag{6.6}$$

However, this expression captures only the contribution from sources (i.e., the fluctuating number of wounded nucleons). The full observable also depends on how each wounded nucleon emits particles as a function of rapidity. Specifically, Ref. [18] assumes a linear fragmentation function for a single wounded nucleon:

$$F(\eta) = a + b\eta, \quad \eta \in [-Y, Y].$$

We define the forward emission probability p as the probability that a forward-moving wounded nucleon emits a particle into its own hemisphere. That is:

$$p = \frac{\int_0^Y F(\eta)\, d\eta}{\int_{-Y}^Y F(\eta)\, d\eta} = \frac{aY + \frac{b}{2}Y^2}{2aY} = \frac{1}{2} + \frac{bY}{4a}.$$

Note that here the forward emission probability p completely determines the asymmetry of the fragmentation function in the interval $[0, Y]$. Solving for the slope b, we find:

$$\frac{b}{a} = \frac{4}{Y}\left(p - \frac{1}{2}\right).$$

Now, using the definition of $\langle a_1^2 \rangle$ from Ref. [18], we obtain:

$$\langle a_1^2 \rangle = \frac{b^2 Y^2}{a^2} \cdot \frac{\langle (w_F - w_B)^2 \rangle}{\langle w_F + w_B \rangle^2} = 4\,(2p-1)^2 \cdot \frac{\langle (w_F - w_B)^2 \rangle}{\langle w_F + w_B \rangle^2}. \tag{6.7}$$

The coefficient $\langle a_1^2 \rangle$ is determined by the structural asymmetry of the fireball (i.e., the relative fluctuations in the number of forward- and backward-going wounded nucleons), but also depends on the asymmetry in particle emission

[1] Note that the notation in Ref. [18] uses w_L and w_R to denote left- and right-moving wounded nucleons, respectively. This corresponds to $w_B \equiv w_L$ and $w_F \equiv w_R$ in the notation used in this work.

from these nucleons into the forward and backward rapidity intervals $[0, Y]$ and $[-Y, 0]$.

Moreover, the Eq. (6.7) demonstrates the direct connection between the observable Σ, as defined in Eq. (6.5), and the leading odd-order Chebyshev coefficient $\langle a_1^2 \rangle$ within the wounded nucleon model:

$$\Sigma = 1 + \frac{\overline{n}}{4} \langle w_F \rangle \langle a_1^2 \rangle + \frac{\overline{n}}{k}(2p-1)^2. \tag{6.8}$$

This shows that both $\langle a_1^2 \rangle$ and Σ carry information about the longitudinal asymmetry of the fireball as well as the asymmetry of particle emission from the source.

5. **Special case: pA collisions in WNM**

   To complete the above discussion, we now derive the expression for $\Sigma_{\mathrm{pA}}^{WNM}$ in proton–nucleus (pA) collisions in the wounded nucleon model. In this case, there is only one nucleon associated with the proton projectile that we label as the forward-going wounded nucleon. Substituting $w_F = 1$ into Eq. (6.4) leads to a simplified expression for the $\Sigma_{\mathrm{pA}}^{WNM}$ observable:

$$\Sigma_{\mathrm{pA}}^{WNM} = 1 + \frac{\overline{n}}{2} \cdot C^2 \cdot \left[\frac{\mathrm{Var}(w_B)}{\langle w_B \rangle (1 + \langle w_B \rangle)} + \frac{2}{k} \right]. \tag{6.9}$$

   This form reveals that for a given p, the fluctuation measure $\Sigma_{\mathrm{pA}}^{WNM}$ in p–Pb collisions is entirely controlled by the nuclear side of the system, and the proton acts as a fixed, single-source emitter.

Properties and limitations of the Δ quantity in the wounded constituent model

The primary focus of this study has been on the Σ variable. Nevertheless, for completeness, we also briefly address the Δ observable.

In symmetric collisions (e.g. Pb–Pb with pseudorapidity windows symmetric around midrapidity), the normalisation factor $C_\Delta = \langle n_B \rangle - \langle n_F \rangle$ vanishes, and thus Δ is undefined.

In asymmetric systems, such as p–Pb, Δ can be defined. In the wounded nucleon

model, for $\langle w_F \rangle = 1$ and $C \neq 0$ one obtains:

$$\Delta_{\mathrm{pA}}^{\mathrm{WNM}} = 1 + \frac{\bar{n}}{[\langle w_B \rangle C_- + C_+]\,[C_- + \langle w_B \rangle C_+]} \times \left[\frac{4\langle w_B \rangle C^2}{k} - \frac{2\,\mathrm{Var}(w_B)}{\langle w_B \rangle} \left(C_- C_+ + \langle w_B \rangle \right) \right], \tag{6.10}$$

where $C_\pm = 1 \pm C$.

A more detailed discussion of the general properties and limitations of Δ in the wounded constituent model is provided in Appendix B.

6.1.2 Monte Carlo simulations

The numerical calculations of the Σ in wounded nucleon and wounded quark models in Pb–Pb or Xe–Xe collisions were based on a simple Monte Carlo Glauber-like simulation. A detailed description of the calculation procedure can be found in Ref. [5], which is briefly summarised in the following steps:

Collision geometry:

The Monte Carlo simulation described the collision geometry of Pb–Pb interactions at $\sqrt{s_{\mathrm{NN}}} = 2.76$ and 5.02 TeV, and Xe–Xe interactions at $\sqrt{s_{\mathrm{NN}}} = 5.44$ TeV, on the basis of the spatial distributions of wounded nucleons and wounded quarks.

The nuclei were represented as a superposition of nucleons, with their positions defined using a Woods-Saxon density profile, while quark positions within nucleons were determined using an exponential density function, see Fig. 6.3.

The collision process was modelled by approximating nucleons and quarks as following straight-line trajectories, with their interactions being governed by $\sqrt{s_{\mathrm{NN}}}$-dependent inelastic cross section σ_{ii}^{inel}, where i stands for constituent type (nucleon "N" or quark "q"). The value of the cross section did not depend on the number of individual constituent-constituent collisions.

The inelastic nucleon-nucleon cross sections, σ_{NN}^{inel}, were taken from ALICE experimental measurements reported in Refs. [93, 94]. The quark–quark inelastic cross section σ_{qq}^{inel} was chosen such that integrating the probability distribution $P(b)$ over all impact parameters b, weighted by the area element $2\pi b\mathrm{d}b$, reproduced the total inelastic nucleon–nucleon cross section. This method follows the procedure described in Refs. [116, 119].

A nucleon is considered wounded if it overlaps with the nucleons of the other nucleus in a region of transverse distance radius $d_{NN} \leq \sqrt{\frac{\sigma_{NN}^{inel}}{\pi}}$. Similarly, **a quark**

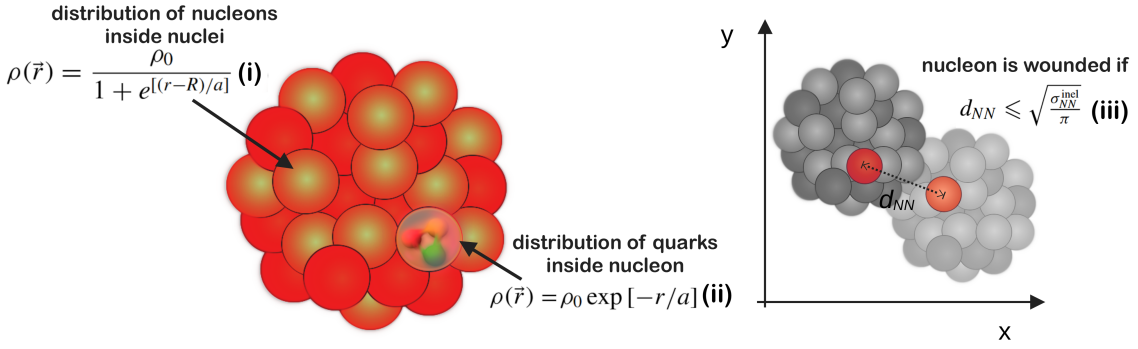

Figure 6.3: (Left) The location of nucleons in the nucleus is described by a nuclear density profile modelled by a Woods-Saxon spherically symmetric density function (i), where R is the nuclear radius, a is the skin depth, and $r = |\vec{r}|$ is the distance from the nucleus centre. The distribution of three constituent quarks inside the nucleon is given by the exponential density function (ii). In formula, $a = r_p/\sqrt{12}$, where r_p = 0.81 fm is the proton's charge radius [117, 118]. The factor $\sqrt{12}$ arises because for a three-dimensional exponential distribution $\rho(r) \propto e^{-r/a}$ one has $\langle r^2 \rangle = 12a^2$, so matching the RMS radius to the proton radius r_p requires choosing $a = r_p/\sqrt{12}$. (Right) Illustration of the criteria for a wounded nucleon. A nucleon is considered wounded if its distance to another nucleon, d_{NN}, satisfies $d_{NN} \leq \sqrt{\frac{\sigma_{NN}^{inel}}{\pi}}$, where σ_{NN}^{inel} is the inelastic nucleon-nucleon cross section.

is considered wounded if it overlaps with the quarks of the other nucleus in a region of transverse distance radius $d_{qq} \leq \sqrt{\frac{\sigma_{qq}^{inel}}{\pi}}$.

Particle production:

Particle production from wounded constituents was assumed to follow a negative binomial distribution, Eq. (6.2). Particle production was considered in two distinct pseudorapidity regions:

- **In the vicinity at midrapidity:** It was assumed that a wounded nucleon produces particles into the sum of forward and backward η intervals (F+B), each with a width of $\delta\eta = 0.2$, following a negative binomial distribution. The values of the NBD parameters $\overline{n}$ and k for Xe–Xe and Pb–Pb collisions at $\sqrt{s_{\rm NN}}$ = 2.76, 5.02, and 5.44 TeV were interpolated based on experimental pp data from Refs. [14, 120].

- **In forward η regions[2]:** The particle emission in forward regions was modelled to mimic the centrality determination method provided by the ALICE V0

[2]Following ALICE terminology, the "forward region" relates to the pseudorapidity coverage of the forward detectors (both on the positive and negative η sides, e.g., V0A and V0C), i.e.,

detector. Particle production from a wounded nucleon into the forward region was estimated based on the NBD with parameters adopted from the Glauber-NBD fit to V0 detector amplitudes published by ALICE in Ref. [93].

In the wounded quark model, the values of NBD parameters were estimated by scaling values of $\overline{n}$ and k determined for WNM by the average number of wounded quarks per wounded nucleon in an elementary collision for a given energy. The values of $\overline{n}$ and k parameters of NBD for WNM and WQM for midrapidity and forward η region are fully listed in Ref. [5].

Forward-backward pseudorapidity distribution

Particles emitted in the considered pseudorapidity region are assigned to the forward or backward pseudorapidity interval with emission probability p. If a particle originates from a forward-moving constituent, it is assigned to the forward interval with probability p and to the backward interval with probability $1 - p$. Conversely, if the particle comes from a backward-moving source, it is assigned to the forward interval with probability $1 - p$ and to the backward interval with probability p. This assignment procedure is illustrated in Fig. 6.2. The parameter p is a free parameter of the model.

Determination of centrality class:

Simulated data were divided into centrality classes based on values of the impact parameter and particle multiplicity in the forward regions. As detailed in the original work Ref. [5], the geometrical properties of Pb–Pb and Xe–Xe collisions, such as average values of wounded nucleons for a given centrality class obtained in this simple toy model, aligned well with the values published by the ALICE Collaboration in Ref. [93].

The generated distributions of wounded nucleons and quarks were used to compute Σ using the analytical formula Eq. (6.4). Additionally, full Monte Carlo simulations, with implemented particle production from wounded constituents, were performed to calculate Σ based on its definition in Eq. (3.52). The main findings of this study are discussed in the following sections.

close to the beam direction. This usage should not be confused with the “forward" convention in forward–backward correlation analyses, where it typically refers only to the positive η hemisphere.

6.2 Results for the Σ in the Wounded Nucleon and Wounded Quark Models

6.2.1 Centrality dependence

The results for Σ in the wounded nucleon and wounded quark models for Pb–Pb collisions at $\sqrt{s_{\mathrm{NN}}} = 5.02$ TeV are shown in Figure 6.4. The analysis covers wide centrality classes (Δ centrality = 10%) ranging from central $(0 - 10\%)$ to peripheral collisions $(70 - 80\%)$. Results are presented for selected probability values of p, varying from ∼0.5 to 0.64, as a function of centrality.

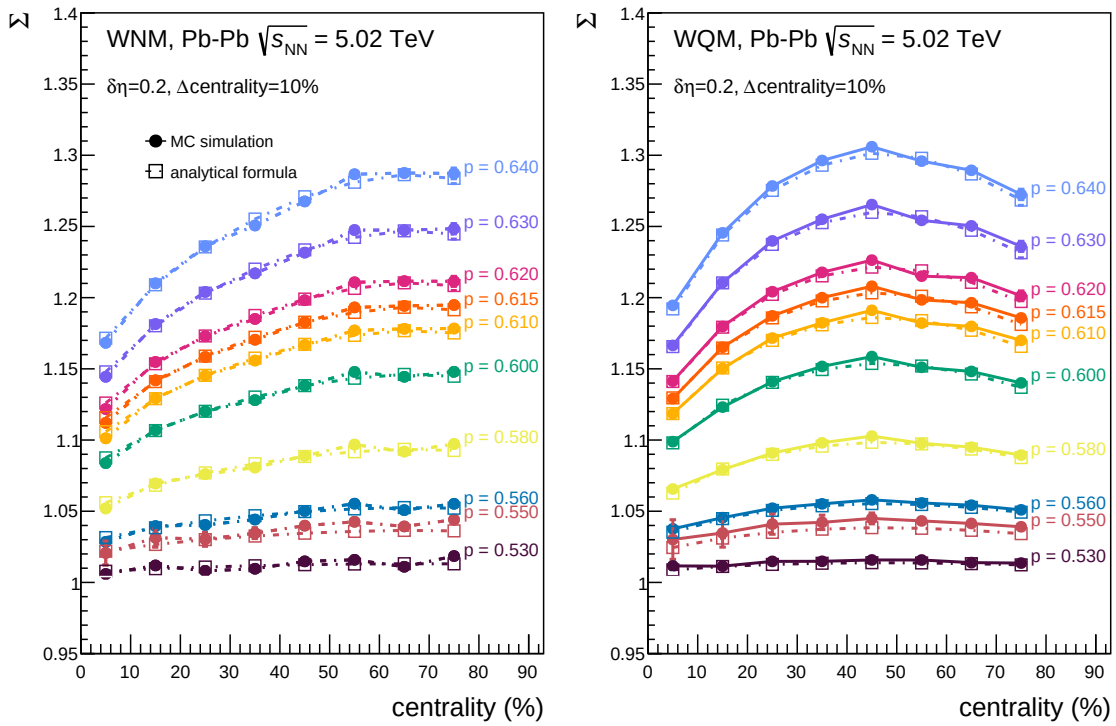

Figure 6.4: The Σ observable obtained in WNM (left panel) and WQM (right panel) for Pb–Pb collisions at $\sqrt{s_{\mathrm{NN}}} = 5.02$ TeV as a function of centrality class. Results are presented for several values of the probability p. Statistical uncertainties are labelled with vertical bars. Centrality selection is made via the impact parameter. Plot from Ref. [5]. For clarity, the figure shows only the results starting from $p = 0.53$, as adding lower-p values would reduce the readability of the plot.

Within statistical uncertainties, there is full agreement between the values of Σ derived from the analytical formula Eq. (6.4) and those based on the definition of the observable under consideration obtained from the full numerical Monte Carlo simulations incorporating particle production. This cross-check validates the use of

the analytical method for further analysis. Given its computational efficiency, all subsequent results for the WNM and WQM will be based solely on the analytical formula.

Three distinct features in the results are immediately evident in Fig. 6.4, which are:

- **Impact of probability p:** As p increases, Σ increases in both WNM and WQM. This growth in values of Σ seems to be more pronounced in the wounded quark model compared to the wounded nucleon model.

  For $p \to 0.5$, the Σ value tends towards unity ($\Sigma \to 1$) across all centrality classes as expected from the analytical formula.

- **Trend with centrality:** The observable Σ exhibits a non-trivial dependence on collision centrality. In WNM, it increases monotonically from central to peripheral collisions. In contrast, in WQM, values of Σ reach a maximum around mid-central collisions ($40 - 50\%$) before decreasing slightly in the most peripheral events. As described by Eq. (6.4), it is observed that larger values of the emission probability p amplify this centrality dependence.

  For $p > 0.5$, both WNM and WQM reproduce the trend with centrality observed in experimental data reported by ALICE, Fig. 5.6. This agreement is particularly evident for larger values of p near 0.6.

- **Intrinsic dependence on system size:** The Σ values change progressively with centrality. This variation is not due to differences in the characteristics of the particle-producing source, which are assumed to be centrality independent in the model, but rather because Σ is *not* a strongly intensive quantity in the WNM and WQM.

  This interpretation is supported by Eqs. (6.4) and (6.5). From the analytical expression, it is evident that the centrality dependence is a consequence of an intrinsic sensitivity to the number of wounded constituents. Therefore, it is particularly interesting to analyse how fluctuations in the number of sources and the choice of centrality estimator influence this observable. The following section explores these effects in detail.

6.2.2 Centrality bin width and centrality estimator dependence

Figure 6.5 reports the dependence of Σ on the width of the centrality class (Δ centrality). Presented results were obtained in terms of wounded nucleon and

wounded quark models for Pb–Pb collisions at $\sqrt{s_{\mathrm{NN}}} = 5.02$ TeV. Values of Σ were determined for different centrality classes of Pb–Pb collisions, from central to peripheral. The width of each centrality class varied around its centre, from a maximum range of 10%, where the largest contribution from volume fluctuations is expected, down to 1% centrality bin width. Findings are presented for two different centrality selection criteria: via the impact parameter b and via the particle multiplicity N_{ch}.

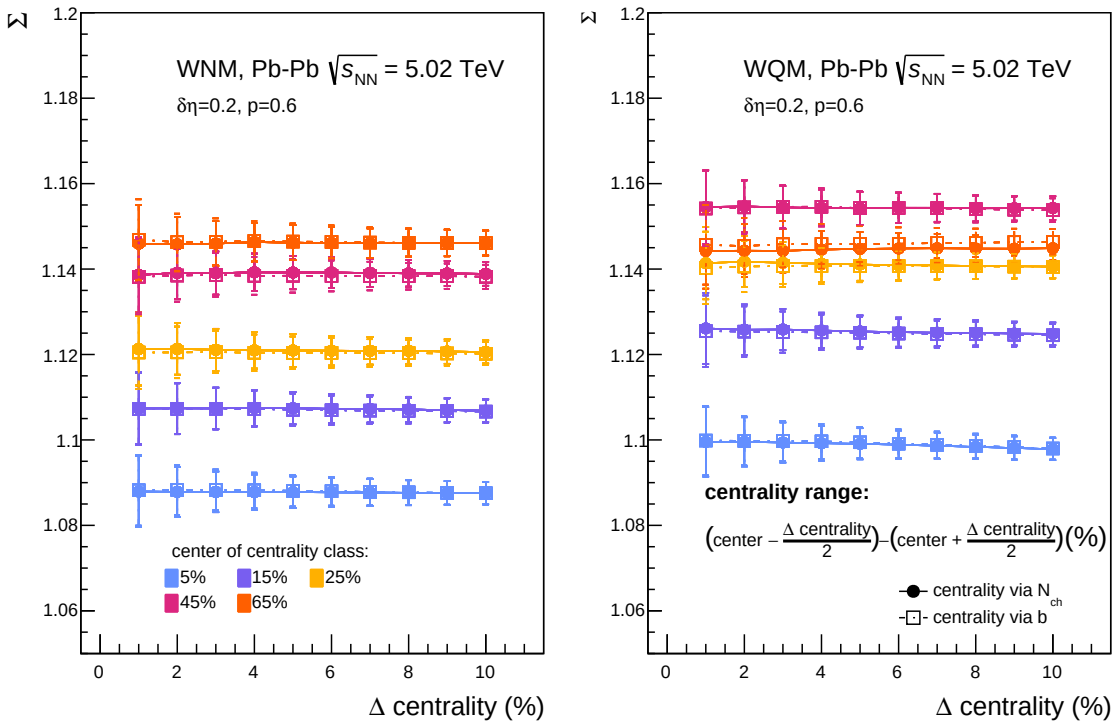

Figure 6.5: The Σ observable obtained in WNM (left panel) and WQM (right panel) for Pb–Pb collisions at $\sqrt{s_{\mathrm{NN}}} = 5.02$ TeV, drawn as a function of centrality class size (Δ centrality), for a fixed value of the probability $p = 0.6$. The results are obtained for different centrality selection methods: via impact parameter b and via particle multiplicity N_{ch}. The width of the centrality class (Δ centrality $\leq 10\%$) changes from 1% to 10%. The ranges of centrality class for a given centrality bin width can be deduced from the formula in the figure. The different colours of the data points correspond to different centralities in Pb–Pb collisions. Statistical uncertainties are labelled with vertical bars. Plot from Ref. [5].

From the behaviour of the data points in Fig. 6.5, it is evident that Σ, as determined in the WNM and WQM, does not depend on the centrality bin width. This implies that the observable is **insensitive to volume fluctuations** within the wounded constituent framework.

A direct comparison of the results obtained for two different centrality selection methods reveals that Σ remains **insensitive to the way centrality is determined**.

At first glance, the predictions derived from the analytical formula seem to contradict the behaviour of Σ reported in Fig. 6.5. On one hand, Σ, as determined in symmetric nucleus-nucleus collisions within the wounded nucleon or wounded quark modes, shows a direct dependence on the variance of the asymmetry between the number of forward- and backward-moving wounded nucleons, represented as $\Sigma \propto \langle (w_B - w_F)^2 \rangle = \mathrm{Var}(w_B - w_F)$. On the other hand, Fig. 6.5 demonstrates that Σ does not appear to depend on volume fluctuations or the centrality estimator.

These *strongly-intensive-quantity-like* properties of Σ, observed for centrality classes with widths Δ centrality $\leq 10\%$ in symmetric nucleus-nucleus collisions, closely resemble the behaviour reported by the ALICE Collaboration in Fig. 5.1. Their origin can be understood theoretically, as discussed in the following section.

6.3 Robustness of the Σ observable to volume fluctuations and centrality estimator choice in wounded constituent model

6.3.1 Σ independence of the volume fluctuations

The expression for the Σ in symmetric nucleus-nucleus collisions, Eq. (6.5), contains only one term that is related to the variation of wounded nucleons $\langle (w_F - w_B)^2 \rangle = \mathrm{Var}(w_F - w_B)$. This term reflects fluctuations of the forward–backward imbalance of wounded sources. Since this imbalance can depend on the total number of wounded sources $w = w_F + w_B$, one might expect some sensitivity to system-size fluctuations, which in the wounded nucleon model are typically associated with $\mathrm{Var}(w)$. Therefore, any potential dependence of observables Σ on volume fluctuations in the wounded constituent framework can be fully deduced by analysing the component $\mathrm{Var}(w_B - w_F)$.

Using the law of total variance, the term above can be expressed as:

$$\mathrm{Var}(w_B - w_F) = \mathbb{E}\left[\mathrm{Var}(w_B - w_F \mid w)\right] + \mathrm{Var}\left(\mathbb{E}[w_B - w_F \mid w]\right), \tag{6.11}$$

where:

- $\mathbb{E}[\mathrm{Var}(w_B - w_F \mid w)]$ is the average[3], over the distribution of w, $P(w)$, in a

[3]Conditional expectations are written as $\mathbb{E}[\cdot \mid w]$, while default expectation symbol is $\langle \cdot \rangle$.

given centrality sample, of the event-by-event forward-backward asymmetry fluctuations of the difference between types of wounded constituents at fixed total number of wounded sources w. The properties of this term, including its expansion around $\langle w \rangle$, are discussed in detail in Appendix C.

- $\mathrm{Var}(\mathbb{E}[w_B - w_F \mid w]) = 0$ for symmetric systems (Pb–Pb, Xe–Xe), since

$$\mathbb{E}[w_B - w_F \mid w] = 0,$$

  which follows from the symmetry between the two colliding nuclei.

With the second term vanishing, the total variance reduces to:

$$\mathrm{Var}(w_B - w_F) = \mathbb{E}[\mathrm{Var}(w_B - w_F \mid w)]\,. \tag{6.12}$$

For a narrow distribution of total number of wounded sources $P(w)$, the width $\mathrm{Var}(w)$ is small and the leading behaviour is well approximated by

$$\mathbb{E}[\mathrm{Var}(w_B - w_F \mid w)] \approx \mathrm{Var}(w_B - w_F \mid w = \langle w \rangle), \tag{6.13}$$

which follows from expanding $\mathrm{Var}(w_B - w_F \mid w)$ around $w = \langle w \rangle$ and neglecting higher–order terms (see Appendix C). This approximation explains why $\mathrm{Var}(w_B - w_F)$, and therefore Σ, remain essentially invariant with respect to the centrality–bin width for sufficiently narrow bins, $\Delta\text{centrality} \leq 10\%$.

Numerical validation of relations Eq. (6.12) was explicitly tested in Fig. 6.6. Figure 6.6 also compares the values of $\mathbb{E}[\mathrm{Var}(w_B - w_F \mid w)]$ with the leading Taylor approximation, $\mathrm{Var}(w_B - w_F \mid \langle w \rangle)$, and with the same expression supplemented by the next correction term. For $\Delta\text{centrality} \leq 10\%$, the leading approximation already provides an accurate description of the data, while adding the next expansion term improves the agreement over the entire centrality range. This demonstrates that higher-order contributions are negligible for bins narrower than 10%.

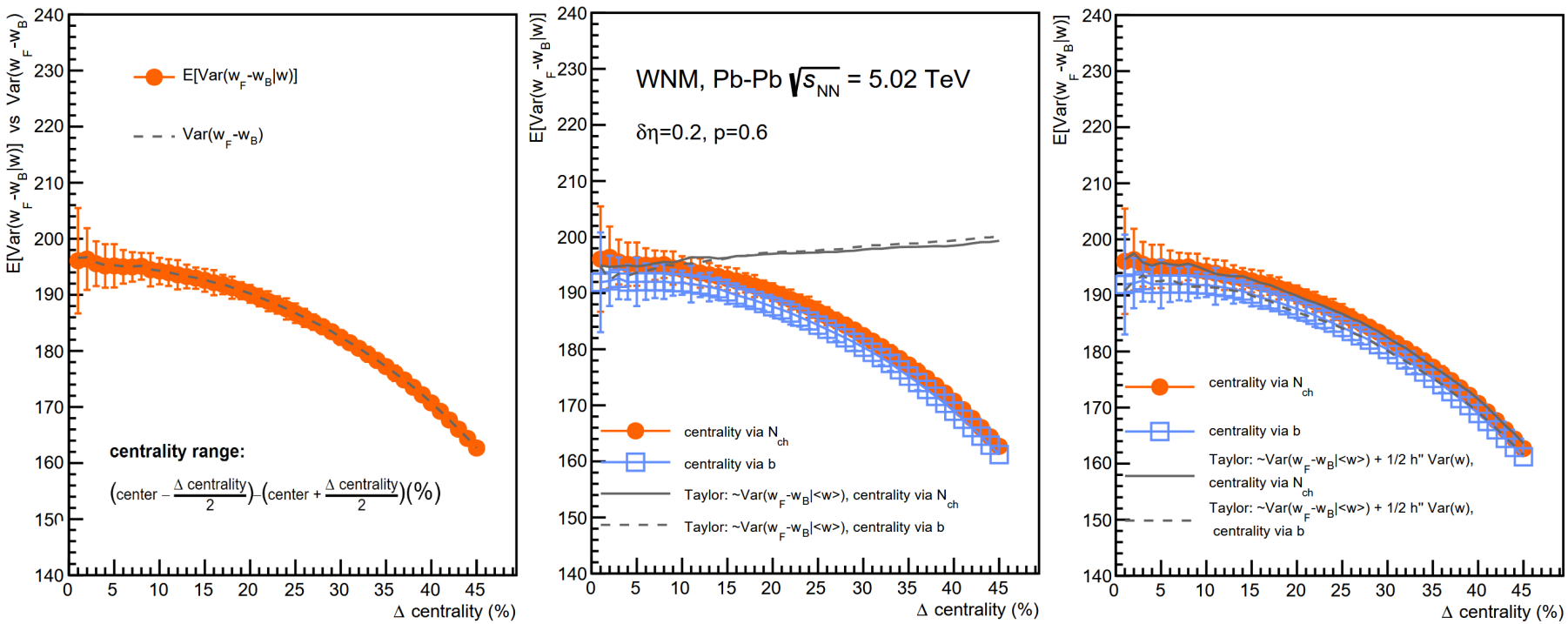

Figure 6.6: Dependence of $\mathrm{Var}(w_B - w_F)$ and $\mathbb{E}[\mathrm{Var}(w_B - w_F \mid w)]$ on the centrality class width (Δcentrality). The centrality class centre is fixed at 25%, while centrality class width Δ centrality varies from 1% to 45%. The left panel shows the comparison between $\mathrm{Var}(w_B - w_F)$ and $\mathbb{E}[\mathrm{Var}(w_B - w_F \mid w)]$. The middle panel compares $\mathbb{E}[\mathrm{Var}(w_B - w_F \mid w)]$ with its leading Taylor approximation, while the right panel includes the next-order correction term proportional to $\frac{1}{2}h''(\langle w \rangle)\,\mathrm{Var}(w)$, where $h''(\langle w \rangle) = \frac{d^2}{dw^2}\mathrm{Var}(w_B - w_F \mid w)\Big|_{w=\langle w \rangle}$.

6.3.2 Independence on choice of centrality selection method

The insensitivity of the observable Σ to the centrality estimator C_E implies the condition

$$\Sigma_{C_{E_1}} = \Sigma_{C_{E_2}}, \tag{6.14}$$

where C_{E_1} and C_{E_2} label different centrality selection methods, such as N_{ch} or b. For Σ given by Eq. (6.5), a sufficient (though not necessary) condition for Eq. (6.14) to hold is that both the mean number of forward-going wounded sources, $\langle w_F \rangle$, and the variance of the forward–backward asymmetry, $\mathrm{Var}(w_F - w_B)$, remain unchanged under different centrality selection method.

The distribution of the total number of wounded nucleons, $P(w)$, is itself defined with respect to the centrality estimator C_E used to select the events, i.e. $P(w) = P(w \mid C_E)$. In principle, different estimators may therefore lead to slightly different $P(w)$ distributions and could affect $\langle w_F \rangle$ or the quantity $\mathrm{Var}(w_B - w_F)$, and consequently the value of Σ. In the following, only forward-backward symmetric centrality estimators are considered, i.e. estimators that do not bias the forward-backward partition of wounded sources at fixed w.

The mean number of forward-going wounded sources can be written as

$$\langle w_F \rangle_{C_E} = \sum_w P(w \mid C_E)\, \mathbb{E}[w_F \mid w]. \tag{6.15}$$

Therefore, the stability condition for the mean can be expressed as

$$\langle w_F \rangle_{C_{E_1}} = \langle w_F \rangle_{C_{E_2}}. \tag{6.16}$$

For symmetric collisions, where $\mathbb{E}[w_F \mid w] = w/2$, this condition is equivalent to

$$\langle w \rangle_{C_{E_1}} = \langle w \rangle_{C_{E_2}}. \tag{6.17}$$

Model calculations, presented in the top right panel of Fig. 6.7, demonstrate that this equality holds not only for narrow centrality bins but also for much wider bins, up to Δcentrality $\approx 30\%$. This behaviour is expected, since different centrality estimators are designed to reproduce the same average number of wounded nucleons for a given centrality class, even though they may differ in the magnitude of event-by-event fluctuations [57, 121].

For narrow centrality bins (Δcentrality $\leq 10\%$), Eqs. (6.12), (6.13) and (6.17) provide a good approximation, explaining why term $\mathrm{Var}(w_F - w_B) \approx \mathrm{Var}(w_B - w_F \mid$

$\langle w \rangle_{C_E}$) remains insensitive to the choice of centrality estimator.

For wider centrality bins (Δcentrality $> 10\%$), $P(w)$ broadens, and higher-order terms in the Taylor expansion of $\mathrm{Var}(w_F - w_B \mid w)$ including terms proportional to $\mathrm{Var}(w)$ could, in principle, introduce differences between estimators. However, in the present wounded constituent model calculations (see Fig. 6.6), term $\mathbb{E}[\mathrm{Var}(w_B - w_F \mid w)]$ remains consistent within uncertainties for different centrality selection methods even for wide bins. With increasing centrality-bin width, the sensitivity of $\mathrm{Var}(w)$ to the choice of centrality estimator gradually decreases and becomes negligible for Δcentrality $\gtrsim 25\%$, where the corresponding $P(w \mid C_E)$ distributions obtained with different estimators are very similar. A direct comparison of these distributions, as well as values of $\mathrm{Var}(w)$ and $\langle w \rangle$ for different widths of centrality classes, is presented in Appendix C.

6.3.2.1 Interpreting Σ in terms of conditional variance

For narrow centrality bins (Δ centrality $\leq 10\%$), taking into account Eqs. (6.12) and (6.13), the expression for Σ in symmetric nucleus–nucleus collisions, Eq. (6.5), can be rewritten as:

$$\Sigma \approx 1 + \frac{\overline{n}}{2}(2p-1)^2 \left[\frac{\mathrm{Var}(w_F - w_B \mid w = \langle w \rangle)}{\langle w \rangle} + \frac{2}{k} \right]. \tag{6.18}$$

This reformulation makes it evident that, in the wounded constituent framework, the properties of Σ are directly governed by the fluctuations of the asymmetry between forward- and backward-moving wounded constituents at fixed average system size $\langle w \rangle$.

The key observations are as follows:

- For centrality classes narrower than Δcentrality $\leq 10\%$, all terms in Eq. (6.18) are effectively free from volume fluctuations. As a result, Σ is also a volume–fluctuation–free quantity within this range.

- Both $\mathrm{Var}(w_F - w_B \mid w = \langle w \rangle)$ and $\langle w \rangle$ are insensitive to the choice of centrality estimator. This invariance ensures that Σ remains robust against the centrality selection method.

- The ratio $\frac{\mathrm{Var}(w_F - w_B \mid w = \langle w \rangle)}{\langle w \rangle}$ is sensitive to the average number of wounded constituents in the given centrality class, but not to event-by-event fluctuations in w, provided that the class width does not exceed Δcentrality $\leq 10\%$. As

a result, Σ remains insensitive to volume fluctuations, although it exhibits a centrality dependence driven by the variation of the average system size $\langle w \rangle$.

The relation Eq. (6.18) explains the observed properties of the Σ in the wounded constituent framework concerning centrality selection method and centrality bin width dependence reported in Fig. 6.5. We conclude that, in the WNM, Σ is not a strongly intensive observable, as it is sensitive to the system size $\langle w \rangle$, which accounts for the centrality trends observed in Figs. 6.4 and 6.5. At the same time, Σ retains some strongly intensive–like properties for moderate centrality class widths. Analogous conclusions can be drawn within the wounded quark model.

6.4 The connection between Σ and partial covariance

The partial correlation technique was introduced in Section 3.2.4 as one of the remedies used to eliminate the spurious effects of volume fluctuations. Here, we focus on partial covariance — the unnormalised counterpart of partial correlation — and show that within the wounded nucleon model, partial covariance is directly related to the Σ observable in symmetric nucleus–nucleus collisions.

6.4.1 Σ as a proxy for the partial covariance between wounded constituents

In the general case, **the partial covariance is defined as:**

$$\mathrm{Cov}(X, Y \bullet Z) = \mathrm{Cov}(X, Y) - \frac{\mathrm{Cov}(X, Z)\mathrm{Cov}(Y, Z)}{\mathrm{Var}(Z)}, \tag{6.19}$$

which measures the degree of relation between two random variables X and Y after removing the effect of the controlling random variable Z.

A detailed overview of the implementation of partial covariance and correlations in the domain of heavy-ion physics is provided in Refs. [60, 61]. When the sample satisfies the affine dependence condition

$$\mathbb{E}(X \mid Z) = a + BZ, \tag{6.20}$$

the partial covariance becomes closely related to the conditional covariance and can be approximated as

$$\mathrm{Cov}(X, Y \bullet Z) \simeq \mathbb{E}_Z[\mathrm{Cov}(X, Y \mid Z)]\,. \tag{6.21}$$

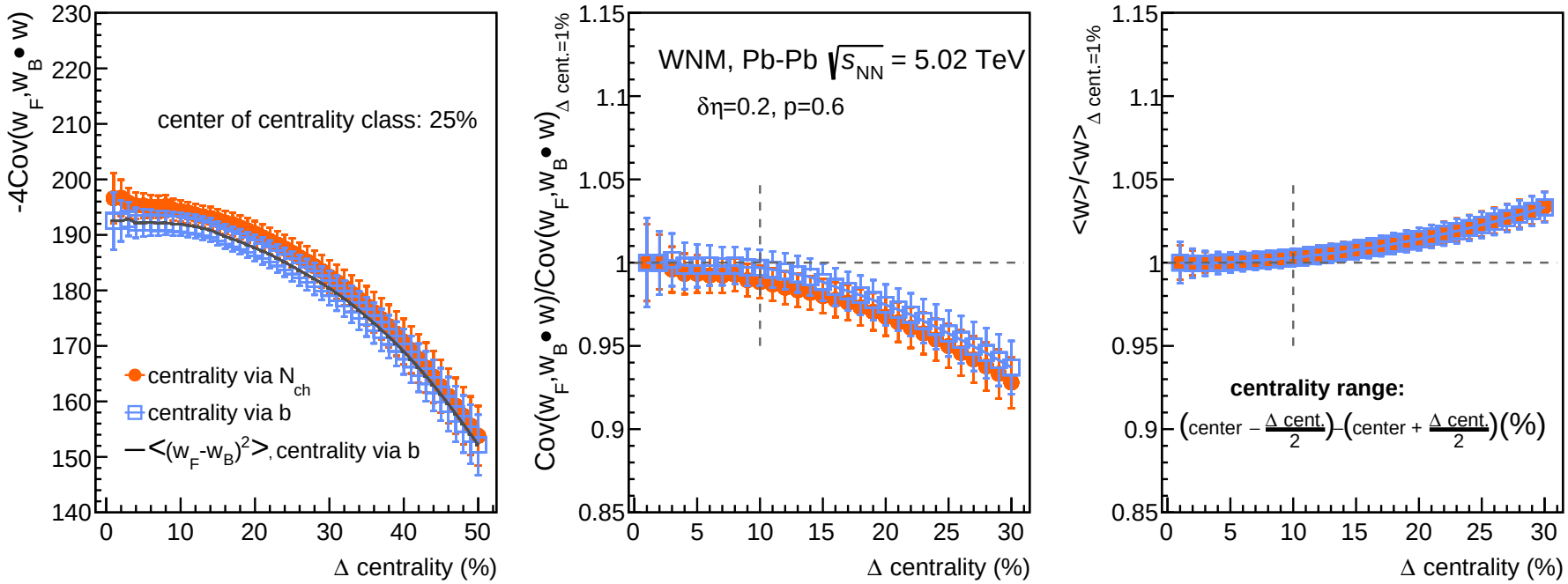

Figure 6.7: The partial covariance $\mathrm{Cov}(w_F, w_B \bullet w)$ and average number of wounded nucleons $\langle w \rangle$ as a function of the width of centrality class (Δ centrality). The centre of the centrality class is 25%, and the width of the centrality class changes from Δ centrality =1% up to Δ centrality =50%. The left panel shows the value of partial covariance $\mathrm{Cov}(w_F, w_B \bullet w)$, the middle and right panels display the partial covariance value and the average number of wounded nucleons $\langle w \rangle$, respectively, both normalized to their values determined at Δ centrality =1%. The ranges of centrality classes for a given centrality bin width can be deduced from the formula in the figure. Plot from Ref. [5].

We have shown in Ref. [5] that that in symmetric collisions, such as Pb–Pb, where $\mathrm{Var}(w_F) = \mathrm{Var}(w_B)$ and $\langle w_F \rangle = \langle w_B \rangle$, the following relation holds:

$$\langle (w_B - w_F)^2 \rangle = -4\mathrm{Cov}(w_F, w_B \bullet w = w_F + w_B). \tag{6.22}$$

The right-hand side of this equation represents the partial covariance between the forward- and backward-moving wounded nucleons, with the total number of wounded nucleons, $w = w_F + w_B$, serving as a control variable. The negative sign is a reflection of anti-correlation between forward and backward-moving wounded nucleons at fixed w. The left panel of Fig. 6.7 visually confirms Eq. (6.22).

In Ref. [60], Broniowski and Olszewski introduced the use of partial covariance between forward and backward multiplicities as a remedy for spurious volume (centrality) fluctuations. Within a **superposition model**, such as the wounded nucleon or wounded quark models, the method allows one to impose centrality constraints directly at the level of **particle sources** rather than final-state hadrons. In this notation, S_F, S_B, and S_C denote the *number of sources* in the forward, backward, and reference (centrality) rapidity windows, respectively. The formalism further assumes that forward sources contribute only to the forward pseudorapidity region, while backward sources contribute only to the backward region. The scaled partial covariance is then defined as

$$C(S_F, S_B \bullet S_C) = \bar{C}(n_F, n_B) - \frac{\bar{C}(n_F, n_C)\,\bar{C}(n_B, n_C)}{\overline{\mathrm{Var}}(n_C)},$$

where $C(n_F, n_B) = \mathrm{Cov}(n_F, n_B)/(\langle n_F \rangle \langle n_B \rangle)$ denotes the scaled covariance, the overline indicates subtraction of autocorrelations, and n_C is the number of particles in the reference bin used to define centrality.

The Broniowski–Olszewski formalism, in practice, coincides with the wounded nucleon picture in the limit $p \to 1$, i.e., at large $|\eta|$, where forward- and backward-going wounded nucleons predominantly emit into their respective hemispheres. In this regime, the measurement of $\mathrm{Cov}(w_F, w_B \bullet w)$ can therefore be regarded as a specific realisation of the Broniowski–Olszewski approach, namely:

$$\mathrm{Cov}(S_F, S_B \bullet S_C) \;=\; \mathrm{Cov}(w_F, w_B \bullet w), \quad \text{for } p \to 1 \text{ and } S_C = w. \tag{6.23}$$

Taking relation Eq. (6.22) into account, the formula Eq. (6.5) for Σ in symmetric

nucleus-nucleus collisions can be rewritten in terms of the partial covariance as:

$$\Sigma = 1 + \frac{\overline{n}}{2}(2p-1)^2 \left[\frac{-4\mathrm{Cov}(w_F, w_B \bullet w)}{\langle w \rangle} + \frac{2}{k}\right]. \tag{6.24}$$

The relation above Eq. (6.24) has the following implications:

- In symmetric collisions within the wounded constituent framework, the observable Σ is a proxy for the partial covariance between the forward- and backward-moving wounded sources, with the constraint imposed on the total number of sources. In the limit $p \to 1$, this expression coincides with the $C(S_F, S_B \bullet S_C)$ formalism introduced by Broniowski and Olszewski.

- Within the wounded constituent framework, both observables capture the same underlying physics: forward-backward fluctuations of the initial source distribution, constrained at the level of particle-emitting sources, not final-state hadrons.

- Σ provides a simpler and more practical approach to quantify longitudinal correlations than the partial covariance technique, without requiring subtraction of autocorrelations and reconstruction of the full covariance matrix across the entire η range.

6.5 Comparison between experimental results and wounded constituent models predictions

Figures from 6.8 to 6.10 provide an overview of the results on forward-backward correlations with Σ in the wounded nucleon and wounded quark models for Pb–Pb collisions at $\sqrt{s_{\mathrm{NN}}} = 2.76$ and 5.02 TeV, as well as Xe–Xe collisions at $\sqrt{s_{\mathrm{NN}}} = 5.44$ TeV. The data points are presented as a function of centrality in intervals of Δ centrality = 10%. Each figure compares theoretical predictions with experimental measurements of Σ obtained using the ALICE detector at the LHC. The ALICE data points are redrawn from Ref. [105, 104]. The experimental results are presented for various fixed values of the pseudorapidity separation gap ($\Delta\eta$) between the forward and backward intervals. The wounded nucleon and wounded quark model predictions are presented for different values of the model parameter probability p, which was tuned to provide the best fit to the experimental data. The error bars in the figures for WNM and WQM results represent total uncertainties, incorporating

both statistical uncertainties and systematic uncertainties due to variations in $\overline{n}$ and k.

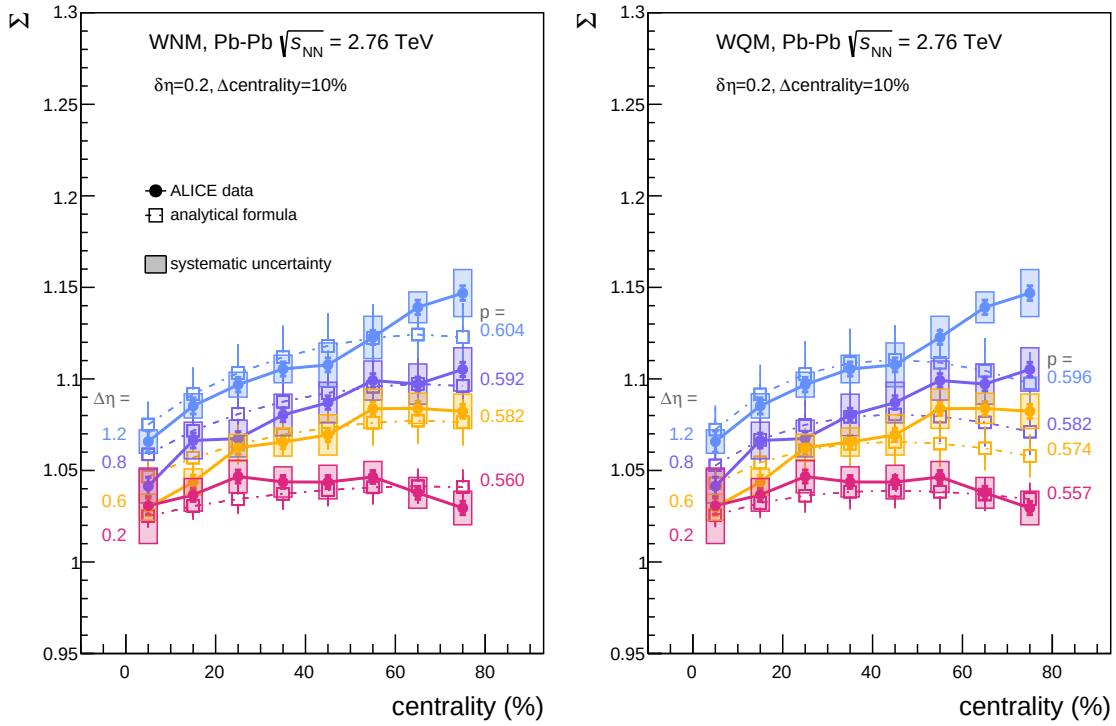

Figure 6.8: The centrality dependence of strongly intensive quantity Σ obtained in WNM (left panel) and WQM (right panel) for Pb–Pb collisions at $\sqrt{s_{\mathrm{NN}}} = 2.76$ TeV. Data points are drawn for selected fixed values of probability p. Theoretical predictions in each panel are compared with ALICE experimental results, redrawn from Ref. [105] for several values of the pseudorapidity gap: $\Delta\eta$ =1.2, 0.8, 0.6, 0.2. For the models, the marked uncertainty bars denote the total uncertainty. Plot from Ref. [5].

The findings presented in Figs. 6.8 to 6.10 indicate the following:

– The WNM and WQM effectively reproduce the experimental results for the Σ observed in Xe–Xe and Pb–Pb collisions. Qualitatively, the wounded nucleon model demonstrates better alignment with the Pb–Pb data, particularly in peripheral regions, as seen in Figs. 6.8 and 6.9. On the other hand, the best agreement between the experimental results on Σ and the theoretical description, both WNM and WQM, is seen for the Xe–Xe collision, Fig. 6.10.

– The models also accurately reflect how Σ values behave with centrality reported in the experimental data. The Σ increases from central to peripheral collisions. Equation (6.5) indicates that this growth is attributed to a term associated

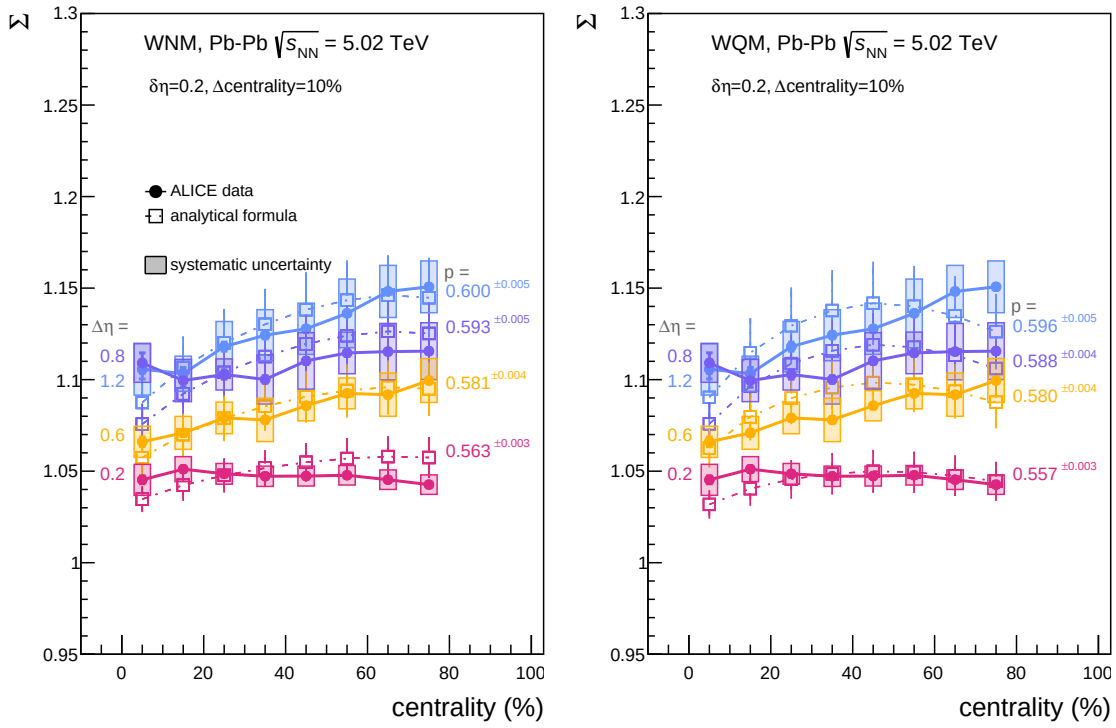

Figure 6.9: The centrality dependence of strongly intensive quantity Σ obtained in WNM (left panel) and WQM (right panel) for Pb–Pb collisions at $\sqrt{s_{\mathrm{NN}}} = 5.02$ TeV. Data points are drawn for selected fixed values of probability p. Theoretical predictions in each panel are compared with ALICE experimental results, redrawn from Ref. [105] for several values of the pseudorapidity gap: $\Delta\eta$ =1.2, 0.8, 0.6, 0.2. For the models, the marked uncertainty bars denote the total uncertainty. Plot from Ref. [5].

with wounded nucleons (quarks), as the other components of the Σ formula remain robust against changes in centrality.

– In particular, the studied models successfully reproduce the energy dependence of the Σ observed in the experimental data, that is, the increase in the observable values with the system energy, regardless of the system type. According to the Eq. (6.5), it is clear that the energy dependence of $\overline{n}$ and k reported in pp collisions plays a significant role in the observed behaviour. Specifically, an increase in $\overline{n}$ and a decrease in k with respect to collision energy contribute to this trend.

– The values of Σ in the wounded nucleon (quark) model show a sensitivity to the probability value p. Both WNM and WQM adequately describe the data within the studied kinematic range of η when the probability values p exceed

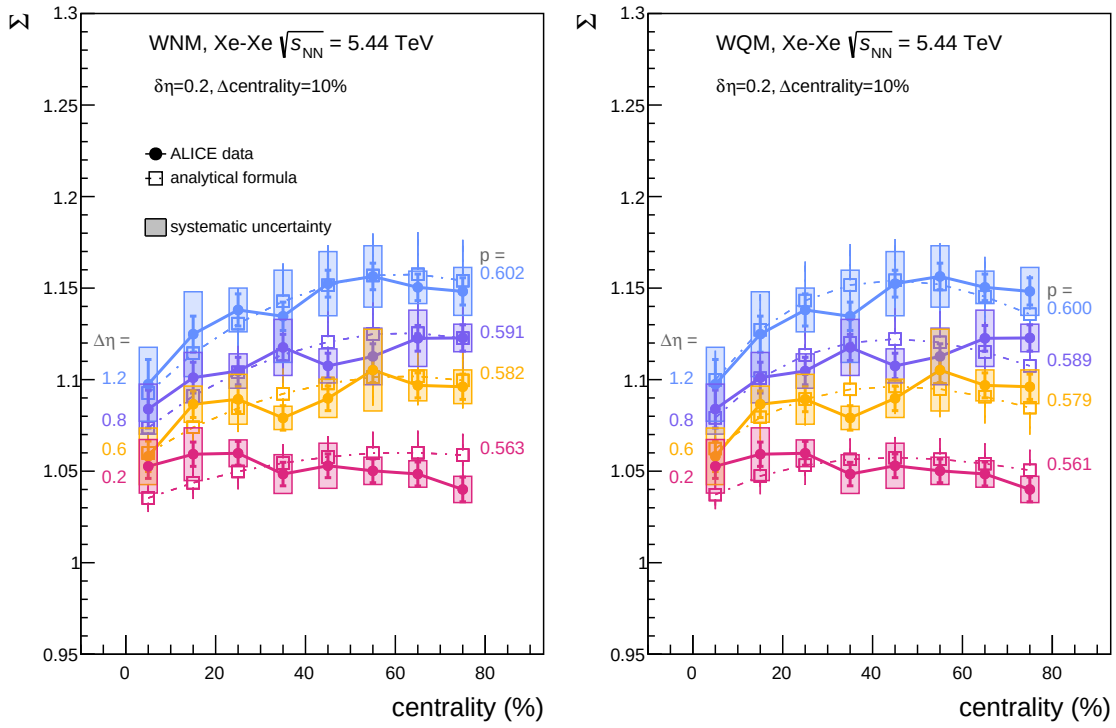

Figure 6.10: The centrality dependence of strongly intensive quantity Σ obtained in WNM (left panel) and WQM (right panel) for Xe–Xe collisions at $\sqrt{s_{\mathrm{NN}}} = 5.44$ TeV. Data points are drawn for selected fixed values of probability p. Theoretical predictions in each panel are compared with ALICE experimental results, redrawn from Ref. [105] for several values of the pseudorapidity gap: $\Delta\eta$ =1.2, 0.8, 0.6, 0.2. For the models, the marked uncertainty bars denote the total uncertainty. Plot from Ref. [5].

0.5. It was observed that, to reproduce the data, the probability p must vary with pseudorapidity.

– The relation between probability p and pseudorapidity is illustrated in Fig. 6.11. From this figure, it emerges that within the limits of uncertainty, p shows a universal trend as a function of pseudorapidity, regardless of the type of colliding system or its energy within the studied energy range.

An important point concerns the role of short-range correlations in the interpretation of Σ in WNM and WQM. In the formulation of the wounded constituent model presented in this chapter, neither resonance decays nor other microscopic sources of SRC are introduced explicitly as separate particle-emitting source types. Instead, they are effectively absorbed into the parametrisation of the single-nucleon (quark) multiplicity distribution (described by the NBD) and the emission probability p, which jointly

encode the short-range dynamics of particle production. This construction allows the model to reproduce the observed decrease of Σ with increasing pseudorapidity gap (as discussed in Chapter 5) without introducing explicit resonance decays, cluster emission, and other local mechanisms that generate SRC contributions.

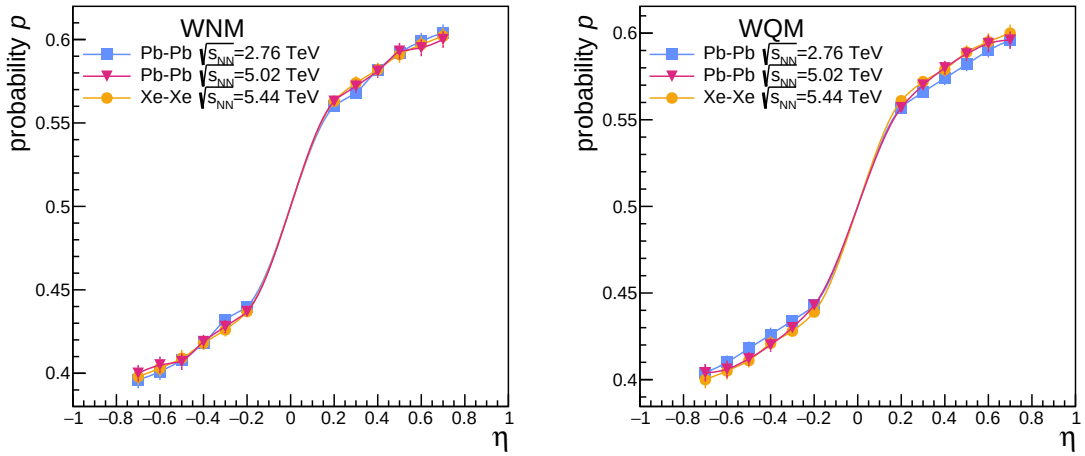

Figure 6.11: Probability p as a function of pseudorapidity obtained in WNM (left panel) and WQM (right panel) for Pb–Pb and Xe–Xe collisions. Values of p are shown with total uncertainties, which are dominated by the systematic uncertainty of the experimental data for Σ and by the uncertainty on the NBD parameters. Plot from Ref. [5].

6.6 Reconstructing the fragmentation function, $F(\eta)$, from forward-backward correlation

6.6.1 Standard approach to fragmentation function determination

The fragmentation function, $F(\eta)$, represents the pseudorapidity single-particle density that describes how a wounded constituent, such as a wounded nucleon or quark, contributes to particle production. In a two-component framework, where wounded constituents moving forward and backward are distinguished, $F(\eta)$ can be determined from measurements of the single-particle pseudorapidity distribution, $N(\eta)$, using relation Eq. (6.1).

By rearranging Eq. (6.1), one can express the fragmentation function $F(\eta)$ as follows:

$$F(\eta) = \frac{1}{2}\left(\frac{N(\eta)+N(-\eta)}{\langle w_F\rangle + \langle w_B\rangle} + \frac{N(\eta)-N(-\eta)}{\langle w_F\rangle - \langle w_B\rangle}\right) \tag{6.25}$$

A major drawback of this approach is that Eq. (6.25) **applies only to asymmetric collisions** where $\langle w_F \rangle \neq \langle w_B \rangle$, see Ref [112]. In symmetric cases ($\langle w_F \rangle = \langle w_B \rangle$), the second term in this equation becomes undefined.

6.6.1.1 New approach: reconstructing the fragmentation function from Σ

One method for determining the fragmentation function in a symmetric pp collision was proposed in Ref. [122] based on the study of the average numbers of produced particles together with pairs of particles in different symmetric and asymmetric pseudorapidity intervals.

For the first time, Ref. [5] demonstrates that forward-backward correlations, measured through the Σ variable, provide **a general method for extracting the fragmentation function of a wounded nucleon or quark, applicable to both asymmetric and symmetric nucleus-nucleus collisions.**

The new method relies on the fact that the Σ in the wounded constituent model provides direct information about the probability value p. This value is linked to the single nucleon fragmentation function, as described by Eq. (6.3). By combining Eqs. (6.1) and (6.3), one obtains:

$$\begin{aligned} \int_F F(\eta)\, d\eta &= p \int_F \left(F(-\eta) + F(\eta)\right)\, d\eta \\ &= \frac{p}{\langle w_F \rangle + \langle w_B \rangle} \int_F \left(N(-\eta) + N(\eta)\right)\, d\eta. \end{aligned} \tag{6.26}$$

where $N(\eta) \equiv \frac{dN(\eta)}{d\eta}$.

New approach to reconstructing fragmentation function $F(\eta)$

For a sufficiently narrow pseudorapidity interval F, relation Eq. (6.26) simplifies to:

$$F(\eta) \approx \frac{p}{\langle w_F \rangle + \langle w_B \rangle} \left(N(-\eta) + N(\eta)\right). \tag{6.27}$$

Figure 6.12 presents the fragmentation function of wounded nucleons and wounded quarks as a function of η. The data points were determined for minimum-bias events as well as for different centrality classes in Pb–Pb collisions at $\sqrt{s_{\mathrm{NN}}} = 5.02$ TeV, based on Eq. (6.27). The values of the probability p used in the formula are listed in Fig. 6.11 and were extracted by optimising the fit between the Σ values obtained from the wounded constituent model and the experimental results from ALICE.

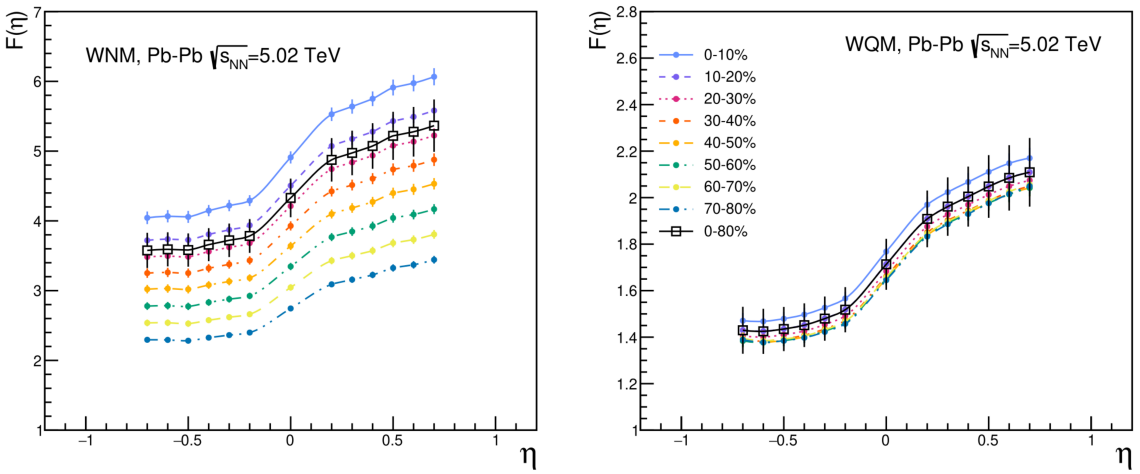

Figure 6.12: The wounded nucleon (left panel) and quark (right panel) fragmentation functions extracted from symmetric Pb–Pb collisions at $\sqrt{s_{\rm NN}}$=5.02 TeV as a function of η for different centrality classes. In figures, error bars mark the total uncertainty of $F(\eta)$, to its values contributed the uncertainty of the parameter p and the uncertainty of $N(\pm\eta)$ determination reported in Refs. [123]. Plot from Ref. [5].

For $\eta = 0$, the probability value was set to $p = 0.5$, in agreement with the behaviour of the data points in Fig. 6.11. The number of wounded constituents, $\langle w_F \rangle + \langle w_B \rangle$, including both nucleons and quarks, was generated through Monte Carlo simulations, as discussed in Section 6.1.2.

The values of $N(\pm\eta)$ were taken from charged-particle multiplicity densities measured in Pb–Pb collisions at $\sqrt{s_{\rm NN}} = 5.02$ TeV by ALICE, as reported in Ref. [123]. The analysis in Ref. [123] considered a 0–80% centrality range for the minimum-bias selection, as the 80% centrality class is affected by contamination from electromagnetic processes. Since Ref. [123] does not directly provide $dN_{ch}/d\eta$ values for the 0–80% centrality range, these values were estimated from the available data as an arithmetic average, with uncertainties computed as the quadratic sum of individual errors.

As shown in Fig. 6.12, the wounded nucleon fragmentation function exhibits slight shape variations across different centrality classes, with its magnitude increasing from peripheral to central collisions. In contrast, the wounded quark fragmentation function remains more universal, showing a consistent shape and similar magnitude across all analysed centrality classes. These findings qualitatively align with previous observations of wounded nucleon and wounded quark fragmentation functions in asymmetric d+Au collisions at $\sqrt{s_{\rm NN}} = 200$ GeV obtained using the standard approach, as reported in Ref. [116]. However, the fragmentation function extracted in this study exhibits a more pronounced dependence on pseudorapidity compared

to the trends reported in Ref. [116]. Further investigation is required to clarify this difference.

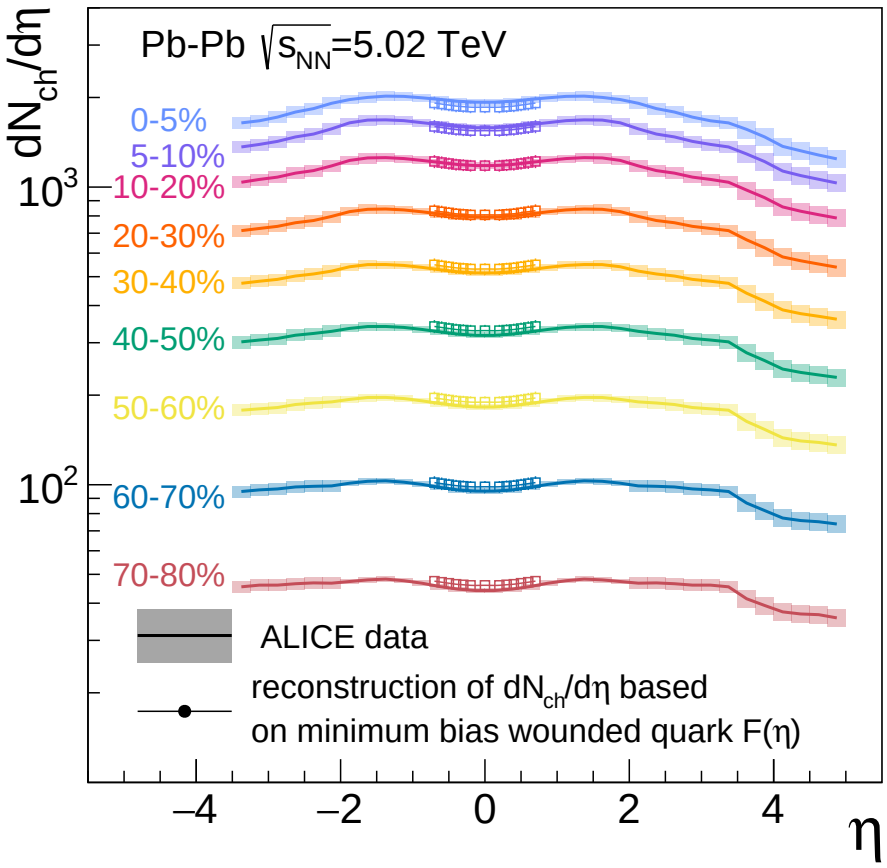

Figure 6.13: Charged-particle multiplicity distributions $N(\eta) \equiv dN_{\mathrm{ch}}/d\eta$ for Pb–Pb collisions at $\sqrt{s_{\mathrm{NN}}} = 5.02$ TeV. The distributions are reconstructed using the minimum-bias fragmentation function $F(\eta)$ for wounded quarks, extracted with a novel method based on the Σ observable. The reconstructed distributions are shown as points, while the ALICE data are shown as lines. Shaded areas and bars indicate uncertainties for ALICE data and the reconstructed distributions, respectively. Figure adapted from Ref. [5].

6.6.1.2 Reconstructing the charged particle multiplicity distribution from $F(\eta)$ in WQM

To validate the extracted minimum-bias fragmentation function of wounded quarks, $F(\eta)$, it was applied to determine the charged-particle density in Pb–Pb collisions at $\sqrt{s_{\rm NN}} = 5.02$ TeV according to Eq. (6.1), for different centrality classes. The resulting $dN_{ch}/d\eta$ distributions were then compared with the measurements reported by the ALICE experiment, as shown in Fig. 6.13. A reasonable level of agreement is observed between the reconstructed results and the experimental data over the considered range of η and centralities.

6.7 Exploratory predictions for small systems: pp and p–Pb collisions

While the present study primarily focuses on nucleus–nucleus collisions, it is instructive to test the wounded constituent framework in the small-system limit and for asymmetric collisions. The following results are exploratory model-based predictions and aim to verify the behaviour of Σ, and to a lesser extent Δ, in proton–proton and proton–lead collisions, in WNM and WQM frameworks. **This section is intended as a consistency cross-check and to provide benchmarks for small systems within the wounded constituent model.**

The predictions were obtained at $\sqrt{s_{\rm NN}} = 5.02$ TeV. Figures 6.14 and 6.15 present the behaviour of the observables as a function of multiplicity class (pp) and centrality percentile (p–Pb), respectively. For the p–Pb system, results were studied for two centrality bin widths (2% and 10%) to probe the sensitivity of the observables to volume fluctuations, and for two centrality estimators: (i) forward region particle multiplicity and (ii) impact parameter.

6.7.1 Predictions for pp collisions

In the case of pp collisions, only predictions from the wounded quark model are considered, as presented in Fig. 6.14. This choice follows from the fact that, within the WNM, the observable in pp collisions is fixed by definition to $\Sigma = 1 + \frac{\overline{n}}{k}(2p-1)^2$ (see Eq. (6.4)). The present analysis does not aim to reproduce multiplicity spectra in pp collisions; instead, pp results are shown solely to illustrate the predicted value of the Σ observable in this system.

The dependence of Σ on the multiplicity class reported in Fig. 6.14 is negligible,

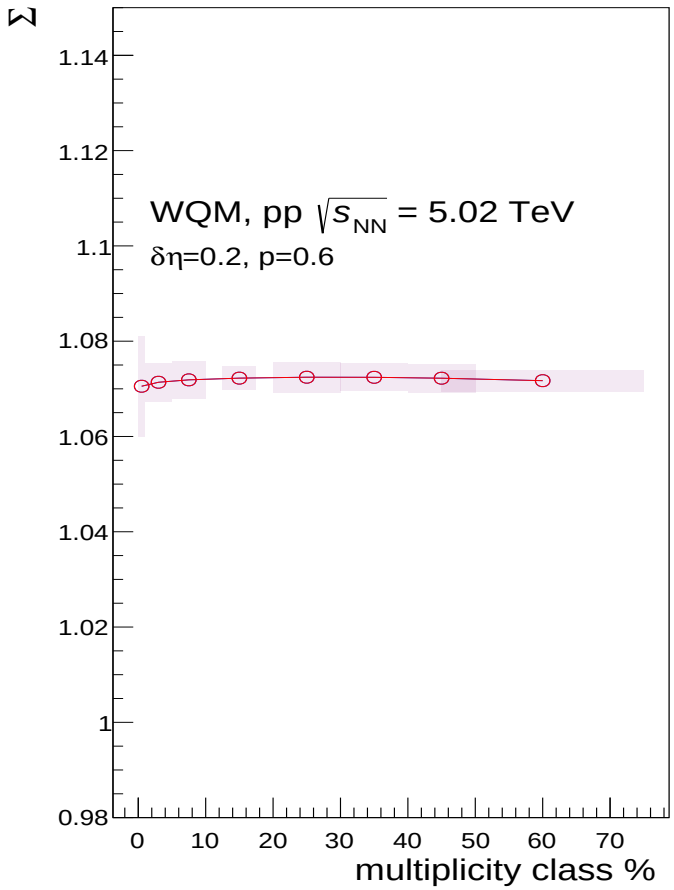

Figure 6.14: Predicted values of Σ for pp collisions at $\sqrt{s} = 5.02$ TeV in the wounded quark model, shown as a function of multiplicity class. The results are shown for $\delta\eta = 0.2$ and with the parameter p fixed at 0.6 The shaded bands represent statistical uncertainties: their horizontal extent corresponds to the width of the multiplicity classes, which were chosen to reproduce those used in the experimental pp results reported in Fig. 5.7, while their vertical extent indicates the statistical uncertainty of the model calculation.

with observed variations remaining below 0.2%. These fluctuations are well within the expected statistical uncertainties and are not of physical significance.

This behaviour is consistent with the definition of the Σ in WQM. Equation (6.5) indicates that the centrality (or multiplicity) dependence of Σ arises solely through the fluctuation term $\frac{\langle (w_B - w_F)^2 \rangle}{\langle w_F \rangle}$.

In the simulation of pp collisions, the total number of possible wounded sources is strictly limited to three wounded quarks per proton. The denominator $\langle w_F \rangle$ is bounded from below by unity, while the numerator $\langle (w_B - w_F)^2 \rangle$ is restricted to very small values due to the maximum of three wounded quarks per proton. Consequently, their ratio remains small and stable across all multiplicity classes, ensuring that the dependence of Σ on centrality is negligible. A natural next step would be to investigate the sensitivity of Σ to the assumed number of constituent quarks within the WQM framework in pp collisions, which we leave for future studies.

This wounded quark model-based prediction stands in contrast to experimental observations (see Fig. 5.7), which indicate a non-trivial trend of Σ with multiplicity

class. While the simulations were performed at $\sqrt{s} = 5.02$ TeV and the referenced measurements were obtained at $\sqrt{s} = 13$ TeV, the energy difference is unlikely to account for the discrepancy. Qualitatively, the multiplicity dependence of Σ is not expected to evolve significantly with collision energy. The experimental evaluation of this finding is one of the aims of future tasks planned by the author.

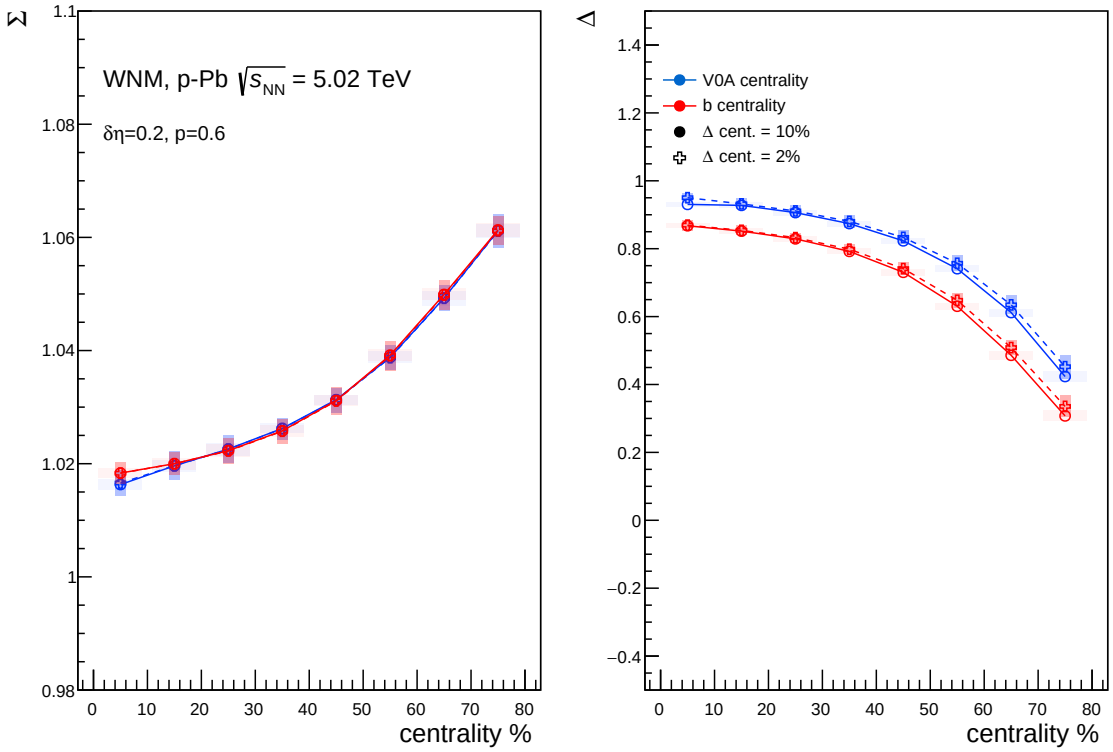

Figure 6.15: Predicted values of Σ and Δ quantity for p–Pb collisions at $\sqrt{s} = 5.02$ TeV in the wounded nucleon model as a function of centrality class. Results are shown for two centrality bin widths Δ centrality = 2% and 10%. Centrality is determined either from the impact parameter b or from the charged-particle multiplicity in the V0A acceptance. The results are shown for $\delta\eta = 0.2$ and with the parameter p fixed at 0.6 The shaded bands represent statistical uncertainties: their horizontal extent corresponds to the width of the multiplicity classes, while their vertical extent indicates the statistical uncertainty of the model calculation.

6.7.2 Predictions for p–Pb Collisions

For the p–Pb system, predictions were obtained in both the WNM and WQM. Due to the asymmetric nature of the proton-nucleus interaction, in addition to the observable Σ, the quantity Δ was also evaluated for pairs of pseudorapidity intervals symmetrically placed around midrapidity ($\eta = 0$).

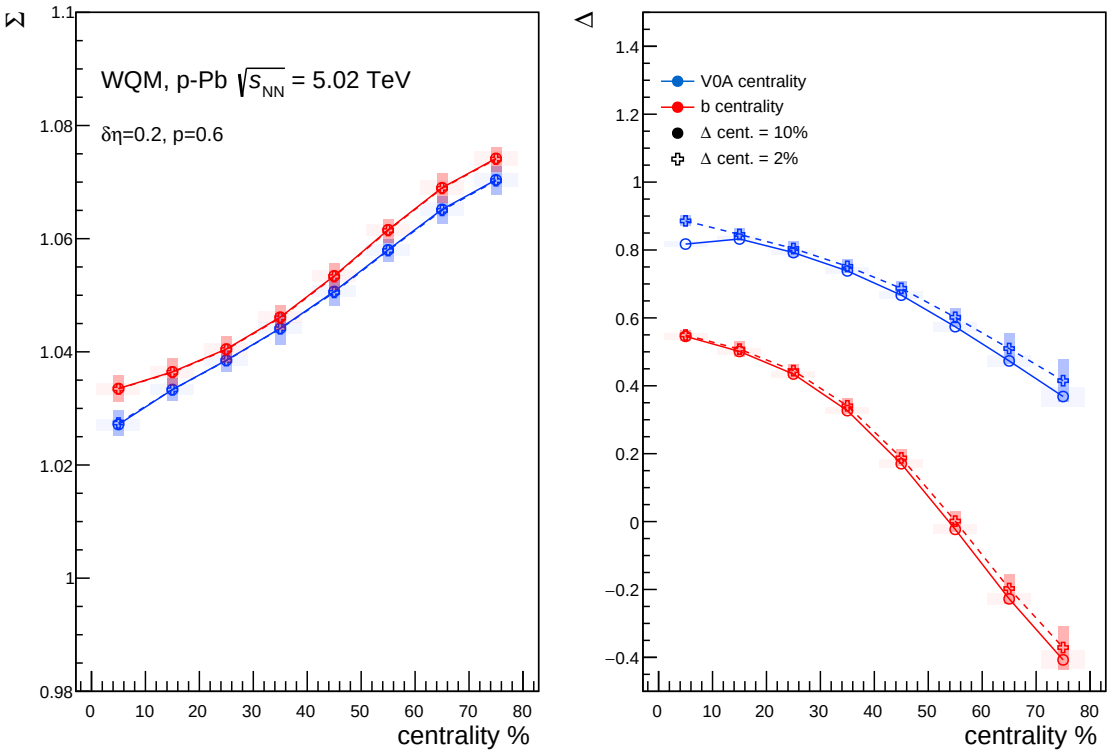

Figure 6.16: Predicted values of Σ and Δ quantity for p–Pb collisions at $\sqrt{s} = 5.02$ TeV in the wounded quark model as a function of centrality class. Results are shown for two centrality bin widths Δ centrality = 2% and 10%. Centrality is determined either from the impact parameter b or from the charged-particle multiplicity in the V0A acceptance. The results are shown for $\delta\eta = 0.2$ and with the parameter p fixed at 0.6 The shaded bands represent statistical uncertainties: their horizontal extent corresponds to the width of the multiplicity classes, while their vertical extent indicates the statistical uncertainty of the model calculation.

Results for Σ and Δ are shown in Figs. 6.15 and 6.16 for the WNM and WQM, respectively. The findings exhibit the following trends with centrality:

– Σ increases with centrality percentile (i.e. toward more peripheral collisions);

– Δ decreases with centrality percentile.

These qualitative features are reproduced in both WNM and WQM.

Neither observable is a strongly intensive quantity, and the observed dependencies on centrality are attributable to the centrality evolution of the number of wounded constituents and their fluctuations, as expressed analytically in Eqs. (6.4) and (6.10). In the WQM, both forward- and backward-going wounded constituent fluctuations

contribute, whereas in the WNM, w_F is fixed to unity and only fluctuations in w_B are relevant.

A noteworthy feature is the differing sensitivity of the two observables. In the wounded nucleon model, Σ shows only weak dependence on the centrality estimator and bin width, whereas in the wounded quark model, this dependence is much more pronounced. By contrast, Δ varies strongly in both models and is highly sensitive to the choice of centrality estimator and bin width.

At the time of writing, there are no published experimental results on forward-backward correlations in p–Pb collisions using the Σ and Δ observables. Therefore, the results presented here provide model-based predictions from the WNM and WQM, which may serve as benchmarks for future experimental studies.

6.8 Summary and Conclusions

This chapter has presented a detailed study of forward–backward correlations in heavy-ion collisions at LHC energies within the wounded constituent framework. The main focus was primarily on the behaviour of the Σ observable in **symmetric nucleus–nucleus collisions** (Pb–Pb and Xe–Xe). We also explored the first predictions for the Σ in **small systems** (pp and p–Pb), as well as the forward–backward fluctuation observable Δ in asymmetric **p–Pb collisions**. The main conclusions of this chapter are as follows:

1. *Breakdown of strong intensive quantity Σ in wounded constituent models*
   While Σ was originally introduced as a strongly intensive quantity, this study shows that it loses this property in the wounded constituent framework. A two-component scenario of forward- and backward-moving constituents directly breaks the assumption of the independent source model. As a result, Σ becomes sensitive to the average number of wounded constituents (system size) and their fluctuations in both the wounded nucleon and wounded quark models. Similarly, Δ is not a strongly intensive quantity in WNM and WQM. However, it shows a more complex dependence on both the average number of wounded constituents and their fluctuations than Σ.

2. *Wounded source emission probability p as a tuning parameter*
   In the wounded nucleon model, the emission probability p regulates how likely a source is to emit into a forward or backward pseudorapidity bin. For $p \neq 0.5$, forward- and backward-moving wounded constituents become statistically

distinct because they emit asymmetrically particles into the forward and backward pseudorapidity intervals. For $p = 0.5$, the statistical equivalence between forward- and backward-moving wounded sources is restored, the wounded constituent model converges to the independent source model, and Σ recovers its strongly intensive quantity character.

The values of the parameter p are defined as a function of pseudorapidity. Its increasing trend with η was determined by comparing model predictions with experimental results for Σ. The obtained results are in overall agreement with the probability values reported in Ref. [74] determined for σ_C, a different forward-backward correlation observable.

3. *Strongly–intensive–like behaviour in symmetric collisions*
   Despite losing the status of a strongly intensive quantity, in symmetric nucleus–nucleus collisions Σ still exhibits some of the **strongly-intensive-like properties**:

   - it is insensitive to volume fluctuations;
   - it is independent of the centrality estimator.

   Both statements hold provided that the centrality bins are narrow (Δ centrality $\leq$ 10%).

   The origin of this behaviour lies in the fact that, within such narrow classes, Σ is determined predominantly by fluctuations of the forward–backward imbalance of wounded constituents at an approximately fixed $\langle w \rangle$. In this regime, the fluctuations of the forward-backward asymmetry at fixed $\langle w \rangle$ show very weak dependence on the centrality selection method.

   This behaviour is fully consistent with experimental results reported by the ALICE Collaboration.

4. *Physical interpretation: longitudinal fireball fluctuations*
   The observable Σ, as defined in wounded constituent models of symmetric nucleus-nucleus collisions, can serve as a practical representation of more complex correlation measures. In particular, it acts as a proxy for the partial covariance between the forward and backward initial sources. Physically, Σ captures directly information about the fluctuations of the forward-backward asymmetry between the number of wounded constituents. This asymmetry reflects fluctuations in the longitudinal shape of the fireball and is closely related

to the first odd Chebyshev coefficient $\langle a_1^2 \rangle$, which quantifies the longitudinal deformation.

5. *Predictive power of WNM and WQM models*
   Both the wounded nucleon and wounded quark models **reproduce ALICE's experimental data** for Σ in Pb–Pb and Xe–Xe collisions, **outperforming more sophisticated models** like HIJING, AMPT, and EPOS. These findings highlight the remarkable success of the wounded constituent approach in describing complex correlation phenomena using simple superposition assumptions.

6. *Predictions for small systems: pp and p–Pb collisions*
   Predictions were also made for small systems using the wounded nucleon and wounded quark frameworks. In **pp collisions**, Σ remains constant across multiplicity classes in the wounded quark model, contrary to experimental trends that show a clear increase. This discrepancy indicates that the wounded constituent framework, although effective for large systems, does not capture the mechanisms that dominate correlations in small systems. This limitation points to the possible role of an additional particle-production mechanism beyond the wounded constituent framework.

   In **p–Pb collisions**, both Σ and Δ are explicitly sensitive to volume fluctuations, dominantly driven by fluctuations of sources in the lead nucleus. Both observables exhibit a strong dependence on centrality. The observable Δ, in particular, shows a higher sensitivity to volume fluctuations and the choice of centrality estimator, whereas Σ remains comparatively more stable. These results provide **baseline theoretical benchmark** within the wounded constituent framework for future measurements of forward–backward fluctuation and correlations in small systems with Σ and Δ quantities.

7. *Reconstruction of the fragmentation function based on forward-backward Σ measurements*
   This study introduces a significant methodological advancement: a new technique for reconstructing the fragmentation function $F(\eta)$ of wounded constituents. This method relies on the relation between Σ and the emission probability p. It offers a more general approach that allows for the determination of $F(\eta)$ even in symmetric systems, in comparison to the standard technique based on (pseudo)rapidity density distributions, which only works for asymmetric collision types.

Fragmentation functions were extracted for both the wounded nucleon and wounded quark across different centrality classes and minimum bias data samples. Notably, the fragmentation function of the wounded quark shows a relatively stable shape across centralities, suggesting a more universal character providing a reasonable though not fully quantitative description of the charged-particle density distributions measured by the ALICE experiment.

In summary, this chapter demonstrates that even within a simple framework of the wounded constituent model, one can account for a wide range of phenomena related to forward–backward correlations and fluctuations. Based on the observed agreement between the model and the experimental data, we deduced that event-by-event fluctuation of longitudinal fireball asymmetry is the dominant factor governing forward-backward correlations in symmetric nucleus-nucleus collisions.

Further studies

The results of this chapter point to several open directions for future research. First, the wounded nucleon model predicts that Σ should remain independent of the choice of centrality estimator over the full centrality range; however, its independence from volume fluctuations holds only for narrow centrality bins ($\leq 10\%$). An experimental analysis of Σ performed in wider centrality bins would therefore provide a direct test of this prediction. Second, the present study has been limited to symmetric collision systems and symmetric forward–backward pseudorapidity intervals. Extending the analysis to asymmetric intervals around midrapidity ($\eta = 0$) would allow one to investigate how Σ and Δ behave under these conditions and whether new effects emerge. Finally, in p–Pb collisions, the model predicts that Σ and Δ are influenced by fluctuations of the number of sources in the Pb nucleus and by the choice of centrality estimator. An experimental measurement of Σ and Δ in p–Pb would be an important test of these predictions. Further extensions of this analysis to other collision systems and collision energies are straightforward and self-evident.

Chapter 7

A broader perspective on Σ correlations and fluctuations

Experimental data on forward-backward correlations with Σ, measured at the LHC, reveal two opposite, system-dependent trends as a function of multiplicity (centrality) across pp, Pb–Pb, and Xe–Xe collisions (see Chapter 5 for details). None of the models discussed so far can reproduce these trends simultaneously in both small and large systems. This is not unexpected. Particle production in heavy-ion collisions, possibly altered by collective or medium effects, may not follow the same mechanisms as those observed in small systems.

Rather than proposing a specific dynamical explanation for these differences, the aim of this chapter is simply to study the statistical properties of Σ under the assumption that several independent source types may contribute simultaneously to particle production. This approach allows the different fluctuation mechanisms contributing to Σ to be identified and interpreted without relying on a specific microscopic dynamical model.

Accordingly, in this chapter, Σ is discussed within *the multi-source superposition framework*, which is a simple and natural extension of the Independent Source Model introduced in Section 3.3.1.1. The primary purpose of this approach is to gain a broader perspective on event-by-event correlations and fluctuations, grounded in the statistical definition of Σ. This generalised framework allows one to examine how the number of sources, their emission characteristics, and their fluctuations influence the observable, independently of detailed microscopic assumptions.

It is important to emphasise that the framework is not intended as a dynamical model designed to resolve all open questions, but rather as a controlled statistical tool that disentangles how different fluctuation mechanisms manifest themselves in Σ within a broad class of superposition-based descriptions.

7.1 Generalised framework: multi-source fluctuation approach

The multi-source superposition framework assumes that different types of statistically independent sources contribute to particle production, while allowing the event-by-event numbers of those source types to fluctuate and to be correlated.

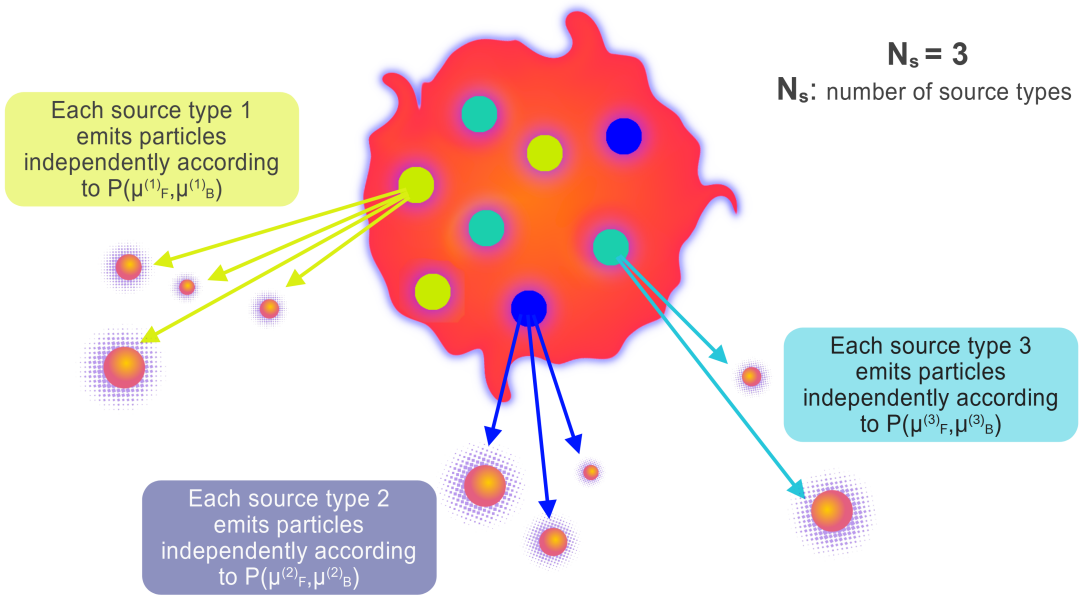

Figure 7.1: Illustration of the multi-source superposition framework. The system contains $N_S = 3$ types of sources, each emitting particles independently according to its own distribution $P(\mu_F^{(i)}, \mu_B^{(i)})$, **where $i = 1, 2, 3$ is a source counter labelling the source types included in the superposition.**

Within this framework, a **source** is an independent particle-emitting entity. It contributes to the forward and backward pseudorapidity intervals in a single event. The index i is a **source-type label** that distinguishes different classes of sources in the superposition. Each source is characterised by its joint emission distribution $P(\mu_F^{(i)}, \mu_B^{(i)})$ and by the assumption of *source independence*. This means the stochastic emission of one source does not influence any other source.

The number of sources of each type, s_i, may fluctuate from event to event, and the number of different source types may be mutually correlated. A source may represent an elementary emitter (such as a string, wounded nucleon or constituent quark) or an *effective emitter composed of several microscopic objects* (e.g. clusters, fused sets of i individual strings), treated as a single source with its own mean emission and fluctuation profile.

Superposition principle and multiplicities: In the superposition picture, the total forward and backward multiplicities are sums over emissions from all sources,

$$n_{F(B)} = \sum_{i=1}^{N_S} \sum_{k=1}^{s_i} \mu_{F(B)}^{(i,k)}. \tag{7.1}$$

where N_S denotes the total number of distinct source types, s_i is the event-by-event number of sources of type i, and $\mu_{F(B)}^{(i,k)}$ denotes the emission of an individual source.

Since all sources of a given type share the same emission distribution, taking event averages yields the standard factorisation,

$$\langle n_{F(B)} \rangle = \sum_{i=1}^{N_S} \langle s_i \rangle \, \langle \mu_{F(B)}^{(i)} \rangle, \tag{7.2}$$

which is a characteristic feature of superposition models.

In this chapter, we restrict the discussion to **symmetric collision systems** (pp, Xe–Xe, Pb–Pb), with forward and backward pseudorapidity intervals placed symmetrically around midrapidity, $\eta = 0$. In such systems, the mean forward and backward multiplicities are equal, which implies the constraint

$$\langle n_F \rangle = \langle n_B \rangle \quad \Rightarrow \quad \sum_{i=1}^{N_S} \langle s_i \rangle \left(\langle \mu_F^{(i)} \rangle - \langle \mu_B^{(i)} \rangle \right) = 0. \tag{7.3}$$

This symmetry condition is assumed throughout the remainder of this chapter.

7.2 Statistical decomposition of Σ: Three mechanisms

Within the multi-source superposition framework, where the forward and backward multiplicities are given by Eq. (7.1), the observable Σ follows directly from the law of total covariance (see Appendix D). Its general form reads:

$$\Sigma = \sum_{i=1}^{N_S} \xi_i^{(I)} \, E_i + \sum_{i=1}^{N_S} \xi_i^{(II)} \, \mathrm{Var}(s_i) + \sum_{1 \le i < j \le N_S} 2 \, \xi_{ij}^{(III)} \, \mathrm{Cov}(s_i, s_j). \tag{7.4}$$

Definitions of E_i and ξ coefficients: Quantities E_i and ξ appearing in Eq. (7.4) are determined by the forward–backward emission properties of a given source type i:

$$E_i \equiv \frac{\mathrm{Var}\left(\mu_F^{(i)} - \mu_B^{(i)}\right)}{\langle \mu_F^{(i)} + \mu_B^{(i)} \rangle}, \qquad A_i \equiv \langle \mu_F^{(i)} \rangle - \langle \mu_B^{(i)} \rangle,$$

$$\xi_i^{(I)} = \frac{\langle s_i \rangle \langle \mu_F^{(i)} + \mu_B^{(i)} \rangle}{\sum_{k=1}^{N_S} \langle s_k \rangle \langle \mu_F^{(k)} + \mu_B^{(k)} \rangle}, \qquad \xi_i^{(II)} = \frac{A_i^2}{\sum_{k=1}^{N_S} \langle s_k \rangle \langle \mu_F^{(k)} + \mu_B^{(k)} \rangle},$$

$$\xi_{ij}^{(III)} = \frac{A_i A_j}{\sum_{k=1}^{N_S} \langle s_k \rangle \langle \mu_F^{(k)} + \mu_B^{(k)} \rangle}.$$

Equation (7.4) separates the contributions from

- intrinsic stochastic emission (E_i),
- fluctuations of the number of sources ($\mathrm{Var}(s_i)$),
- correlations between source types ($\mathrm{Cov}(s_i, s_j)$).

Alternative formulation via relative source type fluctuations: Using the identity

$$\mathrm{Cov}(s_i, s_j) = \tfrac{1}{2} \left[\mathrm{Var}(s_i) + \mathrm{Var}(s_j) - \mathrm{Var}(s_i - s_j) \right],$$

Eq. (7.4) can be rewritten in a form that explicitly isolates fluctuations of the relative source composition:

$$\Sigma = \sum_{i=1}^{N_S} \xi_i^{(I)} E_i + \sum_{i=1}^{N_S} \left(\xi_i^{(II)} + \sum_{j \neq i} \xi_{ij}^{(III)} \right) \mathrm{Var}(s_i) - \sum_{1 \leq i < j \leq N_S} \xi_{ij}^{(III)} \, \mathrm{Var}(s_i - s_j). \quad (7.5)$$

This reformulation makes explicit the dependence of Σ on *relative* fluctuations of number of different source types, captured by $\mathrm{Var}(s_i - s_j)$.

7.3 Multi-source superposition as a unifying framework for particle production models

The general expression for Σ, Eq. (7.5), provides a common statistical structure in which different particle-production scenarios correspond simply to different choices of source types, their emission profiles, and their fluctuations. In this sense, a broad class of phenomenological approaches can be viewed as specific realisations of the same underlying superposition logic.

Figure 7.2 summarises predictions for the Σ observable for Pb–Pb collisions at $\sqrt{s_{\mathrm{NN}}} = 2.76$ TeV for three phenomenological approaches: The Wounded Nucleon Model [5] and The Single String and The String Fusion Models as described in [110].

All three sets of data points are generated from the same formalism of multi-source superposition, Eq. (7.5), with the only difference underlying in the assumptions about: (i) **number of source types (N_S)**, (ii) **forward-backward emission symmetry ($A_i = \langle\mu_F^{(i)}\rangle - \langle\mu_B^{(i)}\rangle$)** and (iii) **emission fluctuation profiles (E_i)**. The explicit assumptions and numerical values of all these quantities for each of the considered scenarios are listed in Appendix E.

Each model realisation isolates a different fluctuation component of the general expression (7.5):

- **Single String Model:** $N_S = 1$, $A_1 = 0$. Only intrinsic emission fluctuations contribute. This corresponds to the Independent Source Model limit (see Appendix E.1).
- **Wounded Nucleon Model:** $N_S = 2$, $A_1 = -A_2 \neq 0$. The observable is dominated by fluctuations of the relative number of forward- and backward-moving sources, i.e. $\mathrm{Var}(s_1 - s_2)$ (see Appendix E.3).
- **String Fusion Model:** $N_S \approx 200$ (clusters composed of $i = 1, \ldots, 200$ overlapping strings), $A_i = 0$. Several symmetric source classes contribute, so Σ becomes a weighted average of their intrinsic fluctuation terms E_i (see Appendix E.2). The value $N_S \approx 200$ is not a model assumption but the maximal cluster rank that emerges directly from the string-construction procedure described below. In peripheral collisions, only a small subset of these ranks appears.

In both the Single String and String Fusion Models, the construction of particle-emitting sources was performed based on wounded quark coordinates in the transverse plane. A string was formed between two wounded quarks from opposite nuclei (one from the forward-moving nucleus (F) and one from the backward-moving nucleus (B)) whenever their transverse separation satisfied:

$$(x_F - x_B)^2 + (y_F - y_B)^2 < R_{qq}^2 = 0.2 \text{ fm},$$

and the spatial position of the resulting string was defined as the arithmetic mean of their transverse coordinates:

$$x_{\text{string}} = \tfrac{1}{2}(x_F + x_B), \quad y_{\text{string}} = \tfrac{1}{2}(y_F + y_B).$$

In the Single String Model, all such strings were treated as independent and identically

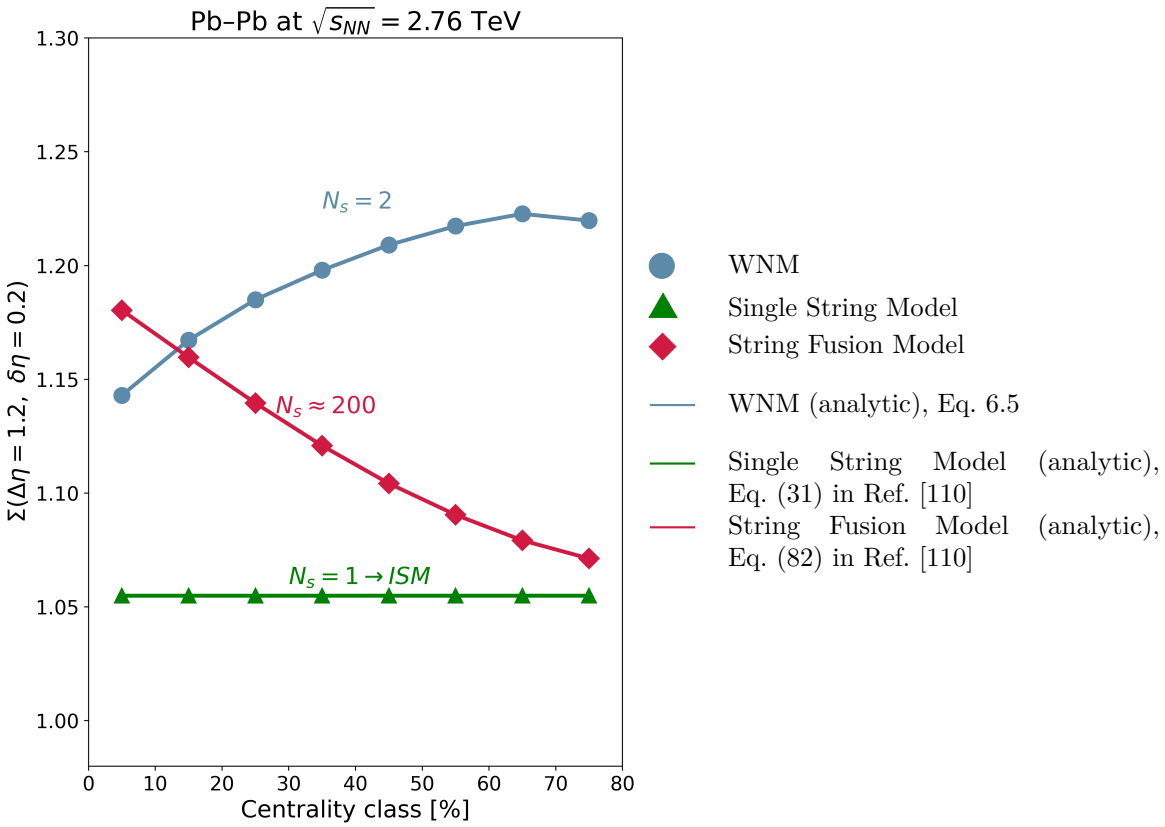

Figure 7.2: Solid markers show the values of Σ obtained from the generalised superposition formula (Eq. (7.5)). For the WNM and for the construction of the string–based source geometry, the positions and numbers of wounded nucleons and wounded quarks are taken from the GLISSANDO simulation [119] of the initial state. The position of wounded quarks was used to determine the distribution of single strings ($N_S = 1$) and fused strings ($N_S > 1$). The emission strengths and correlation functions of the string sources follow the parametrisation of the phenomenological string–fusion model [110] (with numerical values listed in Table E.1), whereas the WNM emission parameters are taken consistently with Chapter 6 and are likewise summarised in Table E.1. Lines correspond to the analytical expressions for each model. All results are shown for $\Delta\eta = 1.2$ and $\delta\eta = 0.2$. The statistical uncertainties of Σ are of the order of 10^{-4} and are therefore not visible in the figure, as they are smaller than the marker size.

emitting sources, with emission parametrised as described in Ref. [110].

In contrast, in the String Fusion Model, the same criterion $R_{qq} = 0.2$ fm was used to generate the initial set of strings, but strings located within a distance $R_{\text{string}} = 0.5$ fm were grouped into spatial clusters representing fused sources. Each such cluster is treated as a single effective particle-emitting source. The effective multiplicity from a cluster composed of i overlapping strings was scaled as $\sqrt{i}$,

following the parametrisation introduced in Ref. [110]. This scaling reflects the reduced emission efficiency in regions of overlapping colour fields and provides a consistent effective treatment of fused emitters as composite sources of rank i.

The three scenarios were selected to lead to distinctly different centrality trends of Σ, as seen in Figure 7.2. In reality, particle production is likely governed by a combination of overlapping processes rather than a single dominant mechanism. This means that observed trends in Σ, such as its centrality dependence, may emerge as a net result of multiple fluctuation components, each associated with different source types. Disentangling these contributions remains a key challenge and may require selecting kinematic regions or particle species that enhance sensitivity to specific underlying mechanisms. Nevertheless, the general superposition framework introduced in this chapter may provide insight into this problem.

7.4 Limitations and broader implications

The multi-source superposition framework is a purely statistical construction. As a consequence, it does not include any dynamical interactions such as colour reconnection, string repulsion, or collective medium effects, all of which could introduce correlations beyond those contained in Eq. (7.5). If such interactions are present, the clean decomposition of Σ into emission-, number-, and source-type-fluctuation terms may no longer hold.

A further simplification is the assumption that each source type has an emission profile that does not change with centrality. Instead of modelling gradual modifications of a single source, the framework absorbs such effects through additional effective source types (e.g. different ranks of fused strings), which preserves analytical simplicity.

The results presented here apply to symmetric systems with symmetric forward-backward acceptances. Although the formalism can be generalised to asymmetric cases, additional terms appear and the decomposition becomes less transparent.

Despite these limitations, the framework might be valuable because it provides a controlled statistical baseline: it allows one to determine whether the observed behaviour of Σ can be explained by independent superposition alone.

The analysis based on the observable Σ is not restricted to forward–backward correlations. The same formalism can be applied to any pair of particle classes (e.g. particle/antiparticle, positive/negative charge, or net-conserved-charge fluctuations) by interpreting the source asymmetry $A_i \equiv \langle \mu_X^{(i)} \rangle - \langle \mu_{\bar{X}}^{(i)} \rangle$ (with $X/\bar{X}$ denoting, e.g., par-

ticle/antiparticle or positive/negative charge) in a more general sense. In particular, Eq. (3.51) shows that Σ coincides with the ratio of cumulants $\kappa_2(X-\bar{X})/\kappa_1(X+\bar{X})$, implying that observables often assumed to be volume-independent may still retain sensitivity to changes in the underlying source composition. Thus, a non-trivial centrality dependence does not by itself signal dynamical effects, and clarifying the role of source-composition fluctuations in such cumulant ratios represents a promising direction for future investigation.

7.5 Synthesis of results

The multi-source superposition framework provides a unified statistical description of Σ that extends both the Independent Source Model and the two-component wounded constituent approach. The general expression derived here separates the observable into three fluctuation components and allows diverse particle-production models to be mapped onto common structural elements. Single-source scenarios reduce to pure emission fluctuations; string-fusion realisations correspond to weighted combinations of multiple symmetric source types; and wounded-type models are driven by relative source-type fluctuations. These mechanisms naturally generate the distinct centrality trends seen in Fig. 7.2.

Although not a dynamical model, the framework serves as a diagnostic tool for identifying which fluctuation components dominate in different systems. Its next natural test is a more detailed confrontation with Glauber-like Monte Carlo generators, such as GLISSANDO [119, 124, 125] and MC PHOBOS [126], where different source-type structures can be implemented and systematically examined. A first comparison using GLISSANDO has already been performed in this work, demonstrating the feasibility of such a detailed source-level analysis.

Chapter 8

Conclusions and Summary

The objective of this thesis was to examine **the forward-backward correlations and multiplicity fluctuations** in heavy-ion collisions using the **Σ** observable. The specific aim of the present study was to determine what physical information the Σ variable carries, whether it is relevant to **the early-stage dynamics** of the collision, and what its advantages and limitations are compared to other fluctuation and correlation measures used in modern relativistic nuclear collision physics.

As a starting point, the Σ quantity was positioned within a broader context of observables related to correlations and fluctuations. This allowed for a better understanding of **the statistical and physical significance** of Σ and highlighting its connections with more widely recognised observables.

One of the main achievements of this work is **the first experimental** determination of the value of Σ at LHC energies in heavy-ion collisions (Pb–Pb and Xe–Xe) in the ALICE experiment.

In addition, the available results for proton-proton collisions enabled a direct comparison of the dependence of Σ on centrality (in heavy-ion systems) with its dependence on multiplicity class in pp reactions. This comparison revealed clear differences in the observed trends and poses a serious challenge to existing phenomenological models. At the same time, it motivated a deeper theoretical interpretation of Σ, initially within the framework of a two-component wounded nucleon model, and later through a generalised multi-source superposition framework.

Detailed numerical results, data, and figures were discussed in the conclusions of each chapter. The following points summarise the common properties of the Σ observable seen in experimental results, and provide its phenomenological interpretation. This overview presents a subjective selection of results which, in the author's opinion, contribute most to a deeper understanding of the Σ variable and the information it provides on the physics of forward-backward correlations and the

mechanism of particle production in ultrarelativistic collisions.

(1) Experimental results for Pb–Pb and Xe–Xe show that Σ does not depend on the method of centrality selection or contribution from volume fluctuations. This is a valuable feature, as it implies that the results obtained with this observable are closer to genuine dynamical phenomena. Also, it allows comparisons across different energies, centrality classes, and experiments. Although this robustness was initially attributed to the strongly intensive character of Σ, further analysis within the wounded constituent model showed that it arises from the statistical properties of this variable and specific relations between particle-emitting sources.

(2) In all systems, an increase in Σ is observed with growing separation $\Delta\eta$ between forward and backward pseudorapidity intervals. This effect has often been interpreted as a suppression of short-range correlations at large distances.

(3a) Σ shows a clear centrality dependence: it increases with centrality percentile in Pb–Pb and Xe–Xe, but decreases with multiplicity in pp collisions. This behaviour indicates that Σ is sensitive to system size and thus cannot be considered a strongly intensive quantity. This interpretation is supported by results obtained within the wounded constituent model, the string fusion model, and the generalised multi-source framework.

(3b) The observed dependence of Σ on centrality also reveals the limitations of more sophisticated models. HIJING, AMPT, and EPOS-LHC all fail to provide a consistent description of Σ across heavy-ion collisions measured by ALICE. Wounded nucleon and wounded quark models reproduce the trend in Pb–Pb and Xe–Xe, but not in pp collisions. In contrast, string-based models correctly describe the pp trends.

The multi-source superposition approach, which accounts for fluctuations in the number and type of emission sources with different particle-emission profiles, suggests that the observed change in the behaviour of Σ might arise from a transition between different dominant fluctuation mechanisms in small and large systems.

(4) In symmetric collisions, the observable Σ is sensitive to asymmetries present in the system, both in particle emission and in the distribution of sources between forward and backward hemispheres. This connection, regardless

of the specific dynamical model, follows directly from the definition of Σ, which by construction is linked exclusively to odd Chebyshev coefficients in the longitudinal-correlation expansion. It also emerges naturally in both the wounded constituent model and the generalised multi-source framework.

(5) First predictions for p–Pb systems within the wounded nucleon and quark models indicate that both Σ and Δ depend on the centrality estimator, bin width, and centrality class. These effects require experimental verification and may provide deeper insight into the properties of the system created in these collisions.

(6) The implications of the multi-source superposition approach can be extended to other observables, such as net-particle fluctuations. The centrality dependence of these quantities may also arise from fluctuations and correlations between different source types and from emission-related effects, rather than from other dynamics-linked factors.

This work presents an example of a close integration between experimental data analysis and the development of suitable interpretative tools, enabling the testing of physical models across a broad range of collision systems. The observable Σ, introduced in the context of forward-backward correlations, has proven to be not only a stable and comparable quantity but also a sensitive indicator of the structural properties of particle emission sources.

Acknowledgements

My deepest gratitude goes to Prof. Andrzej Rybicki, who has supported me at every stage of my scientific career. His encouragement, invaluable advice, and remarkable patience have greatly shaped my development as a scientist. I feel privileged to collaborate with him and to share not only professional work but also warm and inspiring discussions with such a genuinely kind spirit. I also appreciate his excellent taste in books, many of which he recommended to me, as usual, with spoilers included.

I am deeply indebted to Prof. Adam Bzdak for inspiring me to study Σ within the wounded nucleon model and for the many valuable discussions we have shared, as well as for his critical comments and insightful advice, especially regarding the theoretical interpretation of experimental results. I also owe much to Prof. Wojciech Broniowski, whose numerous discussions on the methodology of correlations and fluctuations, as well as his introduction of me to the subject of partial correlations, have provided important guidance. His thoughtful remarks have been of great value for the advancement of my research.

I am equally grateful to Prof. Marek Kowalski, the leader of our group, who has always believed in me and supported the development of my scientific career. I greatly appreciate his broad curiosity about the scientific world beyond physics and the many engaging discussions we have shared, which have been both inspiring and a refreshing break from my own field.

Special thanks go to Prof. Jacek Otwinowski, from whom I have learned so much about the ALICE detector and the work within the Collaboration. I am also deeply thankful to Prof. Adam Matyja, my office mate, always ready to share his vast knowledge and whose positive and kind attitude I value greatly. I would further like to thank my colleagues from the NZ23 department — Dr Nikolaos Davis, Dr Sándor Lökös, Dr Antoni Marcinek, Dr Vitalii Ozvenchuk, and Dr Sahil Upadhyaya — for their constant support and for creating such a fantastic and friendly team to work with. I am also sincerely grateful to Prof. Mariola Kłusek-Gawenda for her continuous support, motivation, and inspiration, which have accompanied me

throughout this work.

I wish to thank the ALICE Collaboration for providing the data that made this work possible. I am also very grateful to all its members for the inspiring atmosphere of cooperation, the pleasure of working together, and the help I have received. In particular, I would like to thank Dr Igor Altsybeev and Dr Mesut Arslandok for their invaluable comments and guidance regarding the experimental analysis.

Finally, my deepest gratitude goes to my family for giving me the chance to pursue what I truly love and for their constant support of my choices. I am especially thankful to Harsh for his love, patience, and for the countless discussions on every possible topic, which continue to enrich both my life and my work. I also warmly thank my Indian family for welcoming me so kindly as one of their own. Last but not least, I wish to thank my cat Freddie, also known as Fredzio, for always reminding me when it was the right time to take a break from work.

This work was supported by the Polish National Science Centre (NCN), grant no. 2021/43/D/ST2/02195.

Bibliography

[1] M. Bluhm *et al.* *"Dynamics of critical fluctuations: Theory – phenomenology – heavy-ion collisions"*. *Nucl. Phys. A*, 1003:122016, 2020. doi: 10.1016/j.nuclphysa.2020.122016.

[2] N. Armesto, L. McLerran, and C. Pajares. *"Long Range Forward-Backward Correlations and the Color Glass Condensate"*. *Nucl. Phys. A*, 781:201–208, 2007. doi: 10.1016/j.nuclphysa.2006.10.074.

[3] M. I. Gorenstein and M. Gaździcki. *"Strongly Intensive Quantities"*. *Phys. Rev. C*, 84:014904, 2011. doi: 10.1103/PhysRevC.84.014904.

[4] ALICE Collaboration. *"ALICE Institutes"*, 2024. URL https://alice-collaboration.web.cern.ch/collaboration/alice_institute. Accessed: 2025-07-07.

[5] I. Sputowska. *"Forward-backward correlations with the Σ quantity in the wounded-constituent framework at energies available at the CERN Large Hadron Collider"*. *Phys. Rev. C*, 108:014903, 2023. doi: 10.1103/PhysRevC.108.014903.

[6] M. L. Miller *et al.* *"Glauber modeling in high energy nuclear collisions"*. *Ann. Rev. Nucl. Part. Sci.*, 57:205–243, 2007. doi: 10.1146/annurev.nucl.57.090506.123020.

[7] W. Busza, K. Rajagopal, and W. van der Schee. *"Heavy Ion Collisions: The Big Picture, and the Big Questions"*. *Ann. Rev. Nucl. Part. Sci.*, 68:339–376, 2018. doi: 10.1146/annurev-nucl-101917-020852.

[8] W. Kittel and E. A. De Wolf. *Soft multihadron dynamics*. World Scientific, 2005. ISBN 978-981-256-295-1.

[9] A. Białas, M. Bleszyński, and W. Czyż. *"Multiplicity Distributions in Nucleus-Nucleus Collisions at High-Energies"*. *Nucl. Phys. B*, 111:461–476, 1976. doi: 10.1016/0550-3213(76)90329-1.

[10] S. Basu *et al.* *"Multiplicity and pseudorapidity density distributions of charged particles produced in pp, pA and AA collisions at RHIC & LHC energies"*. *J. Phys. G*, 48(2):025103, 2020. doi: 10.1088/1361-6471/abc05c.

[11] J. F. Grosse-Oetringhaus and K. Reygers. *"Charged-Particle Multiplicity in Proton-Proton Collisions"*. *J. Phys. G*, 37:083001, 2010. doi: 10.1088/0954-3899/37/8/083001.

[12] Z. Koba, H. B. Nielsen, and P. Olesen. *"Scaling of multiplicity distributions in high-energy hadron collisions"*. *Nucl. Phys. B*, 40:317–334, 1972. doi: 10.1016/0550-3213(72)90551-2.

[13] W. Thome *et al.* (Aachen-CERN-Heidelberg-Munich Collaboration). *"Charged Particle Multiplicity Distributions in pp Collisions at ISR Energies"*. *Nucl. Phys. B*, 129:365, 1977. doi: 10.1016/0550-3213(77)90122-5.

[14] P. Ghosh. *"Negative binomial multiplicity distribution in proton-proton collisions in limited pseudorapidity intervals at LHC up to $\sqrt{s} = 7$ TeV and the clan model"*. *Phys. Rev. D*, 85:054017, 2012. doi: 10.1103/PhysRevD.85.054017.

[15] C. A. Pruneau. *Data Analysis Techniques for Physical Scientists*. Cambridge University Press, Cambridge, 2017.

[16] C. Pruneau, S. Gavin, and S. Voloshin. *"Methods for the study of particle production fluctuations"*. *Phys. Rev. C*, 66:044904, 2002. doi: 10.1103/PhysRevC.66.044904.

[17] Y. Zhou. *"Review of anisotropic flow correlations in ultrarelativistic heavy-ion collisions"*. *Adv. High Energy Phys.*, 2016:9365637, 2016. doi: 10.1155/2016/9365637.

[18] A. Bzdak and D. Teaney. *"Longitudinal fluctuations of the fireball density in heavy-ion collisions"*. *Phys. Rev. C*, 87(2):024906, 2013. doi: 10.1103/PhysRevC.87.024906.

[19] M. Aaboud *et al.* (ATLAS Collaboration). *"Measurement of forward-backward multiplicity correlations in lead-lead, proton-lead, and proton-proton collisions with the ATLAS detector"*. *Phys. Rev. C*, 95(6):064914, 2017. doi: 10.1103/PhysRevC.95.064914.

[20] G. Aad *et al.* (ATLAS Collaboration). *"Forward-backward correlations and charged-particle azimuthal distributions in pp interactions using the ATLAS detector"*. *JHEP*, 07:019, 2012. doi: 10.1007/JHEP07(2012)019.

[21] ATLAS Collaboration. *"Measurement of two–particle correlations in s = 13 TeV proton–proton collisions at the LHC with the ATLAS detector"*. Technical report, CERN, Geneva, 2015. URL https://cds.cern.ch/record/2037663.

[22] J. Adam *et al.* (ALICE Collaboration). *"Insight into particle production mechanisms via angular correlations of identified particles in pp collisions at $\sqrt{s}$ = 7 TeV"*. *Eur. Phys. J. C*, 77(8):569, 2017. doi: 10.1140/epjc/s10052-017-5129-6. [Erratum: Eur.Phys.J.C 79, 998 (2019)].

[23] S. A. Bass, P. Danielewicz, and S. Pratt. *"Clocking hadronization in relativistic heavy ion collisions with balance functions"*. *Phys. Rev. Lett.*, 85:2689–2692, 2000. doi: 10.1103/PhysRevLett.85.2689.

[24] S. Jeon and S. Pratt. *"Balance functions, correlations, charge fluctuations and interferometry"*. *Phys. Rev. C*, 65:044902, 2002. doi: 10.1103/PhysRevC.65.044902.

[25] B. Abelev *et al.* (ALICE Collaboration). *"Net-Charge Fluctuations in Pb-Pb collisions at $\sqrt{s_{\rm NN}}$= 2.76 TeV"*. *Phys. Rev. Lett.*, 110(15):152301, 2013. doi: 10.1103/PhysRevLett.110.152301.

[26] S. Acharya *et al.* (ALICE Collaboration). *"General balance functions of identified charged hadron pairs of (π,K,p) in Pb–Pb collisions at $\sqrt{s_{\rm NN}}$= 2.76 TeV"*. *Phys. Lett. B*, 833:137338, 2022. doi: 10.1016/j.physletb.2022.137338.

[27] C. Pruneau *et al.* *"Accounting for nonvanishing net-charge with unified balance functions"*. *Phys. Rev. C*, 107(1):014902, 2023. doi: 10.1103/PhysRevC.107.014902.

[28] A. Bzdak, V. Koch, and N. Strodthoff. *"Cumulants and correlation functions versus the QCD phase diagram"*. *Phys. Rev. C*, 95(5):054906, 2017. doi: 10.1103/PhysRevC.95.054906.

[29] M. Asakawa and M. Kitazawa. *"Fluctuations of conserved charges in relativistic heavy ion collisions: An introduction"*. *Prog. Part. Nucl. Phys.*, 90:299–342, 2016. doi: 10.1016/j.ppnp.2016.04.002.

[30] M. Kitazawa and X. Luo. *"Properties and uses of factorial cumulants in relativistic heavy-ion collisions"*. *Phys. Rev. C*, 96(2):024910, 2017. doi: 10.1103/PhysRevC.96.024910.

[31] W. Broniowski and A. Olszewski. *"Statistical moments in superposition models and strongly intensive measures"*. *Phys. Rev. C*, 95(6):064910, 2017. doi: 10.1103/PhysRevC.95.064910.

[32] B. E. Aboona *et al.* (STAR Collaboration). *"Precision Measurement of Net-Proton-Number Fluctuations in Au+Au Collisions at RHIC"*. *Phys. Rev. Lett.*, 135(14):142301, 2025. doi: 10.1103/9l69-2d7p.

[33] H. Adhikary *et al.* (SHINE Collaboration). *"Measurements of higher-order cumulants of multiplicity and net-electric charge distributions in inelastic proton-proton interactions by NA61/SHINE"*. *Eur. Phys. J. C*, 84:921, 2024. doi: 10.1140/epjc/s10052-024-13076-y. [Erratum: Eur.Phys.J.C 85, 341 (2025)].

[34] A. Bzdak *et al.* *"Mapping the Phases of Quantum Chromodynamics with Beam Energy Scan"*. *Phys. Rept.*, 853:1–87, 2020. doi: 10.1016/j.physrep.2020.01.005.

[35] V. Vovchenko *et al.* *"Connecting fluctuation measurements in heavy-ion collisions with the grand-canonical susceptibilities"*. *Phys. Lett. B*, 811:135868, 2020. doi: 10.1016/j.physletb.2020.135868.

[36] S. Ejiri, F. Karsch, and K. Redlich. *"Hadronic fluctuations at the QCD phase transition"*. *Phys. Lett. B*, 633:275–282, 2006. doi: 10.1016/j.physletb.2005.11.083.

[37] A. Bialas and V. Koch. *"Event by event fluctuations and inclusive distribution"*. *Phys. Lett. B*, 456:1–4, 1999. doi: 10.1016/S0370-2693(99)00479-7.

[38] A. Capella and J. T. Thanh Van. *"Long-range rapidity correlations in hadron-nucleus interactions"*. *Phys. Rev. D*, 29:2512–2516, Jun 1984. doi: 10.1103/PhysRevD.29.2512. URL https://link.aps.org/doi/10.1103/PhysRevD.29.2512.

[39] C. Pajares. *"Long range correlations, event simulation and parton percolation"*. *Nucl. Phys. A*, 854:125–130, 2011. doi: 10.1016/j.nuclphysa.2010.06.008.

[40] A. Bzdak. *"Forward-backward multiplicity correlations in the wounded nucleon model"*. *Phys. Rev. C*, 80:024906, 2009. doi: 10.1103/PhysRevC.80.024906.

[41] V. V. Vechernin. *"Forward–backward correlations between multiplicities in windows separated in azimuth and rapidity". Nucl. Phys. A*, 939:21–45, 2015. doi: 10.1016/j.nuclphysa.2015.03.009.

[42] J. Adam *et al.* (ALICE Collaboration). *"Forward-backward multiplicity correlations in pp collisions at $\sqrt{s}$ = 0.9, 2.76 and 7 TeV". JHEP*, 05:097, 2015. doi: 10.1007/JHEP05(2015)097.

[43] W. Braunschweig *et al.* *"Charged multiplicity distributions and correlations in e^+e^- annihilation at PETRA energies". Z. Phys. C - Particles and Fields*, 45: 193–208, 1989. doi: 10.1007/BF01674450.

[44] L. Rangan *et al.* (HRS Collaboration). *"Charged particle multiplicity distributions in e + e annihilation at 29 GeV: a comparison with hadronic data". Zeitschrift für Physik C*, 35, 1987. doi: 10.1007/BF01570767.

[45] R. Akers *et al.* (OPAL Collaboration). *"Multiplicity and transverse momentum correlations in multi - hadronic final states in e+ e- interactions at $\sqrt{s}$ = 91.2-GeV". Phys. Lett. B*, 320:417–430, 1994. doi: 10.1016/0370-2693(94)90680-7.

[46] M. Arneodo *et al.* (European Muon Collaboration). *"Multiplicities of charged hadrons in 280 GeV/c muon-proton scattering". Nucl. Phys. B*, 258:249–266, 1985. doi: 10.1016/0550-3213(85)90611-X.

[47] G. T. Jones *et al.* (Birmingham-CERN-Imperial Coll-Munich (MPI)-Oxford-Univ Coll London Collaboration). *"Multiplicity distributions of charged hadrons in neutrino p and anti-neutrino p charged current interactions". Z. Phys. C*, 54:45–54, 1992. doi: 10.1007/BF01881707.

[48] V. V. Aivazyan *et al.* (NA22 Collaboration). *"Forward - Backward Multiplicity Correlations in π^+p, K^+p and pp Collisions at 250-GeV/c". Z. Phys. C*, 42: 533, 1989. doi: 10.1007/BF01557658.

[49] S. Uhlig *et al.* *"Observation of Charged Particle Correlations Between the Forward and Backward Hemispheres in pp Collisions at ISR Energies". Nucl. Phys. B*, 132:15–28, 1978. doi: 10.1016/0550-3213(78)90254-7.

[50] R. E. Ansorge *et al.* (UA5 Collaboration). *"Charged Particle Correlations in $\bar{P}P$ Collisions at c.m. Energies of 200-GeV, 546-GeV and 900-GeV". Z. Phys. C*, 37:191–213, 1988. doi: 10.1007/BF01579906.

[51] T. Alexopoulos *et al.* (E735 Collaboration). *"Charged particle multiplicity correlations in $p\bar{p}$ collisions at $\sqrt{s}$ = 0.3-TeV to 1.8-TeV"*. *Phys. Lett. B*, 353: 155–160, 1995. doi: 10.1016/0370-2693(95)00554-X.

[52] B. I. Abelev *et al.* (STAR Collaboration). *"Growth of Long Range Forward-Backward Multiplicity Correlations with Centrality in Au+Au Collisions at $\sqrt{s_{\rm NN}}$=200 GeV"*. *Phys. Rev. Lett.*, 103:172301, 2009. doi: 10.1103/PhysRevLett.103.172301.

[53] P. L. Jain and G. Das. *"Correlations in multiparticle production"*. *Phys. Rev. D*, 23:2506–2511, Jun 1981. doi: 10.1103/PhysRevD.23.2506. URL https://link.aps.org/doi/10.1103/PhysRevD.23.2506.

[54] G. Singh *et al.* *"Long-range correlations in nucleus–nucleus interactions at ultrahigh energies"*. *Phys. Rev. C*, 39:1835–1839, 1989. doi: 10.1103/PhysRevC.39.1835.

[55] S. Ahmad *et al.* *"Short- and long-range multiplicity correlations in relativistic heavy-ion collisions"*. *International Journal of Modern Physics E*, 22(09): 1350066, 2013. doi: 10.1142/S0218301313500663. URL https://doi.org/10.1142/S0218301313500663.

[56] S. Ahmad *et al.* *"Search for Long-Range Correlations in Relativistic Heavy-Ion Collisions at SPS Energies"*. *Adv. High Energy Phys.*, 2015:615458, 2015. doi: 10.1155/2015/615458.

[57] V. P. Konchakovski *et al.* *"Forward-backward correlations in nucleus-nucleus collisions: baseline contributions from geometrical fluctuations"*. *Phys. Rev. C*, 79:034910, 2009. doi: 10.1103/PhysRevC.79.034910.

[58] I. Sputowska (for the ALICE Collaboration). *"Forward-Backward Correlations and Multiplicity Fluctuations in Pb–Pb Collisions at $\sqrt{s_{NN}}$ = 2.76 TeV from ALICE at the LHC"*. *MDPI Proc.*, 10(1):14, 2019. doi: 10.3390/proceedings2019010014.

[59] S. De *et al.* *"Method for the Analysis of Forward-Backward Multiplicity Correlations in Heavy-Ion Collisions"*. *Phys. Rev. C*, 88(4):044903, 2013. doi: 10.1103/PhysRevC.88.044903.

[60] A. Olszewski and W. Broniowski. *"Partial correlation analysis method in ultra-relativistic heavy-ion collisions"*. *Phys. Rev. C*, 96(5):054903, 2017. doi: 10.1103/PhysRevC.96.054903.

[61] W. Broniowski and A. Olszewski. *"Partial correlation analysis in ultra-relativistic nuclear collisions"*. In *13th Workshop on Particle Correlations and Femtoscopy (WPCF 2018)*, Kraków, Poland, 2018.

[62] *"ALICE/NA61/SPbSU Seminar: Discussion of the report by I. Sputowska, "Strongly intensive quantities and partial correlations""*. Online seminar (Zoom), September 2020. URL https://indico.cern.ch/event/959715/.

[63] P. C. Riedi. *Thermal Physics: An Introduction to Thermodynamics, Statistical Mechanics and Kinetic Theory*. The Macmillan Press Ltd, London, 1976. ISBN 978-0-333-18397-7. doi: 10.1007/978-1-349-15669-6.

[64] J. Cleymans *et al.* *"Statistical model predictions for particle ratios at* $\sqrt{s_{\mathrm{NN}}} = 5.5$ *TeV"*. *Phys. Rev. C*, 74:034903, 2006. doi: 10.1103/PhysRevC.74.034903.

[65] A. Andronic *et al.* *"Decoding the phase structure of QCD via particle production at high energy"*. *Nature*, 561(7723):321–330, 2018. doi: 10.1038/s41586-018-0491-6.

[66] S. Acharya *et al.* (ALICE Collaboration). *"Measurements of Chemical Potentials in Pb-Pb Collisions at* $\sqrt{s_{\mathrm{NN}}} = 5.02\ TeV''$. Phys. Rev. Lett., 133(9) : 092301, 2024. *doi* : .

[67] M. Gaździcki, M. I. Gorenstein, and M. Mackowiak-Pawlowska. *"Normalization of strongly intensive quantities"*. *Phys. Rev. C*, 88(2):024907, 2013. doi: 10.1103/PhysRevC.88.024907.

[68] E. Sangaline. *"Strongly Intensive Cumulants: Fluctuation Measures for Systems With Incompletely Constrained Volumes"*. 2015. arXiv:1505.00261 [nucl-th].

[69] M. Gaździcki and S. Mrówczyński. *"A method to study "equilibration" in nucleus–nucleus collisions"*. *Z. Phys. C*, 54:127–132, 1992. doi: 10.1007/BF01555746.

[70] M. Gaździcki. *"A Method to study chemical equilibration in nucleus-nucleus collisions"*. *Eur. Phys. J. C*, 8:131–133, 1999. doi: 10.1007/s100529901070.

[71] S. Mrówczyński. *"Generalizing Phi measure of event-by-event fluctuations in high-energy heavy ion collisions"*. *Phys. Lett. B*, 465:8–14, 1999. doi: 10.1016/S0370-2693(99)01057-6.

[72] R. Quishpe Quishpe. *Longitudinal Fluctuations in Relativistic Heavy Ion Collisions*. PhD thesis, University of Houston, 2022. CERN-THESIS-2022-145.

[73] P. Steinberg *et al.* (PHOBOS Collaboration). *"Forward-backward multiplicity correlations in* $\sqrt{s_{\mathrm{NN}}} = 200$ *GeV Au + Au collisions"*. *Nucl. Phys. A*, 774: 631–634, 2006. doi: 10.1016/j.nuclphysa.2006.06.102.

[74] A. Bzdak and K. Wozniak. *"Forward-backward multiplicity fluctuations in heavy nuclei collisions in the wounded nucleon model"*. *Phys. Rev. C*, 81:034908, 2010. doi: 10.1103/PhysRevC.81.034908.

[75] ALICE Collaboration. *"ALICE Reports Collection"*. URL https://cds.cern.ch/collection/ALICE%20Reports. CERN Document Server.

[76] B. Abelev *et al.* (ALICE Collaboration). *"Long-range angular correlations on the near and away side in p-Pb collisions at* $\sqrt{s_{NN}} = 5.02$ *TeV"*. *Phys. Lett. B*, 719:29–41, 2013. doi: 10.1016/j.physletb.2013.01.012.

[77] S. Acharya *et al.* (ALICE Collaboration). *"Emergence of Long-Range Angular Correlations in Low-Multiplicity Proton-Proton Collisions"*. *Phys. Rev. Lett.*, 132(17):172302, 2024. doi: 10.1103/PhysRevLett.132.172302.

[78] S. Acharya *et al.* (ALICE Collaboration). *"The ALICE experiment: a journey through QCD"*. *Eur. Phys. J. C*, 84(8):813, 2024. doi: 10.1140/epjc/s10052-024-12935-y.

[79] B. B. Abelev *et al.* (ALICE Collaboration). *"Performance of the ALICE Experiment at the CERN LHC"*. *Int. J. Mod. Phys. A*, 29:1430044, 2014. doi: 10.1142/S0217751X14300440.

[80] ALICE Collaboration. *"3D ALICE Schematic RUN2 - with Description"*, 2017. URL https://alice-figure.web.cern.ch/node/11218.

[81] K. Aamodt *et al.* (ALICE Collaboration). *"Alignment of the ALICE Inner Tracking System with cosmic-ray tracks"*. *JINST*, 5:P03003, 2010. doi: 10.1088/1748-0221/5/03/P03003.

[82] J. Alme *et al.* *"The ALICE TPC, a large 3-dimensional tracking device with fast readout for ultra-high multiplicity events"*. *Nucl. Instrum. Meth. A*, 622: 316–367, 2010. doi: 10.1016/j.nima.2010.04.042.

[83] S. Acharya *et al.* (ALICE Collaboration). *"The ALICE Transition Radiation Detector: construction, operation, and performance"*. *Nucl. Instrum. Meth. A*, 881:88–127, 2018. doi: 10.1016/j.nima.2017.09.028.

[84] A. Akindinov *et al.* *"Performance of the ALICE Time-Of-Flight detector at the LHC"*. *Eur. Phys. J. Plus*, 128:44, 2013. doi: 10.1140/epjp/i2013-13044-x.

[85] G. Dellacasa *et al.* (ALICE Collaboration). *"ALICE technical design report of the photon spectrometer (PHOS)"*. Technical Report CERN-LHCC-99-004, CERN, Geneva, March 1999.

[86] U. Abeysekara *et al.* (ALICE Collaboration). *"ALICE EMCal Physics Performance Report"*, August 2010. URL https://cds.cern.ch/record/1283026.

[87] S. Beole *et al.* (ALICE Collaboration). *"ALICE technical design report: Detector for high momentum PID (HMPID)"*. Technical Report CERN-LHCC-98-19, CERN, Geneva, August 1998.

[88] E. Abbas *et al.* (ALICE Collaboration). *"Performance of the ALICE VZERO system"*. *JINST*, 8:P10016, 2013. doi: 10.1088/1748-0221/8/10/P10016.

[89] ALICE Collaboration. *"ALICE technical design report on forward detectors: FMD, T0 and V0"*. Technical Report CERN-LHCC-2004-025, CERN, Geneva, September 2004.

[90] A. Villatoro Tello (for the ALICE Collaboration). *"AD, the ALICE diffractive detector"*. *AIP Conf. Proc.*, 1819(1):040020, 2017. doi: 10.1063/1.4977150.

[91] ALICE Collaboration. *"ALICE Technical Design Report of the Dimuon Forward Spectrometer"*. Technical Report CERN-LHCC-99-22, CERN, August 1999.

[92] ALICE DPG. *"DPG Analysis Tutorial – Physics selection with AODs"*. Presentation, Indico, CERN, November 2017. URL https://indico.cern.ch/event/666222/contributions/2768780/attachments/1551303/2437229/DPG_AnalysisTutorial_20171102.pdf.

[93] ALICE Collaboration. *"Centrality determination in heavy ion collisions"*. Technical Report ALICE-PUBLIC-2018-011, ALICE Collaboration, Geneva, 2018. URL https://cds.cern.ch/record/2636623.

[94] ALICE Collaboration. *"Centrality determination using the Glauber model in Xe-Xe collisions at $\sqrt{s_{\mathrm{NN}}} = 5.44$ TeV"*. Technical Report ALICE-PUBLIC-2018-003, ALICE Collaboration, Geneva, 2018. URL https://cds.cern.ch/record/2315401.

[95] ALICE Collaboration. *"The ALICE definition of primary particles"*. Technical Report ALICE-PUBLIC-2017-005, ALICE Collaboration, Geneva, 2017. URL https://cds.cern.ch/record/2270008.

[96] A. Bzdak and V. Koch. *"Local Efficiency Corrections to Higher Order Cumulants"*. *Phys. Rev. C*, 91(2):027901, 2015. doi: 10.1103/PhysRevC.91.027901.

[97] G. W. Oehlert. *"A Note on the Delta Method"*. *The American Statistician*, 46(1):27–29, 1992. doi: 10.2307/2684406. URL https://www.jstor.org/stable/2684406.

[98] B. Efron. *"Bootstrap Methods: Another Look at the Jackknife"*. *Annals Statist.*, 7(1):1–26, 1979. doi: 10.1214/aos/1176344552.

[99] R. Barlow. *"Systematic errors: Facts and fictions"*. In *Conference on Advanced Statistical Techniques in Particle Physics*, pages 134–144, 7 2002.

[100] X.-N. Wang and M. Gyulassy. *"HIJING: A Monte Carlo model for multiple jet production in p p, p A and A A collisions"*. *Phys. Rev. D*, 44:3501–3516, 1991. doi: 10.1103/PhysRevD.44.3501.

[101] T. Pierog *et al.* *"EPOS LHC: Test of collective hadronization with data measured at the CERN Large Hadron Collider"*. *Phys. Rev. C*, 92(3):034906, 2015. doi: 10.1103/PhysRevC.92.034906.

[102] Z. W. Lin. *"Recent Developments of A Multi-Phase Transport Model"*. *Acta Phys. Polon. Supp.*, 7(1):191–197, 2014. doi: 10.5506/APhysPolBSupp.7.191.

[103] I. Sputowska (for the ALICE Collaboration). *"Event-by-Event correlations and fluctuations with strongly intensive quantities in heavy-ion and pp collisions with ALICE"*. *PoS*, CPOD2021:027, 2022. doi: 10.22323/1.400.0027.

[104] I. Sputowska (for the ALICE Collaboration). *"Event-by-event correlations and fluctuations with strongly intensive quantities in heavy-ion collisions with ALICE"*. *EPJ Web Conf.*, 274:05003, 2022. doi: 10.1051/epjconf/202227405003.

[105] I. Sputowska (for the ALICE Collaboration). *"Forward–backward multiplicity correlations in Pb–Pb and Xe–Xe collisions with strongly intensive quantity Σ"*. ALICE Figure Repository (CERN), 2022. URL https://alice-figure.web.cern.ch/node/21692.

[106] V. Kovalenko. *"Strongly intensive fluctuations and correlations in ultrarelativistic nuclear collisions in the model with string fusion"*. *EPJ Web Conf.*, 204: 03006, 2019. doi: 10.1051/epjconf/201920403006.

[107] A. Erokhin (for the ALICE Collaboration). *"Forward-backward multiplicity correlations with strongly intensive observables in pp collisions"*. In *International Symposium on Multiparticle Dynamics (ISMD 2021)*, Virtual Conference, 10–15 January 2021. URL https://indico.cern.ch/event/854124/contributions/4134683/attachments/2169272/3725102/IS2021_erokhin_strongly.pdf. Presentation at ISMD 2021.

[108] T. Sjöstrand, S. Mrenna, and P. Skands. *"A Brief Introduction to PYTHIA 8.1"*. *Computer Physics Communications*, 178(11):852–867, 2008. doi: 10.1016/j.cpc.2008.01.036.

[109] T. Sjöstrand *et al.* *"An Introduction to PYTHIA 8.2"*. *Computer Physics Communications*, 191:159–177, 2015. doi: 10.1016/j.cpc.2015.01.024.

[110] E. Andronov and V. Vechernin. *"Strongly intensive observable between multiplicities in two acceptance windows in a string model"*. *Eur. Phys. J. A*, 55(1): 14, 2019. doi: 10.1140/epja/i2019-12681-x.

[111] A. Bialas. *"Wounded nucleons, wounded quarks: an update"*. *Journal of Physics G: Nuclear and Particle Physics*, 35(4):044053, mar 2008. doi: 10.1088/0954-3899/35/4/044053.

[112] A. Białas and W. Czyż. *"Wounded nucleon model and Deuteron-Gold collisions at RHIC"*. *Acta Phys. Polon. B*, 36:905–918, 2005.

[113] A. Białas, W. Czyż, and W. Furmański. *"Particle Production in Hadron-Nucleus Collisions and the Quark Model"*. *Acta Phys. Polon. B*, 8:585, 1977.

[114] A. Bialas. *"Wounded Constituents". Acta Phys. Polon. B*, 43:95, 2012. doi: 10.5506/APhysPolB.43.95. [Erratum: Acta Phys.Polon.B 43, 485 (2012)].

[115] A. Bialas and A. Bzdak. *"Wounded quarks and diquarks in high energy collisions". Phys. Rev. C*, 77:034908, 2008. doi: 10.1103/PhysRevC.77.034908.

[116] M. Barej, A. Bzdak, and P. Gutowski. *"Wounded-quark emission function at the top energy available at the BNL Relativistic Heavy Ion Collider". Phys. Rev. C*, 97(3):034901, 2018. doi: 10.1103/PhysRevC.97.034901.

[117] R. Hofstadter, F. Bumiller, and M. R. Yearian. *"Electromagnetic Structure of the Proton and Neutron". Rev. Mod. Phys.*, 30:482–497, Apr 1958. doi: 10.1103/RevModPhys.30.482. URL https://link.aps.org/doi/10.1103/RevModPhys.30.482.

[118] S. S. Adler *et al.* (PHENIX Collaboration). *"Transverse-energy distributions at midrapidity in p+p , d+Au , and Au+Au collisions at* $\sqrt{s_{NN}} = 62.4\breve{}200$ *GeV and implications for particle-production models". Phys. Rev. C*, 89(4):044905, 2014. doi: 10.1103/PhysRevC.89.044905.

[119] P. Bożek *et al. "GLISSANDO 3: GLauber Initial-State Simulation AND mOre..., ver. 3". Comput. Phys. Commun.*, 245:106850, 2019. doi: 10.1016/j.cpc.2019.07.014.

[120] J. Adam *et al.* (ALICE Collaboration). *"Charged-particle multiplicities in proton–proton collisions at* $\sqrt{s} = 0.9$ *to 8 TeV". Eur. Phys. J. C*, 77(1):33, 2017. doi: 10.1140/epjc/s10052-016-4571-1.

[121] W. Broniowski and W. Florkowski. *"Geometric relation between centrality and the impact parameter in relativistic heavy ion collisions". Phys. Rev. C*, 65:024905, 2002. doi: 10.1103/PhysRevC.65.024905.

[122] A. Bzdak. *"Measurement of asymmetric component in proton-proton collisions". Acta Phys. Polon. B*, 41:151, 2010.

[123] J. Adam *et al.* (ALICE Collaboration). *"Centrality dependence of the pseudorapidity density distribution for charged particles in Pb-Pb collisions at* $\sqrt{s_{\rm NN}} = 5.02$ *TeV". Phys. Lett. B*, 772:567–577, 2017. doi: 10.1016/j.physletb.2017.07.017.

[124] W. Broniowski, M. Rybczyński, and P. Bożek. *"GLISSANDO: Glauber initial-state simulation and more..."*. *Comput. Phys. Commun.*, 180:69–83, 2009. doi: 10.1016/j.cpc.2008.07.016.

[125] M. Rybczyński *et al.* *"GLISSANDO 2 : GLauber Initial-State Simulation AND mOre..., ver. 2"*. *Comput. Phys. Commun.*, 185:1759–1772, 2014. doi: 10.1016/j.cpc.2014.02.016.

[126] B. Alver *et al.* *"The PHOBOS Glauber Monte Carlo"*. 2008. arXiv:0805.4411 [nucl-th].

[127] P. Olofsson. *Probability, Statistics, and Stochastic Processes*. John Wiley & Sons, Incorporated, Newark, 2005.

[128] S. M. Ross. *A First Course in Probability*. Pearson Prentice Hall, Upper Saddle River, NJ, 8th edition, 2010. ISBN 978-0-13-603313-4.

Appendix A

Analytical derivation of forward–backward multiplicity correlations using a Chebyshev polynomial expansion

In this appendix, we derive the forward–backward multiplicity correlation measure $\Sigma^{n_F n_B}$ within a framework based on a Chebyshev polynomial expansion of the single-particle pseudorapidity density and the two-particle correlation function in symmetric nucleus–nucleus collisions. The use of Chebyshev polynomials to decompose longitudinal fluctuations was originally proposed by Bzdak and Teaney [18], while the relation to $\Sigma^{n_F n_B}$ is derived here.

A.1 Decomposition in Chebyshev polynomials

The single-particle pseudorapidity density, denoted by $\rho(\eta)$, characterises the longitudinal structure of the fireball. Following Ref. [18], the single-particle rapidity distribution at fixed coefficients $a_0, a_1, \dots$ can be expanded in terms of the orthogonal Chebyshev polynomials of the first kind $T_n(x)$[1] as

$$\rho(\eta; a_0, a_1, \dots) = \rho(\eta) \left[1 + \sum_{i=0}^{\infty} a_i \, T_i\!\left(\frac{\eta}{Y}\right) \right], \tag{A.1}$$

where $\rho(\eta)$ denotes the single-particle pseudorapidity distribution averaged over $a_0, a_1, \dots$ [18]. Here, a_i quantify event-by-event fireball shape fluctuation amplitudes with $\langle a_i \rangle = 0$, and Y sets the longitudinal scale (so that $\eta/Y \in [-1, 1]$).[2]

[1] *Chebyshev polynomials of the first kind* $T_n(x)$: $T_0(x)=1$, $T_1(x)=x$, $T_2(x)=2x^2-1$, $T_3(x)=4x^3-3x$, and $T_n(-x)=(-1)^n T_n(x)$. Orthogonality on $[-1,1]$ holds with weight $(1-x^2)^{-1/2}$: $\int_{-1}^{1} T_i(x) T_k(x) \, [1-x^2]^{-1/2} \, dx = c_i \delta_{ik}$, where $c_0=\pi$ and $c_{i>0}=\pi/2$.

[2] *On* Y: Y is the characteristic (pseudo)rapidity scale, typically taken as about half of the long-range interval over which global fluctuations are analysed. It rescales the argument of $T_n(\eta/Y)$ to the domain $[-1, 1]$. In practice, Y may be chosen as half of the detector acceptance around

Even-indexed polynomials $T_{2n}(x)$ represent symmetric modes with respect to midrapidity, while odd-indexed polynomials $T_{2n+1}(x)$ capture asymmetric modes. The orthogonality of the basis ensures that each term corresponds to an independent component of the fluctuation pattern.

As a reminder, the two-particle density and the corresponding correlation function, introduced earlier in Eq. (3.4), are defined as

$$\rho_2(\eta_1, \eta_2) \equiv \frac{d^2 N_{\mathrm{ch}}}{d\eta_1\, d\eta_2}, \qquad C(\eta_1, \eta_2) \equiv \rho_2(\eta_1, \eta_2) - \rho(\eta_1)\rho(\eta_2), \tag{A.2}$$

If one assumes that long-range two-particle correlations arise solely from the global shape fluctuations encoded in the coefficients a_i, then (see Ref. [18]) the correlation function can be expressed as

$$C(\eta_1, \eta_2) = \frac{dN_{\mathrm{ch}}}{d\eta_1}\,\frac{dN_{\mathrm{ch}}}{d\eta_2}\,\sum_{i,k=0}^{\infty} \langle a_i a_k \rangle\, T_i\!\left(\frac{\eta_1}{Y}\right)\, T_k\!\left(\frac{\eta_2}{Y}\right), \tag{A.3}$$

where $\langle a_i a_k \rangle$ are event-averaged products of the coefficients a_i and a_k.

A.2 Strongly intensive quantity $\Sigma^{n_F n_B}$ in symmetric nucleus–nucleus collisions

Further calculations focus on symmetric nucleus–nucleus collisions, with the forward ($F = [\eta_F,\, \eta_F + \delta\eta]$) and backward ($B = [-\eta_F - \delta\eta,\, -\eta_F]$) intervals of width $\delta\eta$ arranged symmetrically around midrapidity ($\eta = 0$). Under this condition, it is straightforward, as will be shown below, to express the forward–backward measure $\Sigma^{n_F n_B}$ in terms of the Chebyshev-mode expansion introduced above.
For symmetric collisions, $\Sigma^{n_F n_B}$ can be expressed by Eq. (3.55), namely:

$$\Sigma^{n_F n_B} \;=\; \frac{\mathrm{Var}(n_F - n_B)}{2\,\langle n_F \rangle}\,. \tag{A.4}$$

To evaluate this expression within the Chebyshev framework, one rewrites it in terms of the two-particle correlation function $C(\eta_1, \eta_2)$, and subsequently expand it using Eq. (A.3). Based on Eq. (3.13) the forward variance can be

midrapidity, or as a physics-motivated long-range scale (see also [18]).

expressed as:

$$\begin{aligned}\mathrm{Var}(n_F) &= \langle n_F\rangle + \int_F d\eta_1 \int_F d\eta_2\, C(\eta_1,\eta_2) \\ &= \langle n_F\rangle + \int_{\eta_F}^{\eta_F+\delta\eta} d\eta_1 \int_{\eta_F}^{\eta_F+\delta\eta} d\eta_2\ \rho(\eta_1)\rho(\eta_2) \sum_{i,k}\langle a_i a_k\rangle T_i\Big(\tfrac{\eta_1}{Y}\Big)\, T_k\Big(\tfrac{\eta_2}{Y}\Big)\,.\end{aligned} \tag{A.5}$$

Analogously, the backward takes the form:

$$\begin{aligned}\mathrm{Var}(n_B) &= \langle n_B\rangle + \int_B d\eta_1 \int_B d\eta_2\, C(\eta_1,\eta_2) \\ &= \langle n_B\rangle + \int_{-\eta_F-\delta\eta}^{-\eta_F} d\eta_1 \int_{-\eta_F-\delta\eta}^{-\eta_F} d\eta_2\ \rho(\eta_1)\rho(\eta_2) \sum_{i,k}\langle a_i a_k\rangle\, T_i\Big(\tfrac{\eta_1}{Y}\Big)\, T_k\Big(\tfrac{\eta_2}{Y}\Big)\,.\end{aligned} \tag{A.6}$$

Now, changing variables $\eta \to -\eta$ maps the integration limits $[-\eta_F - \delta\eta,\, -\eta_F]$ onto $[\eta_F,\, \eta_F + \delta\eta]$, giving

$$\mathrm{Var}(n_B) = \langle n_B\rangle + \int_{\eta_F}^{\eta_F+\delta\eta} d\eta_1 \int_{\eta_F}^{\eta_F+\delta\eta} d\eta_2\ \rho(-\eta_1)\rho(-\eta_2) \sum_{i,k}\langle a_i a_k\rangle\, T_i\Big(-\tfrac{\eta_1}{Y}\Big)\, T_k\Big(-\tfrac{\eta_2}{Y}\Big)\,. \tag{A.7}$$

Using the parity property of Chebyshev polynomials, $T_i(-x) = (-1)^i T_i(x)$, one obtains

$$\mathrm{Var}(n_B) = \langle n_B\rangle + \int_{\eta_F}^{\eta_F+\delta\eta} d\eta_1 \int_{\eta_F}^{\eta_F+\delta\eta} d\eta_2\ \rho(-\eta_1)\rho(-\eta_2) \sum_{i,k}\langle a_i a_k\rangle (-1)^{i+k}\, T_i\Big(\tfrac{\eta_1}{Y}\Big)\, T_k\Big(\tfrac{\eta_2}{Y}\Big)\,. \tag{A.8}$$

Finally, the covariance is given by form:

$$\begin{aligned}\mathrm{Cov}(n_F, n_B) &= \int_F d\eta_1 \int_B d\eta_2\, C(\eta_1,\eta_2) \\ &= \int_{\eta_F}^{\eta_F+\delta\eta} d\eta_1 \int_{\eta_F}^{\eta_F+\delta\eta} d\eta_2\ \rho(\eta_1)\rho(-\eta_2) \sum_{i,k}\langle a_i a_k\rangle (-1)^{k}\, T_i\Big(\tfrac{\eta_1}{Y}\Big)\, T_k\Big(\tfrac{\eta_2}{Y}\Big)\,.\end{aligned} \tag{A.9}$$

In the midrapidity region at the LHC ($|\eta| \lesssim 1$), the pseudorapidity density is nearly flat and symmetric, thus one can adopt the following approximation $\rho(\eta) \simeq \rho(-\eta) \equiv \rho_0$.

The variance of the difference can then be written as

$$\mathrm{Var}(n_F - n_B) = \mathrm{Var}(n_F) + \mathrm{Var}(n_B) - 2\,\mathrm{Cov}(n_F, n_B), \tag{A.10}$$

Combining the results for $\mathrm{Var}(n_F)$, $\mathrm{Var}(n_B)$, and $\mathrm{Cov}(n_F, n_B)$, expressed in terms of the Chebyshev expansion, gives the final expression:

$$\mathrm{Var}(n_F - n_B) = 2\langle n_F\rangle + \rho_0^2 \sum_{i,k} \langle a_i a_k\rangle \; f_{ik} \left[\int_{\eta_F}^{\eta_F+\delta\eta} T_i\Big(\tfrac{\eta}{Y}\Big)\, d\eta\right]\left[\int_{\eta_F}^{\eta_F+\delta\eta} T_k\Big(\tfrac{\eta}{Y}\Big)\, d\eta\right]. \tag{A.11}$$

Here, f_{ik} is the coefficient depending on the parity of the Chebyshev polynomial:

$$\boxed{f_{ik} \;\equiv\; 1 + (-1)^{i+k} - 2(-1)^k.} \tag{A.12}$$

The values of f_{ik} for the parities of (i, k) are:

	k even	k odd
i even	0	$+2$
i odd	-2	$+\mathbf{4}$

The mixed even-odd and odd-even contributions cancel after symmetrisation of the double sum ($\langle a_i a_k\rangle$=$\langle a_k a_i\rangle$ and products of integrals are symmetric). Hence only *odd-odd* pairs survive in (A.11), with prefactor 4:

$$\mathrm{Var}(n_F - n_B) = 2\langle n_F\rangle + 4\rho_0^2 \sum_{n,m\geq 0} \langle a_{2n+1} a_{2m+1}\rangle \; J_n\, J_m, \tag{A.13}$$

where J_n are integrals defined as:

$$J_n \;\equiv\; \int_{\eta_F}^{\eta_F+\delta\eta} T_{2n+1}\Big(\tfrac{\eta}{Y}\Big)\; d\eta. \tag{A.14}$$

A.3 Evaluating the window integrals J_n

Using the trigonometric identity $T_k(x) = \cos(k \arccos x)$ and the substitution $\eta = Y\cos\theta$ ($d\eta = -Y\sin\theta\, d\theta$), in integral over forward pseudorapidity window

$F = [\eta_F, \eta_F{+}\delta\eta]$ one gets:

$$J_n = \int_{\eta_F}^{\eta_F+\delta\eta} \cos\Big((2n{+}1)\arccos\tfrac{\eta}{Y}\Big)\, d\eta = Y \int_{\theta_2}^{\theta_1} \sin\theta\, \cos\Big((2n{+}1)\theta\Big)\, d\theta$$
$$= \frac{Y}{2}\left[\frac{\cos\big(2n\,\theta_1\big) - \cos\big(2n\,\theta_2\big)}{2n} - \frac{\cos\big((2n{+}2)\theta_1\big) - \cos\big((2n{+}2)\theta_2\big)}{2n{+}2}\right], \qquad (n \geq 1), \tag{A.15}$$

with $\theta_1 = \arccos\Big(\frac{\eta_F}{Y}\Big)$, $\theta_2 = \arccos\Big(\frac{\eta_F+\delta\eta}{Y}\Big)$. For $n = 0$ the regularised limit yields

$$J_0 \;=\; \frac{Y}{2}\Big[\sin^2\theta_1 - \sin^2\theta_2\Big]. \tag{A.16}$$

A particularly transparent case is the half-acceptance window $F = [0, Y]$ (and $B = [-Y, 0]$), for which $\theta_1 = \frac{\pi}{2}$, $\theta_2 = 0$ and one finds the compact values

$$J_0 \;=\; \frac{Y}{2}, \qquad J_n \;=\; Y\,\frac{(2n{+}1)(-1)^n - 1}{4n(n{+}1)} \quad (n \geq 1). \tag{A.17}$$

It is convenient to define $J_n^* \equiv J_n/Y$, i.e. $J_0^* = \frac{1}{2}$, $J_1^* = -\frac{1}{2}$, $J_2^* = \frac{1}{6}$, $J_3^* = -\frac{1}{8}, \ldots$

A.5 Final expression for $\Sigma^{n_F n_B}$

With $\langle n_F \rangle = \rho_0\, \delta\eta$ and Eq. (A.13), the $\Sigma^{n_F n_B}$ becomes

$$\boxed{\Sigma^{n_F n_B} = 1 \;+\; \frac{2\rho_0}{\delta\eta} \sum_{n,m\geq 0} \langle a_{2n+1} a_{2m+1} \rangle\, J_n\, J_m = 1 \;+\; \frac{2\rho_0 Y^2}{\delta\eta} \sum_{n,m\geq 0} \langle a_{2n+1} a_{2m+1} \rangle\, J_n^* J_m^*.} \tag{A.18}$$

For the symmetric choice $F = [0, Y]$, $B = [-Y, 0]$ (so $\delta\eta = Y$) and using (A.17):

$$\boxed{\Sigma^{n_F n_B} = 1 \;+\; 2\rho_0 Y \sum_{n,m\geq 0} \langle a_{2n+1} a_{2m+1} \rangle\, J_n^* J_m^*, \qquad J_0^* = \tfrac{1}{2},\; J_1^* = -\tfrac{1}{2},\; J_2^* = \tfrac{1}{6}, \ldots} \tag{A.19}$$

Remarks: (i) Only odd Chebyshev modes (asymmetry) contribute to $\mathrm{Var}(n_F{-}n_B)$ due to parity, with an overall factor 4 from f_{ik}. (ii) If the average single-particle density $\rho(\eta)$ is not constant but remains an even function, $\rho(-\eta) = \rho(\eta)$, and the forward/backward intervals are mirror-symmetric, the parity argument above still applies and only odd Chebyshev modes contribute to $\mathrm{Var}(n_F{-}n_B)$ and $\Sigma^{n_F n_B}$; the effect of the η-dependence enters solely through

the weighted integrals:

$$J_n^{(\rho)} = \int_F \rho(\eta)\, T_{2n+1}\left(\frac{\eta}{Y}\right)\, d\eta$$

and the mean multiplicity $\langle n_F \rangle$.

Appendix B

Properties and limitations of the Δ quantity in the wounded constituent model

B.1 Limitations of the Δ observable

The definition of the strongly intensive observable Δ, given in Eq. (3.53), includes the normalization factor

$$C_\Delta = \langle n_B \rangle - \langle n_F \rangle.$$

This quantity cannot be evaluated for collisions where

$$C_\Delta = 0 \quad \Longrightarrow \quad \langle n_F \rangle = \langle n_B \rangle,$$

which occurs, for example, in symmetric collision systems such as Pb–Pb, where the forward and backward pseudorapidity intervals are symmetric around midrapidity.
In systems where one expects $\langle n_F \rangle \neq \langle n_B \rangle$, like asymmetric p–Pb collisions, Δ in the wounded constituent model can be expressed in the general form as

$$\Delta = \frac{C \cdot f_1(\langle w_F \rangle, \langle w_B \rangle, \langle w_F^2 \rangle, \langle w_B^2 \rangle, \langle w_F w_B \rangle)}{C \cdot f_2(\langle w_F \rangle, \langle w_B \rangle)}, \tag{B.1}$$

where

- $C = 2p - 1$ is the *emission asymmetry parameter*,
- $f_1(\langle w_F \rangle, \langle w_B \rangle, \langle w_F^2 \rangle, \langle w_B^2 \rangle, \langle w_F w_B \rangle)$ and $f_2(\langle w_F \rangle, \langle w_B \rangle)$ are model-dependent functions of the wounded constituent distribution moments.

Indeterminacy of Δ for $C \to 0$

The expression for Δ becomes **undefined** in the limit $C \to 0$, i.e. when $p = 0.5$. In this case, the average multiplicities in the forward and backward windows coincide:

$$\langle n_F \rangle - \langle n_B \rangle = \mu(2p-1)(\langle w_F \rangle - \langle w_B \rangle).$$

Thus, for symmetric windows one finds

$$\langle n_F \rangle = \langle n_B \rangle \iff (2p-1)(\langle w_F \rangle - \langle w_B \rangle) = 0.$$

That is, either $p = 0.5$, or $\langle w_F \rangle = \langle w_B \rangle$, or both. Since the denominator $\langle n_B \rangle - \langle n_F \rangle$ vanishes, Δ is undefined. This happens not only in symmetric systems (Pb–Pb), but also in asymmetric ones (p–Pb) if $p = 0.5$.

B.2 Case: $C \neq 0$ and $\langle n_F \rangle \neq \langle n_B \rangle$

If $\langle n_F \rangle \neq \langle n_B \rangle$ and $C \neq 0$, the observable Δ takes the explicit form

$$\Delta = 1 + \frac{\bar{n}}{[\alpha_w C_- + C_+]\,[C_- + \alpha_w C_+]} \Bigg[\frac{4\alpha_w C^2}{k} + \frac{C_- C_+ (1+\alpha_w)}{\langle w_F \rangle} \left(\mathrm{Cov}(w_F, w_B) - \frac{\mathrm{Var}(w_B)}{\alpha_w} \right) + \Delta^{w_F w_B} \left(C_- C_+ + \alpha_w (1 + C^2) \right) \Bigg], \tag{B.2}$$

with

- $C_+ = 1 + C$,
- $C_- = 1 - C$,
- $\alpha_w = \frac{\langle w_B \rangle}{\langle w_F \rangle}$,
- $\Delta^{w_F w_B} = \frac{\mathrm{Var}(w_F)\cdot\alpha_w - \mathrm{Var}(w_B)\cdot\frac{1}{\alpha_w}}{\langle w_B \rangle - \langle w_F \rangle}$.

The function is even in C, decreases to a minimum as $C \to 0$, and increases with $|C|$, reaching

$$\Delta|_{C=\pm 1} = 1 + \bar{n}\left(\frac{1}{k} + \frac{\Delta^{w_F w_B}}{2} \right).$$

B.3 Special case: pA collisions in WNM

In the wounded nucleon model for proton–nucleus collisions, $\langle w_F \rangle = 1$. For $C \neq 0$ the formula simplifies to

$$\Delta_{\mathrm{pA}}^{\mathrm{WNM}} = 1 + \frac{\bar{n}}{[\langle w_B \rangle C_- + C_+]\,[C_- + \langle w_B \rangle C_+]} \times \left[\frac{4\langle w_B \rangle C^2}{k} - \frac{2\,\mathrm{Var}(w_B)}{\langle w_B \rangle} \left(C_- C_+ + \langle w_B \rangle \right) \right]. \tag{B.3}$$

Similarly to $\Sigma_{\mathrm{pA}}^{\mathrm{WNM}}$, the $\Delta_{\mathrm{pA}}^{\mathrm{WNM}}$ observable depends solely on the number of wounded nucleons in the nucleus and their fluctuations.

Appendix C

Properties of $\mathbb{E}[\mathrm{Var}(w_B - w_F \mid w)]$

To understand the role of the conditional variance term $\mathbb{E}[\mathrm{Var}(w_B - w_F \mid w)]$ in explaining the behaviour of Σ within the wounded constituent framework, we examine its statistical properties. The following steps demonstrate how this quantity can be approximated by the variance at a fixed average number of wounded nucleons, thereby explaining its robustness against changes in centrality class width and centrality selection method.
By statistical definition,

$$\boxed{\mathbb{E}[\mathrm{Var}(w_B - w_F \mid w)] = \sum_w P(w)\,\mathrm{Var}(w_B - w_F \mid w)} \tag{C.1}$$

where $P(w)$ is the distribution of the total number of wounded nucleons in the selected centrality class. This equality holds exactly and will serve as our starting point.
When $P(w)$ is narrow and approximately symmetric around its mean $\langle w \rangle$, $\mathrm{Var}(w_B - w_F \mid w)$ can be expanded in a Taylor series around $w = \langle w \rangle$:

$$\begin{aligned}\mathrm{Var}(w_B - w_F \mid w) \approx \mathrm{Var}(w_B - w_F \mid w = \langle w \rangle) + (w - \langle w \rangle)\,\frac{d}{dw}\mathrm{Var}(w_B - w_F \mid w)\Big|_{w=\langle w \rangle} \\ + \frac{1}{2}(w - \langle w \rangle)^2\,\frac{d^2}{dw^2}\mathrm{Var}(w_B - w_F \mid w)\Big|_{w=\langle w \rangle} + \dots\end{aligned} \tag{C.2}$$

Substituting into the sum over w, Eq. (C.1) gives:

$$\begin{aligned}\mathbb{E}[\mathrm{Var}(w_B - w_F \mid w)] \approx \mathrm{Var}(w_B - w_F \mid \langle w \rangle) \underbrace{\sum_w P(w)}_{=1} \\ + \frac{d}{dw}\mathrm{Var}(w_B - w_F \mid w)\Big|_{w=\langle w\rangle} \underbrace{\sum_w P(w)\,(w - \langle w\rangle)}_{=0} \\ + \frac{1}{2}\,\frac{d^2}{dw^2}\mathrm{Var}(w_B - w_F \mid w)\Big|_{w=\langle w\rangle} \underbrace{\sum_w P(w)\,(w - \langle w\rangle)^2}_{=\mathrm{Var}(w)} + \ldots\end{aligned} \tag{C.3}$$

The linear term vanishes because:

$$\sum_w P(w)\,(w - \langle w\rangle) \;=\; \sum_w P(w)\,w \;-\; \langle w\rangle \sum_w P(w) \;=\; \langle w\rangle - \langle w\rangle \cdot 1 \;=\; 0,$$

which follows directly from the definition of the mean $\langle w\rangle$. As a result:

$$\begin{aligned}\mathbb{E}[\mathrm{Var}(w_B - w_F \mid w)] \;\approx\; \mathrm{Var}(w_B - w_F \mid \langle w\rangle) + \\ + \;\frac{1}{2}\,\mathrm{Var}(w)\;\frac{d^2}{dw^2}\mathrm{Var}(w_B - w_F \mid w)\Big|_{w=\langle w\rangle} \;+\; \ldots\end{aligned} \tag{C.4}$$

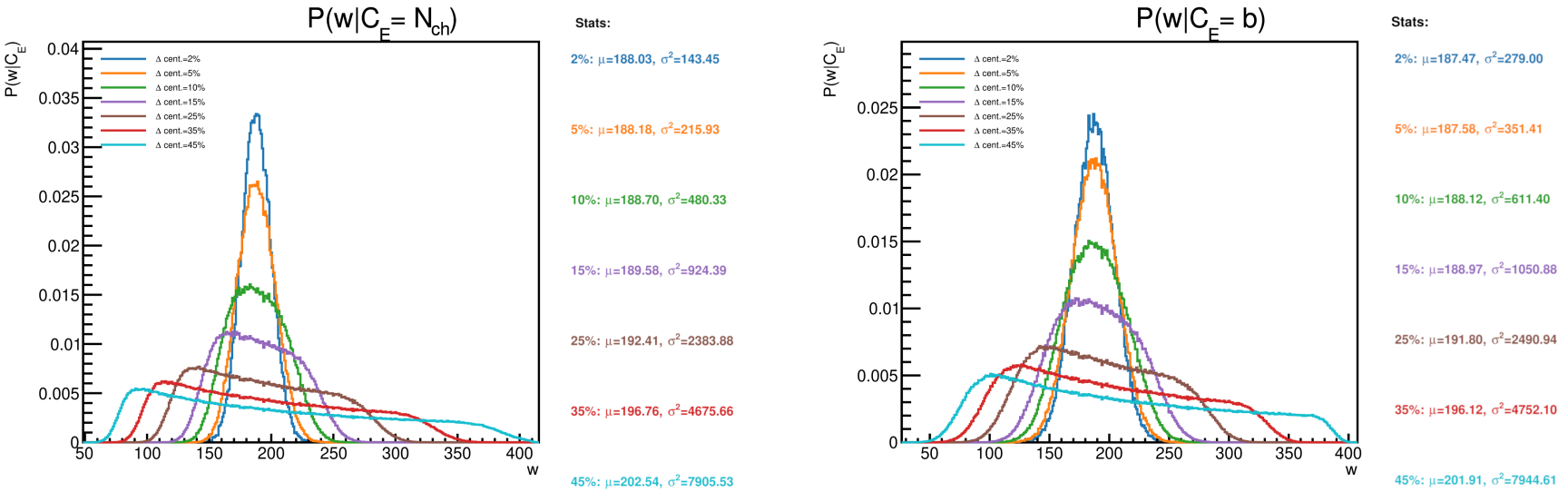

Figure C.1: Probability distributions $P(w \mid C_E)$ of the number of wounded nucleons w for different widths of centrality classes, defined using two centrality estimators C_E: cuts on charged-particle multiplicity N_{ch} (left) and cuts on impact parameter b (right). Different colours correspond to different centrality interval widths, all centred at a fixed centrality of 25%, with widths ranging from 2% to 45%. For each case, the mean value $\langle w \rangle$ and the variance $\sigma^2 = \mathrm{Var}(w)$ are listed. The mean values obtained with both estimators are nearly identical and evolve similarly with the bin width.

Appendix D

Derivation of Σ via the law of total variance and covariance

This appendix presents a general derivation of the quantity Σ assuming a multi-source scenario described in Chapter 7. The derivation uses only the law of total variance and the law of total covariance [127, 128], while allowing for correlations between different types of particle-emitting sources.

Definitions

Let the total number of particles in the forward and backward bins be denoted by:

$$n_F = \sum_{i=1}^{N_s} \sum_{k=1}^{s_i} \mu_F^{(i,k)}, \quad n_B = \sum_{i=1}^{N_s} \sum_{k=1}^{s_i} \mu_B^{(i,k)}, \tag{D.1}$$

where:

- s_i: number of sources of type i, fluctuating event by event,
- $\mu_F^{(i,k)}$, $\mu_B^{(i,k)}$: number of particles from the k-th source of type i going into the forward and backward pseudorapidity innterval.

All sources of a given type are assumed to be statistically identical, and all particle productions are independent across different source types.

Mean multiplicities

$$\langle n_F \rangle = \sum_{i=1}^{N_s} \langle s_i \rangle \langle \mu_F^{(i)} \rangle, \qquad \langle n_B \rangle = \sum_{i=1}^{N_s} \langle s_i \rangle \langle \mu_B^{(i)} \rangle$$

Variance of n_F and n_B

Using the law of total variance, one can express the variance of the number of particles n_F in terms of the conditional variance and mean, with constraints applied to the set of sources $\{s_i\}_{i=1}^{N_s} = (s_1, s_2, \ldots, s_{N_s})$, where s_i denotes the number of sources of type i in each event. The relation is given by:

$$\mathrm{Var}(n_F) = \mathbb{E}[\mathrm{Var}(n_F \mid \{s_i\})] + \mathrm{Var}\left(\mathbb{E}[n_F \mid \{s_i\}]\right),$$

which, based on Eq. (D.1), can be further expanded to:

$$\mathrm{Var}(n_F) = \sum_{i=1}^{N_s} \langle s_i \rangle \mathrm{Var}(\mu_F^{(i)}) + \sum_{i=1}^{N_s} \mathrm{Var}(s_i) \langle \mu_F^{(i)} \rangle^2 + \sum_{i \neq j} \mathrm{Cov}(s_i, s_j) \langle \mu_F^{(i)} \rangle \langle \mu_F^{(j)} \rangle \tag{D.2}$$

An analogous expression holds for $\mathrm{Var}(n_B)$.

Covariance Between n_F and n_B

Using the law of total covariance:

$$\mathrm{Cov}(n_F, n_B) = \mathbb{E}[\mathrm{Cov}(n_F, n_B \mid \{s_i\})] + \mathrm{Cov}\left(\mathbb{E}[n_F \mid \{s_i\}], \mathbb{E}[n_B \mid \{s_i\}]\right),$$

one can express covariance between the number of particles measured in forward and backward rapidity intervals $\mathrm{Cov}(n_F, n_B)$ as follows:

$$\mathrm{Cov}(n_F, n_B) = \sum_{i=1}^{N_s} \langle s_i \rangle \mathrm{Cov}(\mu_F^{(i)}, \mu_B^{(i)}) + \sum_{i=1}^{N_s} \mathrm{Var}(s_i) \langle \mu_F^{(i)} \rangle \langle \mu_B^{(i)} \rangle + \sum_{i \neq j} \mathrm{Cov}(s_i, s_j) \langle \mu_F^{(i)} \rangle \langle \mu_B^{(j)} \rangle \tag{D.3}$$

Definition of Σ

For symmetric forward and backward bins (i.e. $\langle n_F \rangle = \langle n_B \rangle$) the Σ quantity defined by Eq. (3.53) can be simplified to form:

$$\Sigma = \frac{\mathrm{Var}(n_F) + \mathrm{Var}(n_B) - 2\,\mathrm{Cov}(n_F, n_B)}{\langle n_F \rangle + \langle n_B \rangle}.$$

Final General Expression for Σ

Combining the expressions above X with ...yields:

$$\begin{aligned}\Sigma =&\frac{1}{M}\Bigg[\sum_{i=1}^{N_s}\langle s_i\rangle\left(\mathrm{Var}(\mu_F^{(i)})+\mathrm{Var}(\mu_B^{(i)})-2\mathrm{Cov}(\mu_F^{(i)},\mu_B^{(i)})\right)\\&+\sum_{i=1}^{N_s}\mathrm{Var}(s_i)\left(\langle\mu_F^{(i)}\rangle-\langle\mu_B^{(i)}\rangle\right)^2\\&+\sum_{i\neq j}^{N_s}\mathrm{Cov}(s_i,s_j)\left(\langle\mu_F^{(i)}\rangle\langle\mu_F^{(j)}\rangle+\langle\mu_B^{(i)}\rangle\langle\mu_B^{(j)}\rangle-2\langle\mu_F^{(i)}\rangle\langle\mu_B^{(j)}\rangle\right)\Bigg],\end{aligned}\tag{D.4}$$

where

$$M\ \equiv\ \sum_{k=1}^{N_s}\langle s_k\rangle\Big(\langle\mu_F^{(k)}\rangle+\langle\mu_B^{(k)}\rangle\Big).$$

This expression can be algebraically transformed into a more compact and physically transparent form:

$$\begin{aligned}\Sigma =& \frac{1}{M}\Bigg[\sum_{i=1}^{N_s}\underbrace{\langle s_i\rangle\Big(\mathrm{Var}(\mu_F^{(i)})+\mathrm{Var}(\mu_B^{(i)})-2\,\mathrm{Cov}(\mu_F^{(i)},\mu_B^{(i)})\Big)}_{\langle s_i\rangle(\langle\mu_F^{(i)}\rangle+\langle\mu_B^{(i)}\rangle)\frac{\mathrm{Var}(\mu_F^{(i)})+\mathrm{Var}(\mu_B^{(i)})-2\mathrm{Cov}(\mu_F^{(i)},\mu_B^{(i)})}{\langle\mu_F^{(i)}\rangle+\langle\mu_B^{(i)}\rangle}}\\&+\sum_{i=1}^{N_s}\mathrm{Var}(s_i)(\langle\mu_F^{(i)}\rangle-\langle\mu_B^{(i)}\rangle)^2+\sum_{\substack{i,j=1\\i\neq j}}^{N_s}\mathrm{Cov}(s_i,s_j)(\langle\mu_F^{(i)}\rangle-\langle\mu_B^{(i)}\rangle)(\langle\mu_F^{(j)}\rangle-\langle\mu_B^{(j)}\rangle)\Bigg]\\=&\sum_{i=1}^{N_s}\underbrace{\frac{\langle s_i\rangle(\langle\mu_F^{(i)}\rangle+\langle\mu_B^{(i)}\rangle)}{M}}_{\xi_i^{(I)}}\underbrace{\frac{\mathrm{Var}(\mu_F^{(i)})+\mathrm{Var}(\mu_B^{(i)})-2\,\mathrm{Cov}(\mu_F^{(i)},\mu_B^{(i)})}{\langle\mu_F^{(i)}\rangle+\langle\mu_B^{(i)}\rangle}}_{E_i}\\&+\sum_{i=1}^{N_s}\underbrace{\frac{(\langle\mu_F^{(i)}\rangle-\langle\mu_B^{(i)}\rangle)^2}{M}}_{\xi_i^{(II)}}\mathrm{Var}(s_i)\\&+\sum_{1\leq i<j\leq N_s}2\underbrace{\frac{(\langle\mu_F^{(i)}\rangle-\langle\mu_B^{(i)}\rangle)(\langle\mu_F^{(j)}\rangle-\langle\mu_B^{(j)}\rangle)}{M}}_{\xi_{ij}^{(III)}}\mathrm{Cov}(s_i,s_j)\\=&\sum_{i=1}^{N_s}\xi_i^{(I)}E_i+\sum_{i=1}^{N_s}\xi_i^{(II)}\mathrm{Var}(s_i)+\sum_{1\leq i<j\leq N_s}2\,\xi_{ij}^{(III)}\mathrm{Cov}(s_i,s_j).\end{aligned}\tag{D.5}$$

The expression Eq. (D.5) is the most general form of Σ within the multi-source superposition framework for symmetric collisions, valid for any number and type of

sources, assuming only statistical independence of emissions from different sources and the applicability of the law of total variance and covariance.

Appendix E

Multi-source superposition as a unifying framework for particle production models

The following appendix introduces specific assumptions regarding the nature of the sources and their emission characteristics. Under these assumptions, various commonly studied particle production models, such as the Wounded Nucleon (or Quark) Model and string-based models, emerge as special cases of the generalised superposition framework derived in Chapter 7. This illustrates how different physical scenarios can be derived from the same underlying statistical structure by appropriately specifying the source dynamics and composition.

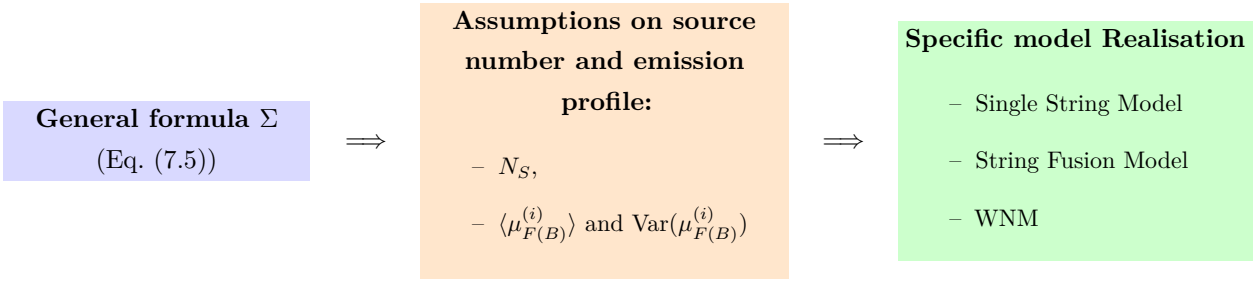

E.1 One-source-type model

The simplest case within the generalised framework corresponds to a system where all particles originate from a single type of source ($N_S = 1$). This scenario fulfils the assumptions of Independent Source Model, introduced in Ref. [3], in which the Σ observable reflects only the intrinsic forward-backward fluctuations of individual sources.

In symmetric collisions, with forward and backward intervals located at equal distances from $\eta = 0$, the condition of forward–backward symmetry in particle production, $\langle n_F \rangle = \langle n_B \rangle$, implies that for $N_S = 1$ the source[1] must, on average, emit

[1]Since only a single source type is considered, the source index i is omitted for clarity.

particles symmetrically:

$$\langle \mu_F \rangle = \langle \mu_B \rangle, \qquad \mathrm{Var}(\mu_F) = \mathrm{Var}(\mu_B).$$

Under this condition it is easy to show, the general expression for Σ, Eq. 7.5, simplifies significantly:

$$\Sigma = E_1 = \Sigma^{\mu_F \mu_B}$$

to the strongly intensive observable $\Sigma^{\mu_F \mu_B}$ defined for a single emission source.
In this case, the Σ value is independent of system size, as no contribution arises from source number fluctuations or relative fluctuations between source types. Hence, any observed centrality or system-size dependence of Σ would signal a violation of ISM assumptions.

Realisation: Independent Identical String Model

The model introduced in Ref. [110] provides a clear realisation of the one-source scenario, $N_S = 1$. In this framework, a single type of string source is considered, where each string emits particles independently into the forward and backward bins with identical statistical properties. The emission from a single string is expressed in terms of the normalised two-particle string correlation function $\Lambda(\Delta\eta)$, which quantifies correlations between particles emitted from the same string as a function of their rapidity separation.
The average multiplicity and correlations from a single source are parametrised as follows:

Quantity	**Formula**	
$\langle \mu_F \rangle$	$\mu_0 \delta\eta \quad \rightarrow$	where μ_0 is a distribution density of particles from single string
$\langle \mu_B \rangle$	$\mu_0 \delta\eta \quad \rightarrow$	$\delta\eta$ is the width of pseudorapidity interval
$\mathrm{Var}(\mu_F)$	$\langle \mu_F \rangle \left(1 + \langle \mu_F \rangle \Lambda(0)\right)$	
$\mathrm{Var}(\mu_B)$	$\langle \mu_B \rangle \left(1 + \langle \mu_B \rangle \Lambda(0)\right)$	
$\mathrm{Cov}(\mu_F, \mu_B)$	$\langle \mu_F \rangle^2 \Lambda(\Delta\eta) \quad \rightarrow$	for not overlapping F and B intervals

Substituting the above expressions into the general formula for Σ given by Eq. (7.5) yields:

$$\Sigma = \underbrace{1 + \mu_0 \delta\eta \left(\Lambda(0) - \Lambda(\Delta\eta)\right)}_{E_1 = \Sigma^{\mu_F \mu_B}}, \tag{E.1}$$

which is a formula Eq. (31) derived within the string model in the paper Ref. [110].

E.2 Multi-source-type model under the forward-backward constraint of emission symmetry

A natural extension of the single-source scenario involves a framework with multiple distinct source types, $N_S > 1$. Here, we consider that all sources emit particles symmetrically into forward and backward pseudorapidity intervals, which immediately implies $A_i = \langle \mu_F^{(i)} \rangle - \langle \mu_B^{(i)} \rangle = 0$ for all i.

This constraint has an important consequence: all fluctuation terms in the general expression for Σ that depend on forward–backward asymmetries of the source emission vanish. In particular, the coefficients multiplying $\mathrm{Var}(s_i)$ and $\mathrm{Var}(s_i - s_j)$ (i.e. the $\xi_i^{(II)}$ and $\xi_{ij}^{(III)}$ contributions) become zero.

As a result, under the symmetry condition the observable Σ receives weighted contributions exclusively from intrinsic emission fluctuations of each source type E_i:

$$\Sigma \;=\; \sum_{i=1}^{N_S} \xi_i^{(I)}\, \Sigma^{\mu_F^{(i)} \mu_B^{(i)}}. \tag{E.2}$$

It is evident that in this scenario, Σ is **not** a strongly intensive quantity, since the weighting terms $\xi_i^{(I)}$ depend explicitly on the average number of sources of type i. As a result, Σ becomes sensitive to the relative abundances of different source types, which may in turn depend on system size or centrality. Eq. (E.2) shows that Σ characterises the fluctuations of an effective source, obtained as a weighted average of the different source types according to their relative contributions to the total particle production.

Realisation: Simple string-fusion model

The string fusion scenario proposed in Ref [110] provides a simple realisation of multi-source pictures with symmetric emission for each of the different string types. In this framework, several colour strings, when they overlap in the transverse plane, coalesce into a cluster that fragments as a *single, higher-rank source*. Clusters composed of i elementary strings are treated as distinct source types ($i = 1, 2, \ldots, N_S$), each characterised by on average symmetric FB emission.

The fusion process reduces the total number of independent sources and creates new source types corresponding to clusters formed by i overlapping elementary strings. This process modifies both the mean multiplicity and the two-particle correlation function $\Lambda^{(i)}(\Delta\eta)$, affecting both correlation strength and length [110].

The average multiplicity and correlations from a single string of type i (class of i fused single strings) are parametrised as follows:

Quantity	**Formula**	
$\langle \mu_F^{(i)} \rangle$	$\mu_0^{(i)} \delta\eta \quad \rightarrow$	where $\mu_0^{(i)}$ is a distribution density of particles from string type i
$\langle \mu_B^{(i)} \rangle$	$\mu_0^{(i)} \delta\eta \quad \rightarrow$	$\delta\eta$ is the width of pseudorapidity interval
$\mathrm{Var}(\mu_F^{(i)})$	$\langle \mu_F^{(i)} \rangle \left(1 + \langle \mu_F^{(i)} \rangle \Lambda^{(i)}(0)\right)$	
$\mathrm{Var}(\mu_B^{(i)})$	$\langle \mu_B^{(i)} \rangle \left(1 + \langle \mu_B^{(i)} \rangle \Lambda^{(i)}(0)\right)$	
$\mathrm{Cov}(\mu_F^{(i)}, \mu_B^{(i)})$	$\langle \mu_F^{(i)} \rangle^2 \Lambda^{(i)}(\Delta\eta)$	

For symmetric collisions, the final expression for Σ takes the form:

$$\Sigma = \sum_{i=1}^{N_S} \xi_i^{(I)} \underbrace{\left(1 + \mu_0^{(i)} \delta\eta \left[\Lambda^{(i)}(0) - \Lambda^{(i)}(\Delta\eta)\right]\right)}_{\Sigma^{\mu_F^{(i)} \mu_B^{(i)}}}. \tag{E.3}$$

which coincides with the formula Eq. (82) for Σ derived in Ref. [110].

E.3 Two-source model with asymmetric forward–backward emission

In contrast to the two frameworks discussed in the previous sections, particle production may also originate from sources with asymmetric emission profiles into F and B pseudorapidity intervals, $\langle \mu_F^{(i)} \rangle \neq \langle \mu_B^{(i)} \rangle$. In this section, we focus on a scenario involving two such source types, s_1 and s_2. For two types of sources, $N_S = 2$, the general formula Eq. (7.5) reduces to the expression:

$$\begin{aligned} \Sigma = {} & \xi_1^{(I)} E_1 + \xi_2^{(I)} E_2 \\ & + \left[\xi_1^{(II)} + \xi_{12}^{(III)}\right] \mathrm{Var}(s_1) \\ & + \left[\xi_2^{(II)} + \xi_{21}^{(III)}\right] \mathrm{Var}(s_2) \\ & - \frac{1}{2}\left(\xi_{12}^{(III)} + \xi_{21}^{(III)}\right) \mathrm{Var}(s_1 - s_2). \end{aligned} \tag{E.4}$$

It is easy to verify that the terms proportional to $\mathrm{Var}(s_1)$ and $\mathrm{Var}(s_2)$ disappear when the corresponding combinations of coefficients satisfy the condition:

$$\xi_i^{(II)} + \frac{1}{2}\left(\xi_{12}^{(III)} + \xi_{21}^{(III)}\right) = 0. \tag{E.5}$$

This simplification applies when the average forward-backward emissions of both

sources are related by symmetry, such that

$$\langle \mu_F^{(1)} \rangle - \langle \mu_B^{(1)} \rangle = -\left(\langle \mu_F^{(2)} \rangle - \langle \mu_B^{(2)} \rangle \right).$$

Under this condition, only the fluctuation term proportional to $\mathrm{Var}(s_1 - s_2)$ remains, representing fluctuations of the forward-backward source imbalance. This particular scenario is realised in the wounded constituent model discussed in Chapter 6.

Realisation: Wounded Constituent Model

The Wounded Constituent Model, introduced in detail in Chapter 6, can be understood as a specific realisation of the general multi-source superposition framework developed in Chapter 7.

In this scenario, particle production originates from two types of wounded constituents: forward-moving and backward-moving. We denote by s_1 the number of forward-moving wounded constituents and by s_2 the number of backward-moving wounded constituents.

Each wounded constituent contributes particles to the sum of F+B intervals according to a distribution that can be characterised by mean,$\langle \mu_0 \rangle$ and variance $\mathrm{Var}(\mu_0)$. The emission between the two bins follows a binomial splitting with probability p for forward-moving sources (and symmetrically for backward-moving sources), as described in Refs. [122, 116, 5]. The emission profile characteristics of wounded constituents are:

Quantity	**Formula**	**Quantity**	**Formula**
$\langle \mu_F^{(1)} \rangle$	$p\langle \mu_0 \rangle$	$\langle \mu_B^{(1)} \rangle$	$(1-p)\langle \mu_0 \rangle$
$\langle \mu_F^{(2)} \rangle$	$(1-p)\langle \mu_0 \rangle$	$\langle \mu_B^{(2)} \rangle$	$p\langle \mu_0 \rangle$
$\mathrm{Var}(\mu_F^{(1)})$	$p(1-p)\langle \mu_0 \rangle + p^2\,\mathrm{Var}(\mu_0)$	$\mathrm{Var}(\mu_B^{(1)})$	$p(1-p)\langle \mu_0 \rangle + (1-p)^2\,\mathrm{Var}(\mu_0)$
$\mathrm{Var}(\mu_F^{(2)})$	$p(1-p)\langle \mu_0 \rangle + (1-p)^2\,\mathrm{Var}(\mu_0)$	$\mathrm{Var}(\mu_B^{(2)})$	$p(1-p)\langle \mu_0 \rangle + p^2\,\mathrm{Var}(\mu_0)$
$\mathrm{Cov}(\mu_F^F, \mu_B^F)$	$p(1-p)\left(\mathrm{Var}(\mu_0) - \langle \mu_0 \rangle\right)$	$\mathrm{Cov}(\mu_F^B, \mu_B^B)$	$p(1-p)\left(\mathrm{Var}(\mu_0) - \langle \mu_0 \rangle\right)$

From the wounded constituents' emission profile characteristics listed in the Table above, it is evident that:

- in this framework, the emission averages satisfy the relations $\langle \mu_F^{(1)} \rangle = \langle \mu_B^{(2)} \rangle$ and $\langle \mu_F^{(2)} \rangle = \langle \mu_B^{(1)} \rangle$, which naturally fulfil the condition of Eq. (E.5).
- for symmetric collisions, $\langle s_1 \rangle = \langle s_2 \rangle$, the general expression, Eq. (7.5), on Σ within multi-source superposition model reduces to the form:

$$\Sigma = 4p(1-p) + (2p-1)^2 \cdot \frac{\mathrm{Var}(\mu_0)}{\langle \mu_0 \rangle} + \frac{(2p-1)^2 \langle \mu_0 \rangle}{2\langle s_1 \rangle} \cdot \mathrm{Var}(s_1 - s_2).$$

  Here, we make no assumptions about the specific form of the emission distribution for a wounded constituent. The Σ quantity depends only on $\langle \mu_0 \rangle$, and $\mathrm{Var}(\mu_0)$, regardless of assumed distribution shape.

Negative Binomial emission: Assuming that the number of particles produced by each wounded constituent follows a NBD (Eq. (6.2)), with parameters obtained from pp data in the combined $F + B$ interval, one has:

$$\langle \mu_0 \rangle = \frac{\bar{n}}{2}, \qquad \mathrm{Var}(\mu_0) = \frac{\bar{n}}{2} + \frac{(\bar{n}/2)^2}{k/2}, \tag{E.6}$$

where $\bar{n}$ and k refer to the fit of the multiplicity distribution in the whole $F + B$ interval in pp collisions. Substituting these into the expression for Σ gives:

$$\Sigma = 1+(2p-1)^2 \cdot \frac{\bar{n}}{k} + \frac{(2p-1)^2\,\bar{n}}{4\langle s_1 \rangle} \cdot \mathrm{Var}(s_1 - s_2) = 1+(2p-1)^2 \cdot \frac{\bar{n}}{2} \cdot \left(\frac{2}{k} + \frac{\mathrm{Var}(s_1 - s_2)}{2\langle s_1 \rangle} \right). \tag{E.7}$$

In the present section we denote the numbers of sources of type 1 and type 2 by s_1 and s_2, respectively. These correspond directly to the quantities w_F and w_B used in Chapter 6:

$$s_1 \equiv w_F, \qquad s_2 \equiv w_B.$$

With this identification, the above expression for Σ is in full agreement with Eq. (6.5).

Parametrisation of intrinsic emission and correlation inputs

The model calculations presented in Chapter 7 require specifying the intrinsic emission properties of each source type. For string-based scenarios, the forward–backward correlation structure of a single string is parametrised using the exponential form introduced in Ref. [110]:

$$\Lambda(\Delta\eta) = \Lambda_0 \, \exp\left(-\frac{|\Delta\eta|}{\eta_{\mathrm{corr}}} \right). \tag{E.8}$$

Here, Λ_0 denotes the correlation amplitude at zero separation and η_{corr} is the characteristic correlation length.

In the String Fusion Model, a cluster of i overlapping strings is treated as an effective source with modified multiplicity and correlation scale, following Ref. [110]:

$$\Lambda^{(i)}(\Delta\eta) = \Lambda_0^{(i)} \, \exp\left(-\frac{|\Delta\eta|}{\eta_{\mathrm{corr}}^{(i)}} \right), \qquad \Lambda_0^{(i)} = \Lambda_0, \qquad \eta_{\mathrm{corr}}^{(i)} = \frac{\eta_{\mathrm{corr}}}{\sqrt{i}}. \tag{E.9}$$

The numerical values of all intrinsic emission parameters used in the WNM, Single String Model, and String Fusion Model are listed in Table E.1. Only intrinsic (per–source) emission and correlation parameters are included; geometry-dependent quantities such as the number of sources or fusion-cluster composition are not part of this table.

Model	**Mean multiplicity**	**Correlation amplitude** Λ_0	**Correlation length** η_{corr}
WNM	$\overline{n} = 1.94$ $k = 1.2$ $p = 0.64$	—	—
Single String	$\mu_0 = 0.8$	0.55	1.43
String Fusion	$\mu_0^{(i)} = 0.8\sqrt{i}$	$\Lambda_0^{(i)} = 0.55$	$\eta_{\text{corr}}^{(i)} = 1.43/\sqrt{i}$

Table E.1: The lists all numerical parameters used in the WNM, Single String, and String Fusion model realisations presented in Chapter 7. These values define the emission strengths and correlation scales required to reproduce the model curves in Fig. 7.2.